Universitat de Barcelona

Oscillatory pipe flow of wormlike micellar solutions

Laura Casanellas Vilageliu

Oscillatory pipe flow of wormlike micellar solutions

PhD Thesis

Laura Casanellas Vilageliu

Advisor: Dr. Jordi Ortín Rull

Barcelona, January 2013

Programa de Doctorat en Física

Departament d'Estructura i Constituents de la Matèria

La paciència i la persistència són les mares de la ciència

(Dita popular versionada)

Agraïments

Quan vaig anar a parlar per primera vegada amb el meu director de tesi, em va ensenyar el video de l'Hormiguero en què el presentador corre per sobre d'una piscina plena d'un fluid grogós i no s'enfonsa. Aquest primer contacte amb els fluids no-Newtonians, fins llavors completament desconeguts per mi, em va fascinar. Mica en mica m'he adonat que efectivament aquests fluids omplen el nostre dia a dia i que entendre el seu comportament pot ser molt rellevant a nivell pràctic, però també des d'un punt de vista més fonamental. Després, quan la gent que he anat coneixent durant els anys del doctorat em preguntava, "i tu què fas?", els ensenyava il·lusionada aquest mateix video.

La recerca que he fet durant aquests anys ha estat majoritàriament experimental. Això ha significat passar hores al laboratori a prop de l'experiment i preparant el fluid que estàvem estudiant. Crec que hi ha pocs físics que tinguin l'oportunitat de *veure* la recerca que duen a terme, i per mi ha estat sens dubte un privilegi. Llegint tesis anteriors d'altres companys m'he adonat que hi ha vivències que estant íntimament lligades a una tesi experimental. Hi ha alts i baixos, quan el sistema experimental deixa de funcionar o quan els temps d'entrega dels proveïdors s'eternitzen. Però també hi ha una alegria immensa quan els experiments surten com esperaves i una gran satisfacció en veure que la teva investigació aporta un petit granet de sorra al progrés científic. També hi ha una vessant més humana que en el meu cas ha estat la companyonia al laboratori, les reunions amb el director de tesi, els congressos i estades internacionals, les converses amb el mecànic, o les trucades al tècnic del reòmetre. En aquest aspecte més personal voldria agrair a continuació a un conjunt de persones la seva contribució, d'una manera o una altra, a aquesta Tesi.

En primer lloc vull agrair al meu director, el Prof. Jordi Ortín, el suport incondicional que m'ha donat durant tots aquests anys, així com el seguiment constant del treball que he realitzat. També, la motivació que m'ha encomanat per fer recerca, i la manera de fer les coses sempre molt curosa. Ha estat també molt valuós l'aprenentatge en l'escriptura de treballs científics, asseguts un al costat de l'altre al seu despatx, i sens dubte la correcció d'aquest mateix manuscrit.

En segon lloc m'agradaria agrair als companys i companyes del departament

els bons moments que hem passat junts. En particular, als meus col·legues de laboratori: en Ramon Planet als inicis i en Xavier Clotet després, amb qui he compartit moltes hores al laboratori, sovint a les fosques, i amb un soroll de fons prou insuportable. Merci per totes les taques d'oli de silicona que he col·leccionat als pobres pantalons! Per descomptat també a tots els cohabitants del despatx, que no han estat pocs, els veïns del despatx del costat, i els amics i amigues amb els que hem anat a dinar cada dia, en busca del menú més "suculent": Pau Bitlloch, Jordi Soriano, Guillermo Rodríguez, Carles Blanch, Oriol Ríos, Claudia Trejo, Xavier Fontané, Marta Manzanares, Rodrigo Ledesma i Marc Pradas, i perdoneu que no us pugui mencionar a tota la resta.

També voldria donar les gràcies a tots els investigadors amb els que he tingut l'oportunitat de discutir sobre la nostra recerca: en Jaume Casademunt, en Laureano Ramírez i l'Esteban Meca, i també inicialment en Carles Panadès i en Francisco Marquès. I'd like to thank Alexander Morozov for the interest he has shown in our experimental research during his visits to Barcelona and in several international meetings. Thank you also for suggesting me to go to MIT for my research stays.

I had an excellent experience at MIT. I really want to thank Prof. Gareth H. McKinley for his invaluable guidance, kind advice, and the fruitful collaboration that we started. It was also a great pleasure for me to work with Chris Dimitriou and Thomas Ober. I'd like to thank also all the other people from NNF, specially Aditya Jaishankar, Bavand Keshavarz and Simon Haward, for making me feel as part of the group.

Els experiments realitzats durant la Tesi han estat possibles gràcies al suport tècnic rebut per part de l'equip del Taller mecànic del CCITUB, del qual voldria agrair especialment la dedicació d'en Manel Quevedo, així com el disseny electrònic realitzat per l'Albert Comerma. También querría agradecer a Roberto Steinbrüggen, de la empresa Haake, el soporte técnico tan constante que siempre nos ha proporcionado y la disponibilidad que nos ha ofrecido para poder realizar medidas en su laboratorio.

I finalment voldria agrair a totes les persones amb les que he conviscut aquests darrers anys i que m'han animat al llarg de la tesi, preguntant-me com m'anaven els experiments, prenent cafès i gots de vi, i en definitiva, compartint penes i alegries. Elles són totes les amigues farmacèutiques, les bruixes, els compis de pis, els companys de la carrera i moltes més, que ara em deixo. També vull agrair a la meva família el recolzament, confiança i ànim! que sempre m'han donat, i molt especialment durant tots aquests anys de tesi. I un darrer agraïment molt especial se'l mereix en Bruno. Gràcies per estar al meu costat tot aquest temps, fer-me veure les coses amb més humor i animar-me a seguir endavant, encara una mica més!

Aquesta tesi ha estat possible gràcies a la beca de Formació del Professorat Universitari que em va ser concedida pel Ministeri d'Educació, a una beca de col·laboració amb el Departament d'Estructura i Constituents de la Matèria de la Universitat de Barcelona, i al finançament rebut de la Generalitat de Catalunya (2009SGR00014) i del Ministeri d'Educació (FIS2006-03525 i FIS2010-21924-C02-02) al Grup de Recerca en Física no Lineal.

Barcelona, 25 de gener de 2013

Contents

Outline of the Thesis

The goal of this Thesis is to study the oscillatory pipe flow of wormlike micellar solutions. We analyze the laminar oscillatory flow of viscoelastic fluids using the Maxwell and Oldroyd-B models. The theoretical predictions obtained for the laminar velocity profiles are validated by carrying out time-resolved Particle Image Velocimetry (PIV) experiments in a vertical pipe at small driving amplitudes. Increasing the amplitude of the oscillations the laminar flow evolves towards more complex flows, both in space and time. We study experimentally the transition from laminar to vortical flows, in which axisymmetric vortex rings are formed, and the transition to non-axisymmetric flows, observed at even larger driving amplitudes.

The Thesis is organized as follows. We first review in Chap. 1 some of the basic concepts needed to understand the research undertaken. In Sec. 1.1 we present the main properties of complex fluids and in particular of wormlike micellar solutions. In Sec. 1.3 basic notions of rheology are introduced, including well-known constitutive models for viscoelastic fluids, rheometric tests that are commonly used to characterize the linear and non-linear rheology of these fluids, as well as flow visualization techniques required to gain spatial information of the flow. We end this first chapter by reviewing in Sec. 1.4 previous theoretical and experimental work on wall-bounded oscillatory flows, both for Newtonian and complex fluids.

An important part of the work developed in this Thesis has been the design, construction and calibration of the system that generates the oscillatory motion of the fluid, as well as the implementation of the PIV technique used to measure the fluid velocity in a meridional plane of the tube. An extensive description of the experimental setup and the measuring method is provided in Chap. 2.

The rheological characterization of the micellar solutions used in the experiments is presented in Chap. 3.

Chapter 4 is devoted to the characterization of the laminar oscillatory flow of wormlike micellar fluids in a vertical pipe. This problem is addressed theoretically in Sec. 4.1. We focus in two different ideal situations: the laminar oscillatory flow generated by the synchronous oscillation of two infinite parallel plates, and

the laminar flow in an infinitely long vertical pipe when the oscillatory motion is induced by the synchronous oscillation of the top and bottom ends. In order to describe the viscoelastic properties of the fluid we use the upper-convected Maxwell and the Oldroyd-B constitutive equations. In Sec. 4.2 we do a quantitative comparison of our theoretical predictions with the experimental results of the piston-driven laminar oscillatory flow of a CPyCl/NaSal [100:60] mM solution in a vertical cylinder of large aspect ratio.

In Chaps. 5 and 6 we focus on the transition from laminar to more complex flows at controlled forcings.

We first analyze the flow behavior at local scale. We construct an stability phase diagram (Sec. 5.1) for thew whole range of accessible driving parameters. In Sec. 5.3 we characterize the onset of the hydrodynamic instability that gives rise to the generation of vortex rings and perform a quantitative analysis of the vortical flow. In Sec. 5.4 we extend the analysis to non-axisymmetric flows generated at larger forcings.

The vortical flow presents a large scale spatial organization all over the tube length (Sec. 6.1) as well as interesting dynamic flow behavior at long time scales (Sec. 6.2). Chapter 6 ends with a discussion of potential instability mechanisms that may be responsible for the instability of the laminar flow.

The conclusions of the Thesis are drawn in Chap. 7.

Finally, to fulfill the requirements of the University of Barcelona, in Chap. 8 we enclose a summary of the Thesis in Catalan. In this summary we briefly review the introductory concepts, describe the experimental setup, and report the most relevant results.

This document includes also a list of the publications produced during the Thesis, and three Appendices that provide useful additional information. In Appx. A we present a detailed derivation of the tensors required for the theoretical analysis of the laminar oscillatory flow addressed in Sec. 4.1. In Appx. B we report on the Stereo-PIV system that is currently being implemented in the laboratory. And in Appx. C we provide complementary results, obtained in Prof. McKinley's laboratory at MIT, on the transient shear flow of wormlike micellar solutions in a cone-plate geometry.

Chapter 1

Introduction

The study of fluid mechanics received a growing interest by the end of the XVIIth century. At that time Newton wrote the *Principia* (1687), in which he regarded fluids as continuous media and stated that *the resistance arising from the want of slipperiness in the parts of a fluid is, other things being equal, proportional to the velocity with which the parts of the fluid separate from one another*. Nowadays, this relation is known as the Newtonian equation, and the constant of proportionality is the shear viscosity. Some decades later Bernouilli devoted himself to the study of flow in tubes, and developed Bernoulli's theorem about the conservation of *living forces*, which first appeared in his *Hydrodynamica* in 1738. His contemporary d'Alembert also did a great contribution to the field, developing mathematical equations governing irrotational flows of incompressible fluids as well as a field description of media in motion. Euler pursued the study of fluid motion. He published several articles within 1752 and 1761 in which he presented the equation of continuity, introduced the concept of fluid pressure, and derived the dynamical equations for ideal fluids. It was not until 1820, when Navier established the dynamical equations which govern the motion of incompressible viscous fluids, that a resistance force accounting for the internal friction of fluids was again introduced. Navier interpreted the shear viscosity in terms of the intermolecular forces. In 1845 the publication of Stokes contributions promoted the usage of the general equations for viscous fluids in England (Truesdell, 1953).

In this early stage most of the research was conducted from a mathematical point of view. It was difficult to obtain reliable experimental data, which was sometimes incomplete or obscure, as stated by Euler (Truesdell, 1953). These problems were largely overcome during the XXth century (Raffel et al., 2007) with the development of visualization techniques and the fast improvement of the required computational tools (Guyon et al., 2001). Nowadays there is indeed an enormous amount of accessible, accurate experimental and numerical data that

enables a continuously increasing understanding of flow behavior. Fluid mechanics embraces at present the study of many different problems that encompass aerodynamics, meteorological phenomena, ocean dynamics, turbulence, hydrodynamic instabilities and rheology, among others. Not surprisingly, these research areas attract the attention of applied mathematicians as well as mechanical and chemical engineers, who have addressed fluid mechanics problems from a more practical perspective.

The physical approach on which this Thesis is rooted possibly lies halfway between mathematical and engineering approaches. The research accomplished during the Thesis, presented in this manuscript, has been developed as rigorously and systematically as possible but special attention has been paid also to a physical interpretation of the observed flow phenomena.

1.1 Complex fluids

Early observations of unusual flow behavior started at the beginning of the XXth century, with the emergence of chemical industry and polymer processing (Bird et al., 1987). The Navier-Stokes equations were not capable to predict the motion of these *unusual* fluids. Even the ordinary division of the states of matter in *solid - liquid - gas*, according to which a liquid should take the shape of the container in which it resides, was not either so well suited for these materials. In general, we can call *complex* fluids to all *thick, rubbery, gooey and pasty substances that defy the classical definitions of solids and liquids* (Larson, 1999). Complex fluids may exhibit an intermediate viscoelastic behavior between solids and liquids, since they can maintain its shape at short timescales but flow at longer times. In opposition to *Newtonian* fluids, which have constant viscosity, complex fluids usually exhibit a non-Newtonian response with a rate-dependent shear viscosity. In most cases the viscosity decreases with increasing shear rates (*shear-thinning* fluids), but it can also increase, which is the case of *shear-thickening* fluids. *Yield stress* fluids also show non-Newtonian properties since they do not flow below a minimum applied stress, and *thixotropic* fluids exhibit a time-dependent viscosity.

An additional important feature of complex fluids is the existence of normal stress differences: under shear flow the fluid responds with an additional force normal to the shearing direction. They are responsible for the striking *rod climbing* effect, Fig. 1.1(a), in which a fluid rises up a rotating rod that is placed inside a fluid container, instead of moving to the edges as would be expected for a Newtonian fluid. They also give rise to the *die swell* effect (Fig. 1.1(b)) which occurs in polymer extrusion when a polymeric fluid increases the diameter of the jet after exiting a die end.

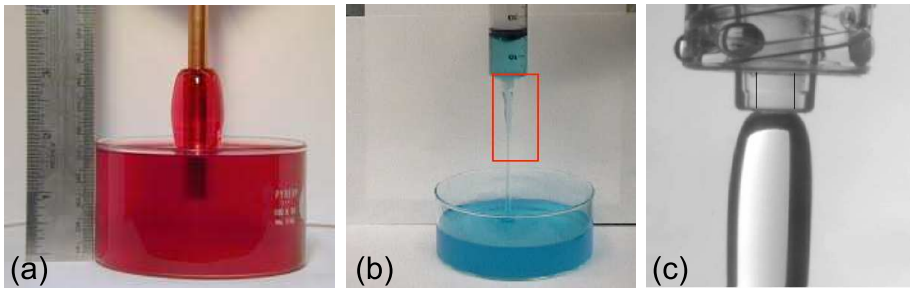

Figure 1.1: Anomalous flow behavior exhibited by complex fluids. (a): Rod-climbing; (b): Tubeless siphon; (c): Die swell (source: http://web.mit.edu/nnf).

Other amazing phenomena of complex fluids include the *tubeless siphon* effect, shown in Fig. 1.1(b), where the fluid is aspirated even when the syringe nozzle is above the free surface of the fluid container, the appearance of recirculation zones in contraction flows, elastic recoil, the formation of stable long filaments, or drag reduction in turbulent flows (Bird et al., 1987).

There is a large variety of different complex fluids which vastly include polymeric liquids and melts, particle suspensions, foams and emulsions, liquid crystals, and surfactant solutions. We can find them in numerous industrial applications. They are common in foodstuffs, like cheese, ice-cream and chocolate. They are also relevant for pharmaceuticals, cosmetics and personal care products. Shampoo, nail polish, lipstick or toothpaste have rheological properties that have been fine-tuned for precise final product performance. Molten polymers are involved in many different manufacturing processes like extruded polyethylene cable jacketing or injection-molded polyurethane car bumpers. Other fluids relevant for industrial purposes with complex rheological properties are oil-field fluids like drilling muds, waxy crude oils and paints (Larson, 1999).

Many biofluids present in living systems also show interesting complex features. Their particular rheological properties are linked to the physiological function they have to perform. Blood is a suspension of red blood cells dispersed in plasma. The ability of red blood cells to deform, which allows them to pass through narrow capillaries, is directly related to blood viscoelasticity. Another example is given by synovial fluid localized in joints. It acts as lubricant by reducing the friction between cartilage and the surrounding tissue, which is achieved partly thanks to its shear-thinning properties. Polymeric solutions of intermediate filaments, actin, peptide fibrils or microtubules of eukaryotic cells also exhibit complex features. And in particular nucleic acid is an interesting example because, thanks to its large size, it can be used to do rheological experiments of single molecules (Waigh, 2007).

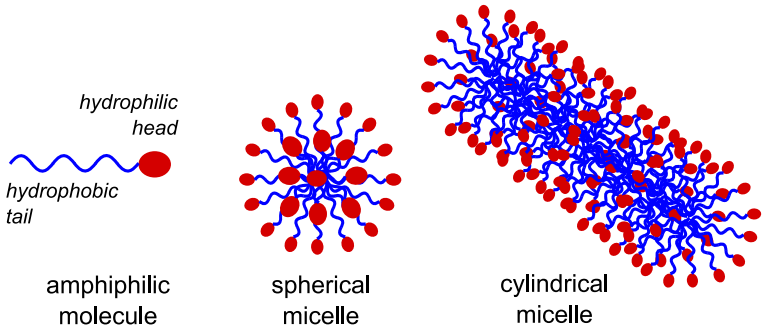

Figure 1.2: Schematic view of self-assembled surfactants.

1.1.1 Wormlike micellar solutions

Surfactant solutions are a particular example of complex fluids (Cates and Fielding, 2006). Surfactant molecules are amphiphilic, with a hydrophylic head and a hydrophobic tail (Fig. 1.2). When solved in water, the formation of micelles is energetically favorable above a critical micellar concentration (CMC), being typically low in wormlike micelles (e.g. of the order of 10^{-4} M for CTAB/KBr, Cates and Fielding (2006)). The ionic strength of the hydrophilic head sets the shape of the amphiphilic molecule. For big heads the electromagnetic repulsive forces lead to conic-like molecules that arrange forming spherical micelles. As the ionic strength is weakened, for example by the addition of a counter-ion, the size of the head decreases and induces the formation of cylindrical (or wormlike) micelles (Fig. 1.2), in which we are mainly interested. For even smaller head sizes the amphiphilic molecules look cylindrical and can form bilayers.

Cylindrical 'giant' micelles can easily exceed their persistence length (which is the length over which substantial bending occurs (de Gennes, 1979)) and behave as a polymer flexible chain. Common values of the persistence length for giant micelles range between 10 to 20 nm (Cates and Fielding, 2006). This resemblance between flexible polymers and cylindrical micelles enables to use arguments developed for polymeric solutions to wormlike micellar solutions. In this sense we can define the dilute regime as the concentration range where micelles rarely overlap between each other, and slightly viscoelastic properties are only given by the behavior of individual micelles in solution. Above the overlap concentration the wormlike micelles start to overlap forming entanglements, which is known as the semi-dilute regime, or concentrated regime for higher micellar concentrations (Bird et al., 1987). In the semi-dilute regime entanglements between flexible wormlike micelles form a mesoscopic network which is mainly responsible for the viscoelastic response of the fluid. Wormlike micelles are also known as *living polymers* because, unlike polymeric solutions, they have the ability to re-

assemble after breakage (Cates and Fielding, 2006). The characteristic relaxation time of the fluid can be interpreted in terms of the reptation-reaction model,

$$t_{relax} = (t_b t_R)^{1/2}, \tag{1.1}$$

where t_b is the breakage time of the micelles and t_R is the reptation time (being the reptation mode the sliding motion of one micelle on top of another one without breakage being involved). In the limit of fast breakage time compared to the reptation time, the overall kinetic process is dominated by the rapid breakage which leads to a dominant average micellar size and a mono-exponential stress relaxation, which coincides with the relaxation time of the Maxwell model (Sec. 1.3.1).

Micellar solutions are used in different practical applications like detergents, emulsifiers, encapsulants or lubricants (Larson, 1999). More importantly, they have been extensively employed during the last decades for scientific purposes since Rehage and Hoffmann (1991) realized that these fluids nicely behave according to the Maxwell constitutive equation with a single relaxation time, at small shear rates. At larger shear rates they typically exhibit strong shear-thinning. Wormlike micellelar solutions constitute nowadays a canonical fluid for the study of experimental and theoretical rheology and fluid dynamics (Olmsted, 2008). Some of the most commonly used species of wormlike micelles that are formed by the combination of a surfactant with a strongly binding counterion (that is normally a salt), at suitable concentrations and temperature, are CPyCl/NaSal (Rehage and Hoffmann, 1991; Berret et al., 1994; Grand et al., 1997; Britton and Callaghan, 1997; Porte et al., 1997; Méndez-Sánchez et al., 2003), CTAB/$NaNO_3$ (Cappelaere and Cressely, 1997; Lerouge and Decruppe, 2000; Lerouge et al., 2006, 2008; Masselon et al., 2008; Fardin et al., 2009), CTAB/NaSal (Shikata et al., 1988; Azzouzi et al., 2005; Decruppe et al., 2001), CTAB/KBr (Radulescu et al., 2003), among others. A comprehensive list of wormlike micellar solutions exhibiting different rheological behaviors is provided in Lerouge and Berret (2009). The time-dependent flow of micellar solutions has been extensively studied by different authors. The pioneering work of Rehage and Hoffmann (1991) focused on the oscillatory shear flow and start-up shear flow of CPyCl/NaSal solutions in a cone plate geometry. The oscillatory flow of micellar solutions was further investigated by Fischer and Rehage (1997), Méndez-Sánchez et al. (2003), Hu and Lips (2005) and in particular experiments under large amplitude oscillatory shear flows (LAOS) were performed by Ewoldt et al. (2008), Boukany and Wang (2008) and Dimitriou et al. (2012). Start-up flows have also been widely studied in different geometries by Grand et al. (1997), Lerouge and Decruppe (2000), Decruppe et al. (2001), Bécu et al. (2004), Hu and Lips (2005), Lerouge et al. (2008), and Pipe et al. (2010).

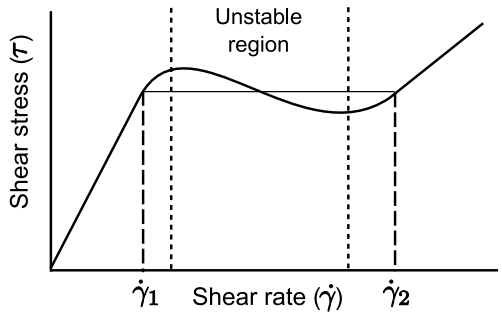

Figure 1.3: Schematic diagram of a non-monotonic flow curve, typical of a fluid exhibiting shear banding.

1.1.2 Shear banding

A broad range of complex fluids may respond to shear by separating in two or more coexisting macroscopic bands with markedly different viscosities. This phenomenon is known as *shear banding*. Complex fluids with slow relaxation time scales are likely to exhibit shear banding (Olmsted, 2008). Few examples of shear-banding fluids include polymer solutions and melts (Tapadia et al., 2006; Hu, 2010), granular suspensions (Fall et al., 2009), foams (Krishan and Dennin, 2008), and yielding fluids (Møller et al., 2008; Divoux et al., 2010). But more specifically several species of wormlike micelles (obtained for a precise range of surfactant concentration and temperatures) have been extensively studied during the last decades and have emerged as a model system to understand shear-banding phenomena (Olmsted, 2008; Manneville, 2008; Lerouge and Berret, 2009).

Shear-banding fluids display a nonmonotonic stress vs. shear rate curve, shown schematically in Fig. 1.3. The flow curve exhibits a linear viscoelastic regime at small shear rates, but it becomes unstable above a critical shear rate, $\dot{\gamma}_c$. In the unstable region (and under imposed shear rates) the homogeneous state becomes unstable and the fluid reorganizes in a new heterogeneous configuration with different stable shear bands. Different bands have different microstructural organization, corresponding to different degrees of alignment of the wormlike micelles under shear, that can be detected using birefringence measurements (Berret, 1997; Ober et al., 2011). Different bands support different local shear rates: a low shear rate, $\dot{\gamma}_1$, and a high shear rate, $\dot{\gamma}_2$ (both at a common shear stress). The average (imposed) shear rate of the fluid is given by the lever rule as

$$\dot{\gamma} = (1 - f)\dot{\gamma}_1 + f\dot{\gamma}_2, \tag{1.2}$$

where f and $(1 - f)$ are the volume fractions of the highly and lowly sheared bands. Following the lever rule, f increases from 0 to 1 as the applied shear rate

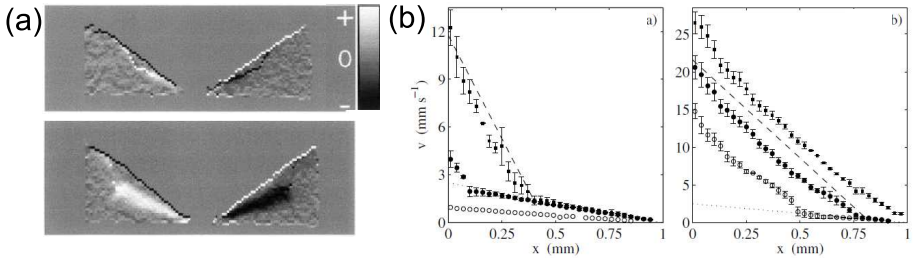

Figure 1.4: Experimental evidence of shear banding formation in wormlike micellar solutions under steady shear flow. (a): Cone-plate geometry (Britton and Callaghan, 1997). (b): Cylindrical-Couette geometry (Salmon et al., 2003).

$\dot{\gamma}$ is increased. Britton and Callaghan (1997) first observed the formation of shear bands using Nuclear Magnetic Resonance (NMR) in a cone and plate geometry under *steady* shear for a wormlike micellar solution of CPyCl/NaSal [100:60] mM (Fig. 1.4(a)). Three different shear bands were arranged normal to the velocity gradient direction, with one high-shear-rate band at the center of the gap and two bands with low shear rate at the boundaries. Subsequent steady experiments were performed by Salmon et al. (2003) and Lettinga and Manneville (2009) with comparable wormlike micellar solutions in a cylindrical Couette geometry, using dynamic light scattering and ultrasonic velocimetry (Fig. 1.4(b)). They showed that in this geometry only two different shear bands form, with a high-shear-rate band next to the moving cylinder and a low-shear-rate band next to the stationary one. These different behaviors observed in different devices presumably arise from the different interplay between boundary conditions and the intrinsic stress gradient imposed by the flow geometry (Adams et al., 2008).

During my research stay in the Hatsopoulos Microfluids Laboratory at MIT we showed that micellar solutions in a cone-plate geometry also exhibit shear band formation under *oscillatory* shear flows when the applied deformation exceeds a shearing threshold, typically $Wi > 1$ (Dimitriou et al., 2012). We observed the transition from linear velocity profiles at small deformations ($Wi < 1$) to three banded velocity profiles at larger deformations (coincident with the results of Britton and Callaghan (1997) obtained for the same geometry) with a rather smooth variation of the shear rate along the gap (Fig. 1.5).

Some wormlike micellar solutions only exhibit transient shear banding in which the shear bands are not steady but display a substantial spatio-temporal evolution, and in some cases vanish after a certain time, typically larger than the relaxation time of the fluid (López-González et al., 2004; Bécu et al., 2004; Hu and Lips, 2005; Miller and Rothstein, 2007; Hu et al., 2008). An extensive review of shear banding transitions in semidilute and concentrated giant micelles is provided in Lerouge and Berret (2009).

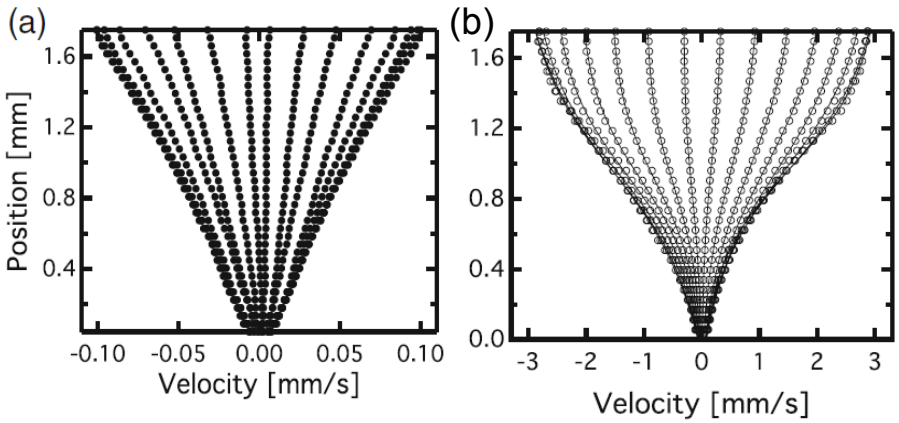

Figure 1.5: Linear (a) and shear banded (b) velocity profiles for a CPyCl/NaSal [100:60] mM wormlike micellar solution under oscillatory shear flow in a cone-plate geometry (Dimitriou et al., 2012).

1.2 Elastic instabilities

Laminar flows become unstable after the rapid increase of small perturbations that result from an imbalance between stabilizing and destabilizing effects. In Newtonian fluids the instability can be induced by inertia, surface tension or buoyancy forces, among other effects (Drazin, 2002). The Kelvin - Helmoltz instability, for example, is generated by a vorticity gradient that tends to destabilize the interface between two fluids and manifests with the formation of waves (Fig. 1.6(a)).

The onset of an instability can be monitored in terms of particular parameters or dimensionless numbers that naturally arise from the governing equations of the flow. In Newtonian fluids different flow regimes can be achieved by continuously increasing the dimensionless Reynolds number (Re), that sets the relative importance of inertia to the damping viscous force. A nice example appears in the wake of a vertical cylinder transverse to the flow direction inside a Newtonian fluid moving at constant velocity along the horizontal coordinate. The Reynolds number is defined as $Re = UL/\nu$, where U is the typical flow velocity, L is the characteristic length of the geometry, and ν is the kinematic viscosity of the fluid. At $Re \ll 1$ the flow is laminar everywhere. As $Re \geq 1$ the laminar flow becomes unstable and a pair of steady vortices form at the rear of the cylinder. At larger Re numbers beautiful time dependent vortices form downstream (also known as von Kármán vortex street), Fig. 1.6(b), and at even larger Re the flow eventually becomes turbulent (Guyon et al., 2001).

In polymeric fluids hydrodynamic instabilities have been reported in the range of $Re \ll 1$ (the viscosity of these fluids is usually large), where inertial forces are negligible. In the inertialess regime the nonlinearities required to trigger the flow

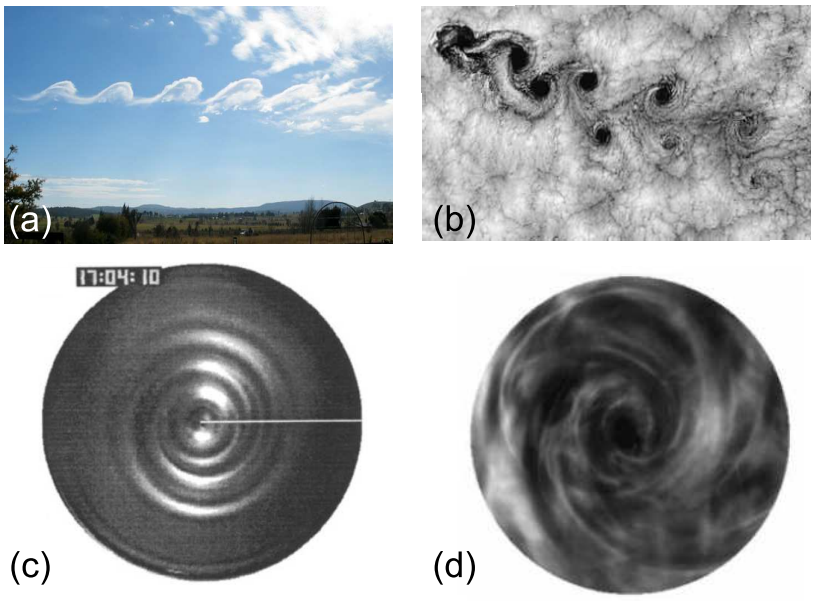

Figure 1.6: Experimental observation of hydrodynamic instabilities. (a): Kelvin-Helmholtz instability visible by clouds in Mount Duval in Australia (source: http://en.wikipedia.org); (b): von Kármán street observed in the Juan Fernández Islands off the Chilean coast (source: http://en.wikipedia.org); (c): Elastic instability of PIB/PB Boger fluid in a plate-plate geometry. The formation of outward-propagating Archimedean spirals is observed (Byars et al., 1994); (d): Elastic turbulence of Boger fluids in a plate-plate geometry under steady shear (Groisman and Steinberg, 2000).

instability come from the complex stress-strain relation of the polymeric fluid. The relevant dimensionless numbers in viscoelastic fluids are the Deborah (De) and the Weissemberg (Wi) numbers (Morozov and van Saarloos, 2007). The Deborah number sets the interplay between the characteristic relaxation time of the fluid λ and the time scale of the flow,

$$De = \lambda / t_{flow}. \tag{1.3}$$

In oscillatory flows the time scale of the flow can be defined as the inverse of the oscillation frequency, ω_0. In the limit of $De \to 0$ the fluid relaxes much faster than the typical time scale of the flow and Newtonian flow behavior is recovered. For $De > 1$ the relaxation time of the fluid is larger than the time scale of the flow and fluid elasticity dominates the flow behavior. The Wi number sets the relative importance of the fluid relaxation time to the local deformation time scale for a fluid element, $t_{def} \simeq 1/\dot{\gamma}$, so that

$$Wi = \lambda \dot{\gamma}. \tag{1.4}$$

In oscillatory flows the amplitude of the applied shear rate is given by $\dot{\gamma}_0 = \gamma_0\omega_0$, where γ_0 is the dimensionless amplitude of the deformation. The Weissemberg number reads then, $Wi = \lambda\gamma_0\omega_0$, which can be rewritten in terms of the Deborah number as $Wi = \gamma_0 De$. The Weissemberg number can also be expressed as a function of the first normal stress difference N_1 (the expression for the N_1 is provided in Sec. 4.1), and the shear stress τ, as $Wi = N_1/\tau$ (Bird et al., 1987) . This definition highlights the importance of normal stress differences in setting in the nonlinearities of the fluid response. Analogously to the Re number in Newtonian fluids, as Wi is increased we can explore different flow regimes in viscoelastic fluids (Morozov and van Saarloos, 2007). For $Wi < 1$ the fluid response is expected to be linear and at $Wi > 1$ nonlinearities start to become manifest. In this regime elastic instabilities are likely to appear.

Pakdel and McKinley (1996) established a criterion for the onset of elastic instabilities, based on the curvature of the flow streamlines and fluid elasticity, as

$$(l/R)\, Wi \geq M^2 \tag{1.5}$$

where R is the radius of curvature of the streamlines, l gives a measure of the distance over which perturbations relax along a streamline and M is the threshold value that depends on the particular flow geometry. This criterion can be inferred for any unidirectional flow with curved streamlines, like the cone-plate, plate-plate or the Taylor-Couette geometries. When the streamlines are straight the radius of curvature tends to infinity and the Pakdel-McKinley criterion predicts the base flow to be linearly stable under any flow conditions.

Experimental evidence of elastic instabilities has been reported in several viscometric flows (Shaqfeh, 1996). Usually Boger fluids (Boger, 1977) are used for this kind of experiments because they are highly elastic and have a shear viscosity that remains constant for a large range of shear rates. Boger fluids are obtained by dissolving a small amount of a high molecular weight polymer within a very viscous Newtonian fluid. Common examples are polyisobutylene in polybutene (PIB/PB), polystyrene in low molecular weight polystyrene (PS/PS), or polyacrylamide (PAA) in corn syrup (which was the original recipe of D. Boger). In a cylindrical Couette cell, Larson et al. (1990) observed for a PIB/PB solution the formation of rolls stacked along the gap between concentric cylinders accompanied by a simultaneous increase of the measured torque. The triggering mechanism for this instability was not the centrifugal force responsible for the inertial Taylor-Couette instability, since $Re \simeq 10^{-3}$, but the elasticity of the fluid. In the cone-plate geometry, Magda and Larson (1988) and McKinley et al. (1991) observed the appearance of an elastic instability, and McKinley et al. (1991) and Byars et al. (1994) observed the formation of spirals distributed along the radial coordi-

nate, for a similar PIB/PB solution (Fig. 1.6(c)). Some years later Groisman and Steinberg (2000) showed that a Boger fluid placed in a plate-plate geometry could eventually become *elastically turbulent* at even larger Wi numbers (Fig. 1.6(d)), showing all characteristic features of fully developed turbulence. Wormlike micellar solutions in curved flows are also likely to exhibit hydrodynamic instabilities induced by fluid elasticity. Fardin et al. (2010) studied the Taylor-Couette flow of a shear banding wormlike micellar solution, CTAB/$NaNO_3$. They observed that for large enough Wi, and within the high shear rate branch of the flow curve, the flow undergoes a subcritical instability which leads to a random flow state that presents features typical of elastic turbulence. And Majumdar and Sood (2011) reported a purely elastic turbulence for a non-shear-banding surfactant system, CTAT.

Morozov and van Saarloos (2005) proposed an extension of the Pakdel - McKinley criterion for parallel shear flows with straight streamlines. Parallel shear flow is known to be linearly stable to perturbations of infinitesimal amplitude. However Morozov argued that the stable laminar flow might undergo a subcritical (nonlinear) instability. Finite perturbations would curve the straight streamlines of the base flow, and for large enough amplitudes the perturbed flow should become unstable for large Wi numbers. The threshold for the nonlinear transition is predicted to decrease for increasing Wi numbers as $1/Wi^2$. Recent experiments carried out by Pan et al. (2012) with a polymeric solution provide experimental verification for the existence of such nonlinear instabilities in parallel shear flows. Using a straight microfluidic channel where the flow was perturbed by placing a number of obstacles at the entrance of the channel they showed that above a critical flow rate and a critical size of the perturbation, a sudden onset of large velocity fluctuations occurred, indicating presence of a subcritical instability.

1.3 Rheology

In 1920, Bingham proposed the new term rheology, derived from the Greek word, $\rho\epsilon\iota\nu$, to flow (Macosko, 1994). Generally speaking, rheology studies the fluid flow behavior. In particular rheology focuses on the constitutive equations that relate the stress and strain experienced by a material. And a more practical side of rheology deals with rheometric tests used to characterize the material functions of fluids, whose constitutive equations are unknown.

1.3.1 Constitutive models for viscoelastic fluids

Viscoelastic fluids exhibit an intermediate flow behavior between ideal solids and liquids. At small time scales they behave as elastic solids, but at larger time scales (typically larger than a characteristic relaxation time of the fluid) they flow as ordinary dissipative fluids. Constitutive equations for complex fluids are intended to reproduce this intermediate viscoelastic behavior, as well as other non-Newtonian effects (such as shear-thinning and thickening, yield-stress, etc.) described so far.

Complex fluids have a precise microstructure, that typically ranges from 100 μm to 10 nm, which is mainly responsible for the striking observed phenomena (Larson, 1999). Microscopic models look at this molecular microstructure and establish relations between the bulk flow behavior and fluid structure using statistical mechanics methods. The simplest microscopic model describes the polymeric (or micellar) fluid as an ensemble of elastic dumbbells formed by two beads connected by an elastic spring. When the elastic spring is considered to be Hookean the model provides, on the one hand, shear material properties that are independent of the applied shear rate, and on the other hand an extensional viscosity that infinitely increases at finite elongational rate. This model has the same form as the Oldroyd-B constitutive equation obtained in continuum mechanics (and discussed in more detail below in this section), so that it allows to infer different microscopic properties from results obtained in continuum mechanics (Bird et al., 1987). A more realistic elastic dumbbell behavior is achieved with the so-called FENE model (Finite Extensible Nonlinear Elastic), which considers nonlinear springs with a finite extensibility. Dumbbell models can be further improved by taking into account the hydrodynamic interaction between the dumbbell beads with the surrounding fluid. And a step forward can be achieved by replacing the oversimplified elastic dumbbells by elastic chains with multiple beads interconnected by springs, such as the Rouse model (for Hookean springs) or the Zimm model (when hydrodynamic interactions are incorporated).

From the point of view of an experimentalist macroscopic constitutive equations are more useful in the sense that they allow a direct comparison with experimental data, typically obtained with a rheometer. These models are empirical approximations that do not look into the molecular structure but reproduce the macroscopic rheological fluid behavior.

One of the simplest shear flow experiments can be performed in a plate-plate geometry. In this configuration the fluid is contained between two parallel plates and the flow is generated by moving the upper plate at constant speed u along the x direction while the bottom one is at rest (Fig. 1.7). The resulting shear rate

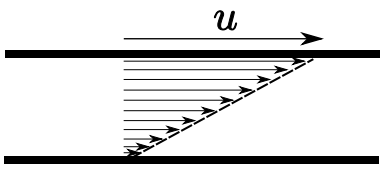

Figure 1.7: Simple shear flow generated in a plate-plate geometry. An external velocity u is applied to the upper plate while the lower one is at rest.

in the cell is given by the velocity gradient along the vertical direction,

$$\dot{\gamma}_{xy} = \frac{\partial u_x}{\partial y}. \tag{1.6}$$

And the general expression for the reate-of-strain tensor reads (tensors and vectors are depicted in bold symbols)

$$\dot{\boldsymbol{\gamma}} = (\boldsymbol{\nabla u}) + (\boldsymbol{\nabla u})^{\dagger}. \tag{1.7}$$

The fluid responds to the applied shear rate with the generation of a shear stress. The total stress tensor, $\boldsymbol{\sigma}$, which is defined as the force per unit area, contains an isotropic and an anisotropic part:

$$\boldsymbol{\sigma} = \boldsymbol{\tau} - p\boldsymbol{\delta} \;\; = \;\; \begin{pmatrix} \tau_{xx} - p & \tau_{xy} & \tau_{xz} \\ \tau_{yx} & \tau_{yy} - p & \tau_{yz} \\ \tau_{zx} & \tau_{zy} & \tau_{zz} - p \end{pmatrix}. \tag{1.8}$$

The hydrostatic pressure, p, only takes part in the isotropic part of the stress tensor. The anisotropic one, that we call for simplicity and from now on *stress*, corresponds to the shear stress (Larson, 1999). Newtonian fluids never exhibit the diagonal terms (τ_{xx}, τ_{yy}, τ_{zz}) in the stress response. In the previous example of the plate-plate geometry the only non-vanishing terms of the tensor $\boldsymbol{\tau}$ are the cross-terms τ_{xy} and τ_{yx} (which are identical since the tensor is symmetric). We can define the normal stress differences N_1 and N_2 as

$$N_1 = \tau_{xx} - \tau_{yy},$$

$$N_2 = \tau_{yy} - \tau_{zz}. \tag{1.9}$$

In Newtonian fluids both N_1 and N_2 are identically zero. However, this is not the case for viscoelastic fluids where particularly N_1 can be very significant.

Stress and shear rate in Newtonian fluids are found in a linear relation, where

the viscosity η is the constant of proportionality:

$$\boldsymbol{\tau} = \eta\dot{\boldsymbol{\gamma}}. \tag{1.10}$$

This is the simplest macroscopic constitutive equation that relates the shear rate with the stress response.

The macroscopic description for viscoelastic fluids combines the elastic behavior, represented by an elastic spring, with the viscous behavior represented by a dissipative dashpot. Depending on the precise configuration of these primary elements we obtain different constitutive equations (Maxwell model, Kelvin-Voigt, generalized Maxwell, Burgers model, ...).

The Maxwell model is obtained by considering an elastic spring and a dissipative dashpot connected in series. It is the simplest linear model that can successfully predict the stress relaxation of viscoelastic fluids. The Maxwell model reads (Bird et al., 1987),

$$\tau + \lambda\frac{\partial\tau}{\partial t} = \eta_0\dot{\gamma} \tag{1.11}$$

where τ is the shear stress, $\dot{\gamma}$ is the rate of shear deformation, and η_0 and λ are the zero-shear viscosity and characteristic relaxation time of the fluid. The upper-convected Maxwell model (UCM) is the frame invariant version of the Maxwell model. It requires the replacement of partial temporal derivatives for upper-convected derivatives which are frame invariant (depicted with the subscript (1)), and the usage of the tensorial notation for the stress and rate of deformation (depicted in bold symbols),

$$\boldsymbol{\tau} + \lambda\boldsymbol{\tau}_{(1)} = \eta_0\boldsymbol{\gamma}_{(1)}. \tag{1.12}$$

The upper-convected derivative for the stress tensor reads

$$\boldsymbol{\tau}_{(1)} = \frac{D}{Dt}\boldsymbol{\tau} - \left\{(\boldsymbol{\nabla u})^{\dagger}\cdot\boldsymbol{\tau} + \boldsymbol{\tau}\cdot(\boldsymbol{\nabla u})\right\}, \tag{1.13}$$

where the total time derivative can be expressed as $\frac{D}{Dt}\boldsymbol{\tau} = \frac{\partial\boldsymbol{\tau}}{\partial t} + \boldsymbol{u}\cdot\boldsymbol{\nabla\tau}$. And the upper-convected derivative for the rate-of-strain tensor is just

$$\boldsymbol{\gamma}_{(1)} = \dot{\boldsymbol{\gamma}}. \tag{1.14}$$

An important feature of both the Maxwell and UCM models is that they have a single relaxation time. These models successfully reproduce the shear rheology of wormlike micelles at low shear rates.

The Oldroyd-B constitutive equation (also known as Convected Jeffreys model) introduces a second relaxation time also known as *retardation* time (Bird et al.,

1987). The Oldroyd-B model represents a solution of a Maxwellian viscoelastic fluid (which is typically a polymeric fluid), with a single relaxation time λ and a rate independent viscosity η_p, solved in a Newtonian solvent with constant viscosity η_s. The Oldroyd-B constitutive equation reads:

$$\boldsymbol{\tau} = \boldsymbol{\tau}_s + \boldsymbol{\tau}_p \tag{1.15a}$$

$$\boldsymbol{\tau}_s = \eta_s \boldsymbol{\gamma}_{(1)} \tag{1.15b}$$

$$\boldsymbol{\tau}_p + \lambda \boldsymbol{\tau}_{p(1)} = \eta_p \boldsymbol{\gamma}_{(1)}. \tag{1.15c}$$

The stress tensor $\boldsymbol{\tau}$ is the sum of the solvent and polymeric contributions (denoted by the subindex s and p, respectively). $\boldsymbol{\gamma}$ is the rate-of-strain tensor. The viscosity of the solution is given by the sum of the solvent and polymeric contributions, $\eta = \eta_s + \eta_p$. The fraction η_s/η is called the viscosity ratio, denoted in the following by X. The retardation time can be expressed in terms of the viscosity ratio as $\lambda_2 = \lambda X$. It is worth noting that the Oldroyd-B constitutive equation interpolates between two limiting behaviors. For $X = 0$ the Newtonian contribution of the solvent vanishes, and the UCM constitutive equation is recovered. The other limiting behavior is attained for $X = 1$, when the elastic contribution of the polymer vanishes and the Newtonian relation is recovered. The Oldroyd-B model is well realized experimentally by Boger fluids in shear flow. Both the UCM and Oldroyd-B models are called *quasi-linear* models. Although these models have a shear stress equation for unidirectional flow that is linear, the upper convected derivatives introduce nonlinearities that brings about first normal stress difference, $N_1 = \tau_{xx} - \tau_{yy}$, different from zero. However, these models cannot predict non zero second normal stress differences (Bird et al., 1987).

All models presented so far fail in predicting common nonlinear features observed in wormlike micellar solutions that appear at considerably large shear rates. Specifically, the shear-thinning behavior and the decrease of the first normal stress coefficient, $\psi = N_1/\dot{\gamma}^2$, with increasing shear rates (Bird et al., 1987). The single-mode Giesekus model (Bird et al., 1987) is an extension of the Oldroyd-B model which introduces the first quadratic term in shear stress:

$$\boldsymbol{\tau} = \boldsymbol{\tau}_s + \boldsymbol{\tau}_p \tag{1.16a}$$

$$\boldsymbol{\tau}_s = \eta_s \boldsymbol{\gamma}_{(1)} \tag{1.16b}$$

$$\boldsymbol{\tau}_p + \lambda \boldsymbol{\tau}_{p(1)} - \alpha \frac{\lambda}{\eta_p} \{\boldsymbol{\tau}_p \cdot \boldsymbol{\tau}_p\} = \eta_p \boldsymbol{\gamma}_{(1)}. \tag{1.16c}$$

The model has an additional parameter α or *mobility factor*, that typically ranges from zero to one, which can be associated with the anisotropic hydrodynamic

drag exerted on the polymer molecules. The Giesekus model can predict a large decrease of both the viscosity and first normal stress coefficient with the shear rate, as well as non-zero second normal stress coefficient. And in particular this model successfully reproduces the nonlinear shear banding flow of semi-dilute wormlike micelles (Larson, 1999; Yesilata et al., 2006). More recently, Vasquez et al. (2007) have proposed the VCM model that aims to capture the relevant physical interactions of the fluid. It describes the fluid microstructure as the ensemble of two different species of long and short micelles that mutually break and recombine. This model provides a good understanding of inhomogeneous flows and is able to capture transient features of these flows.

1.3.2 Rheometric tests

A rheometer is the required apparatus to do the rheometric tests and get the stress-strain data of the fluid to be characterized. Depending on the kind of flow that the instrument generates, we can broadly separate between rheometers that produce a shear flow, in which we are interested, and those that create an extensional flow. Shear flows can be achieved between a moving and a fixed surface (known as drag flows) or driven by a pressure difference between two different locations (pressure driven flows). In drag flows the stress-strain data is inferred from deformation-torque measurements, while in pressure driven flows it is obtained from the pressure drop and flux measurements. In both cases the velocity gradient that appears within the sample is perpendicular to the flow direction.

In homogeneous flows stress and strain are independent of the position in the sample, which makes them very convenient for rheometric measurements. The cone-plate geometry, in the limit of small cone angles, is the most extensively used geometry to experimentally achieve homogeneous drag flows. Since it provides a constant shear rate along the radial coordinate, and allows to obtain N_1 measurements directly from the total thrust, it is particularly convenient for the study of non-Newtonian fluids (Macosko, 1994). Capillary flows are pressure driven flows that provide non-homogeneous deformations (the shear rate is always maximum close to the walls and zero at the center). A main advantage of capillaries is that they generate flows with no free surface and thus they avoid possible edge failure of the sample (thus allowing a considerably larger accessible range of shear rates) and sample evaporation.

Figure 1.8: Reproduction of the water tunnel exhibited in the German Aerospace Center DLR, Göttingen (Germany).

1.3.3 Flow visualization techniques

Visualization techniques allow to spatially resolve the velocity field and gain information of the fluid flow organization. While a standard rheometer allows to distinguish a linear regime from a nonlinear one, using visualization techniques we may be able to identify the mechanism responsible for the nonlinear response of the fluid. In shear banding fluids, some of these techniques allow to visualize the formation of different shear bands. In particular these techniques allow to discriminate shear banding from other nonlinear effects such as wall slip. They are also very convenient in characterizing the emergence of secondary flows at large Re or Wi numbers.

Pioneering experiments on flow visualization were first done by Prandtl in 1904, who added a suspension of mica particles on the surface of water, to characterize the flow pattern generated in a water tunnel after different model objects like cylinders, prisms or wings (Fig. 1.8). Particle Tracking Velocimetry (PTV) and Particle Image Velocimetry (PIV) are very commonly used visualization techniques (Adrian, 1991; Raffel et al., 2007) based on particle tracking methods. PTV uses low seeding densities and individual particles are tracked. This leads to non-homogeneous measurements of the velocity field. PIV, instead, uses higher particle densities which allow to extract the local mean velocity of the flow with a high spatial resolution (PIV will be discussed in detail in Sec. 2.2). One drawback of these techniques is that they are restricted to transparent fluids. Nuclear Mag-

netic Resonance (NMR) (Callaghan, 2008), ultrasonic velocimetry (Lettinga and Manneville, 2009), and dynamic light scattering (Salmon et al., 2003) are other techniques that have also been extensively used for flow visualization of wormlike micellar solutions (Manneville, 2008).

1.4 Wall-bounded oscillatory flows

Wall-bounded oscillatory flows of Newtonian and complex fluids are found in many practical situations. Oscillatory pipe flows are specially important in physiology in connection with the circulatory and respiratory systems of human beings, as well as in industrial processes such as fluid pumping, secondary oil recovery or filtration, and in acoustics. Pulsating flows are of particular interest also in the rheological characterization of complex fluids.

1.4.1 Newtonian fluids

The oscillatory flow of Newtonian fluids is governed by the Reynolds number $Re = U_0 a/\nu$ (where U_0 is the amplitude of cross-sectional mean velocity, a is the distance from the symmetry axis of the geometry to the sidewalls, and ν is the fluid kinematic viscosity) and the Stokes parameter, $\Lambda = a/\delta$, where $\delta = (2\nu/\omega_0)^{1/2}$ is the thickness of the boundary layer at the sidewalls, and ω_0 is the frequency of oscillation (Crandall, 1926). Using the Stokes parameter we can distinguish 'narrow' ($\Lambda < 1$) from 'wide' configurations ($\Lambda > 1$). In 'narrow' settings viscous damping dominates over inertia and the laminar flow is lamellar, while in 'wide' systems the viscous boundary layer is confined next to the walls and an inviscid core moves in the center.

Crandall (1926) derived the first analytical solution of the velocity profile of a Newtonian fluid in a straight cylinder, in an oscillatory flow induced by a harmonic pressure gradient. Wall-bounded oscillatory flows were later extensively studied by Lambossy (1952) and Womersley (1955). The latter expressed the velocity profile in terms of modulus and phase. He also noted that the degree of departure from the normal parabolic form (the Poiseuille profile corresponding to a steady pressure gradient) increased with driving frequency and that the phase lag varied across the pipe. He also computed the rate of flow (the quantity of liquid passing through any cross-section per unit time) in terms of the imposed pressure gradient, a relationship that is useful to make contact with most experiments in which the rate of flow rather than the pressure gradient is imposed (e.g. by the harmonic motion of the endwalls). The experimental work of Müller (1954) provided a verification of the velocity profiles predicted theoretically.

The transition from laminar to turbulent flow of Newtonian fluids in zero-mean oscillatory pipe flow was also investigated experimentally (Sergeev, 1966; Merkli and Thomann, 1975; Hino et al., 1976; Ohmi et al., 1982; Eckmann and Grotberg, 1991; Akhavan et al., 1991). Four main regimes were identified by Ohmi et al. (1982) and Akhavan et al. (1991) in the $Re - \Lambda$ parameter space: (I) laminar flow - (II) disturbed laminar flow (small amplitude perturbations appear during the acceleration phase of the cycle) - (III) intermittently turbulent flow (turbulent bursts appear in the deceleration phase of the cycle) - (IV) and fully turbulent flow. As discussed by Akhavan et al. (1991), flows of type (IV) have not actually been observed experimentally, but it has been observed that flows of type (III) remain turbulent for increasingly larger portions of the cycle as Re increases. Ohmi et al. (1982) compiled the experimental data available at the time and sketched an approximate phase diagram of these different types of flow in the $Re - \Lambda$ parameter space. The diagram shows that for small values of Λ ($\simeq 1$) the flow is laminar up to $Re \simeq 10^3$ and becomes intermittently turbulent at larger Reynolds numbers. Weakly turbulent or intermittent flow at low Reynolds number is only observed for very wide systems, $\Lambda \geq 5$.

1.4.2 Viscoelastic fluids

Time-dependent flows of viscoelastic liquids, in the range of $De > 1$, exhibit many interesting features that are absent in corresponding flows of Newtonian liquids. Thurston studied the laminar oscillatory flow of viscoelastic fluids driven by a sinusoidal pressure gradient, both between infinitely large parallel plates (Thurston, 1959) and in a rigid tube of infinite length and circular cross-section (Thurston, 1960). Using a complex, constant shear viscosity, needed to capture the viscoelastic properties of the fluid, he obtained the equation for the velocity profiles in the rectilinear oscillatory flow in the two geometries. He also made a great effort in measuring the flow properties of blood when oscillated in small rigid tubes (Thurston, 1975). He realized that the pressure gradient could be resolved into a dissipative component in phase with the volume flow, and another one in quadrature, and that at high frequencies the two components showed nonlinear effects. In particular, the component in quadrature became inertial-like due to the shear degradation of the inner blood structure made of aggregates of red blood cells. Theoretical attempts to model the blood flow have also been performed. Recently Moyers-González et al. (2009) used a complex hemorheological constitutive model, based on blood non-homogeneous microstructure, to calculate pressure gradient vs. flow rate in an oscillatory flow of healthy human blood for a wide range of oscillatory frequencies. At low frequencies the flow behavior could be interpreted by a simple linear viscoelastic model and the predictions were found to be in close

agreement with the experimental results obtained by Thurston (1976). At larger frequencies a 'resonance' frequency was found at which the flow rate amplitude showed an enhancement. And at even larger frequencies, the pressure gradient amplitude needed to maintain a constant flow rate amplitude was found to increase with the oscillatory frequency.

Barnes et al. (1969) investigated the effect of an oscillatory pressure gradient around a nonzero mean in straight cylinders. The experimental results obtained for dilute aqueous solutions of polyacrylamide showed a dramatic mean flow rate enhancement at particular values of the mean pressure gradient, as a result of a 'resonance' effect between the fluid elasticity and the oscillatory driving. The enhancement was shown to be of practical significance: the peak value of the fluctuating pressure gradient was lower than the constant pressure gradient needed to produce the same mean flow rate. Their observations were in qualitative agreement with their own theoretical predictions based on a power series expansion of the velocity and shear rate of a fluid characterized by an apparent viscosity $\eta(\dot{\gamma})$. The mechanisms for flow enhancement, using different fluid models, were subsequently studied by several authors including Barnes et al. (1971), Davies et al. (1978), Phan-Thien and coworkers (Phan-Thien, 1978, 1980, 1981; Phan-Thien and Dudek, 1982a,b; Huilgol and Phan-Thien, 1986), Manero and Walters (1980), Herrera (2010), and Siginer (1991). Andrienko et al. (2000) stated that one of the leading mechanisms of mean flow rate enhancement is a coupling between the shear rate-dependent viscosity, when the fluid is described using a nonlinear constitutive equation, and the increase of shear rate due to the oscillatory part of the pressure gradient. The increase of shear rate caused by the oscillations causes a decrease of apparent viscosity if the fluid is shear-thinning wich produces in turn an enhancement in the mean flow rate.

Although both the upper-convected Maxwell and the Oldroyd-B models have a shear stress equation for unidirectional flow that is linear, and thus unable to produce mean flow rate enhancement, they are still capable to predict dramatic deviations of the flow field of viscoelastic fluids from that of a purely viscous fluid. In particular, the instantaneous flow velocities of viscoelastic fluids show an interesting enhancement at certain frequencies. This resonance behavior has been predicted theoretically by several authors (del Río et al., 1998, 2001; Andrienko et al., 2000; Tsiklauri and Beresnev, 2001a,b) and demonstrated experimentally by Castrejón-Pita et al. (2003) for an aqueous micellar solution.

In the theoretical work of del Río et al. (1998, 2001) the zero mean oscillatory flow of a Maxwell fluid in a tube of circular cross-section was analyzed in the inertialess regime by Fourier transformation of the time variable. Assuming laminar flow directed along the axis of the tube, an expression of the radial profile of the fluid velocity was derived, in agreement with Thurston's original derivation

(Thurston, 1960). Defining the dynamic permeability of the tube as the ratio of the average over the tube cross-section of the fluid velocity to the driving pressure gradient, the authors showed that the dynamic permeability is strongly peaked at particular resonant frequencies, dependent on fluid parameters and tube radius.

Andrienko et al. (2000) studied the resonance behavior of a fluid described by the upper-convected Maxwell model with a discrete spectrum of relaxation times. This model includes the single relaxation time UCM and the Oldroyd-B constitutive equations as particular cases. They showed again that instantaneous flow velocities drastically increase at certain (resonant) frequencies of the oscillating pressure gradient, and noticed that the effect becomes more pronounced as the tube radius gets smaller. The resonance behavior persisted when a simple nonlinear constitutive equation (a Tanner model with a single relaxation time) was considered, and for this model the authors showed that the phenomenon of mean flow-rate enhancement is most efficient at the resonance frequencies.

Experimental evidence of the different dynamic responses of Newtonian and viscoelastic fluids in zero-mean oscillatory flow in a vertical pipe was provided by Castrejón-Pita et al. (2003), using laser Doppler anemometry. They observed that while the motion of glycerol at the symmetry axis of the tube showed the purely dissipative response expected for a Newtonian fluid, a wormlike micellar solution showed a resonant dynamic response at particular frequencies. Further experiments (Torralba et al., 2005), using Particle Image Velocimetry, provided the radial velocity profiles of the laminar oscillatory flow of the micellar fluid. More recently, Torralba et al. (2007) studied the stability of the laminar oscillatory flow. They showed that a secondary flow develops in the inertialess regime at high enough drivings, consisting of toroidal vortices stacked along the tube axis. At even higher drivings this vortex structure became itself unstable, and complex nonsymmetric flows developed along the tube.

Chapter 2

Experimental setup

The experimental setup we used consisted on a column of fluid, contained in a vertical transparent cylinder, that was forced to oscillate periodically in time, thanks to the sinusoidal motion of a piston placed at the bottom end of the tube. This setup was the first of this kind ever implemented in the *Laboratori de Física no Lineal*, of the University of Barcelona. Our setup was based on the original setup that operated in the UNAM (Castrejón-Pita et al., 2003; Torralba et al., 2005, 2007), but incorporated several important new features, to be discussed in Sec. 2.3.

During the first stage of the Thesis, the design of the experimental setup was completed. In particular, the mechanism used to generate the oscillatory motion of the piston (Sec. 2.1) was redesigned. Important modifications had to be implemented to guarantee that the oscillations were indeed sinusoidal. The acquisition of an AC motor an reductor in the laboratory also made possible to expand the range of accessible drivings to lower frequencies of oscillation. The setup was completed with the incorporation of a device that enabled to track the piston position in time by means of a Linear Variable Differential Transformer. With the calibration of both the amplitude and oscillation frequency we verified that indeed the setup was able to generate an almost perfect sinusoidal oscillatory motion for a large range of amplitudes and frequencies.

The implementation of a Particle Image Velocimetry system was also accomplished, which made possible the characterization of the fluid velocity field in a meridional plane of the tube with high spatial and temporal resolution (Sec. 2.2).

A detailed description of the different parts of the setup is provided in the following sections.

2.1 Experimental apparatus

The experimental setup that was used to perform all the experiments reported in this Thesis is shown in Figs. 2.1, 2.2, and 2.3. The fluid to study was placed in a vertical rigid tube (a) of transparent methacrylate of circular cross section and 5 cm inner diameter, 60 cm length and 5 mm thickness. The fluid motion was driven by the oscillatory motion of a Teflon piston (c) of the same diameter placed at the bottom end of the cylinder. The top surface of the fluid was covered with a freely moving plastic lid (e), to avoid free interface effects that might interfere with the flow in the bulk. In order to minimize the optical aberrations produced by the curved surface, the tube was contained in a transparent tank (b) built in polycarbonate and filled with glycerol, that matches quite well the refractive index of the methacrylate walls. Possible remaining aberrations were corrected in the post-processing of the images.

2.1.1 Driving the oscillatory motion

Our setup allowed to control both the frequency (ν_0) and amplitude (z_0) of the vertical oscillatory motion of the driving piston. Experimentally accessible frequencies and amplitudes lied within the range 1.0 to 12.0 Hz ($\pm$0.1 Hz) and 0.20 to 6.00 mm ($\pm$0.02 mm) respectively.

Figures 2.1, 2.2, and 2.3(left panel) show that the motion was set by a crankshaft (f) that converts the rotational motion of an AC motor (p) and reductor (n), with final angular frequency $\omega_0 = 2\pi\nu_0$, into the linear vertical oscillatory motion of one end of a metallic lever (h) which pivoted around a fixed shaft at the opposite end (g). The reductor was required for the lowest driving frequencies. Crankshaft, lever and AC motor were mounted on a translational stage (k) that could move horizontally, operated by a DC motor. The vertical cylinder was attached to a rigid metallic framework (j). The connecting rod of the piston (d) ended in a ball bearing that slided on a rectangular opening machined all along the lever, in such a way that the piston followed the oscillations of the lever. The whole device stood on a sturdy horizontal table. The amplitude of the piston oscillation was determined by both the eccentricity of the crankshaft and the distance of the ball bearing to the pivoting end of the lever, which could be modified using an external controller. Hence the amplitude z_0 varied from zero, at the pivoting end, to its maximum, at the crankshaft.

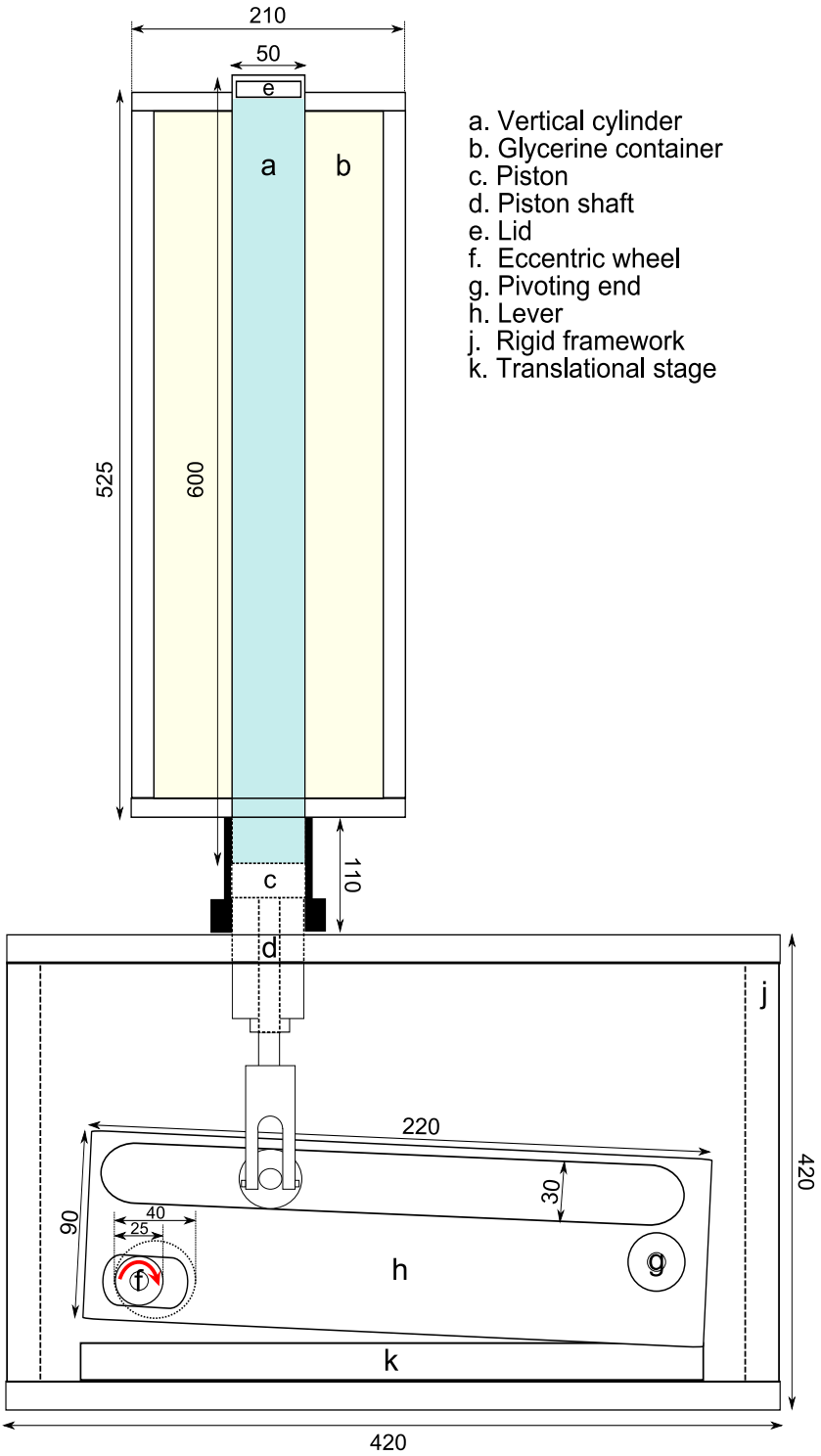

Figure 2.1: Front view of the experimental setup (the sketch is not to scale). The most relevant dimensions (mm) are specified.

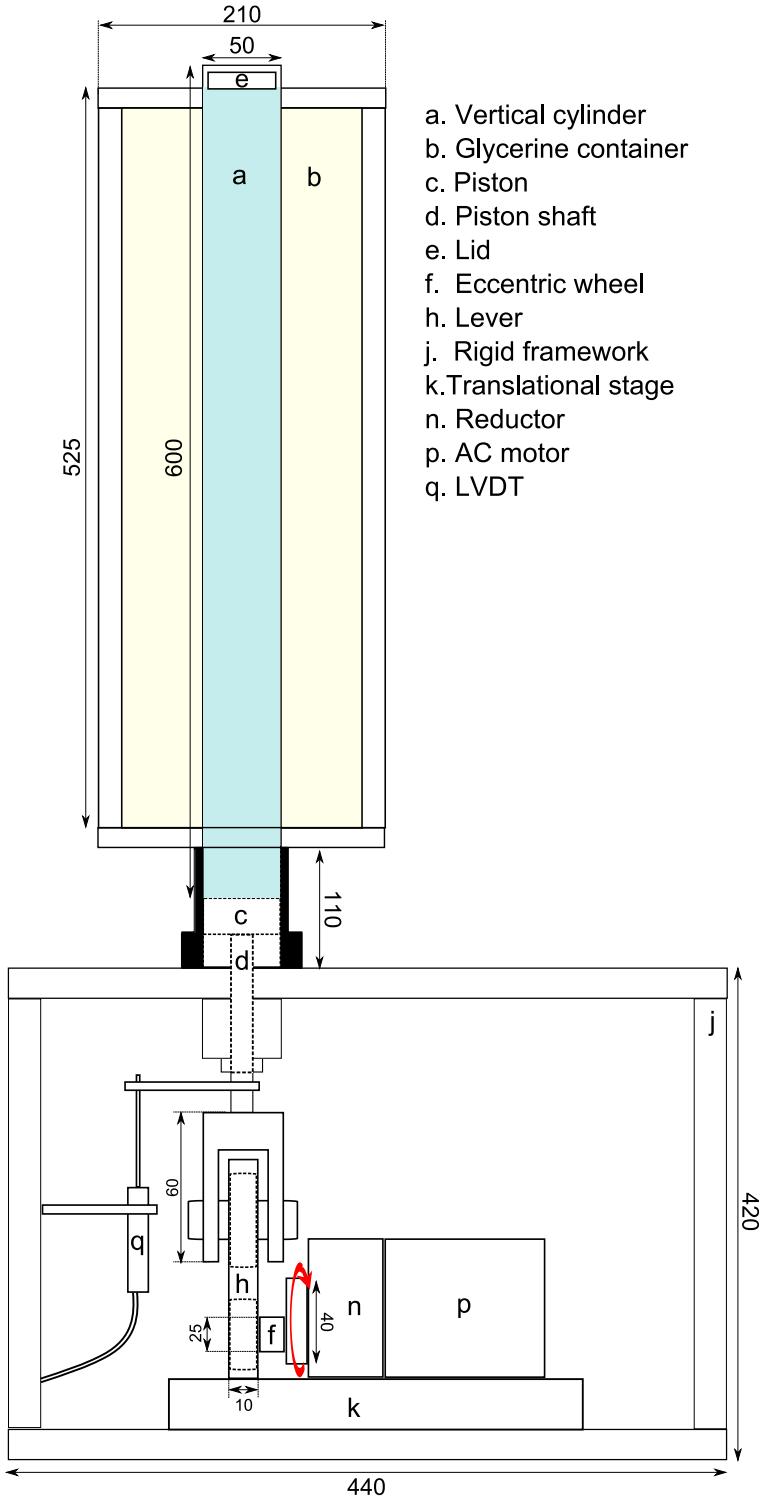

Figure 2.2: Side view of the experimental setup (the sketch is not to scale). The most relevant dimensions (mm) are specified.

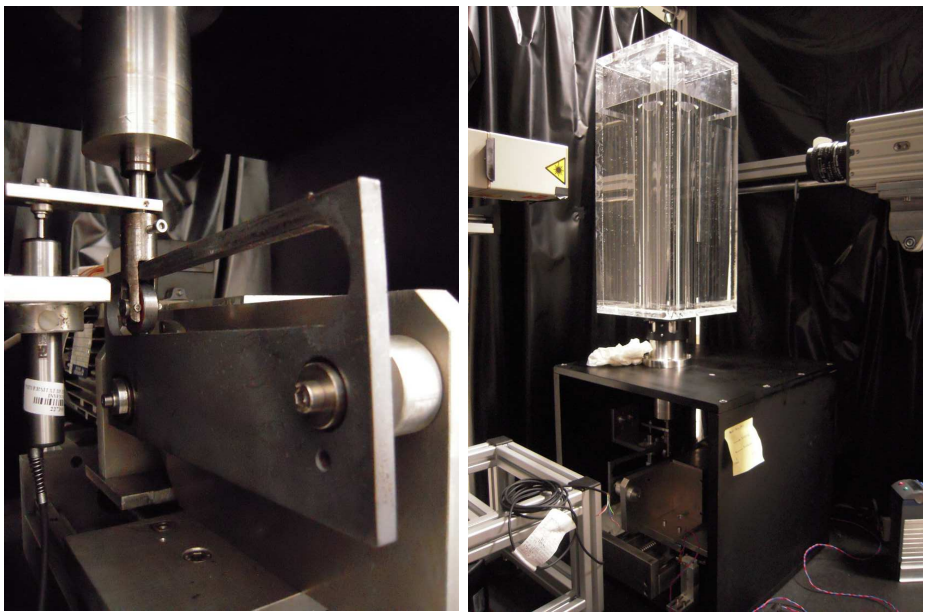

Figure 2.3: Pictures of the actual experimental setup placed in the *Laboratori de Física no Lineal*. Left: generation of the oscillatory motion; Right: general view of the experimental setup.

2.1.2 Monitoring the piston position

The vertical position of the piston was tracked in time using a Linear Variable Differential Transformer (LVDT) with a resolution of 0.03 mm. We performed an harmonic analysis of the LVDT signal using the Fast Fourier Transform and verified that the oscillations of the piston (in the presence of the fluid column) were indeed harmonic. Although the principal harmonic (ω_0) was always clearly dominant, there were however small contributions from the second and occasionally the third harmonics ($2\omega_0$ and $3\omega_0$). The amplitudes of these additional harmonics were more important at the lowest driving frequencies and amplitudes, but they never exceeded 7% of the amplitude of the main frequency component. Nevertheless we found that the presence of these additional harmonics in the driving could not always be disregarded. They are relevant, for example, when comparing laminar velocity profiles to their theoretical predictions (Sec. 4.2).

In Fig. 2.4 we show a reconstruction of the LVDT signal obtained from the sum of all relevant contributions to its frequency spectrum (solid line). In panel (a), which corresponds to the smallest driving amplitude achievable with the experimental setup ($z_0 = 0.20$ mm), deviations from a pure sinusoidal were notable since the relative contributions of the second and third harmonics were 5% and 7% respectively. However, for larger amplitudes the contribution of higher harmonics decreased. In panel (b) we show an example of the LVDT signal obtained

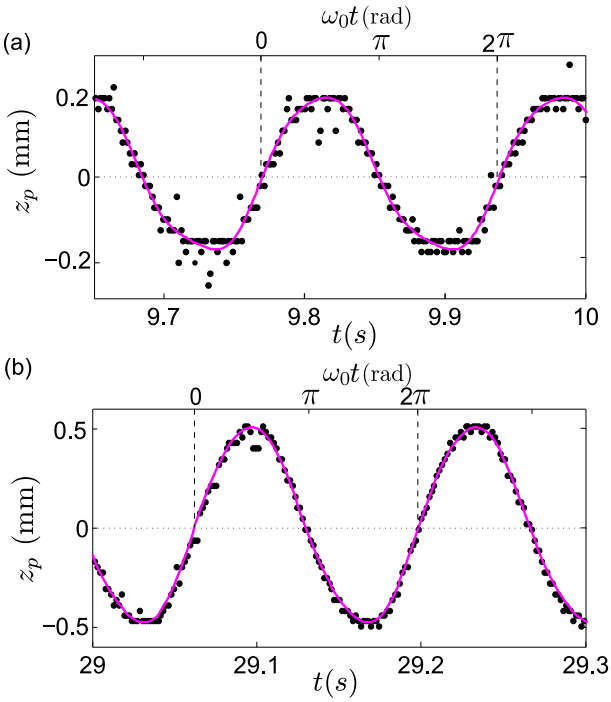

Figure 2.4: LVDT signal measured for two complete periods of oscillation. The solid line is the reconstruction of the LVDT signal based on its spectral contents (see text for details). The time phase $\omega_0 t$ is shown in the top horizontal axis. Panel (a) corresponds to $\omega_0 = 37.1$ rad/s, $z_0 = 0.20$ mm, and (b) to $\omega_0 = 47.1$ rad/s, $z_0 = 0.50$ mm.

for $z_0 = 0.50$ mm, for which the contribution of $2\omega_0$ and $3\omega_0$ were only 3% of the amplitude of the main frequency.

2.1.3 Temperature control

Although the temperature of the fluid in the cylinder could not be modified, we could control the temperature of the laboratory up to ± 1°C. We measured the fluid temperature in every experiment with a digital thermometer, and verified that most of the experiments had been performed at temperatures within the range 24 ± 1°C. We checked also that the temperature variation during a single experiment never exceeded 0.2°C.

We actually do not expect the oscillatory flow of the wormlike micellar fluid to be sensitive to slight variations in temperature. Even though η_0 and λ of wormlike micellar solutions depend strongly on temperature (Chap. 3), we will show theoretically in Sec. 4.1 that the oscillatory flows of Maxwell and Oldroyd-B fluids depend on η_0 and λ mainly through their ratio, which is known to be roughly independent of temperature (Fischer and Rehage, 1997).

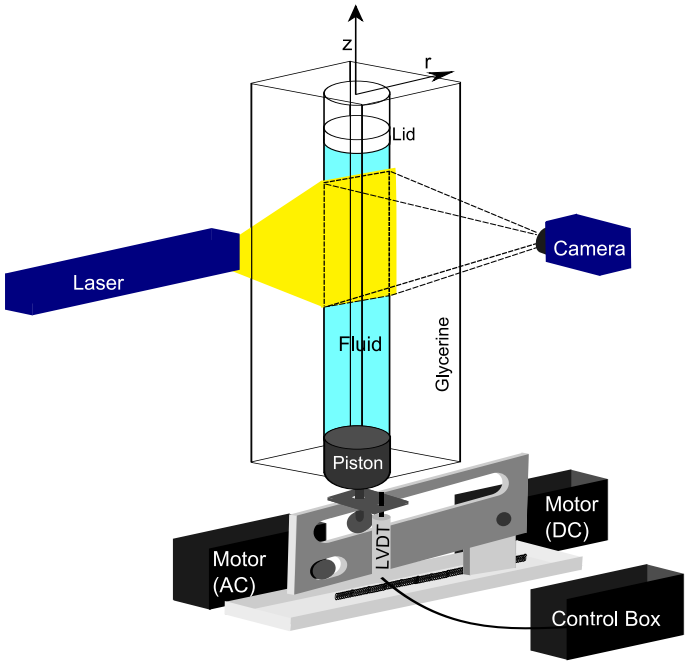

Figure 2.5: Schematic view of the experimental device, including the elements required for Particle Image Velocimetry.

2.2 Time resolved Particle Image Velocimetry

We used a 2D time-resolved PIV technique (Adrian, 1991; Raffel et al., 2007) to measure the velocity field of the oscillatory flow. In Fig. 2.3(right panel) and 2.5 we show a picture and a schematic representation of the PIV system implemented in the laboratory. We measured the two components of the fluid velocity (u_r, u_z) within a meridional plane $r - z$ of the tube. In order to measure the velocity field of the fluid, we had to seed previously the fluid with a small amount of very small, neutrally buoyant particles. We used polyamide particles of 57 μm of diameter and density $\rho = 1016$ kg/m^3 in a volume fraction of 3.5×10^{-5}. We checked that the fluid rheology was not significantly modified for this particle concentration.

2.2.1 Image acquisition

In order to measure the velocity field, an interrogation region of the meridional plane of the tube was illuminated with a pulsed laser sheet of about 1 mm thickness (Diode Laser HSI5000 from Oxford Lasers) and a pulse duration of 50 μs. By placing the laser at the closest possible position to the tube axis (15 cm from the end of the laser head to the tube axis) we ensured that the images were as bright as possible and showed a sharp contrast of the seeding particles with

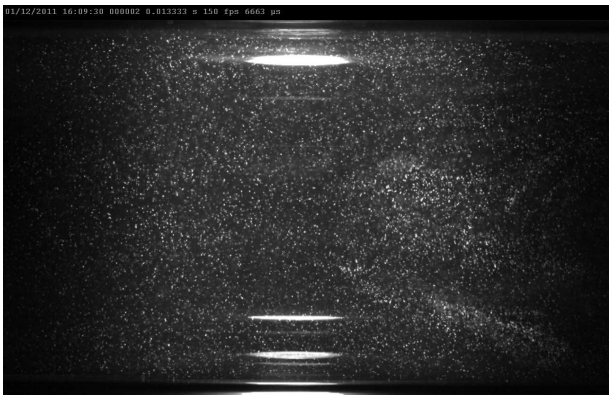

Figure 2.6: PIV image of a meridional plane of the tube (rotated by 90°). The seeding particles correspond to the bright dots. Small reflections are observed next to the tube walls.

respect to the surrounding fluid (which is essential for the post-processing of the images). An example of a PIV image is provided in Fig. 2.6. The light scattered by the particles was recorded with a high speed and high resolution CMOS camera (MotionPro-X3Plus from IDT, 1280×1024 pixels) equipped with a lens of 28 mm and F1.8 (Sigma). We placed the camera again at the closest possible position to the tube axis (25 cm from the CCD sensor to the tube axis) in order to maximize the spatial resolution of the images. In this first configuration, the field of view was a square of about 5×5 cm^2, and the spatial resolution along the z coordinate was 16 pix/mm.

An additional divergent lens ($f = -75.0$ mm, ThorLabs) could be added in the laser path so that the laser sheet was expanded and the illuminated area increased up to approximately 10×5 cm^2 (vertical×horizontal). This was convenient to characterize the unstable flow because it allowed to record a larger tube area and thus gain spatial information about the velocity field. However, in this second configuration we had to place the camera further apart from the tube axis, to be able to capture all the illuminated area, which slightly reduced the vertical spatial resolution to 13 pix/mm.

An external program controlled the shooting parameters of the camera. Both the frame rate and the number of frames (NF) to record could be controlled. The exposure time was given by the inverse of the frame rate, which in all cases was much larger than the shutter time of the camera of about 1 μs. When we performed ramps of the oscillation amplitude (discussed in more detail in Sec. 6.1) this program allowed to control the waiting time between steps (t_w). The camera had an internal trigger that controlled the laser shooting so that the camera recorded only when the light pulses were emitted. The acquired images were equally separated in time. The time interval was chosen such that we recorded

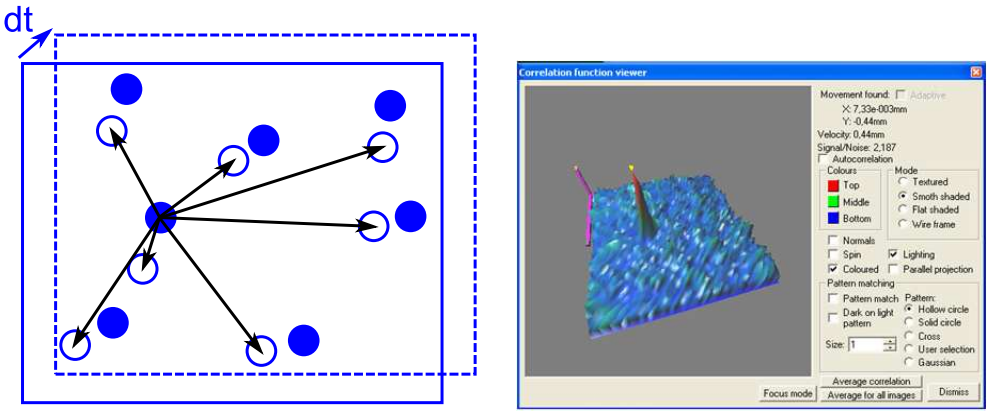

Figure 2.7: Left: sketch of the cross-correlation method used to determine the average displacement of the particles. Filled and empty dots correspond to the particle positions in two consecutive frames. The arrows indicate all the possible displacements of an individual particle between consecutives frames. Right: example of the maximization of the cross-correlation function for a particular position in the meridional plane, provided by the software.

a fixed number of frames per oscillation cycle (NP) at any imposed driving frequency. In the laminar flow regime we used $NP = 20$, and in more complex flows $NP = 40$.

The setup described allowed measurements of the in-plane components of the velocity field in the interrogation region within the meridional plane of the tube. A new stereo-PIV setup (Appx. B) that is currently being implemented in the laboratory will allow to measure also the azimuthal (out-of-plane) component of the velocity field.

2.2.2 PIV post-processing

A commercial PIV Software from Intelligent Laser Applications was used to perform the final post-processing of the images. In order to compute the mean velocity field the interrogation region was divided in square cells. As shown schematically in Fig. 2.7, the software evaluated the mean velocity field in each cell by (i) computing the statistical correlation of the displacements of the seeding particles between consecutive images and (ii) selecting the displacement for which the cross-correlation function was maximum. The overlap between adjoining square cells was set to 50% in both z and r directions. The size of the cell was chosen such that the displacement of the particles between consecutive images was roughly 0.25 times the size of the cell. In the laminar flow regime it was sufficient to use a constant cell size. For applied amplitudes $z_0 \leq 1.0$ mm we normally used a cell of 48×48 pix^2. For larger driving amplitudes the typical displacements of the

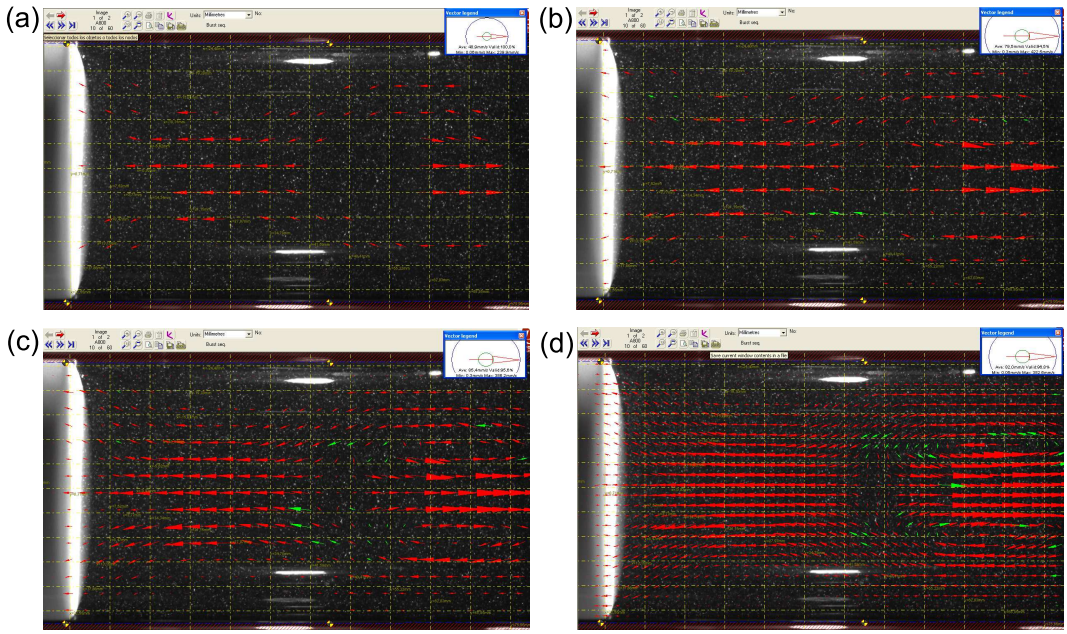

Figure 2.8: Example of the adaptative cross-correlation method. (a) The interrogation size is 128×128 pix^2; (b) 80×80 pix^2; (c) 64×64 pix^2; (d) 48×48 pix^2. The valid PIV velocity vectors are shown in red and the interpolated vectors in green.

particles increased and we chose the cell size accordingly so that it could increase up to 128×128 pix^2 (which is the maximum cell size available in the software).

However, this procedure did not allow to resolve strong local velocity gradients that appeared in non-laminar, more complex flows. An adaptative cross-correlation method allowed to overcome this difficulty by iteratively computing the cross-correlation function several times with decreasing cell sizes. We started with the largest cell size, 128×128 pix^2, and continuously reduced it down to 48×48 pix^2 (Fig. 2.8). The overlap between adjoining square cells was set to 50% regardless of the cell size. In order to eliminate spurious velocity vectors that might result from the cross-correlation process we applied velocity filters. First, a global velocity filter eliminated vectors that were far from the global mean velocity, and next a local velocity filter eliminated velocity vectors in terms of the local mean of the velocity field. At the end we applied an interpolation step that replaced the eliminated spurious vectors by the interpolated values computed by linear interpolation from their nearest neighbors.

A final calibration was required in order to determine the spatial dimensions of the PIV images. We used a hand-made calibration plate in which we had drawn a grid of dots separated by well-known distances. We placed the grid inside the fluid making sure that it was placed in the same meridional plane of the tube where the PIV images were recorded. A calibration image is provided in Fig.

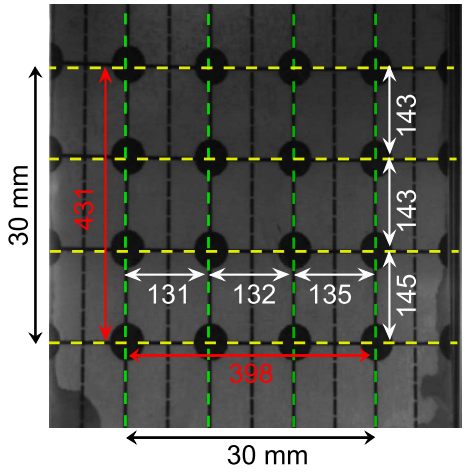

Figure 2.9: Calibration grid used to determine the spatial dimensions of the PIV images. The dimensions of the grid are provided both in mm (real dimensions) and in pixels (after image acquisition).

2.9. We noted that the magnification along the radial and vertical directions was not exactly the same, due to residual cylindrical aberrations that had not been eliminated with the glycerine outer tank. The vertical magnification was larger than the horizontal magnification by a factor $F = 1.1$.

At the end of the entire cross-correlation process, the software provided the in-plane velocity field in a square grid of known distances, for each frame. The azimuthal vorticity field was computed after the velocity field (using a Matlab routine) as

$$\boldsymbol{w} = \boldsymbol{\nabla}_{\parallel} \times \boldsymbol{u} = \left(\frac{\partial u_r}{\partial z} - \frac{\partial u_z}{\partial r} \right) \hat{e_\theta}. \tag{2.1}$$

The uncertainty in the velocity and vorticity measurements was about $\pm 3\%$ and $\pm 5\%$, respectively.

Our experimental setup did not allow to measure the out-of-plane component of the velocity. By computing the local divergence of the in-plane velocity field,

$$\boldsymbol{\nabla}_{\parallel} \cdot \boldsymbol{u} = \frac{\partial u_r}{\partial r} + \frac{\partial u_z}{\partial z}, \tag{2.2}$$

we could gain additional information on u_θ. If $\boldsymbol{\nabla}_{\parallel} \cdot \boldsymbol{u} \neq 0$ (clearly above the noise background) it is certain that $u_\theta \neq 0$. I.e. $\boldsymbol{\nabla}_{\parallel} \cdot \boldsymbol{u}$ should be negligible when $u_\theta \simeq 0$. Conversely, $\boldsymbol{\nabla}_{\parallel} \cdot \boldsymbol{u} = 0$ only implies that $u_\theta \neq u_\theta(\theta)$ but does not rule out the existence of $u_\theta \neq 0$.

2.3 Relevant features of the experimental setup

Our setup in Barcelona presented several new performances, compared to the previous setup available in the UNAM in Mexico. First, instead of fixed values of the driving amplitude (0.8, 1.2, 1.6, 2.0, 2.5 mm), our setup allowed to ramp the amplitude quasi-continuously, in fine steps of 0.02 mm. This allowed to study deviations from linearity of the velocity profiles in the laminar regime. Moreover, the accessible range of driving amplitudes was extended up to 6.00 mm, so that transitions to more complex flows arising at large drivings were accessible to study. Performing ramps of increasing and decreasing amplitude of the applied oscillations allowed us to measure the hysteresis of these transitions.

Second, progress in high speed imaging made possible to carry out time-resolved Particle Image Velocimetry measurements. We could measure up to 200 2D instantaneous velocity fields per second, in a relatively large region of the meridional plane of the cylinder. This fast imaging system allowed us to study the time dependence or the velocity field during an oscillation period with great detail.

Finally, synchronous measurements of the piston position in time allowed to determine the time phase of every acquired image, with a precision of 0.16 rad. The extraction of the time phases enabled to compute the phase lag of the velocity at the tube axis with respect to the piston position, and thus decompose the fluid velocity in magnitude and phase (Sec. 4.2). It made also possible a quantitative comparison of the measured laminar velocity field to theoretical predictions.

Chapter 3

Fluid Rheology

The fluid used to perform the experiments was a surfactant solution made of cetylpiridinium chloride (CPyCl from Sigma Aldrich, $m_0 = 358$ g/mol) and sodium salycilate (NaSal from Sigma Aldrich, $m_0 = 160.1$ g/mol) solved in distilled water, in a concentration [100:60] mM. The solution was prepared by adding weighted amounts of the two chemicals to distilled water. It was shaken vigorously and let it rest for about four days to let the entrained air to leave. The solution was stored in a dark chamber to avoid any possible damage caused by ambient light (Fardin et al., 2012). The surfactant concentration used was above the CMC, and thus the amphiphilic molecules rearranged forming cylindrical (wormlike) micelles. At this surfactant concentration the micelles were found in the semi-dilute regime. The density of the solution was $\rho = 1050$ kg/m^3. We were particularly interested in this wormlike micellar solution, at this precise surfactant and salt concentration, because it was well known to exhibit a Maxwellian behavior at small shear rates, after the work of Rehage and Hoffmann (1991), Berret et al. (1994), and Méndez-Sánchez et al. (2003).

In order to do the rheological characterization of the fluid we used a controlled stress rheometer RheoStress 1 (Thermo Haake), with a cone-plate fixture (a titanium cone of 1° and 60 mm diameter) that is available in our laboratory. Although the rheometer had a controlled-stress design, it enabled to perform experiments controlling either the stress (CS) or the shear rate (CR), for which it used an internal feedback loop. The temperature was controlled using a thermal bath (K15, Thermo Haake) with a resolution of ± 0.1°C. All the experiments shown in this section were performed at $T = 25.0$°C.

Part of the measurements presented in this section were performed also at the Hatsopoulos Microfluids Laboratory, of the Massachusetts Institute of Technology, during my two research stays in the Non-Newtonian Fluid Dynamics (NNF) research group, lead by Prof. G.H. McKinley. This laboratory is equipped with

two different controlled-stress rheometers, AR-G2 and DHR-3 (both from TA Instruments). The main advantage of using the AR-G2 is that a PIV setup can be coupled to it, which allows to do Rheo-PIV experiments under steady or transient shear. The DHR-3 is the latest acquisition of the NNF group. This instrument allows to measure normal forces very accurately. In all rheometers the temperature control is achieved with a Peltier plate that is implemented in the bottom fixture. A microfluidic rheometer, Viscometer/Rheometer-On-a-Chip (VROC, RheoSense Inc.) is also available. This capillary rheometer allows to perform experiments at large shear rates. The temperature inside the channel is controlled by means of a thermal jacket. We conveniently chose the rheometer (and the corresponding geometry) depending on the rheological properties that were to be tested.

We noted slight differences in the absolute value of the rheological properties obtained for the micellar solution when using the Rheostress 1, the AR-G2 and the DHR-3. We presume that these variations appeared as a consequence of the different materials used in the fixtures of the different rheometers. The fixture used with the Haake rheometer was a cone made of titanium. The cone used with the DHR, instead, was made of aluminum. For the AR-G2 we used a transparent quartz plate (to which we attached a thin film on the surface to prevent slip). Differences in surface roughness of these materials (Dimitriou et al., 2012) might lead to distinct wetting properties, which in particular might cause a slight degree of slip on the surface of the fixture and a reduction of the measured *apparent* viscosity (Lettinga and Manneville, 2009). In the following sections the rheometer and fixture employed in each experiment will be specified.

3.1 Linear viscoelasticity

In order to test the linear viscoelastic response of the fluid we performed small amplitude oscillatory shear experiments ($Wi < 1$). In this regime there is no significant damage of the fluid microstructure.

In oscillatory experiments a sinusoidal shear strain is applied and the resulting shear stress is measured (the reverse situation is also possible under CS conditions). The oscillatory strain applied by the rheometer is given by (Bird et al., 1987)

$$\gamma(t) = \gamma_0 \sin(\omega t), \tag{3.1}$$

where γ_0 is the amplitude of the dimensionless deformation and ω is the frequency of oscillation. The resulting rate of shear deformation reads

$$\dot{\gamma}(t) = \dot{\gamma}_0 \cos(\omega t) \tag{3.2}$$

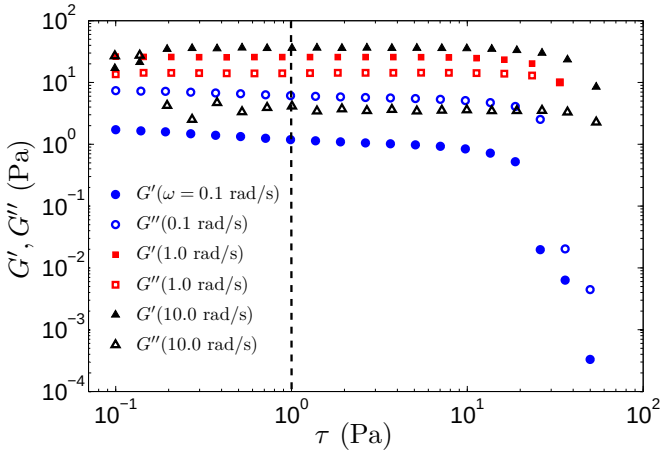

Figure 3.1: Viscoelastic moduli (G', G'') measured at $\omega = 0.1$, 1.0, 10.0 rad/s ($T = 25.0°$C). We used the RheoStress 1 rheometer with cone-plate geometry (titanium cone of 1° and 60 mm diameter). The dashed line is drawn at $\tau = 1$ Pa.

with $\dot{\gamma}_0 = \gamma_0\omega$. The shear stress of the fluid response can be expressed as

$$\tau = \gamma_0 \left[G'(\omega)\sin\omega t + G''(\omega)\cos\omega t\right]. \tag{3.3}$$

In terms of the complex viscosity $\eta^* = \eta'' + \imath\eta'$ this expression is equivalent to:

$$\tau = \dot{\gamma}_0 \left[\eta'(\omega)\cos\omega t + \eta''(\omega)\sin\omega t\right]. \tag{3.4}$$

The term in phase with the applied deformation (G') is called *storage* modulus and accounts for the elastic response of the fluid. The term in quadrature (G'') is the *loss* modulus and accounts for the dissipative behavior of the fluid.

The expressions for the linear viscoelastic moduli given by the single mode Maxwell model are the following (Bird et al., 1987):

$$G' = G_0\frac{\omega^2\lambda^2}{1+\omega^2\lambda^2}, \quad G'' = G_0\frac{\omega\lambda}{1+\omega^2\lambda^2}. \tag{3.5}$$

G_0 is the shear modulus and λ is the relaxation time of the fluid. In the linear viscoelastic regime the viscoelastic moduli are constant and do not depend on the applied strain or stress.

In order to determine experimentally the extent of the linear viscoelastic regime we performed a stress (or strain) sweep at different constant frequencies. The results are shown in Fig. 3.1. We chose $\tau = 1$ Pa as a suitable stress value to study the linear viscoelastic response of the fluid, since it lies within the linear regime for all explored frequencies. The linear rheology was characterized by performing

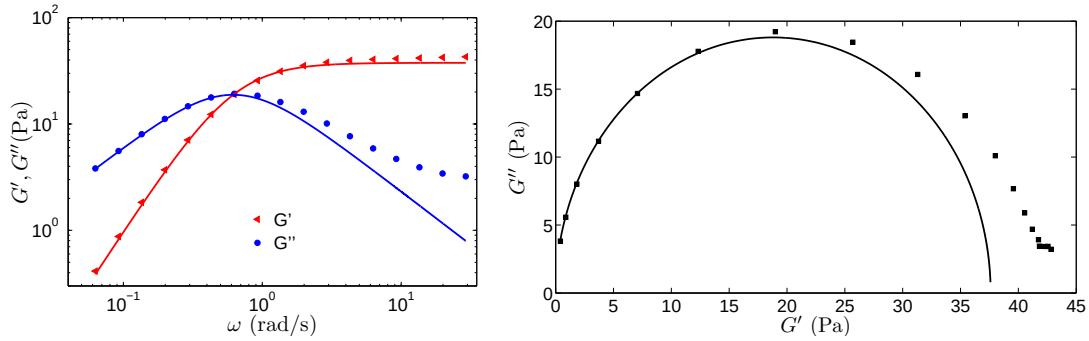

Figure 3.2: Left: Storage and loss moduli versus angular frequency for a CPyCl/NaSal [100:60] mM solution, at $T = 25°$C. We used the RheoStress 1 rheometer with cone-plate geometry (titanium cone of 1° and 60 mm diameter). Experimental results (dots) and analytical fitting curves (solid lines). Right: Cole-Cole plot.

an oscillatory frequency sweep (at a constant stress of 1 Pa) and quantifying the elastic and dissipative response of the fluid at each oscillation frequency. In Fig. 3.2 we show the storage and loss moduli obtained at $T = 25.0°$C. At low frequencies, $\lambda\omega < 1$, both moduli are well described by a single mode Maxwell model (Eqs. (3.5)), represented in solid lines in the figure. The resulting fitting parameters are $G_0 = 37 \pm 1$ Pa and $\lambda = 1.6 \pm 0.1$ s. The viscoelastic data can also be represented in a Cole-Cole plot, G'' versus G'. Data for an ideal Maxwell fluid should lie on a semicircle of radius $G_0/2$ centered at $(0, G_0/2)$, according to

$$\left(G'(\omega) - \frac{G_0}{2}\right)^2 + (G''(\omega))^2 = \left(\frac{G_0}{2}\right). \tag{3.6}$$

Figure 3.2 shows the Cole-Cole plot for our experimental data, and the theoretical prediction for a Maxwell model (solid line). We observe that the wormlike micellar solution exhibits indeed a linear viscoelastic response close to the Maxwell behavior, particularly at low frequencies. Note however that substantial deviations from this linear behavior are observed at large enough frequencies.

3.2 Non-linear viscoelasticity

For larger amplitudes of the applied oscillations ($Wi > 1$) the response of the micellar fluid becomes nonlinear, which results from the reorganization of the fluid microstructure. The Lissajous figures are parametric plots of stress vs. shear strain which are very useful in visually distinguishing the linear and non-linear viscoelastic regimes. When the fluid response is linear the Lissajous figures are elliptical, whereas in the non-linear regime the orbits are still periodic but not

elliptical (Ewoldt et al., 2008). The non-linear viscoelastic stress response of the fluid can be completely represented by a Fourier series as:

$$\tau = \gamma_0 \sum_{n\ odd} \left\{ G'_n(\omega, \gamma_0) \sin n\omega t + G''_n(\omega, \gamma_0) \cos n\omega t \right\}. \tag{3.7}$$

In the linear regime this series is restricted to the first harmonic $n = 1$, but higher order harmonics contribute in the nonlinear regime. Experimentally it is thus not sufficient to measure the first-harmonic viscoelastic coefficients G' and G'' if we aim to fully characterize the non-linear viscoelastic response of the fluid. Ewoldt et al. (2008) showed that the elastic (τ') and viscous (τ'') response can be decomposed in terms of the (orthogonal) Chebyshev polynomials of the first kind, $T_n(x)$, as

$$\tau'(x) = \gamma_0 \sum_{n\ odd} e_n(\omega, \gamma_0) T_n(x), \tag{3.8}$$

$$\tau''(y) = \dot{\gamma}_0 \sum_{n\ odd} \nu_n(\omega, \gamma_0) T_n(y). \tag{3.9}$$

where $x = \gamma/\gamma_0$ and $y = \dot{\gamma}/\dot{\gamma}_0$ are the normalized deformation and shear rate. We refer to $e_n(\omega, \gamma_0)$ and $\nu_n(\omega, \gamma_0)$ as the elastic and viscous Chebyshev coefficients. Higher-order Fourier terms can be conveniently expressed in terms of e_n and ν_n, which provide a physically meaningful interpretation. In the limit of $e_3/e_1 \ll 1$ and $\nu_3/\nu_1 \ll 1$ we recover the linear viscoelastic response. Deviations from linearity can be interpreted in terms of the third harmonic ($n = 3$). For $e_3 > 0$ the fluid experiences an intra-cycle strain stiffening (the elastic stress is higher than the stress corresponding to the first-order contribution alone) while for $e_3 < 0$ the fluid exhibits an intra-cycle strain-softening. Similarly, $\nu_3 > 0$ or $\nu_3 < 0$ correspond to intra-cycle shear-thickening or intra-cycle shear-thinning.

Figure 3.3 shows the Lissajous plots obtained for the micellar solution. The frequency of oscillation was kept constant at $\omega_0 = 0.5$ rad/s and the strain amplitude ranged from $0.2 < \gamma_0 < 5.2$ (in dimensionless units). This single experiment was performed at $T = 22.0°$C. Thus this figure is only intended to report information about the shape of the curves and not to provide the actual values of the stress response. It is clear from the figure that the Lissajous plots indeed evolve from ellipses for small strain amplitudes to just periodic orbits at larger amplitudes. Dimitriou et al. (2012) computed the Chebyshev coefficients for the same micellar solution and observed that the nonlinear response of the micellar solution was strain-stiffening (e.g. $e_3/e_1 = 0.22$ for $Wi = 2.73$ and $T = 22.0°$C).

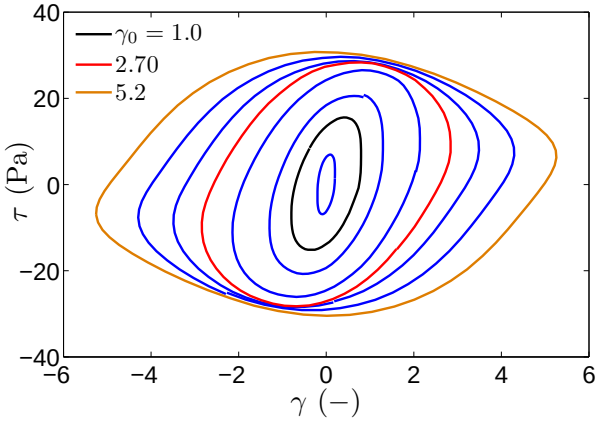

Figure 3.3: Amplitude sweep obtained at $\omega_0 = 0.5$ rad/s, with the AR-G2 and cone-plate geometry (top transparent quartz plate of 50 mm diameter and bottom aluminum cone of 4°), at $T = 22.0$°C).

3.3 Steady shear rheology

We measured the steady shear rheology of the micellar solution at 25.0°C using the Rheostress 1 rheometer with the cone-plate geometry. We performed a shear rate sweep in the direction of increasing shear rate and waited long enough at each shearing value to make sure that the fluid response was steady (a maximum time of 60 s was allowed at each point). Figure 3.4 shows that the solution exhibits an initial linear regime at small shear rates with constant viscosity, $\eta_0 = 52 \pm 1$ Pa·s. This result is in good agreement with the value predicted using the Cox-Merz rule, $\eta_0 \simeq G_0\lambda$. This rule is an empirical relation that allows to relate complex properties obtained under oscillatory shear experiments with steady shear flow measurements at corresponding values of frequency and shear rate (Bird et al., 1987). It states that

$$\eta(\dot{\gamma}) = |\eta^*(\omega)|\Big|_{\omega=\dot{\gamma}}. \tag{3.10}$$

At shear rates larger than a critical shear rate $\dot{\gamma}_c \simeq 0.5$ s^{-1} ($\dot{\gamma}_c \simeq 1/\lambda$) the solution strongly shear thins and the flow curve exhibits a pronounced shear stress plateau, $\tau_{plateau} \simeq 18$ Pa. These results are consistent with previous studies that used identical or similar wormlike micellar solutions (Rehage and Hoffmann, 1991; Berret, 1997; Méndez-Sánchez et al., 2003; Pipe et al., 2010; Ober et al., 2011). Above this critical shear rate the fluid flow becomes unstable against the formation of different shear bands that support different effective viscosities (Cates and Fielding, 2006; Manneville, 2008; Olmsted, 2008; Fardin et al., 2010). The strong shear-thinning behavior can be approximately captured with the non-linear Giesekus model (Eq. (1.16)), as shown in Fig. 3.4 (solid line). The value obtained

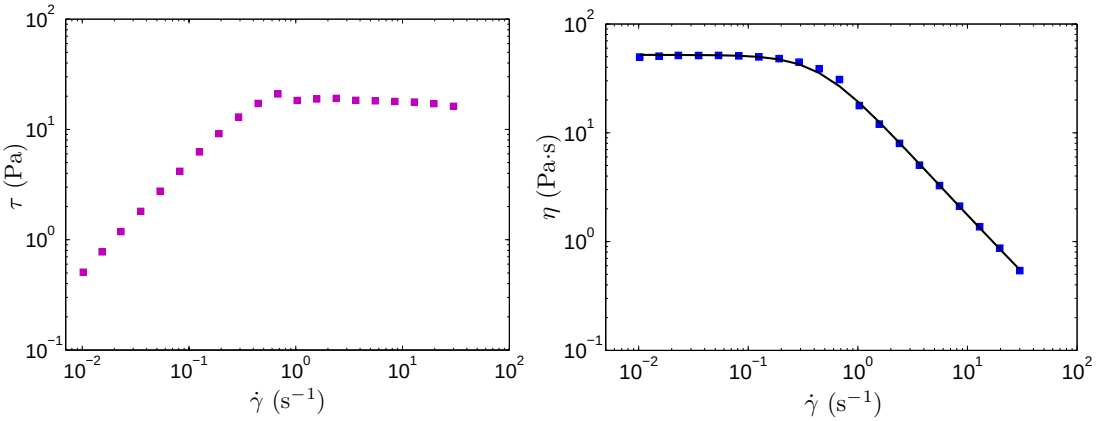

Figure 3.4: Left: Steady flow curve measured at $T = 25.0°C$, using the Rheostress 1 with a cone-plate fixture (titanium cone of 1° and 60 mm diameter). Right: The viscosity is displayed as a function of the applied shear rate. The solid line is the fit obtained for the Giesekus equation.

for the mobility factor is $\alpha \simeq 0.83$.

We can extend the range of applied shear rates using the microfluidic rheometer Viscometer/Rheometer-On-a-Chip (Pipe and McKinley, 2008). The VROC is a capillary rheometer consisting on a high-aspect-ratio rectangular slit of length l =8.8 mm, width w =3.2 mm, and height h =99.6 μm. The flow rate is imposed using a syringe pump and the pressure drop (ΔP) is measured by four in-line pressure transducers distributed along the centerline. The shear stress at the walls (τ_w) can be inferred from the pressure drop using the relation

$$\tau_w = \frac{w}{2l}\Delta P. \tag{3.11}$$

For a Newtonian fluid, the shear rate at the walls can be determined from the imposed volumetric fluid rate (Q) as

$$\dot{\gamma}_{w-N} = \frac{6Q}{hw^2}. \tag{3.12}$$

In order to take into account the shear-thinning of the micellar fluid and derive the *true* shear rate at the walls we applied the Weissenberg-Rabinowitsch-Mooney correction (Pipe and McKinley, 2008),

$$\dot{\gamma}_{true-w} = \frac{\dot{\gamma}_{w-N}}{3}\left(2 + \frac{d\ln\dot{\gamma}_{w-N}}{d\ln\tau_w}\right). \tag{3.13}$$

We show in Fig. 3.5 both the data obtained with the VROC, at large shear rates, and the data obtained with the AR-G2 at smaller shear rates. We observe that

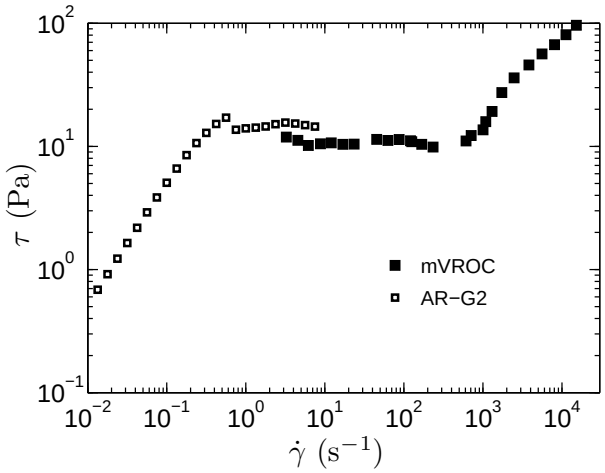

Figure 3.5: Extended flow curve measured at $T = 25.0°C$. At low shear rates we used the AR-G2 (quartz plate of 50 mm diameter with a thin film attached to the surface, and aluminum cone of 4°) and at large shear rates the VROC.

the stress plateau extends over three decades in shear rate, from 0.3 s^{-1} up to approximately 10^3 s^{-1}. Note however that there is a considerable reduction of the value of the stress plateau from that measured at the macroscale with the AR-G2 rheometer ($\tau_{plateau} \simeq 15$ Pa) or using the microfluidic device ($\tau_{plateau} \simeq 10$ Pa). This difference of about 30% might be caused by slip, but it could also be caused by non-local effects, mainly via stress difusion (Cromer et al., 2011; Ober et al., 2011). The relevant lengthscale of the microfluidic device (96 μm) was much smaller than the gap size of the cone-plate fixture (1.75 mm). Brownian motion is thus relatively much more important in the microfluidic device and might have promoted coupling between stress and fluid microstructure.

The steady shear flow curve exhibits an interesting hysteretic behavior when ramping up and down the applied shear rate (Fig. 3.6). For increasing shear rates the flow curve exhibits a bump in stress just above the critical shear rate. This bump in stress is only observed under Controlled Rate conditions and reflects the metastability of this region of the flow curve. This bump softens and eventually disappears for *infinitely* slow curves. For decreasing shear rates, instead, there is no sign of stress bump but a constant stress value is observed all along the unstable region of the flow curve. This hysteretic behavior, together with the nonmonotonicity of the steady flow curve, are two signatures of the underlying shear banding of the solution.

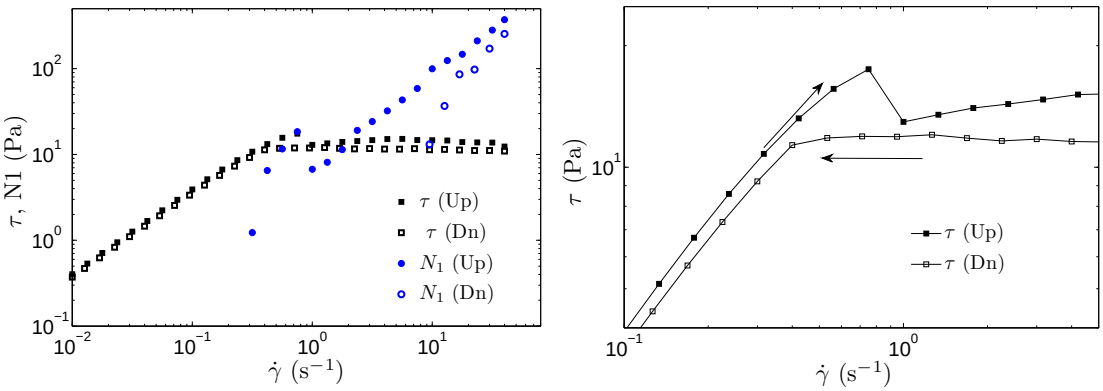

Figure 3.6: Left: Flow curves measured measured at $T = 25.0°$C, at increasing and decreasing shear rates using the DHR-3 (aluminum cone of 2 ° and 60 mm diameter). Both the shear stress and the first normal stress difference are depicted. Right: Zoom in of the hysteretic region.

3.3.1 Normal stress differences

An important feature of wormlike micellar solutions is the existence of first normal stress differences (N_1) under steady shear. The measurements of the normal differences are shown in Fig. 3.6. They were done in the DHR-3 rheometer (which has an axial force transducer required for these measurements) with a cone-plate fixture.

At small shear rates N_1 seemed to exhibit a quadratic dependence with the applied shear rate, $N_1 = \Psi_1 \dot{\gamma}^2$, with a constant stress coefficient Ψ_1 (Pipe et al., 2010). Unfortunately we obtained only two data points belonging to this initial linear viscoelastic regime. Although the DHR-3 has a large sensitivity to normal forces, the normal stress values corresponding to smaller shear rates were too low to be resolved by the rheometer. In the nonlinear regime N_1 showed an almost linear dependence with the shear rate.

This wormlike micellar solution is known to exhibit also non-zero second normal stress differences, N_2. However they are much more difficult to measure experimentally. Previous work of Pipe et al. (2010) reported values of $\Psi_2/\Psi_1 = -0.4$ up to shear rates of $\dot{\gamma} = 50$ s^{-1}.

3.4 Temperature dependence

The rheological characterization of the fluid presented so far in this chapter was performed at $T = 25.0°$C. However, the rheological properties of this fluid are very sensitive to temperature changes (Fischer and Rehage, 1997; Ober et al., 2011).

Temperature (°C)	λ (s)	η_0 (Pa·s)	G_0 (Pa)	$\dot{\gamma}_c$ (s^{-1})
22.0	2.8 ± 0.1	109 ± 5	35 ± 1	0.3
23.0	2.4 ± 0.1	80 ± 4	38 ± 1	0.4
24.0	1.9 ± 0.1	65 ± 2	35 ± 1	0.4
25.0	1.6 ± 0.1	52 ± 2	37 ± 1	0.5

Table 3.1: Linear viscoelastic properties of the wormlike micellar solution CPyCl/NaSal [100 : 60] mM at different temperatures in the range $20.0 - 25.0$°C.

In Table 3.1 we provide the rheological properties for the range of temperatures $T = 20.0 - 25.0$°C. We observe that both the relaxation time and zero-shear viscosity rapidly decrease with increasing temperature. Note however that the shear modulus is less sensitive to temperature and remains roughly constant within the range of explored temperatures (Fischer and Rehage, 1997).

3.5 Concentrated versus diluted solution

We were also interested in a second solution of CPyCl/NaSal with a considerably lower concentration of surfactant and salt [66:40] mM (the relative amount of CPyCl to NaSal is the same for the two solutions: 1.7). This diluted solution was prepared following the same procedure described at the beginning of this section. Its concentration was still above the CMC so that wormlike micelles formed, and at this concentration the solution was within the semi-dilute regime as well. As described by Haward and McKinley (2012), as the surfactant concentration is reduced the viscoelasticity of the solution diminishes: both the relaxation time and zero-shear viscosity rapidly decrease. On the other hand as the concentration of micelles is decreased the linear viscoelastic behavior of the solution progressively deviates from a purely Maxwellian behavior. Figure 3.7 shows the linear viscoelastic characterization obtained with the DHR-3 and cone-plate geometry. In the first panel we show the viscoelastic moduli G' and G'' obtained by performing a frequency sweep at a constant deformation of $\gamma_0 = 10\%$ (which was first checked to lie within the linear regime). The solid line is the fit to the experimental data using the single-mode Maxwell model. In the second panel the corresponding Cole-Cole plot is shown, with the Maxwell fit obtained in the first panel. Although the solution exhibited a manifest viscoelastic behavior, the Maxwell model was not able to accurately reproduce the experimental data obtained for this solution, as shown in the figure. We thus obtained the relaxation time directly from the crossing point ω_c of G' and G'', as $\lambda = 1/\omega_c = 0.3 \pm 0.1$ s. The shear modulus provided by the Maxwell fit for the diluted solution is $G_0 = 5 \pm 1$ Pa.

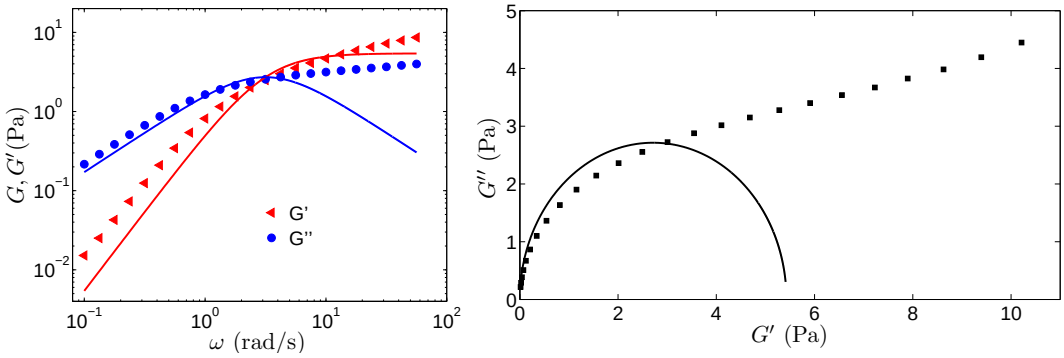

Figure 3.7: Left: Storage and loss moduli versus angular frequency for a CPyCl/NaSal [66:40] mM solution, measured with the DHR-3 rheometer with a cone-plate geometry (aluminum cone of 2° and 50 mm diameter), at $T = 25.0$°C. Experimental results (dots) and analytical fitting curves (solid lines) based on a single mode Maxwell model. Right: Cole-Cole plot.

Concentration (mM)	Temperature (°C)	λ (s)	G_0 (Pa)	η_0 (Pa·s)
[100 : 60]	25.0	1.6 ± 0.1	37 ± 1	52 ± 1
[66 : 40]	25.0	0.3 ± 0.1	5 ± 1	3 ± 1

Table 3.2: Rheological properties of the wormlike micellar solution CPyCl/NaSal at two different surfactant concentrations, [100 : 60] mM and [66:40] mM, at 25.0°C.

The steady flow curve measured using the DHR rheometer and the microfluidic VROC rheometer is shown in Fig. 3.8. This solution exhibits a linear response for shear rates lower than $\dot{\gamma}_c \lesssim 2$ s^{-1}, with a constant shear viscosity of $\eta_0 = 3 \pm 1$ Pa·s. Note that for this diluted solution the Cox-Merz rule does not accurately predict the value of η_0 found experimentally. Above the critical shear rate the fluid strongly shear thins.

A fundamental difference between the two solutions is that the steady flow curve for the diluted solution is monotonic, whereas the flow curve for the concentrated one is clearly nonmonotonic. This monotonicity would imply that, despite exhibiting a pronounced nonlinear shear-thinning response, the diluted solution does not shear band.

Alternatively, we also measured the flow curve at increasing and decreasing shear rates. Fig. 3.8 shows the absence of hysteresis between the two trajectories. There is indeed a perfect overlap in both the shear stress and normal stress differences when ramping up and down the applied shear rate. The absence of hysteresis for the dilute solution is another signature of the absence of shear banding. We further confirmed that the diluted solution does not shear band by performing direct visualization experiments under steady shear flows in a cone-plate geometry.

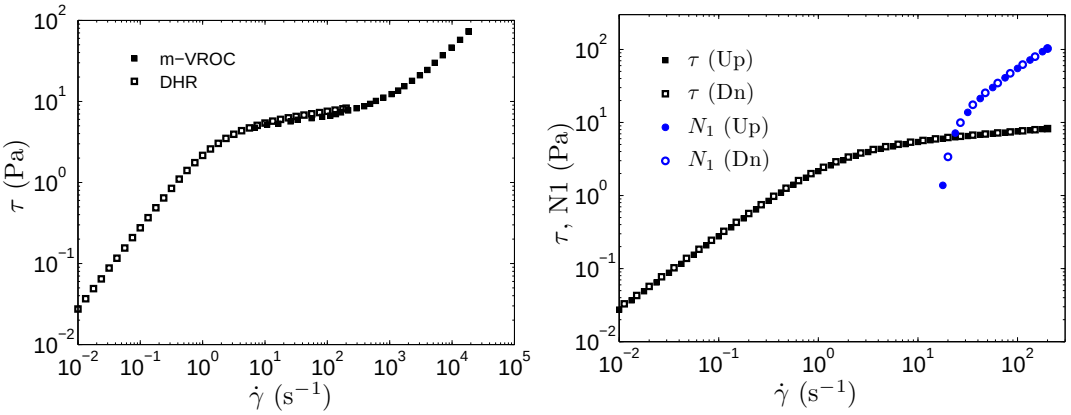

Figure 3.8: Left: Extended flow curve for the dilute solution [66:40] mM, measured at T=25.0°C. At low shear rates we have used the DHR-3 (aluminum cone of 2° and 50 mm diameter) and at large shear rates the VROC. Right: Flow curve and normal stress differences measured at increasing and decreasing shear rates using the DHR-3 (same fixture).

In Appx. C we report the experiments done using a Rheo-PIV setup that allowed to obtain rheological (stress-strain) data and simultaneous information about the velocity profiles inside the sample. We observed that the velocity profiles were linear for small applied shear rates ($Wi < 1$). But more importantly, they remained linear for applied shear rates within the shear-thinning regime ($Wi > 1$). At comparable shear rates the concentrated solution ([100:60] mM) exhibited pronounced nonlinear velocity profiles with three distinct shear bands. These results highlight the crucial influence that the surfactant concentration has on the nonlinear response of the fluid.

In Table 3.2 we present a summary of the main linear viscoelastic properties obtained for both the concentrated, [100:60] mM, and diluted, [66:40] mM, wormlike micellar solutions. Since the rheological response of the two solutions is qualitatively different, we will conveniently use each solution to study different flow behaviors. The concentrated solution will be very convenient for the study of the laminar oscillatory flow in the vertical pipe (Sec. 4.2), since it exhibits a nearly Maxwellian response. On the other hand, the diluted solution will be useful in elucidating the importance of shear banding in triggering the viscoelastic instability observed in oscillatory pipe flow (Sec. 6.3).

Chapter 4

Laminar regime

This chapter is devoted to the study of the laminar oscillatory pipe flow of simple viscoelastic fluids. The laminar regime is achieved by applying small drivings ($Wi < 1$), which correspond to small amplitudes and low frequencies of the imposed oscillatory motion. This regime can be considered to be inertialess ($Re \ll 1$), since the characteristic velocities of the fluid are typically small and the shear viscosity very large. The study of the laminar oscillatory flow is performed at $De > 1$, so that most of the interesting observed flow phenomena presented in this section result from fluid elasticity.

We first address the problem of the laminar oscillatory flow from a theoretical perspective (Sec. 4.1). Next, in Sec. 4.2, we test the validity of our theoretical predictions by performing experiments with a wormlike micellar solution.

4.1 Theoretical analysis

We revisit in this section the generic problem of wall-bounded oscillatory flows of viscoelastic liquids. The two ideal basic geometries in which oscillatory flows can be studied consider the fluid confined either between two infinitely large parallel plates or within an infinitely long tube of circular cross-section. In both cases the flow can be induced by the (synchronous) harmonic oscillatory motion of the sidewalls or by a harmonically oscillating pressure gradient applied in the direction of the sidewalls. We analyze the problem of wall-bounded oscillatory flow from an original perspective. We regard the flow as the result of the interference in time and space of the Ferry shear waves generated either by the moving sidewalls or by the oscillatory pressure gradient. This perspective brings new physical insight that is useful to understand the dramatic deviations of the velocity profiles of viscoelastic liquids from those of Newtonian liquids.

We focus on the periodic steady state of laminar flow that corresponds to small amplitudes and low frequencies of the forcing. In this regime the flow is parallel to the walls, the advective term in the momentum equation vanishes, and the governing equations are linear and therefore accessible to analytical treatment. Furthermore we consider as constitutive equations the upper-convected Maxwell model (UCM) and the Oldroyd-B model. The fact that for both models the shear-stress equation for unidirectional flow is also linear allows to solve the problem of laminar flow analytically.

In Sec. 4.1.1 we first consider Stokes' problem of the flow induced by an infinite oscillatory wall, and obtain expressions for the damping and wavelength of the shear waves generated at the wall. Next, we show that the presence of a second wall parallel to the first one and oscillating synchronously with it leads to resonances at well defined driving frequencies. In Sec. 4.1.2 we consider the oscillatory flow within a straight cylinder of very large aspect ratio induced by the oscillatory motion of the top and bottom endwalls. We derive the expression for the velocity profile in terms of the characteristic lengths of the corresponding shear waves. The relevant features of this velocity profile are studied in Sec. 4.1.3. We identify the conditions for having a resonant response of the velocity field, and study how it disappears with the addition of a Newtonian solvent.

4.1.1 Flow induced by oscillatory plates

A single oscillatory plate

Let us recall in the first place Stokes' problem of an infinite plate that oscillates harmonically in its own plane y–z, along the z axis, with angular frequency ω_0 and oscillation amplitude z_0. The fluid occupies the semi-infinite domain $(x, y, z) \in [0, \infty) \times (-\infty, \infty) \times (-\infty, \infty)$ at one side of the wall. Fluid motion is driven by the wall oscillation, through the no-slip velocity boundary condition:

$$\boldsymbol{u}(0, y, z, t) = (0, 0, z_0\omega_0 \cos(\omega_0 t)), \tag{4.1}$$

where $\boldsymbol{u} = (u_x, u_y, u_z)$ is the velocity field in Cartesian coordinates. In the steady state, when start-up transients have disappeared, the solution for a Newtonian fluid of density ρ and dynamic viscosity η describes an oscillatory boundary layer whose thickness scales with the square root of the oscillation period (Stokes, 1851; Batchelor, 1967):

$$\boldsymbol{u}(x, y, z, t) = (0, 0, z_0\omega_0 e^{-x/x_0} \cos(\omega_0 t - \frac{2\pi}{\lambda_0} x)). \tag{4.2}$$

The solution satisfies the far-field boundary condition $\lim_{x\to\infty} \boldsymbol{u} = (0,0,0)$, and

$$x_0 = \frac{\lambda_0}{2\pi} = \sqrt{\frac{2\eta}{\rho\omega_0}}. \tag{4.3}$$

The length scales x_0 (damping length of the oscillation amplitude) and λ_0 (wavelength of the oscillation) are both given by the thickness of the Stokes boundary layer, since this is the only length scale that can be built from the variables of the problem for a Newtonian fluid. Transverse oscillations are thus overdamped (cannot propagate into the fluid).

Things are different for viscoelastic fluids, which behave as elastic solids on short time scales. Ferry (1942a) showed that Stokes' second problem for a Maxwell fluid (for which stress relaxation is described by a single time constant λ) has also a solution of the form given by (4.2), for which x_0 and λ_0 do not coincide anymore but are related by:

$$x_0 = \frac{\lambda_0}{2\pi}\left[\omega_0\lambda + \sqrt{1+(\omega_0\lambda)^2}\right]. \tag{4.4}$$

The difference between x_0 and λ_0 depends only on the Deborah number ($De = \omega_0\lambda$). It is clear that fluid elasticity ($De > 0$) makes $x_0 > \lambda_0/(2\pi)$, so that transverse oscillations can propagate effectively before they are attenuated. Measurement of the unidirectional propagation of the underdamped, transverse shear waves induced by an oscillating plate (known as Ferry waves (Ferry, 1941, 1942a,b; Adler et al., 1949)) has become a classical method for linear rheological characterization of gels and polymers (Ferry, 1980; Joseph et al., 1986a,b; Bird et al., 1987; Mitran et al., 2008).

Stokes' second problem can be solved analytically also for a viscoelastic fluid described by the Oldroyd-B constitutive equation (Eqs. (1.15)). At small driving amplitudes and low frequencies the flow is laminar. Oscillatory motion of the wall sets the fluid in motion in the direction z and, because of translational invariance along y and z, the base flow is $\boldsymbol{u} = (0,0,u_z(x,t))$. The flow is governed by the Navier–Stokes equation and the continuity equation for an incompressible fluid:

$$\rho\left(\frac{\partial}{\partial t} + \boldsymbol{u}\cdot\nabla\right)\boldsymbol{u} = -\nabla p - \nabla\cdot\boldsymbol{\tau}, \tag{4.5a}$$

$$\nabla\cdot\boldsymbol{u} = 0, \tag{4.5b}$$

where p is the dynamic pressure and $\boldsymbol{\tau}$ the deviatoric part of the stress tensor. A detailed derivation of the stress and strain tensors is provided in Appx. A. In the same Appendix we show also that the convective nonlinearity of the Navier–Stokes equation for this velocity field is identically zero. Using Oldroyd-B Eqs. (1.15) for

the stress tensor, we get

$$\rho\frac{\partial \boldsymbol{u}}{\partial t} = -\nabla p + \eta_s \nabla^2 \boldsymbol{u} - \nabla\cdot\left(-\eta_p \boldsymbol{\gamma}_{(1)} - \lambda \boldsymbol{\tau}_{p(1)}\right). \tag{4.6}$$

For u_z (which is the only non-zero component of the velocity field) this equation reads

$$\rho\frac{\partial u_z}{\partial t} = -\frac{\partial p}{\partial z} + \eta_s\frac{\partial^2 u_z}{\partial x^2} + \eta_p\frac{\partial^2 u_z}{\partial x^2} + \lambda\frac{\partial}{\partial t}\frac{\partial(\boldsymbol{\tau}_p)_{zx}}{\partial x}. \tag{4.7}$$

The last term can be written again in terms of u_z using the Navier–Stokes equation. After some algebra we end up with an equation for $u_z(x,t)$ which couples spatial and temporal derivatives:

$$\rho\left(1+\lambda\frac{\partial}{\partial t}\right)\frac{\partial u_z}{\partial t} - \eta\left(1+\lambda_2\frac{\partial}{\partial t}\right)\frac{\partial^2 u_z}{\partial x^2} = -\left(1+\lambda\frac{\partial}{\partial t}\right)\frac{\partial p}{\partial z}, \tag{4.8}$$

where the relationship $\lambda\eta_s = \lambda_2\eta$ has been used. Since fluid motion is driven solely by the oscillation of the wall at $x = 0$, we set $\partial p/\partial z = 0$ and seek a solution of the form of Eq. (4.2). Recall that this solution satisfies the no-slip boundary condition at the wall and the condition of zero velocity far away from the wall. The transverse wave that satisfies the equation of motion (4.8) has damping length x_0 and wavelength λ_0 given by:

$$x_0 = \sqrt{\frac{2\eta\lambda}{\rho De}}\sqrt{\frac{1+De^2X^2}{De\,(X-1)+\sqrt{\left[1+De^2\right]\left[1+De^2X^2\right]}}}, \tag{4.9a}$$

$$\frac{\lambda_0}{2\pi} = \sqrt{\frac{2\eta\lambda}{\rho De}}\sqrt{\frac{1+De^2X^2}{De\,(1-X)+\sqrt{\left[1+De^2\right]\left[1+De^2X^2\right]}}}, \tag{4.9b}$$

in terms of the Deborah number $De = \omega_0\lambda$ and the viscosity ratio $X = \eta_s/\eta = \lambda_2/\lambda$. To our knowledge these two expressions have not been obtained in the literature before. For $X = 0$ they reproduce the results of Mitran et al. (2008) for an UCM fluid. The relation between these two length scales reads:

$$x_0 = \frac{\lambda_0}{2\pi}\frac{De(1-X)+\sqrt{\left[1+De^2\right]\left[1+De^2X^2\right]}}{1+De^2X}. \tag{4.10}$$

It reduces to Ferry's result for a Maxwell fluid (Eq. (4.4)) for $X = 0$, and to the Newtonian result $x_0 = \lambda_0/(2\pi)$ for $X = 1$. Figure 4.1(a) shows a plot of the damping length x_0 in units of the thickness of the viscous boundary layer $\delta = \sqrt{2\eta\lambda/(\rho De)}$, as a function of De and for different values of X. For $X = 0$ the ratio x_0/δ grows monotonously with De, showing that the extension of the

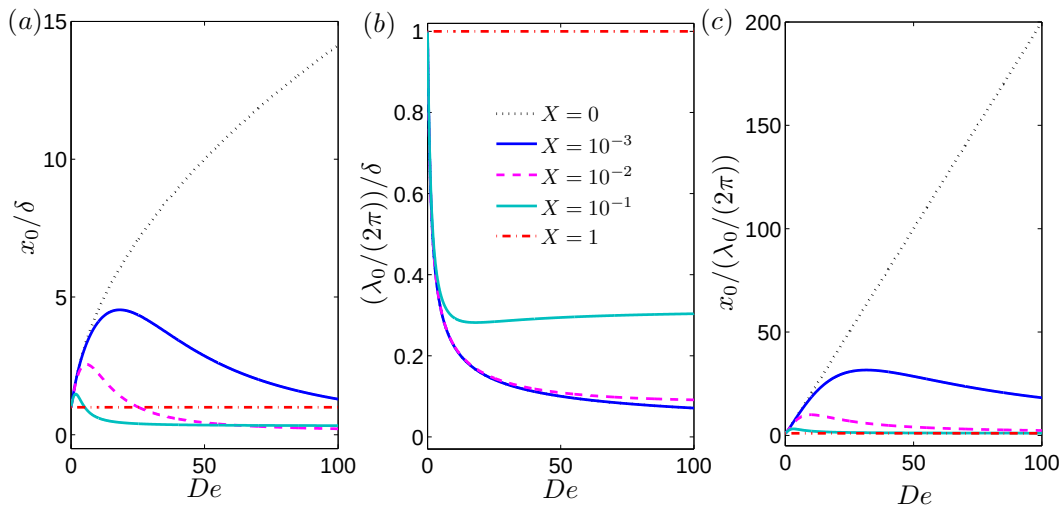

Figure 4.1: Damping length (a) and wavelength (b), in units of the thickness of the viscous boundary layer, as functions of De, for different values of the viscosity ratio X. The last panel (c) shows the ratio of these two length scales.

shear waves is much larger than the purely viscous boundary layer for $De > 0$. It is worth mentioning that in this particular case, and for $De > 1$, the damping length rapidly tends to the finite value $2\sqrt{\eta\lambda/\rho}$. As the Newtonian contribution of the solvent is included, $X > 0$, we see that the ratio x_0/δ goes through a maximum as a function of De and decays to zero, so that we can distinguish a range of De where the extension of the viscoelastic shear waves exceeds δ and another one at larger De where it disappears in practice. Finally, in the Newtonian case we recover $x_0/\delta = 1$.

The second relevant length scale is the wavelength of the shear waves generated at the wall, λ_0. Figure 4.1(b) shows an equivalent plot for $\lambda_0/(2\pi)$ in units of the thickness of the viscous boundary layer, δ. It is remarkable that the wavelength of the viscoelastic shear waves ($X < 1$) falls very quickly below the Newtonian value δ for $De > 0$, and recovers only this value for the Newtonian case $X = 1$.

Finally, Fig. 4.1(c) shows the ratio $x_0/(\lambda_0/(2\pi))$. It is important to note that this ratio is larger than one for all $X < 1$, revealing that viscoelastic shear waves are always underdamped. In particular for UCM we have $x_0 \sim 2De[\lambda_0/(2\pi)]$ as $De > 1$. The ratio of the two length scales decreases monotonously to the Newtonian result $x_0 = \lambda_0/(2\pi)$ for all De as X approaches 1.

Two synchronous parallel oscillatory plates

We extend Stokes' second problem by adding a second infinite plate, parallel to the previous one, at a distance $2a$ in the x direction. The fluid occupies now the domain $(x, y, z) \in [-a, a] \times (-\infty, \infty) \times (-\infty, \infty)$. The second plate oscillates along the z coordinate synchronously with the first one with the same amplitude (z_0) and frequency (ω_0). The introduction of a setup length allows us to define a viscous time scale, $t_v = a^2\rho/\eta$. A third dimensionless parameter can be introduced now as the ratio of the viscous time to the viscoelastic relaxation time, t_v/λ. The oscillatory flow behaviour can be completely characterized then in terms of the three dimensionless variables introduced so far: De, X and t_v/λ.

At this point it is useful to define also a viscoelastic Stokes parameter as $\Lambda_{ve} = a/x_0$. It is related to the (Newtonian) Stokes parameter Λ by $\Lambda/\Lambda_{ve} = x_0/\delta$. In analogy to Λ, the parameter Λ_{ve} is the ratio of the transverse size of the system to the extension of the shear waves generated by the moving walls. 'Narrow' systems correspond to $\Lambda_{ve} < 1$, when viscoelastic shear waves extend through the whole system, and 'wide' systems to $\Lambda_{ve} > 1$, when an inviscid core is present at the center. The ratio x_0/δ shown in Fig. 4.1(a) represents also Λ/Λ_{ve} and therefore can be interpreted as the deviation of the viscoelastic Stokes parameter from the Newtonian one for an Oldroyd-B fluid.

The solution for the fluid velocity results from the composition of the oscillatory boundary layers generated at the two plates (Mitran et al., 2008):

$$\boldsymbol{u}(x, y, z, t) = \left(0, 0, z_0\omega_0 \mathrm{Re}\left\{\frac{\cosh(\kappa x)}{\cosh(\kappa a)}\, \mathrm{e}^{\mathrm{i}w_0 t}\right\}\right), \tag{4.11}$$

where

$$\kappa = \frac{1}{x_0} + \mathrm{i}\frac{2\pi}{\lambda_0}, \tag{4.12}$$

and the length scales x_0 and $\lambda_0/(2\pi)$ are given by Eqs. (4.9). The vertical velocity can be rewritten in terms of a dimensionless velocity amplitude $\tilde{u}(x)$ and the phase lag $\phi(x)$ between the velocity of the fluid and the pressure gradient (which is given by $-\rho z_0\omega_0^2 \sin(\omega_0 t)$):

$$u_z(x, t) = -z_0\omega_0\tilde{u}(x) \sin\left(\omega_0 t - \phi(x)\right). \tag{4.13}$$

Notice that $\tilde{u}(x)$ and $\phi(x)$ are independent of time. For small plate separation ($\Lambda_{ve} < 1$) the boundary layers formed at both plates superpose themselves and originate an interference pattern inside the fluid domain. This leads to a resonant behavior with a huge increase of the velocity amplitude at particular frequencies,

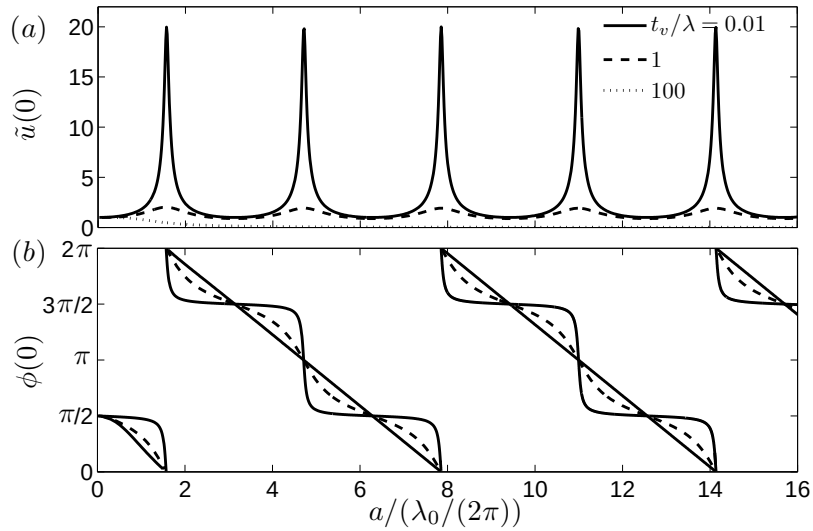

Figure 4.2: Velocity amplitude (a) and phase lag (b) at the midpoint between the walls vs. $a/(\lambda_0/(2\pi))$, for three different t_v/λ values and for $X = 0$.

when the interference condition

$$\frac{4a}{\lambda_0} = (1 + 2n), \qquad n = 0,\ 1,\ 2, \ldots \tag{4.14}$$

is satisfied. In Fig. 4.2 we show the velocity amplitude at the center of the domain, $\tilde{u}(0)$, as a function of the ratio of the distance a to the shear wavelength $\lambda_0/(2\pi)$. We focus the analysis here on a fluid described by the UCM model ($X = 0$). When the interference condition is satisfied, the velocity at the center becomes resonant. The periodicity of the interference condition (4.14) leads to equidistant peaks on the horizontal axis, placed at $a/(\lambda_0/(2\pi)) = \pi/2, 3\pi/2, \ldots$. It is worth noting that the choice of $a/(\lambda_0/(2\pi))$ for the horizontal axis makes the position of the resonant peaks universal (independent of fluid parameters and setup dimensions). Naturally, for constant t_v/λ (constant fluid parameters and setup dimensions) this axis is a monotonically increasing function of De, i.e. of the dimensionless driving frequency.

Figure 4.2(a) shows $\tilde{u}(0)$ for three different values of t_v/λ. Notice that the viscoelastic Stokes parameter can be rewritten in terms of the ratio of the viscous time to the relaxation time, t_v/λ, as $\Lambda_{ve} = \sqrt{t_v/\lambda}\, f(De, X = 0)$, where $f(De, X)$ is a function of De and X only. Thus, for given De and X, increasing t_v/λ by a factor of 100 as in the figure is equivalent to increase Λ_{ve} by a factor of 10. For $t_v/\lambda \ll 1$ the resonant behavior is manifest. At $t_v/\lambda = 1$ the velocity magnitude at the center has already strongly decreased. And for $t_v/\lambda \gg 1$ the resonances completely disappear and the velocity amplitude tends rapidly to zero for $De > 1$.

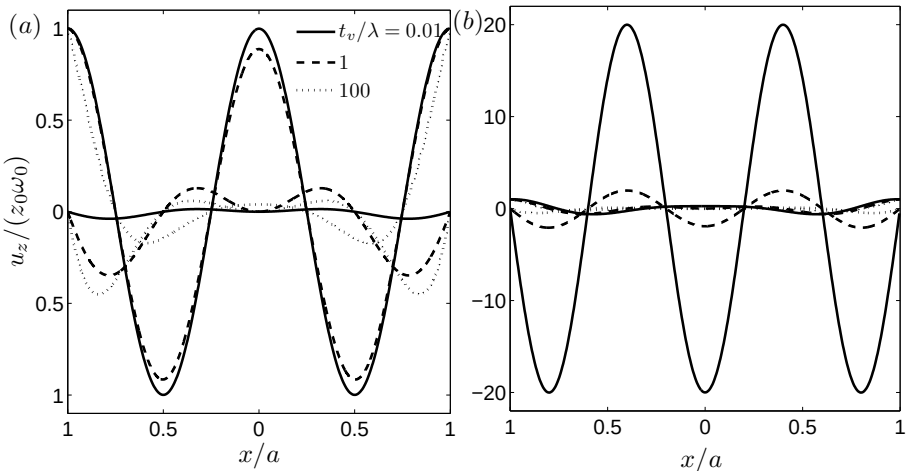

Figure 4.3: Vertical velocity profiles vs. dimensionless transverse coordinate x/a at two time phases $\omega_0 t = 0$ (the velocity at the walls is $z_0\omega_0$), and $\omega_0 t = \pi/2$ (the velocity at the walls is 0), for three different t_v/λ values. The velocity is measured in units of $z_0\omega_0$, and $X = 0$ (UCM). In (a) $a/(\lambda_0/(2\pi)) = 2\pi$ and in (b) $a/(\lambda_0/(2\pi)) = 5\pi/2$.

For a fixed De and fluid rheology the progressive disappearance of the resonances is associated with the transition from a 'narrow' system ($\Lambda_{ve} < 1$) to a 'wide' system ($\Lambda_{ve} > 1$).

An alternative strategy to determine the location of the resonant peaks is to compute $\phi(0)$, the phase lag between the velocity at the symmetry axis and the pressure gradient, as a function of $a/(\lambda_0/(2\pi))$ (Fig. 4.2(b)). As a result of constructive interferences, at resonances the fluid in the center moves in phase (or in phase opposition) with the driving pressure gradient, giving rise to the described magnification of the velocity amplitude. Out of the resonances the phase lag approaches abruptly either $\pi/2$ or $3\pi/2$ and the fluid at the center moves out of phase with respect to the driving pressure gradient. Destructive interferences result in very low values of the velocity magnitude. For $t_v/\lambda \geq 1$, even though $\phi = 0$ or π at the resonant peaks again, the phase lag varies smoothly through the whole phase range.

Our study of the oscillatory flow between two parallel plates ends by analyzing the velocity profile in the fluid domain. We show in Fig. 4.3 the curves of $u_z(x,t)$ in units of the amplitude of the plate velocity $z_0\omega_0$. In panel (a) we show the velocity profile corresponding to $a/(\lambda_0/(2\pi)) = 2\pi$, which is a minimum of the velocity amplitude in Fig. 4.2(a). It is clear that for $t_v/\lambda \ll 1$ ('narrow' system) the oscillating profile is maintained from plate to plate, as a result of the large damping wavelength. In this situation the fluid flow organizes in several parallel layers, with alternating upward/downward motion, that oscillate with the periodicity of the moving walls. As t_v/λ increases (wide 'systems') the shear waves cannot

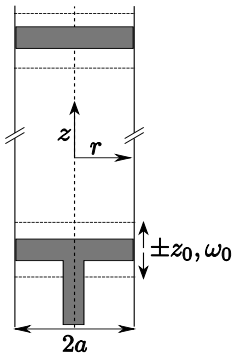

Figure 4.4: Sketch of the problem setup. Shown are the top and bottom lids that oscillate synchronously with amplitude z_0 and angular frequency ω_0, and the vertical and radial coordinates.

propagate through the entire geometry and the velocity magnitude flattens at the center. Finally, for $t_v/\lambda \gg 1$ the velocity at the center is zero. A similar behavior is shown in Fig. 4.3(b) for a resonance peak at $a/(\lambda_0/(2\pi)) = 5\pi/2$. Note however the different scale in the vertical axis, as a result of the constructive interference of the shear waves.

4.1.2 Zero-mean oscillatory flow in an infinite cylinder

Motivated by the simplicity of its mathematical treatment, we have studied in the previous section the oscillatory flow in a rectangular geometry. However, most wall-bounded oscillatory flows of physiological interest and industrial applications involving fluid pumping or oil recovery take place in cylindrical tubes. Typically a cylindrical geometry is more accessible experimentally than a parallel-plate geometry. The idealized boundary conditions can be satisfied in tubes of large aspect ratio. Gerrard and Hughes (1971) have shown that for a Newtonian fluid the recirculation induced by the presence of the top and bottom endwalls has no influence on the flow in the middle of the tube for aspect ratios above 20.

We consider a fluid contained in an infinitely long cylinder of radius a. The flow is induced by a pressure gradient in the axial direction that varies harmonically in time. In practice, as shown in Fig. 4.4, the pressure gradient is usually produced by the oscillatory motion of the top and bottom lids according to $z(t) = z_0 \sin(\omega_0 t)$. The velocity field $\boldsymbol{u}$ is now given in cylindrical coordinates $(r, \theta, z) \in [0, a] \times [0, 2\pi] \times (-\infty, \infty)$. The flow is governed by the Navier–Stokes equations and the condition of incompressibility, and no-slip velocity boundary conditions are imposed on all walls. The velocity is zero on the cylindrical wall and the z-component at the two endwalls oscillates in time as $z_0\omega_0 \cos(\omega_0 t)$. At sufficiently

low Re the flow is laminar. Because of the spatial symmetries of the equations of motion and of the boundary conditions this basic flow is axisymmetric, follows the direction of the cylinder axis z and is translationally invariant along this direction. The velocity field reduces then to $\boldsymbol{u} = (0, 0, u_z(r, t))$.

Our purpose is to obtain the base flow $u_z(r, t)$ for an Oldroyd-B fluid. We follow the same procedure that led to Eq. (4.8) for Stokes' second problem, now in cylindrical coordinates, and we get

$$\rho\left(1+\lambda\frac{\partial}{\partial t}\right)\frac{\partial u_z}{\partial t} - \eta\left(1+\lambda_2\frac{\partial}{\partial t}\right)\left(\frac{1}{r}\frac{\partial u_z}{\partial r}+\frac{\partial^2 u_z}{\partial r^2}\right) = -\left(1+\lambda\frac{\partial}{\partial t}\right)\frac{\partial p}{\partial z}. \quad (4.15)$$

The steady-state response of u_z to a harmonically varying $\partial p/\partial z$ can be obtained by a Fourier transform method. In the frequency domain the equation for the mode of frequency ω_0 is a Bessel equation of the first kind, whose general solution is

$$U(\beta r) = C_1 J_0(\beta r) + C_2 Y_0(\beta r) + U^p. \quad (4.16)$$

J_0 and Y_0 are zero-order Bessel functions of the first and second kind respectively, and U^p is a particular solution. This general solution is well known. The novelty of our approach is to identify the reciprocal length β with

$$\beta = \frac{2\pi}{\lambda_0} + \mathrm{i}\frac{1}{x_0}, \quad (4.17)$$

where λ_0 and x_0 are precisely the wavelength and damping length of the 'Ferry' waves for an Oldroyd-B fluid, given by Eqs. (4.9).

The oscillatory flow induced in a cylinder at rest by the motion of the endwalls is equivalent to the flow that would result from oscillating the cylinder sidewall with the endwalls at rest, observed in the reference frame of the sidewall. As discussed by Panadès et al. (2011) the oscillating reference frame is not an inertial frame of reference. For an incompressible flow in which the density ρ is a constant the inertial body force term that must be included in the Navier–Stokes equations is a gradient that can be incorporated in the pressure term, thereby recovering exactly the same formulation as in the case of a fixed sidewall.

Since the motion of the cylinder sidewall induces radially propagating 'Ferry' shear waves, the parameter β, that sets the length scale in the argument of the two Bessel functions, can be expressed directly in terms of x_0 and λ_0. The condition that the velocity remains finite imposes $C_2 = 0$. For the flow to be translationally invariant along z the pressure gradient must be homogeneous along the tube (independent of z) and, because the acceleration of the endwalls is $-z_0{\omega_0}^2 \sin(\omega_0 t)$,

the pressure gradient must take the form

$$\frac{\partial p}{\partial z} = -\rho {\omega_0}^2 \mathrm{Im}\left\{\Delta \mathrm{e}^{\mathrm{i}\omega_0 t}\right\}, \tag{4.18}$$

where ρ is the density of the fluid and Δ is a coefficient proportional to z_0 that must be determined by continuity at either of the two endwalls. The pressure gradient can be expressed also in terms of amplitude and phase as:

$$\frac{\partial p}{\partial z} = -\rho z_0 {\omega_0}^2 \tilde{p} \sin\left(\omega_0 t - \varphi\right), \tag{4.19}$$

where φ is the phase lag between pressure gradient and piston acceleration. Taking these conditions into account we end up with the following expression for the z component of the fluid velocity in the tube:

$$u_z(r,t) = \omega_0 \mathrm{Re}\left\{\Delta\left[1 - \frac{J_0(\beta r)}{J_0(\beta a)}\right]\mathrm{e}^{\mathrm{i}\omega_0 t}\right\}. \tag{4.20}$$

In order to determine the factor Δ we impose continuity, by assuming that the volume scanned by the piston in one quarter of the oscillation coincides with the volume of liquid displaced in this same time interval, computed by integration of Eq. (4.20) in space and time (Eckmann and Grotberg, 1991). This leads to the following expression for Δ:

$$\Delta = -z_0 \frac{J_0(\beta a)}{J_2(\beta a)}, \tag{4.21}$$

where J_0 and J_2 are zero and second-order Bessel functions of the first kind respectively. The final expression for the velocity reads:

$$u_z(r,t) = -z_0 \omega_0 \mathrm{Re}\left\{\frac{J_0(\beta a)}{J_2(\beta a)}\left[1 - \frac{J_0(\beta r)}{J_0(\beta a)}\right]\mathrm{e}^{\mathrm{i}\omega_0 t}\right\}, \tag{4.22}$$

which constitutes a main original result of our analysis. It is worth noting that the same result has been obtained by Blennerhassett and Bassom (2006) for a Newtonian fluid. This expression can also be rewritten in terms of amplitude and phase as:

$$u_z(r,t) = -z_0 \omega_0 \tilde{u}(r) \sin\left(\omega_0 t - \varphi - \phi(r)\right) \tag{4.23}$$

where $\phi(r)$ is the phase lag between the velocity and the pressure gradient.

Our expression (4.22) for the fluid velocity recovers the behavior of a Maxwell fluid when the limit $X = 0$ for the damping length and wavelength is taken in Eqs. (4.9). The fact that this expression for $u_z(r,t)$ does not coincide exactly with similar results obtained for a Maxwell fluid by del Río et al. (1998), Andrienko et al. (2000), and Tsiklauri and Beresnev (2001a) is due to the fact that

these authors did not impose the condition of continuity (Eq. (4.21)). Their result applies to a pressure-gradient-controlled oscillatory flow, while ours applies to a volume-controlled oscillatory flow. When we discuss the resonant behaviour of this system we will see that these two different control modes lead to qualitatively and quantitatively different results for $u_z(r,t)$. This difference is important when trying to compare theoretical predictions to experimental results, which are usually performed under volume-controlled conditions.

The velocity profile for a Newtonian fluid is also given by Eq. (4.22), but now x_0 and $\lambda_0/(2\pi)$ of Eq. (4.17) are equal to $\sqrt{2\eta/(\rho\omega_0)}$, so that $\beta^2 = \mathrm{i}\omega_0\rho/\eta$ and Eq. (4.22) reduces to the result of Blennerhassett and Bassom (2006).

4.1.3 Flow behavior

This section is devoted to analyze the flow behavior and the properties of the vertical velocity profiles described by Eq. (4.22) with the value β given by Eq. (4.17). To carry out the analysis in increasing order of complexity we start by revising the Newtonian behavior, examine next the case of a fluid described by the UCM model, and discuss finally the results for the Oldroyd-B model.

Newtonian fluid

The laminar oscillatory flow of a Newtonian fluid contained in a straight cylinder is well documented after the work of Lambossy (1952), Müller (1954) and Womersley (1955), reviewed in Chap. 1. The velocity profile in the radial direction, given by Eq. (4.22), is governed solely by the Stokes parameter, $\Lambda = a/\delta$, with $\delta = \sqrt{2\eta/(\rho\omega_0)}$. Figure 4.5 shows the dimensionless vertical velocity profiles $u_z(r,t)/(z_0\omega_0)$ as functions of the dimensionless radial coordinate r/a, for two time phases $\omega_0 t = 0, \pi/2$ and three different values of Λ. For $\Lambda < 1$ ('narrow' systems) the instantaneous velocity profile recovers the parabolic Poiseuille form that would correspond to a steady pressure gradient. This limit can be obtained for vanishing βa (long driving period in comparison to the viscous time $a^2\rho/\eta$) in Eq. (4.22), and the expression of the velocity profile reads

$$u_z(r,t) = 2z_0\omega_0\left(1 - r^2/a^2\right)\cos\left(\omega_0 t\right). \tag{4.24}$$

For larger Λ the velocity profile departs from the Poiseuille-like form. The velocity magnitude at the tube axis decreases, and the possibility of a reversal of the flow becomes more apparent. For $\Lambda > 1$ ('wide' systems) the boundary layer localizes near the tube walls and a central inviscid core dominates the flow.

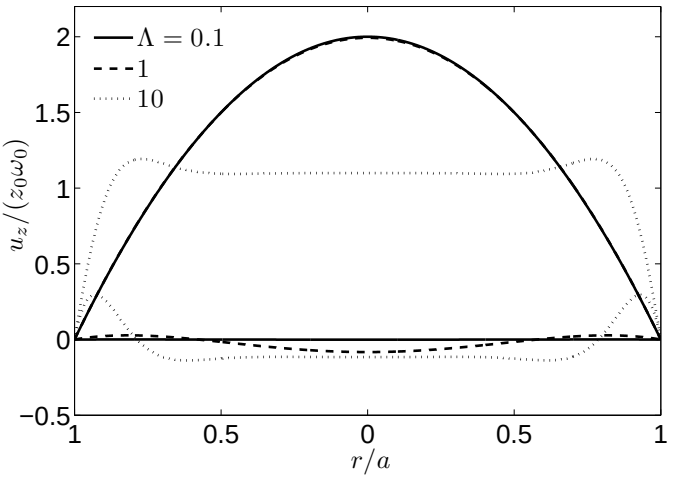

Figure 4.5: Dimensionless vertical velocity profiles along the radial coordinate r/a, at two time phases $\omega_0 t = 0$ (profiles of large amplitude) and $\omega_0 t = \pi/2$ (profiles of small amplitude) and for three different values of Λ. The fluid considered is Newtonian ($X = 1$).

Upper-Convected Maxwell fluid

We consider now a viscoelastic fluid described by the UCM constitutive equation. The flow behavior is governed by the dimensionless parameters t_v/λ and De.

Magnitude and phase lag of the velocity at the tube axis

From Eq. (4.22), the velocity at the tube axis is given by:

$$u_z(0,t) = -z_0\omega_0 \mathrm{Re}\left\{\left[\frac{J_0(\beta a)-1}{J_2(\beta a)}\right] \mathrm{e}^{\mathrm{i}\omega_0 t}\right\}. \tag{4.25}$$

This equation predicts a resonant behavior, comparable to the one that we obtained in Sec. 4.1.1 for the rectangular geometry. However, the cylindrical symmetry of the equations brings about interesting features in the resonant pattern. Figure 4.6 shows the influence of the setup dimensions on the formation of resonances inside the tube. It is clear that the resonant behavior only occurs for $t_v/\lambda \leq 1$. The position of the resonant peaks is, again, universal in the axis $a/(\lambda_0/(2\pi))$. For $De > 1$ (and $X = 0$) this axis can be rewritten as $De\sqrt{t_v/\lambda}$, which coincides with the empirical choice made by del Río et al. (1998, 2001). In Fig. 4.6, therefore, increasing values of a/λ_0 for a given t_v/λ correspond to increasing De. In the cylindrical geometry the resonant peaks are no longer equidistant along the horizontal axis, but appear at the positions where the modulus of $J_2(\beta a)$

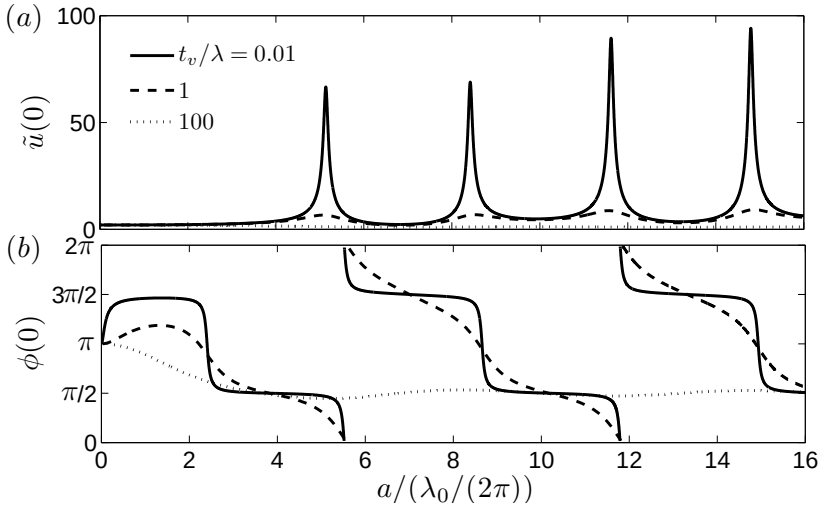

Figure 4.6: (a): Magnitude of the vertical velocity at the cylinder axis in units of $z_0\omega_0$, vs. the non-dimensional ratio $a/(\lambda_0/(2\pi))$, for an UCM fluid ($X = 0$). (b): Phase lag between the fluid velocity at the tube axis and the oscillating pressure gradient. Both panels show the curves for three different values of t_v/λ.

is minimum, as follows from Eq. (4.25). And, also differently from the rectangular geometry, the velocity magnitude of the resonant peaks (measured in units of the piston velocity) is larger for increasing De. Remarkably, the inclusion of the continuity condition (4.21) suppresses a first resonant peak at $a/(\lambda_0/(2\pi)) \simeq 2.5$ reported by del Río et al. (1998, 2001), and makes the first resonance to appear at higher De. As predicted for the rectangular geometry, the resonant behavior becomes much weaker for $t_v/\lambda \geq 1$, and disappears for 'wide' tubes ($t_v/\lambda \gg 1$).

The phase lag $\phi(0)$ between the velocity at the tube axis and the pressure gradient is shown in Fig. 4.6(b). In contrast with the rectangular case, $\phi(0) = \pi$ at $De = 0$ because of the continuity condition. In 'narrow' tubes the phase lag abruptly changes from $\phi = 0, \pi$ (the velocity is in phase with the driving pressure gradient) near the resonant peaks, to $\phi = \pi/2, 3\pi/2$ far from the resonances. This abrupt change of phase is slightly shifted from the resonance peak for the first resonance, due to the non-zero phase lag φ between the pressure gradient and the piston acceleration imposed by the continuity condition. This shift however gradually disappears at larger De. On the other hand, as the viscous time dominates over the viscoelastic relaxation time the resonances fade out and the phase lag smoothly varies between 0 and 2π for the whole range of De. For $t_v/\lambda \gg 1$ the interferences have disappeared completely and the velocity at the center of the tube moves nearly in quadrature with the oscillatory pressure gradient for all De.

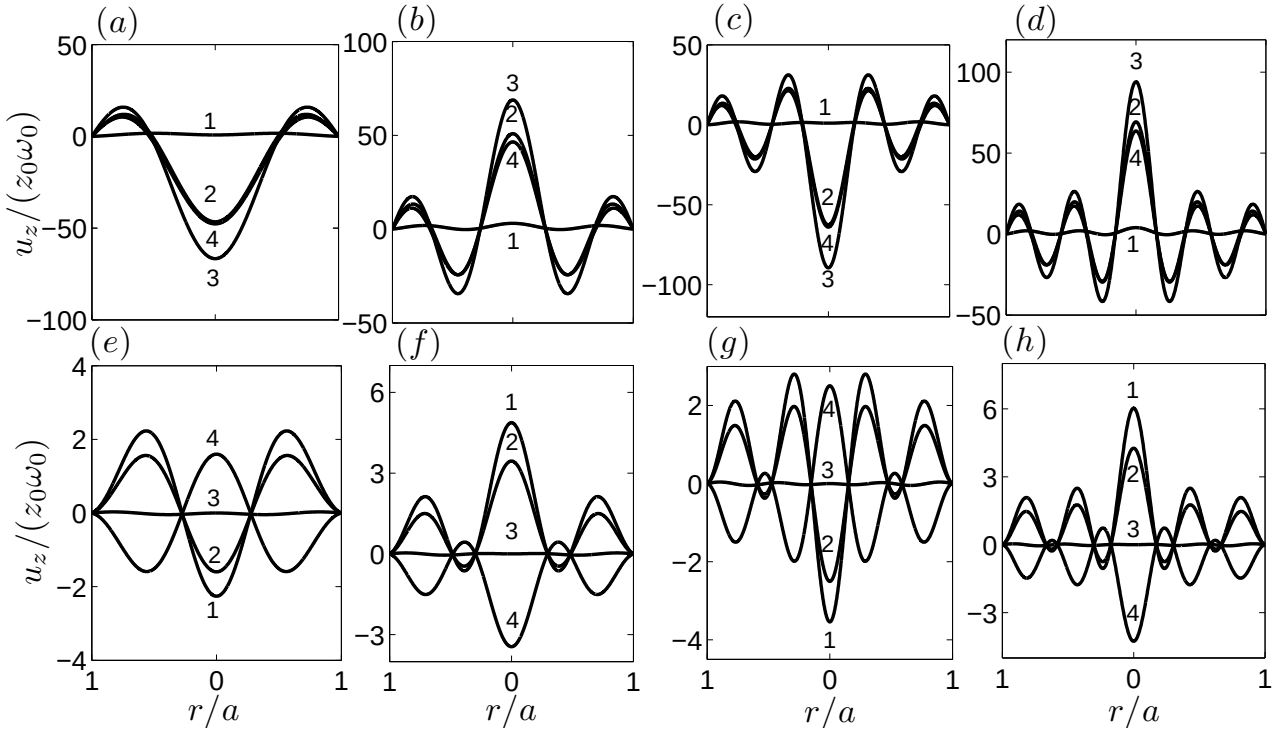

Figure 4.7: Dimensionless velocity profiles for $a/(\lambda_0/(2\pi)) = 5.13$ (a), 8.42 (b), 11.62 (c), and 14.79 (d); and $a/(\lambda_0/(2\pi)) = 6.80$ (e), 9.91 (f), 13.20 (g), and 16.31 (h). The four profiles shown in each panel correspond to the time phases $\omega_0 t = 0, \pi/4, \pi/2, 3\pi/4$, numbered as 1, 2, 3, 4. The plot is for an UCM fluid ($X = 0$) and a 'narrow' tube ($t_v/\lambda = 0.01$).

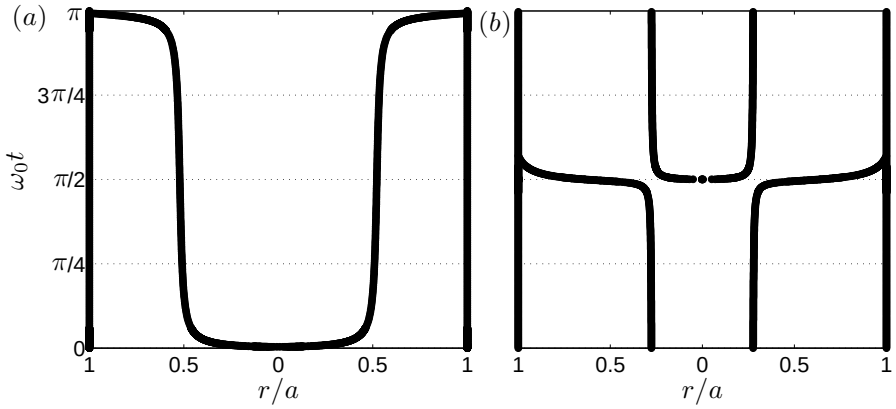

Figure 4.8: Radial position of quiescent points at time phases $\omega_0 t$ that span half an oscillation period. Panel (a) corresponds to $a/(\lambda_0/(2\pi)) = 5.13$ and panel (b) to $a/(\lambda_0/(2\pi)) = 6.80$. The plot is for an UCM fluid ($X = 0$) and a 'narrow' tube ($t_v/\lambda = 0.01$).

Velocity profiles under resonant conditions

We focus now on flow conditions such that $t_v/\lambda < 1$, so that the mutual interaction of the underdamped shear waves results in a rich flow behavior. In the cylindrical geometry the fluid flow organizes forming concentric cylindrical layers of alternating upward/downward motion that oscillate with the periodicity of the piston. Figure 4.7 shows the instantaneous velocity profiles corresponding to the first four maxima (*top*) and minima (*bottom*) of the resonance curve of Fig. 4.6 for $t_v/\lambda = 0.01$. Since the same velocity profile (with reversed sign) is recovered every half-driving period, we show only time phases $\omega_0 t$ in the interval $[0, \pi)$. At the resonances (panels a–d) the velocity is in phase with the sinusoidal piston acceleration. For this reason the velocity is minimum at $\omega_0 t = 0$ and maximum at $\omega_0 t = \pi/2$. Conversely, out of the resonances (panels e–h) the velocity is nearly in quadrature with the piston acceleration, and the behaviour is reversed. At the minima of the resonance curve, in particular, the velocity is minimum at $\omega_0 t = \pi/2$ and maximum at $\omega_0 t = 0$. It is also apparent from Fig. 4.7 that for large De (large a/λ_0 for given fluid parameters and tube radius) the flow becomes more inflectional, i.e. an increasing number of cylindrical layers inside the tube move with opposite velocity. Adjacent layers are separated by *quiescent surfaces* of zero velocity (*quiescent points* in the two-dimensional representation of the velocity profile). It is worth noting however that these surfaces are not steady in time. Figure 4.8 shows the radial position of the axisymmetric pair of quiescent points that appear inside the tube at all time phases within half a driving period. The quiescent points remain at fixed positions for almost the whole oscillation. However, in the short period of time when the velocity magnitude is very small

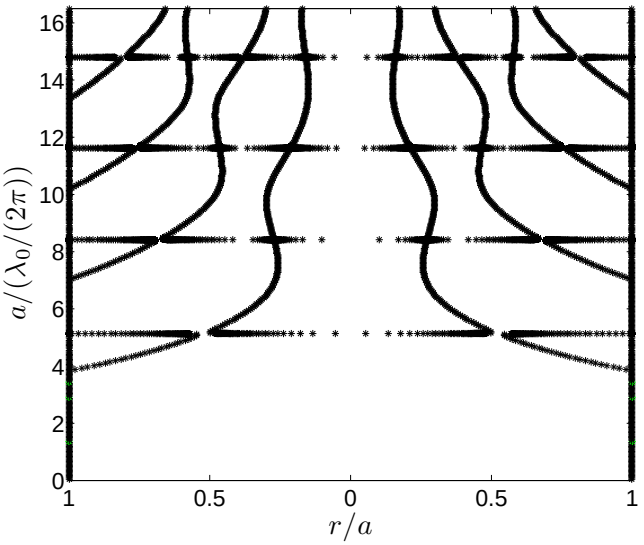

Figure 4.9: Radial position of quiescent points at $\omega_0 t = 0$ for increasing $a/(\lambda_0/(2\pi))$. The plot is for an UCM fluid ($X = 0$) and a 'narrow' tube ($t_v/\lambda = 0.01$).

everywhere across the tube these points rapidly move towards the tube walls. At the resonances (panel a) this time phase is $\omega_0 t = 0$, while out of the resonances (panel b) it is $\omega_0 t = \pi/2$. Plotting the radial position of the quiescent points at $\omega_0 t = 0$ for increasing a/λ_0 (increasing De) (Fig. 4.9) we see that the quiescent points delocalize exactly at resonances. This plot therefore provides an alternative way to determine the resonances of the system. The fact that for increasing De the flow behavior becomes more and more inflectional is also apparent from this figure. At low De the flow is quiescent only at the tube walls. As De increases a pair of axisymmetric quiescent points appears close to the tube walls, and progressively detaches from the walls and approaches the tube axis, until a new pair of quiescent points appears on the walls. This process is repeated once and again for increasing De, leading to a flow highly organized in multiple regions of alternate upward/downward motion. This increasingly inflectional flow structure, and the fact that the velocity magnitude is proportional to the frequency of oscillation ω_0, make that the local rate of shear deformation inside the tube increases very rapidly with De.

Oldroyd-B fluid

We analyze here the oscillatory flow of an Oldroyd-B fluid Eq. (4.22) in terms of the viscosity ratio $X = \eta_s/\eta$, always for 'narrow' systems $t_v/\lambda < 1$. This investigation is related to the work of Andrienko et al. (2000), who considered

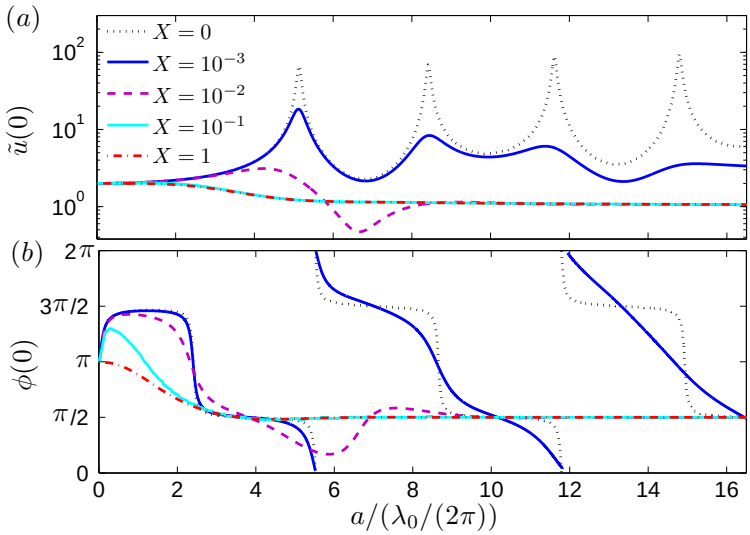

Figure 4.10: Dimensionless velocity magnitude at the tube axis (a) and phase lag between the fluid velocity at the tube axis and the pressure gradient (b) vs. the dimensionless ratio $a/(\lambda_0/(2\pi))$, for an Oldroyd-B fluid ($t_v/\lambda = 0.01$). Different lines correspond to different values of the viscosity ratio X.

a fluid model with a discrete spectrum of relaxation times in a cylindrical tube under an oscillatory pressure gradient.

The dramatic influence of X on the magnitude of the velocity at the center of the tube is shown in Fig. 4.10(a). For the limiting case $X = 0$ we recover the resonant behavior of the UCM model described in the previous section. As a Newtonian contribution is added to the model ($X > 0$) it is evident from the figure that resonances progressively disappear. This happens already for extremely small viscosity ratios, showing that only very special fluids (like wormlike micellar solutions) are expected to exhibit velocity resonances. For experimentally relevant values of X ($0.1-0.9$) for Boger fluids (James, 2009), the result is indistinguishable from the Newtonian result. The reason must be found in the behaviour of the two characteristic lengths, $\lambda_0/(2\pi)$ and x_0. These two lengths quickly approach each other as X departs from zero (Fig. 4.1(a)), progressively changing underdamped shear oscillations into overdamped oscillations.

The tendency of x_0 and $\lambda_0/(2\pi)$ to take the same value, and hence the disappearance of resonances, is more pronounced at large values of De. These same features are found also in the rectangular geometry discussed in Sec. 4.1.1. Making $X \gtrsim 0$ has a similar effect on the phase lag at the center of the tube, $\phi(0)$, as shown in Fig. 4.10(b). The sharp transitions from $\phi = 0, \pi$ observed near resonances to $\phi = \pi/2, 3\pi/2$ only occur for $X = 0$. As $X \gtrsim 0$ the phase-lag curve quickly smooths and the fluid just oscillates in quadrature with the piston acceleration.

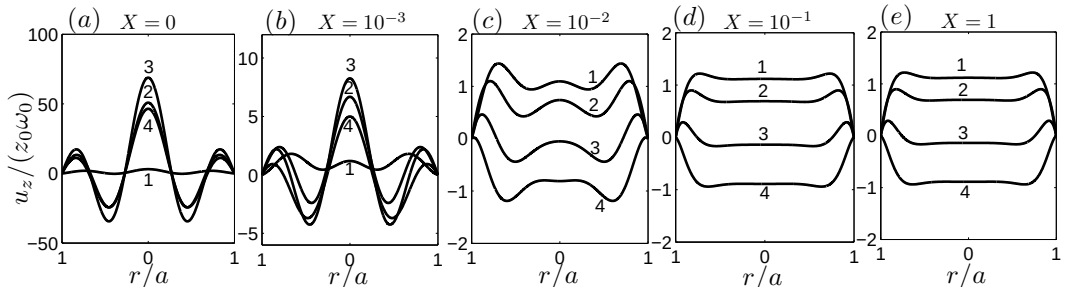

Figure 4.11: Dimensionless velocity profiles of Oldroyd-B fluids ($t_v/\lambda = 0.01$) of different viscosity ratios X, computed at the second resonance, $a/(\lambda_0/(2\pi)) = 8.42$. The profiles are shown at four different time phases ($\omega_0 t = 0, \pi/4, \pi/2, 3\pi/4$) spanning half an oscillation period.

This translates into a phase lag $\phi(0)$ that approaches $\pi/2$ at large De. Oldroyd-B fluids of different X also display a different flow structure. Figure 4.11(a–e) shows indeed that for $X \gtrsim 0$ the flow progressively becomes less inflectional (the number of concentric layers with upward/downward motion decreases) and the magnitude of the velocity is drastically reduced throughout the tube diameter. As a result of both the loss of flow structure and the decrease of the velocity magnitude, the rate of shear deformation also experiences a dramatic decrease for $X \gtrsim 0$. The local shear rate can be derived analytically from Eq. (4.22) as:

$$\dot{\gamma}(r,t) = \frac{\partial u_z(r,t)}{\partial r} = -z_0\omega_0 \mathrm{Re}\left\{\beta \frac{J_1(\beta r)}{J_2(\beta a)} \mathrm{e}^{\mathrm{i}\omega_0 t}\right\}. \tag{4.26}$$

Since $\boldsymbol{u} = (0, 0, u_z(r,t))$, in this problem the shear rate coincides with the magnitude of the vorticity in the azimuthal direction. Figure 4.12 shows the maximum value of the shear rate vs. $a/(\lambda_0/(2\pi))$ for different values of X. The vertical axis is drawn in logarithmic scale to emphasize the abrupt decrease of the shear rate with X.

The laminar periodic flows analyzed in this section constitute basic flows on which more complex situations can be studied. Most notably, features arising from nonlinearities in the constitutive equations accounting for the shear rate dependence of viscosity of viscoelastic fluids. A Floquet stability analysis of the flows studied here can also reveal the possibility of instabilities and bifurcations to more complex flows.

The next Sec. (4.2) is aimed at testing experimentally in a systematic way the theoretical predictions developed in this section. As described in Chap. 3, solutions of wormlike micelles behave according to the Maxwell model at low shear rates. Thus, they are good candidates for this purpose.

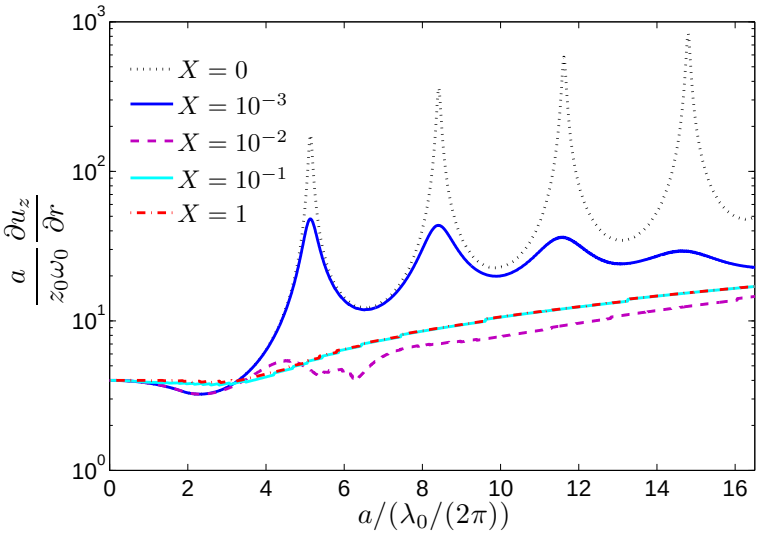

Figure 4.12: Maximum dimensionless shear rate as a function of $a/(\lambda_0/(2\pi))$ for Oldroyd-B fluids ($t_v/\lambda = 0.01$) of different viscosity ratios X.

4.2 Experiments

In this section we report a series of experiments of the oscillatory flow of a micellar solution (CPyCl/NaSal [100 : 60] mM) in a vertical rigid cylinder of large aspect ratio. The experiments were carried out in the *Laboratori de Física no Lineal* of the University of Barcelona, in the context of the present Thesis. A detailed description of the experimental setup and fluid rheology was provided in Chaps. 2, 3. The flow was driven by the harmonic motion of a piston at the bottom end of the cylinder. We focus here on a range of small amplitudes and low frequencies of the forcing ($Re \ll 1$, $Wi \lesssim 1$), for which translationally invariant, rectilinear fluid motion was established in the whole cylinder –except in the vicinity of the top and bottom lids. We make a quantitative comparison of the measured flow fields to the theoretical predictions obtained in Sec. 4.1, based on the Upper Convected Maxwell (UCM) and Oldroyd-B constitutive equations, and discuss the origin of the observed similarities and discrepancies.

This section is organized as follows. First in Sec. 4.2.1 we evaluate the effect of the finite length of the cylinder used in our experiments on the laminar oscillatory flow. In Sec. 4.2.2 we characterize the frequency response of the fluid for the whole range of accessible driving frequencies, decomposed in terms of velocity magnitude and phase lag. Next, in Sec. 4.2.3, the temporal dynamics of the velocity field within an oscillation period is studied, both for resonant and non-

resonant frequencies. Finally, in Sec. 4.2.4, the importance of nonlinearities of the fluid response in the experimental results is analyzed.

In the work presented in this section the setup geometry and the rheological properties of the CPyCl/NaSal solution ensure that the flow is always in the inertialess regime. The Reynolds number, defined as $Re = \rho U a/\eta_0$, where U is the maximum velocity in the flow, ranges from 5×10^{-3} to 0.1 for the largest characteristic velocities. The setup configuration is 'narrow', with $t_v/\lambda \simeq 5\times10^{-3}$. And elasticity is dominant since De goes from 12 to 143. Ideally X should be equal to zero for a wormlike micellar solution. However, values of $X \simeq 10^{-3} - 10^{-4}$ have also been reported in the literature (Yesilata et al., 2006). The solvent viscosity would partially account here for the residual viscosity of the solution at the largest shear rates, when all the micelles would have been completely disentangled and ruptured.

4.2.1 Finite length of the cylinder

The laminar oscillatory flow in an infinite cylinder should be translationally invariant along the vertical axis. However, the finite length of the actual tube used in the experiments causes fluid recirculation at the top and bottom ends. Our results show nevertheless that the distortion of the laminar flow is confined to a small region. We will show in Sec. 6.3 that it is smaller than 20 mm in length from both the top and bottom ends (about a 3% of the tube length). In Fig. 4.13 we show the measured laminar velocity profile at $\omega_0 = 44.0$ rad/s, at 5 different vertical positions, $17, 24, 33, 40$ and 48 cm from the piston, covering most of the tube length. A slight decrease of the peak velocity is observed only for the positions closer to the top and bottom ends. Remarkably, in all positions the no-slip condition is well satisfied at the tube walls. Note that in the figure the radial coordinate takes negative and positive values, to represent symbolically the right and left sides of the tube diameter (this same notation will be used in all remaining sections).

Since the flow in the laminar regime is translationally invariant in the vertical direction for most of the tube length, it is sufficient to characterize the velocity field in a particular region. The results for the laminar regime presented in this section are recorded in a fixed region of 5×5 cm^2, in the middle part of the tube (33 cm from the bottom piston). Radial velocity profiles are obtained by averaging typically 20 different profiles measured simultaneously, spanning a total of 35 mm in the vertical direction.

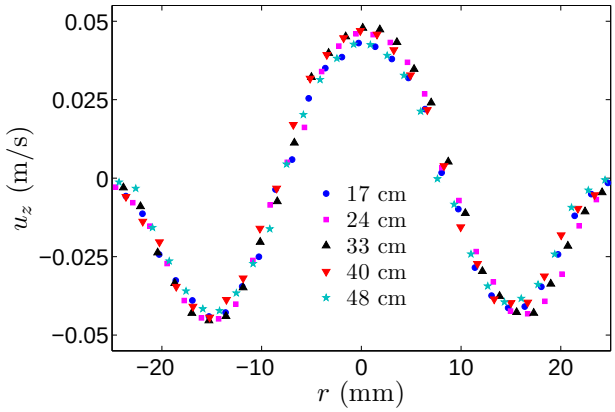

Figure 4.13: Velocity profiles measured at five different vertical positions. The amplitude of oscillation is $z_0 = 0.50$ mm, the frequency $\omega_0 = 44.0$ rad/s, and the time phase is $\omega_0 t = \pi$ in all profiles.

4.2.2 Frequency response

The experimental setup allows to decompose the fluid velocity of the laminar oscillatory flow, $u_z(r,t)$, in velocity magnitude, $u_z(r)$, and phase, $\Psi(r)$, as

$$u_z(r,t) = u_z(r)\sin\left(\omega_0 t - \Psi(r)\right). \tag{4.27}$$

$\Psi(r)$ is the phase lag of the fluid velocity with respect to the piston position. Notice that this phase lag is different from the phase lag between fluid velocity and pressure gradient ($\phi(r)$) and also different from the phase lag between pressure gradient and piston acceleration (φ), which arise more naturally in the theoretical analysis developed in Sec. 4.1. They are all related by

$$\Psi(r) = \phi(r) + \varphi + \pi. \tag{4.28}$$

Since both the magnitude and phase varies along the radial coordinate, we restrict our analysis to the tube axis ($r = 0$). We compute the phase lag $\Psi(0)$ between the fluid velocity and the piston position by comparing the temporal LVDT signal that tracks the piston position, $z_p(t)$, with the velocity of the fluid at the tube axis, $u_z(0,t)$.

Figure 4.14 shows, for example, the fluid velocity $u_z(0,t)$ and the piston position $z_p(t)$ for two driving frequencies, $\omega_0 = 37.1$ rad/s (a) and $\omega_0 = 47.1$ rad/s (b). The phase lag, represented by the arrow spanning the shaded area in the figure, is determined from the zero-crossings with positive slope of these two signals. Besides, the zero-crossing for z_p is used to reset the time phase $\omega_0 t$ to zero on each oscillation, so that the phase lag range is $0 \leq \Psi(0) < 2\pi$.

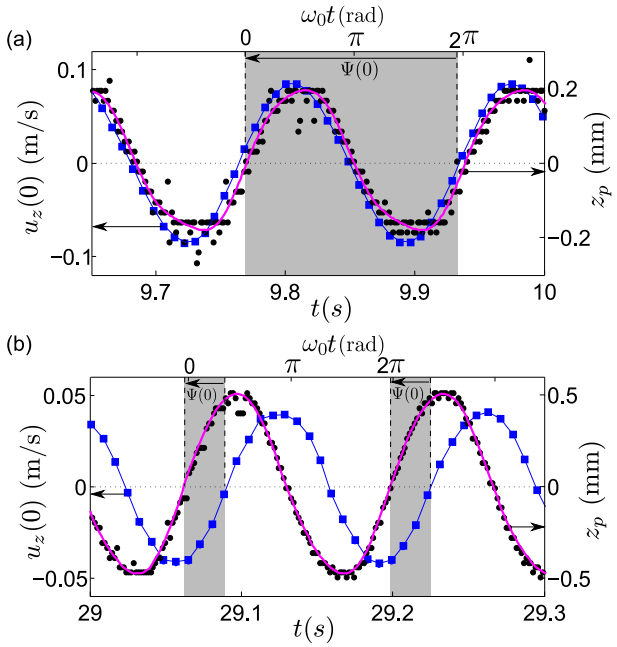

Figure 4.14: Measured velocity at the tube axis ($u_z(0,t)$, blue squares) for two complete periods of oscillation. The experimental error in the velocity is smaller than the symbol size. The LVDT signal ($z_p(t)$, black dots) that tracks the piston position is also shown as a reference, with the scale on the right. The solid line is the reconstruction of the LVDT signal based on its spectral contents. The time phase $\omega_0 t$ is shown in the top horizontal axis. The shaded areas represent the phase lag $\Psi(0)$ of $u_z(0)$ with respect to z_p. Panel (a) corresponds to $\omega_0 = 37.1$ rad/s, $z_0 = 0.20$ mm, and (b) to $\omega_0 = 47.1$ rad/s, $z_0 = 0.50$ mm.

Velocity magnitude

The magnitude of the velocity at the tube axis has been determined from the velocity fields measured by PIV. In Fig. 4.15(a) we show the magnitude of this velocity as a function of ω_0 for the whole range of accessible driving frequencies. The velocity has been made dimensionless by measuring it in units of $z_0\omega_0$ (the amplitude of the driving velocity). The values plotted are the amplitudes of the dominant spectral contribution (at ω_0) to the measured velocities. A strong resonant behavior appears at particular frequencies, with a remarkable increase of the velocity magnitude.

We have also rewritten the horizontal axis as $a/(\lambda_0/(2\pi))$ (top axis), where $\lambda_0/(2\pi)$ is the wavelength of the Ferry waves, because this dimensionless variable has been shown in Sec. 4.1 to make the position of the resonant peaks universal, i.e. independent of fluid properties and setup geometry. Even though we use only one fluid and one pipe radius, it is remarkable that the measured values for the resonant peaks coincide with the theoretically predicted values derived in Sec. 4.1.

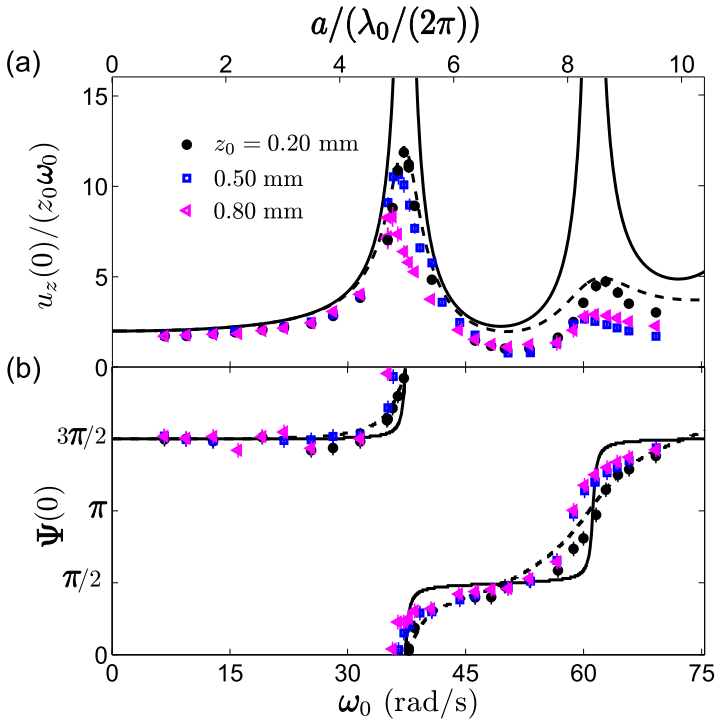

Figure 4.15: Modulus (a) and phase (b) of the first harmonic contribution to the dimensionless velocity at the tube axis, as a function of driving frequency and for three different driving amplitudes. The frequency axis can be defined either in terms of ω_0 (bottom axis) or in terms of the dimensionless ratio $a/(\lambda_0/(2\pi))$ (top axis). The solid line is the theoretical prediction computed for the UCM model, without fitting parameters, and the dashed line the corresponding one for the Oldroyd-B model for $X = 1.6 \times 10^{-3}$.

At this point it is important to recall that these experimental results correspond to a piston-driven flow. In such conditions the two first resonant peaks appear at $a/(\lambda_0/(2\pi)) = 5.1$ and 8.6, in excellent agreement with the values 5.13 and 8.41 predicted theoretically (Sec. 4.1). Our experimental observation is also in fairly good agreement with the result obtained by Castrejón-Pita et al. (2003) for the same micellar solution, using Laser Doppler Anemometry.

Different symbols in Fig. 4.15(a) correspond to three small amplitudes of oscillation, $z_0 = 0.20$, 0.50 and 0.80 mm. We can define a dimensionless driving amplitude γ_0, as $\gamma_0 = z_0/a$. These three amplitudes correspond then to $\gamma_0 = 8 \times 10^{-3}, 2 \times 10^{-2}, 3.2 \times 10^{-2}$, in this geometry. Comparison between the three data sets is possible because the vertical axis has been made dimensionless. At low frequencies ($\omega_0 \leq 31$ rad/s) the fluid response is not sensitive to the amplitude of oscillation, as expected for a linear response. Indeed, the results for 0.20, 0.50 and 0.80 mm in Fig. 4.15(a) are nearly identical at low frequencies. However, close to resonances and at larger driving frequencies ($\omega_0 \gtrsim 50$ rad/s) the response

is not linear anymore and smaller values of the dimensionless velocity are obtained at larger driving amplitudes.

The lines represent the theoretical predictions obtained with the UCM model ($X = 0$, solid line) and the Oldroyd-B model ($X = 1.6 \times 10^{-3}$, dashed line) using the rheological values given in Chap. 3. Note that the UCM curve has been computed without fitting parameters, and that only the value of X has been adjusted to obtain the best qualitative agreement between the Oldroyd-B curve and the small amplitude data. The agreement between experimental data and theoretical curves is excellent at low frequencies up to the first resonance. The discrepancies between experimental and the theoretical curve become more evident at resonances. The UCM model largely overestimates the velocity magnitude at these frequencies. Although the Oldroyd-B model is in better agreement, it does not capture all the observed trends in the measured frequency response.

Phase lag

Measurements of the phase lag as a function of driving frequency provides us with an independent and new method to identify the resonances.

An example of the frequency dependence of the phase lag was already provided in Fig. 4.14. In panel (a), which corresponds to a resonant frequency, the piston and the fluid velocity are in phase. In panel (b), which corresponds to a non-resonant frequency, the two signals are nearly in quadrature.

The results for all explored frequencies are shown in Fig. 4.15(b). For most of the explored frequencies the fluid velocity measured at the tube axis and the piston position are nearly in quadrature, $\Psi(0) \simeq \pi/2$ or $3\pi/2$, which is the result expected for a purely viscous fluid. Close to resonances, though, there is an abrupt change in phase behavior and, at resonance, the two signals move in phase ($\Psi = 0$ at $\omega_0 = 37.1$ rad/s), or in phase opposition ($\Psi(0) = \pi$ at $\omega_0 = 61.6$ rad/s), reflecting the viscoelastic properties of the micellar solution. Measurements of the phase lag therefore corroborate our results for the location of the resonances reported in the previous section.

The theoretical prediction for the phase lag based on the UCM model is in good agreement with the experimental results. The agreement even improves when the model includes the small solvent contribution that was found useful to fit the velocity magnitude (Oldroyd-B model with $X = 1.6 \times 10^{-3}$).

4.2.3 Velocity profiles

Figure 4.16 shows the radial velocity profiles measured by PIV at equally spaced time intervals within an oscillation period, and for three driving frequencies: $\omega_0 = 22.0$ rad/s (left panels), 37.1 rad/s (middle panels), and 47.1 rad/s (right panels). For the three frequencies the relaxation time of the fluid is larger than the characteristic timescale of the driving, i.e. $De = \lambda\omega > 1$. This means that the elasticity of the solution is dominant in the organization of the flow in all three cases.

At the lowest frequency all the fluid moves in the same direction (upward or downward) for most of the oscillation period, and local reversal of the flow occurs only at the time phases where the velocity nearly vanishes. It is worth noting also that the phase lag depends on the radial position and thus gives rise to profiles of different shapes at different time phases. The axisymmetry of the laminar flow is well accomplished by the measured profiles, and the no-slip condition at the tube walls is well satisfied too.

At a higher frequency that corresponds to the first resonance ($\omega_0 = 37.1$ rad/s) the flow organizes in three concentric layers with alternating sign of the velocity. Thus the velocity is zero at the walls and at the quiescent points in the bulk separating adjacent layers. The peak velocity is about four times larger than for $\omega_0 = 22.0$ rad/s, as expected at resonance. The error bars represent the rms dispersion of the ensemble of velocity profiles, measured at the same time but at slightly different heights, and used to determine the mean profiles shown in the figure.

The panels on the right shows the results for an even higher frequency, $\omega_0 = 47.1$ rad/s, past the first resonance. The organization of the flow in three layers is also apparent here, but the magnitude of the peak velocity is smaller because the flow is non resonant. While at resonance the largest measured velocities are localized at the tube axis, at $\omega_0 = 47.1$ rad/s the velocity takes similar peak values for the different concentric layers.

Quiescent points

We have tracked the evolution in time of the quiescent points in the flow. This provides additional interesting information about the velocity profiles. Figure 4.17 shows the radial position of the quiescent points in an oscillation period for the driving frequencies $\omega_0 = 37.1$ rad/s (a) and $\omega_0 = 47.1$ rad/s (b). The quiescent points are almost steady in time within the whole oscillation. However, at the particular time phases when the velocity is very small everywhere they rapidly move and relocate towards the tube walls. The relocation of the quiescent points

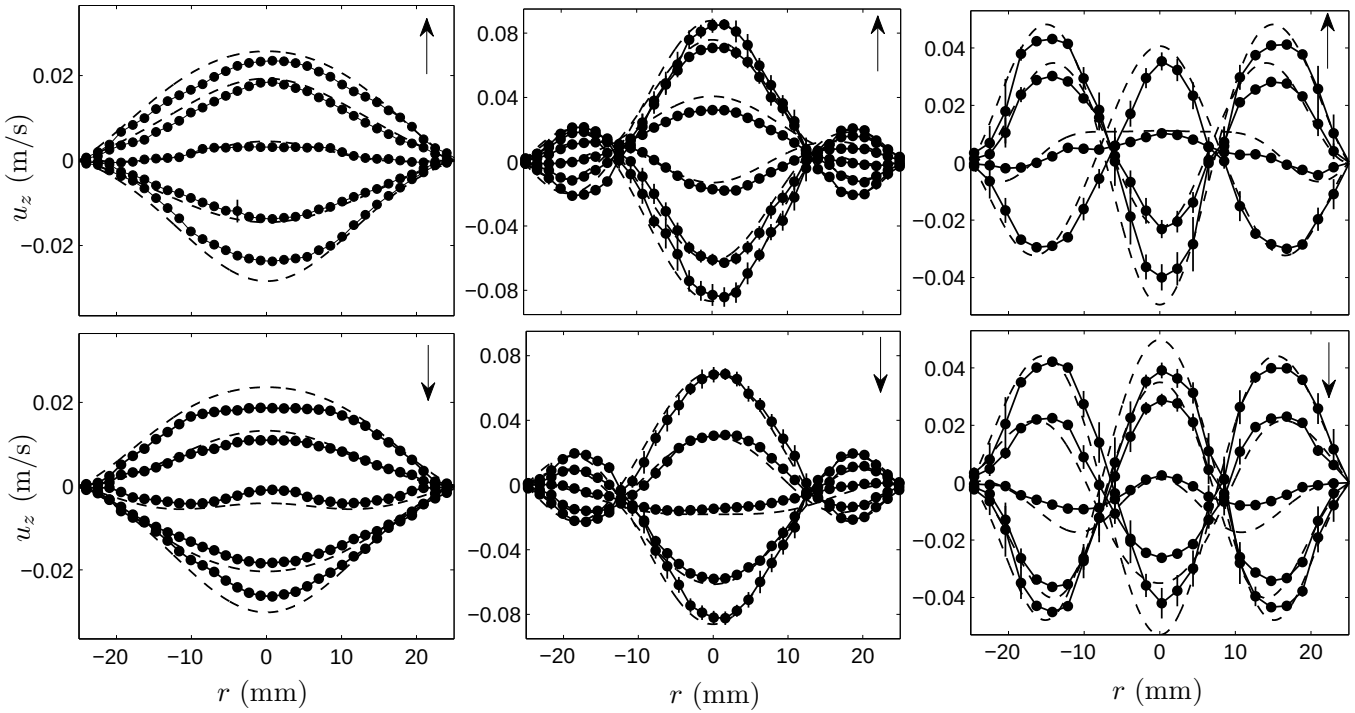

Figure 4.16: Radial velocity profiles measured at three driving frequencies and small amplitudes: $\omega_0 = 22.0$ rad/s, $z_0 = 0.50$ mm (left); $\omega_0 = 37.1$ rad/s, $z_0 = 0.20$ mm (middle); $\omega_0 = 47.1$ rad/s, $z_0 = 0.50$ mm (right). The profiles are equally separated in time and span a complete oscillation period. The vertical arrows indicate the temporal ordering of the profiles. The lines are the corresponding theoretical predictions of the Oldroyd-B model with $X = 1.6 \times 10^{-3}$.

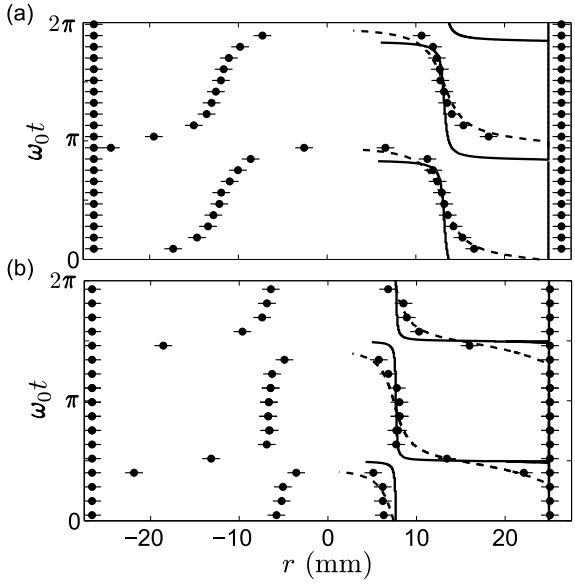

Figure 4.17: Radial location of the quiescent points for $\omega_0 = 37.1$ rad/s, $z_0 = 0.20$ mm (a), and $\omega_0 = 47.1$ rad/s, $z_0 = 0.50$ mm (b). The error bars account for the lateral size of the PIV grid. The lines are the theoretical predictions of the UCM model (solid) and the Oldroyd-B model with $X = 1.6 \times 10^{-3}$ (dashed). They have been plotted only on half of the vertical tube section for clarity.

occurs at $\omega_0 t \simeq 0, \pi$ at the resonant frequency (panel a), and at $\omega_0 t \simeq \pi/2, 3\pi/2$ at the higher, non-resonant frequency (panel b). These observations are in excellent agreement with the theoretical predictions of Sec. 4.1.

The number of quiescent points increases with driving frequency. Figure 4.18 displays the measured radial position of the quiescent points in the whole range of explored frequencies, at a fixed time phase $\omega_0 t = 0$. In this figure we have included also the dimensionless frequency axis $a/(\lambda_0/(2\pi))$ to make contact with the theoretical analysis of Sec. 4.1. It is clear from the figure that the flow becomes more inflectional as we increase the driving frequency: at low frequencies the flow is quiescent only at the walls; above $\omega_0 = 31.4$ rad/s, though, two symmetric additional quiescent points appear in the bulk; and at $\omega_0 = 50.3$ rad/s another symmetric pair comes in. It is also worth noting that exactly at the resonant frequencies the quiescent points in the bulk relocate towards the tube walls, as discussed in the context of the previous figure.

The dashed lines in Figs. 4.16, 4.17 and 4.18 are the theoretical predictions of the Oldroyd-B model with the convenient solvent viscosity ratio $X = 1.6 \times 10^{-3}$ determined in Fig. 4.15. The solid lines are the ones obtained for the UCM model. To compute these curves we have used the most relevant contributions to the frequency spectrum of the imposed driving, namely the one corresponding

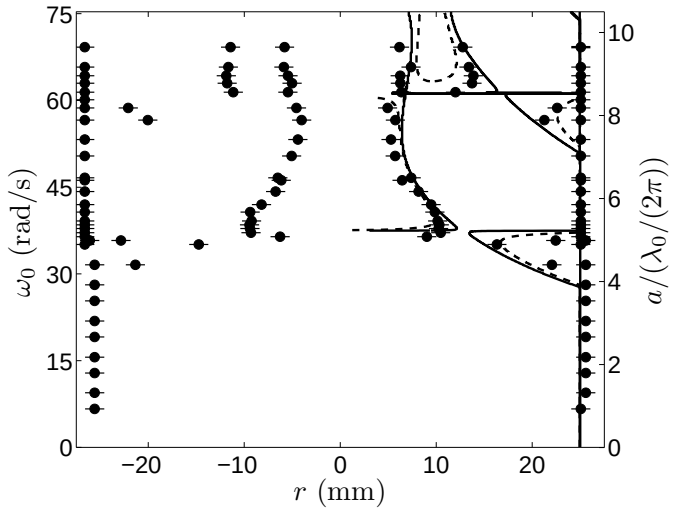

Figure 4.18: Radial location of the quiescent points at the time phase $\omega_0 t = 0$ for $z_0 = 0.50$ mm and the whole range of driving frequencies. The error bars account for the lateral size of the PIV grid. The lines are the theoretical predictions of the UCM model (solid) and the Oldroyd-B model with $X = 1.6 \times 10^{-3}$ (dashed). They have been plotted only on half of the vertical tube section for clarity.

to the nominal driving frequency ω_0 plus the much smaller components of higher harmonics $(2\omega_0, 3\omega_0)$ with their own amplitudes. We have evaluated the profiles at the time phases of the measured profiles.

The overall temporal evolution of the velocity profiles, Fig. 4.16, is very well reproduced by the Oldroyd-B predictions. In every single profile the magnitude of the velocity and the flow structure are well captured, and also there is a good matching of the time phase. In the left and right panels (non-resonant driving frequencies) the theoretical profiles that would have been obtained using the UCM model would be almost indistinguishable from the ones presented. However, at resonance (middle panel) the UCM model would largely overestimate the fluid velocities; introducing an adjustable small solvent contribution provides excellent agreement of the Oldroyd-B model with the measured data.

In what concerns the theoretical prediction of the location of the quiescent points, the lines in Figs. 4.17 and 4.18 show remarkable agreement with the measured data. In both figures the theoretical curves have been computed from the fundamental harmonic only, because higher harmonics of the driving do not modify the result appreciably. In Fig. 4.17 the temporal evolution of the nodes is smooth at resonance (panel a), and very well described by the Oldroyd-B model using the value of X determined from the resonance curve of Fig. 4.15. Out of resonance (panel b), instead, the evolution of the nodes is more abrupt and

better reproduced by the UCM model. Figure 4.18 shows that the frequencies at which the quiescent points relocate, coincident with the resonance frequencies, are predicted very precisely by both the UCM and the Oldroyd-B models. The UCM model reproduces the general trends, with sharper boundaries close to the resonances, while the Oldroyd-B model gives boundaries smoother than the experimental results.

4.2.4 Nonlinearities

Local and apparent shear rates

If we compute the local shear rate as the velocity gradient, $\dot{\gamma}_{loc} = \partial v_z/\partial r$ (Eq. 4.26), undoubtedly the largest shear rates are experienced at resonances. In Fig. 4.19 we show $\dot{\gamma}_{max}$, the maximum local shear rate along the tube radius and in a complete oscillation period, for the whole range of driving frequencies and for $z_0 = 0.20$, 0.50, and 0.80 mm. Above $\omega_0 \gtrsim 10$ rad/s and $z_0 = 0.20$ mm the maximum local shear rate already exceeds the critical shear rate for shear-thinning, $\dot{\gamma}_c \sim 0.4$ s^{-1} (or $Wi \geq 1$). Above this shear rate the response of the micellar solution is not reproduced by the linear Maxwell model. This implies that, occasionally, at the radial positions where $\dot{\gamma}_{loc} > \dot{\gamma}_c$ nonlinear features might be observed in the measured velocity profiles. Notice that $\dot{\gamma}_{loc}$ increases with z_0, since in the linear regime the fluid velocity is proportional to z_0. And $\dot{\gamma}_{loc}$ increases also with ω_0: the velocity profile becomes more inflectional at larger frequencies, with an increasing number of alternating velocity layers, leading to larger velocity gradients in the radial direction.

We can also define an apparent (or global) shear rate as $\dot{\gamma}_{app} = z_0\omega_0/a$. It corresponds to the mean shear rate imposed by the forcing. In Fig. 4.19 it is represented by the solid lines. The apparent shear rate increases linearly with the amplitude and frequency of the driving. It is worth mentioning that an average of the absolute value of the local shear rate along the tube radius in a complete oscillation reproduces $\dot{\gamma}_{app}$ and its linear dependence on ω_0 up to frequencies about 2.5×10^1 rad/s; above this frequency the average still grows with ω_0 but displays the same peak structure than $\dot{\gamma}_{max}$.

When $\dot{\gamma}_{app} > \dot{\gamma}_c$ nonlinear effects start becoming important and influence the overall flow behavior. It is reasonable thus that discrepancies between experiments and linear theoretical predictions become larger for higher frequencies, and even more evident at resonances. Linear theories for the uniaxial flow, like those that can be derived from the UCM or Oldroyd-B models, are not able to capture all the observed features in this regime.

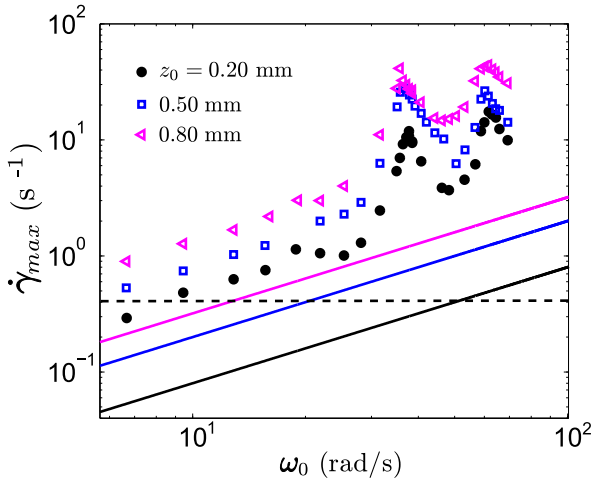

Figure 4.19: Maximum local shear rate experienced by the fluid (symbols) and apparent shear rate (solid lines of corresponding color) as a function of driving frequency and for three different driving amplitudes. The horizontal dashed line is the critical shear rate of the wormlike micellar solution.

Observed anomalies of the velocity profiles

Several other specific features of the velocity profiles are not reproduced by the linear models either. In particular in the left panels of Fig. 4.16 some velocity profiles display an anomalous flat shape in the central region, at the time phases when the velocity magnitude takes largest values. For these particular profiles we have checked that the theoretical predictions would partially account for this tendency of the profiles to flatten if the response of the third harmonic, $3\omega_0$, would be included. Another anomalous feature is observed next to the tube walls, where the measured profiles display a region of almost zero velocity larger than the theoretical counterparts. These unusual features are also observed in the right panel of this same figure, but in this case we have checked that the contribution of a third harmonic is negligible.

This kind of plug-like profiles has been observed already in other rectilinear shear flows of similar wormlike micellar solutions, and have been attributed to shear banding. Typically a transition from a parabolic profile, characteristic of Newtonian fluids, to a plug-like velocity profile with distinct shear bands close to the walls, has been observed as the flow rate is increased. These results have been obtained for cross-rectangular channels of millimetric and micrometric dimensions, using PIV (Nghe et al., 2008; Ober et al., 2011), and for axisymmetric capillary channels of millimetric dimensions using PIV (Yamamoto et al., 2008) or NMR (Mair and Callaghan, 1997). There is a fundamental difference, though,

between previous experiments and the present work. Our study is focused on an oscillatory (non-steady) flow, which induces highly inflectional velocity profiles. On the one hand, this makes difficult to predict the spatial organization of any possible shear bands that might form inside the cylinder. On the other hand, the temporal dependence imposed by the driving frequency introduces an extra time scale related to the periodic destabilization and reformation of the hypothetic shear bands. It is known that shear bands take a certain time to develop (Pipe et al., 2010; Miller and Rothstein, 2007), typically larger than the relaxation time of the fluid. In this sense the experiments carried out here at the lowest driving frequencies would be the only suitable candidates to exhibit shear banding. At larger frequencies the fluid would be subjected locally to unidirectional shear for times too short to form stable bands.

Moderate driving amplitudes

As we increase the driving amplitude the shear rates experienced by the fluid become larger and nonlinearities are likely to appear. This tendency, already discussed in the context of Fig. 4.19, is studied systematically in Fig. 4.20. We show the dependence on oscillation amplitude of the dimensionless velocity profiles measured at $\omega_0 t = \pi$ for a large set of amplitudes (0.20 mm $\leq z_0 \leq$ 2.40 mm, i.e. $8 \times 10^{-3} \leq \gamma_0 \leq 9.6 \times 10^{-2}$) and two forcing frequencies: $\omega_0 = 37.1$ rad/s (resonant frequency) and $\omega_0 = 44.0$ rad/s (non-resonant frequency). At $\omega_0 = 37.1$ rad/s (panel a) the nonlinearities in the fluid response are already manifest at very small amplitudes, around $z_0 = 0.40$ mm. Since at resonances the local shear rates are much larger than for other frequencies, nonlinearities appear first. Above this amplitude the linearity of the flow is not preserved anymore. Conversely, out of resonance (panel b) the fluid response keeps linear with the driving for a much larger range of amplitudes, $z_0 \leq 2.40$ mm. The measured velocity profiles scale with $z_0\omega_0$ for all this range of driving amplitudes.

In order to account for the imposed deformation we define a Weissenberg number based on the local shear rate, $Wi_{loc} = \lambda\dot{\gamma}_{loc}$, and another one based on the apparent shear rate, $Wi_{app} = \lambda\dot{\gamma}_{app}$. The latter coincides with the definition provided in Chap. 1, Eq. (1.4). Notice that $Wi_{app} = \gamma_0 De$, where γ_0 is the dimensionless strain amplitude z_0/a. For most of the explored range of driving frequencies and amplitudes $Wi_{loc} \gg 1$. The fluid experiences shear rates that locally exceed $\dot{\gamma}_c$. However Wi_{app} remains smaller than 1 for a considerable range of driving frequencies. In particular at the smallest amplitude, $z_0 = 0.20$ mm, $Wi_{app} < 1$ until $\omega_0 \simeq 50$ rad/s. This is the reason why a linear theory based on the UCM or Oldroyd-B models is able to reproduce many features of the observed flow behavior.

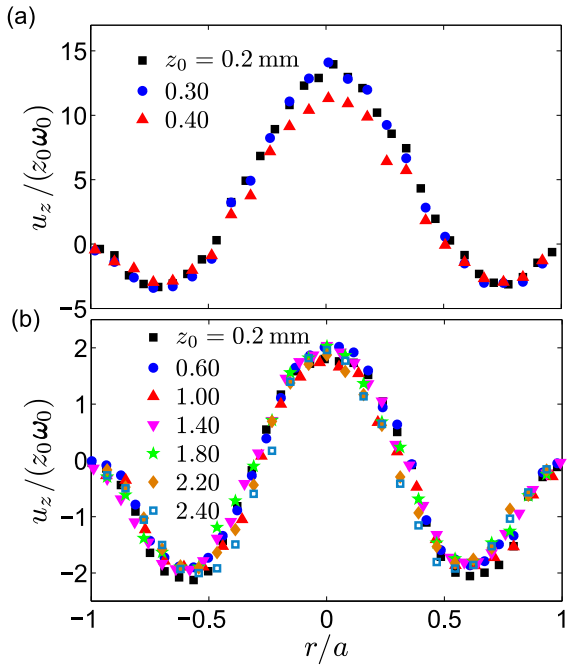

Figure 4.20: Dimensionless velocity profiles measured for a set of driving amplitudes and two driving frequencies, $\omega_0 = 37.1$ rad/s (a) and $\omega_0 = 44.0$ rad/s (b), at the time phase $\omega_0 t = \pi$.

In order to capture the nonlinearities revealed by our experimental data a constitutive equation with a nonlinear equation for the shear stress, to account for the nonmonotonicity of the viscometric flow curve of micellar solutions, would be required. The semiempirical single-mode Giesekus model (Bird et al., 1987) is well known to describe the nonlinear shear flow of semi-dilute wormlike micelles successfully (Yesilata et al., 2006; Larson, 1999). The Johnson-Segalman equation (Cates and Fielding, 2006) has also been extensively used to model the material instability of wormlike micellar solutions and the formation of shear bands. The VCM model proposed by Vasquez and coworkers (Vasquez et al., 2007) can also predict the behavior of inhomogeneous flows. These models might be good candidates to reproduce the nonlinear effects observed in our experiments, that cannot be captured by constitutive models with a linear equation for the shear stress. The experiments reported in this section have been performed with a canonical wormlike micellar solution under well controlled flow conditions, different from more traditional rheometric flows. Hence, they provide original experimental data that could be useful to test the success of nonlinear constitutive equations in predicting complex non-steady flows. However, a nonlinearity of the constitutive equation makes analytical calculations of the oscillatory flow not feasible, and accessible only via numerical calculations. This approach, currently in progress, falls be-

yond the scope of the present work.

Finally, we have observed that at slightly larger amplitudes than 0.40 mm for $\omega_0 = 37.1$ rad/s, and 2.40 mm for $\omega_0 = 44.0$ rad/s, the laminar oscillatory flow eventually becomes unstable. The transition to more complex flows is addressed in the next two chapters.

Chapter 5

Hydrodynamic instabilities: local scale

5.1 Stability phase diagram

We explored the flow behavior exhibited by the micellar solution for the whole range of experimentally accessible forcings: $6.0 \leq \omega_0 \leq 75.0$ rad/s and $0.20 \leq z_0 \leq 6.00$ mm. In terms of dimensionless numbers, it corresponds to $12 \leq De \leq 143$ and $0.1 \leq Wi \leq 34.0$. In Fig. 5.1 we show the stability phase diagram of the laminar base flow measured at the mid-position of the tube plotted as a Pipkin diagram (amplitude vs. frequency, or alternatively, Wi vs. De). The mid-position is placed at 33 cm from the bottom piston and corresponds to *Region 4*, in the tube division that will be made in Sec. 6.1. In order to cover the entire range of accessible parameters we performed ramps of increasing driving amplitudes at every oscillation frequency. The experimental protocol is described in detail in Sec. 5.2.

Three main regions can be distinguished (depicted in different colors in the figure):

- Laminar base flow: It is found at small amplitudes and frequencies of the forcing. Note that for $\omega_0 < 25$ rad/s the laminar base flow is preserved for the whole range of accessible driving amplitudes. This regime has been studied in detail in Chap. 4. The laminar oscillatory flow preserves both the translational and axial symmetry, and follows the periodicity of the forcing. Only small recirculation zones are located close to the top and bottom ends of the cylinder.

- Axisymmetric vortical flow: Above a critical driving the translational symmetry of the laminar flow along the vertical coordinate is broken, whereas the

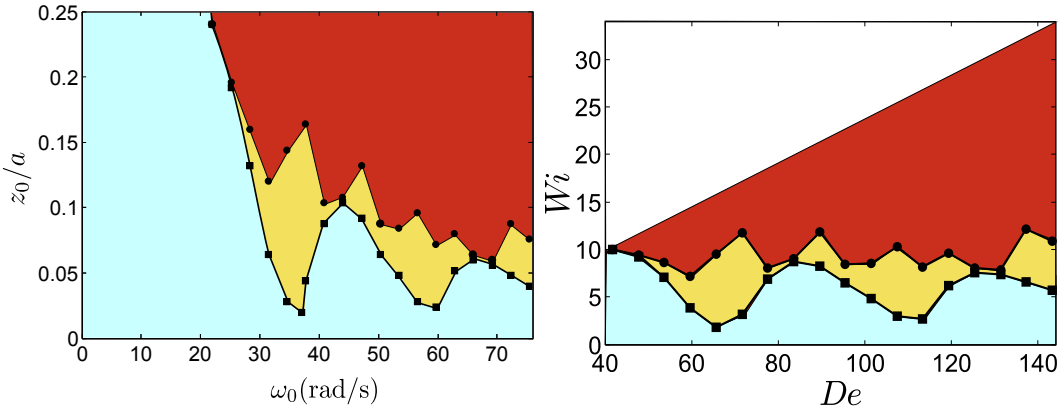

Figure 5.1: Stability phase diagram represented in terms of the (dimensionless) driving amplitude z_0/a vs. driving frequency ω_0 (left), or Wi vs. De (right), measured in the central region of the tube (*Reg. 4*). The laminar base flow is represented in pale blue, the vortical flow in orange and the non-symmetric vortical flow in red. The error bars for z_0/a are given by the dimensionless step size ± 0.004 used to perform the ramps.

axial symmetry remains unaltered. The flow organizes forming quasi-steady toroidal vortices, around the vertical symmetry axis, that are found stacked all along the tube. These vortex rings rotate following the periodicity of the driving. They appear as a pair of counter-rotating vortices when the flow field is measured in a meridional plane of the tube. The threshold for this first instability is not constant. When depicted in terms of amplitude and frequency (Fig. 5.1) it exhibits an interesting frequency dependence that is clearly related to the frequency response of the fluid in the laminar regime. Since in the laminar regime the velocity magnitude at the tube axis peaks at particular driving frequencies, $\omega_0 = 37.1, 62.8$ rad/s, it is not surprising that the instability threshold observed at resonances is considerably smaller than for the rest of the frequency spectrum. In Sec. 5.3 we will characterize in detail the onset of this hydrodynamic instability, and a thorough description of the vortical flow will also be addressed.

- Non-axisymmetric vortical flow: At even larger drivings the vortical flow loses the axial symmetry. The threshold for this second instability decreases for increasing driving frequencies (Fig. 5.1), although it does not exhibit a well-defined frequency dependence. When depicted in terms of Wi, it appears that this second instability occurs in the range $Wi = 10 \pm 2$ for all De. In this regime the oscillatory flow has lost both the vertical translational symmetry and the axial symmetry. The flow organizes forming non-symmetric, deformed vortex rings. Both the onset of this second hydrodynamic instability and the structure of the secondary flow will be studied in Sec. 5.4.

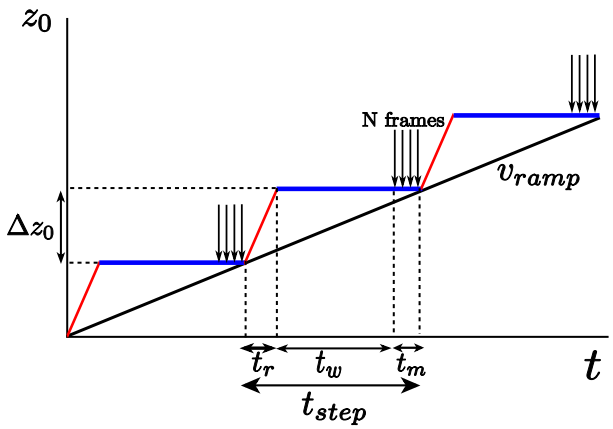

Figure 5.2: Scheme of the experimental protocol used for ramping up/down the driving amplitude.

5.2 Experimental protocol for ramping the driving amplitude

The transition from laminar to more complex flows was studied by performing ramps of increasing/decreasing driving amplitudes at fixed frequency of oscillation (Fig. 5.2). The step amplitude used was typically $\Delta z_0 = 0.10$ mm. We also used $\Delta z_0 = 0.05$ mm or even $\Delta z_0 = 0.02$ mm when a particular range of amplitudes was explored in detail. To ensure that the flow was quasi-steady every time that the driving amplitude was changed, the fluid was allowed to oscillate for a certain waiting time (t_w) before recording the images. Typically $t_w \simeq 30$ s, which is more than 15 times the relaxation time of the viscoelastic fluid. The measuring time (t_m) required to record the images as well as the time spent to ramp the amplitude up and down (t_r) were both much shorter than the waiting time. We defined the velocity of the ramp (v_{ramp}) as the step in amplitude divided by the waiting time (in which both t_m and t_r have been disregarded). Most of the experiments were performed at a common velocity, $v_{ramp} = \Delta z_0/t_w \simeq 3.3 \times 10^{-3}$ mm/s, for both upward and downward amplitude excursions.

5.3 First instability: loss of vertical translational symmetry

In the first part of this section we perform a quantitative analysis of the onset of the first hydrodynamic instability. For the sake of concretion we focus the analysis on a particular driving frequency, $\omega_0 = 31.4$ rad/s. This frequency is smaller than

the first resonance frequency, but large enough to provide an interesting route from laminar to more complex flows as the driving amplitude is increased. In the second part we describe the vortical flow structure (Sec. 5.3.3), and quantify the vortex dynamics using a set of defined properties (Sec. 5.3.4). In the last part (Sec. 5.3.5) we extend the study of the vortical flow to larger driving frequencies, $\omega_0 = 37.1$, 44.0, 56.5 rad/s, in order to understand the influence of the imposed timescale on the vortical flow behavior.

We restrict the study of the vortical flow behavior to the central region of the vertical cylinder (*Reg. 4*). In next chapter a study of the large scale flow structure covering the entire tube length will be addressed.

5.3.1 Onset of the instability

In order to do a quantitative characterization of the transition from laminar to vortical flow, we compute the root-mean-square (rms) fluctuations of the vertical and radial components of the velocity field, u_z, u_r, along the vertical coordinate z. We make the rms fluctuations dimensionless by dividing them by the amplitude of the driving, $z_0\omega_0$, so that a quantitative comparison at different drivings is possible. The expression used for the rms velocity fluctuations averaged in time, over a complete time period, is

$$\left\langle \sigma_{u_{z,r}}(r,t) \right\rangle_t = \frac{1}{z_0\omega_0} \left\langle \sqrt{\frac{1}{N}\sum_i [u_{z,r}(r,z_i,t) - \overline{u}_{z,r}(r,t)]^2} \right\rangle_t . \tag{5.1}$$

And the expression for the rms velocity fluctuations averaged in space, over the tube diameter, is

$$\left\langle \sigma_{u_{z,r}}(r,t) \right\rangle_r = \frac{1}{z_0\omega_0} \left\langle \sqrt{\frac{1}{N}\sum_i [u_{z,r}(r,z_i,t) - \overline{u}_{z,r}(r,t)]^2} \right\rangle_r , \tag{5.2}$$

where $\overline{u}_{z,r}(r,t)$ is the mean velocity obtained from averaging N velocity profiles (typically 40) measured within the interrogation region along the vertical direction z.

Time averaged RMS fluctuations

In Fig. 5.3 (top panels) we show the time averaged rms fluctuations of the two in-plane components of the velocity, measured at $\omega_0 = 31.4$ rad/s and increasing driving amplitudes.

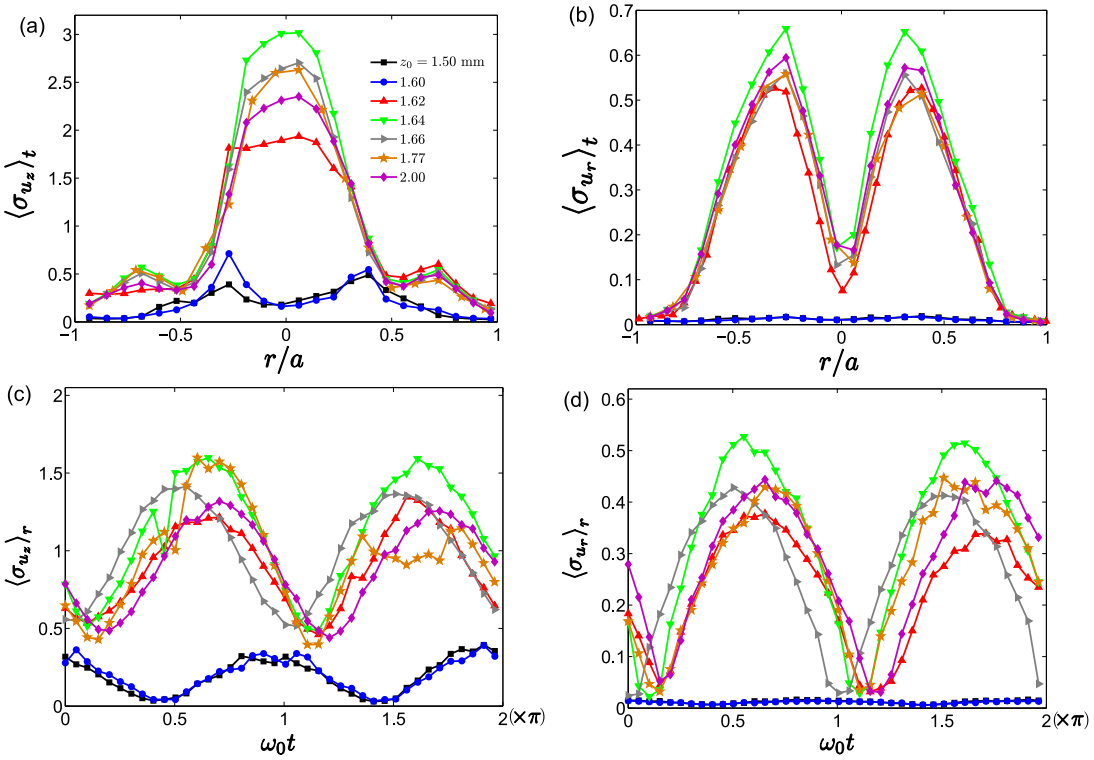

Figure 5.3: Top panels: time averaged rms fluctuations exhibited by the vertical (a) and radial (b) components of the velocity. Bottom panels: radially averaged rms fluctuations exhibited by the vertical (c) and radial (d) components of the velocity. Different symbols correspond to increasing driving amplitudes. The frequency is kept constant at $\omega_0 = 31.4$ rad/s ($De = 59.6$).

In the laminar regime the magnitude of the rms fluctuations should be negligible, since we verified in Sec. 4.2 that in this regime there is no variation of the velocity profiles along the vertical direction in the interrogation region. Non-zero values of the velocity fluctuations thus account for the experimental uncertainty intrinsic to the velocity measurements. Indeed, the fluctuations exhibited by u_r (panel b) show no-well defined structure along the radial coordinate at small amplitudes, $z_0 = 1.50$, 1.60 mm. Similarly, the small peaks exhibited by $u_z(r)$ in panel (a) at symmetric positions, $r/a \simeq \pm 0.3$, at these same amplitudes correspond to the uncertainty in this velocity component. Although small, the peaks appear at the radial positions where the vorticity field takes largest values (Fig. 5.9). However, assuming that $u_\theta = 0$ in the laminar regime, the incompressibility condition $\boldsymbol{\nabla}_{\|} \cdot \boldsymbol{u} = 0$ does not admit a variation of u_z with z simultaneously with $u_r = 0$, as our measurements of Fig. 5.3 seem to indicate. This reinforces the idea that the small peaks observed for the rms fluctuations of u_z indeed account for the experimental uncertainty that results from the cross-correlation PIV process. The

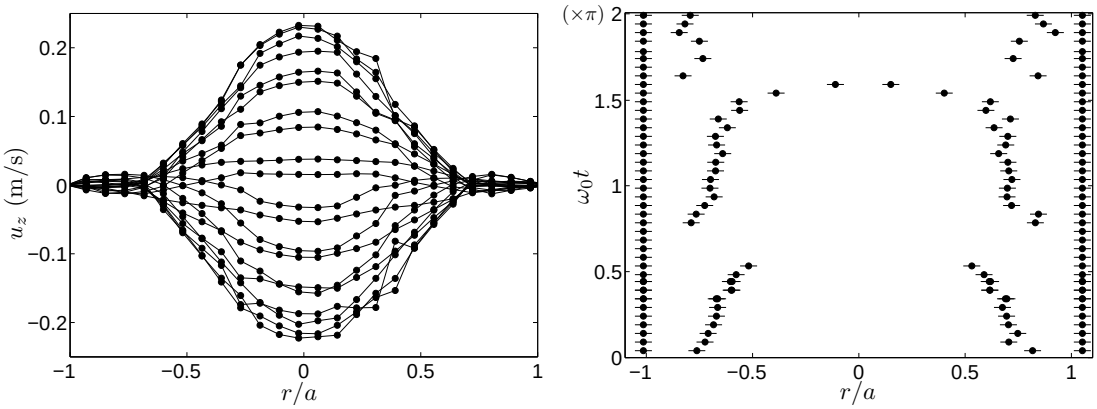

Figure 5.4: Laminar velocity profiles (left) and radial position of the quiescent points (right) obtained at $\omega_0 = 31.4$ rad/s and $z_0 = 1.46$ mm for a complete time period (*Reg. 4*).

PIV software fails in resolving the average velocity field in the presence of large velocity gradients and hence the largest uncertainties are found at these radial positions where the vorticity is more pronounced.

At the particular critical amplitude $z^*_{1-up} = 1.62 \pm 0.02$ mm ($Wi^*_{1-up} = 3.9$) there is an abrupt increase of the velocity fluctuations that corresponds to the breakage of the vertical translational symmetry and the onset of the vortical flow. This sudden increment of the fluctuations occurs at a common driving amplitude for both the radial and vertical components of the velocity.

In the vortical flow, the fluctuations of u_z exhibit a symmetric bell-shaped profile along the radial coordinate, with the largest fluctuations found at the symmetry axis (Fig. 5.3(a)). Besides, they present two secondary peaks located at symmetric radial positions $r/a \simeq \pm 0.7$, and two minima at $r/a \simeq \pm 0.5$. The location of the peaks fairly coincides with the radial position of the quiescent points of the laminar flow observed for most of the oscillation period. We report in Fig. 5.4 the velocity profiles (left panel) and the location of the quiescent points (right panel) for a complete time period, at $\omega_0 = 31.4$ rad/s and $z_0 = 1.46$ mm (laminar flow). As discussed in Sec. 4.2 the position of the quiescent points is not constant in time, but for most of the oscillation period it is placed at $r/a \simeq \pm 0.7$. The position of the minima of the vertical velocity fluctuations matches the position of the geometric center of the vortices, that will be described in Sec. 5.3.4. At the geometric center of the vortices the fluid is locally at rest (Fig. 5.10). Just above and below the vortex centers u_z is nearly zero (but not u_r). Besides, in the adjacent laminar regions u_z is also small. Hence, the fluctuations of the vertical velocity are small at these radial locations.

The fluctuations of u_r depict a symmetric M-shape with marked peaks at

$r \simeq \pm 0.3$ (Fig. 5.3(b)). We will show in Sec. 5.3.4 that these locations correspond to the radial positions of the center of vorticity defined for the vortices.

Close to the tube walls the fluctuations drop to zero. This corroborates that the no-slip condition at the boundaries applies also to the vortical flow.

For increasingly larger amplitudes the dimensionless fluctuations change in magnitude. These variations may result from changes in the vortex strength. However, the location of the vortex at given time phase can considerably change at increasing driving amplitudes, leading to a different vortical flow structure in the interrogation region which may also cause substantial differences in the magnitude of the velocity fluctuations. Nevertheless, the qualitative features of the fluctuations in both u_z and u_r remain unaltered in the vortical flow regime regardless of the driving amplitude.

Radially averaged RMS fluctuations

When averaged over the tube radius, the rms fluctuations of u_z, u_r exhibit a periodicity in time that is twice the periodicity of the imposed driving. In Fig. 5.3 (bottom panels) we show the velocity fluctuations, averaged over the tube diameter, for a complete time period at $\omega_0 = 31.4$ rad/s. At small driving amplitudes ($z_0 < z^*_{1-up}$) the magnitude of the fluctuations of u_r is negligible. The fluctuations of u_z reflect the experimental uncertainty. They exhibit the periodicity of the laminar oscillatory flow: the maximum values are found precisely at the time phases $\omega_0 t = 0$ and π, where the velocity magnitude at the tube axis is largest (and accordingly the experimental uncertainty is also largest), and values close to zero are found at the time phases $\omega_0 t = \pi/2$ and $3\pi/2$, where the velocity is minimum.

At this point it is worth recalling that the driving piston moves as $z_p = z_0 \sin(\omega_0 t)$. At the time phases $\omega_0 t = 0$ and π the piston position and piston acceleration are zero, and the modulus of the velocity of the piston, $v_p = z_0 \omega_0 \cos(\omega_0 t)$, is maximum. Conversely at $\omega_0 t = \pi/2$ and $3\pi/2$ the piston is at one end of its course, and its velocity is zero.

Above z^*_{1-up} there is an abrupt increase of the velocity fluctuations for both components of the velocity. It is accompanied by a sudden qualitative change in the temporal behavior of the fluctuations with respect to those of the laminar flow. In the vortical flow, the rms fluctuations still follow twice the periodicity of the driving. The maximum values of the fluctuations are found now at $\omega_0 t \simeq \pi/2 + 0.2\pi$ and $3\pi/2 + 0.2\pi$. Conversely, the minimum values are at the complementary time phases $\omega_0 t \simeq 0.2\pi$ and $\pi + 0.2\pi$. Since the increase of the fluctuations accounts for the vortex formation, it implies that the vortices are fully developed

at the time phases that maximize the rms fluctuations (see Figs. 5.10 and 5.11). Conversely, the vortices vanish and the fluid flow resembles the flow observed in the laminar regime at the time phases that minimize the rms fluctuations.

Both the fluctuations for u_z and for u_r exhibit a systematic shift of about $\omega_0 t \simeq 0.2\pi$, with respect to the oscillatory motion of the piston, that reaches the largest displacement (and largest absolute piston acceleration) precisely at $\omega_0 t = \pi/2$ and $3\pi/2$. We attribute this temporal shift to a latency time that would be required for the vortex to form in the central region of the tube. Note that there is no qualitative difference in the rms fluctuations observed in the first and second half period of the oscillation. Accordingly, no differences are found between the first and second half period of the velocity and vorticity fields (top and bottom panels in Figs. 5.10, 5.11), except for their sign.

5.3.2 Hysteresis and bifurcation diagram

When the amplitude of the oscillations is ramped down, the reverse transition from vortical to laminar flow occurs at a lower critical driving amplitude $z^*_{1-down} = 1.35 \pm 0.02$ mm (the smallest amplitude at which the flow is vortical). Again this critical amplitude is the same for the vertical and radial components of the velocity, as shown in Fig. 5.5(a,b).

All the features observed for the time-averaged rms fluctuations of the velocity when ramping up the driving amplitude are preserved for downward excursions of the amplitude. The magnitude of the fluctuations is also comparable between upward and downwards ramps. One difference is found for the fluctuations of the vertical velocity once the laminar regime is recovered. The small peaks near $r/a \simeq \pm 0.3$ are absent now.

The temporal periodicity of the spatially averaged rms fluctuations is also preserved. Interestingly, the temporal shift described for the rms fluctuations measured for ramps of increasing driving amplitudes is again observed. The latency time appears now in the reverse temporal direction so that the rms fluctuations peak at $\omega_0 t \simeq \pi/2 - 0.2\pi$ and $3\pi/2 - 0.2\pi$. An intermediate stage has been captured at the critical driving amplitude $z^*_{1-down} = 1.35 \pm 0.02$ mm. At this amplitude the rms fluctuations of u_r exhibit an intermediate temporal behavior: the fluctuations depict the same periodicity described for larger amplitudes, but at the acceleration phases of the piston ($\pi/2 < \omega_0 t < \pi$ and $3\pi/2 < \omega_0 t < 2\pi$) they drop to zero. This would correspond to the premature relaminarization of the oscillatory flow at these time intervals.

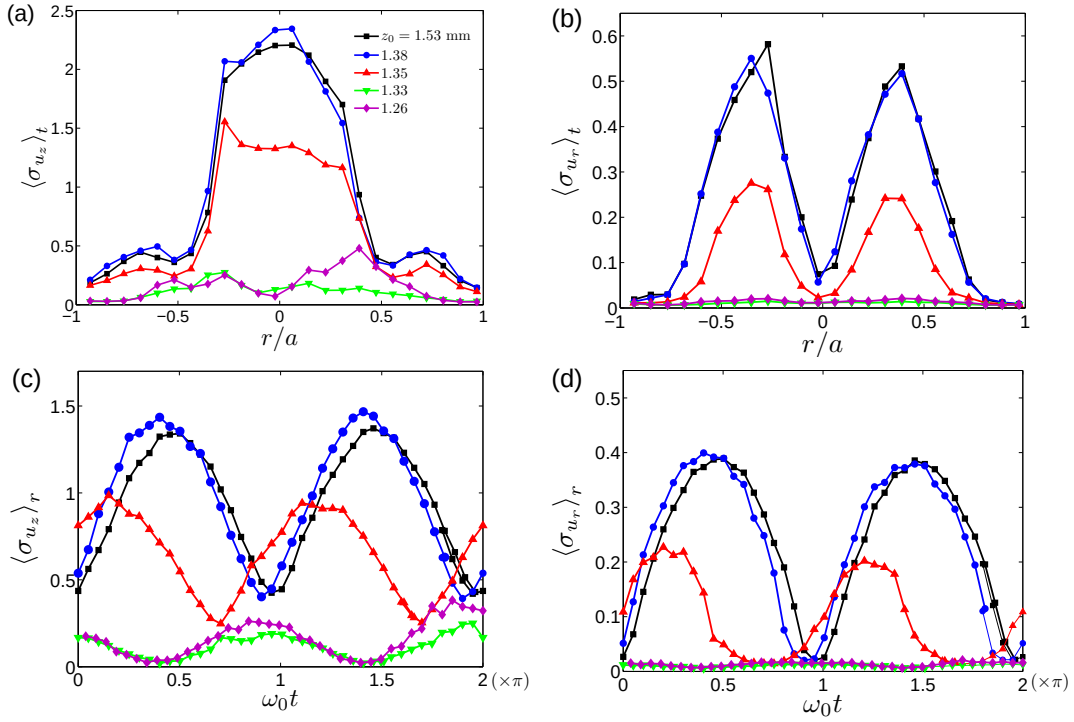

Figure 5.5: Top panels: time-averaged rms fluctuations exhibited by the vertical (a) and radial (b) components of the velocity. Bottom panels: radially averaged rms fluctuations exhibited by the vertical (c) and radial (d) components of the velocity. Different symbols correspond to decreasing driving amplitudes. The frequency is kept constant at $\omega_0 = 31.4$ rad/s ($De = 59.6$).

Hysteresis of the stability phase diagram

The bifurcation from laminar to vortical flow presents hysteresis. The onset of the vortical flow, when ramping up the forcing amplitude z_0, takes place at a larger forcing amplitude than the recovery of the laminar flow when ramping down z_0. A quantitative estimation of the hysteresis can be defined as the difference between the two critical amplitudes:

$$H = z^*_{1-up} - z^*_{1-down}. \tag{5.3}$$

The hysteresis measured for $\omega_0 = 31.4$ rad/s is $H = 0.27 \pm 0.03$ mm, which is much larger than the step size used in the ramps of increasing and decreasing amplitude ($\Delta z_0 = 0.02$ mm). The existence of this marked hysteresis makes us presume that this first instability, from laminar to vortical flow, is subcritical.

A hysteretic behavior of this first hydrodynamic instability has been observed in the whole range of explored frequencies. The hysteretic region is represented in blue in the Pipkin diagrams (z_0/a vs. ω_0 and Wi vs. De) shown in Fig. 5.6.

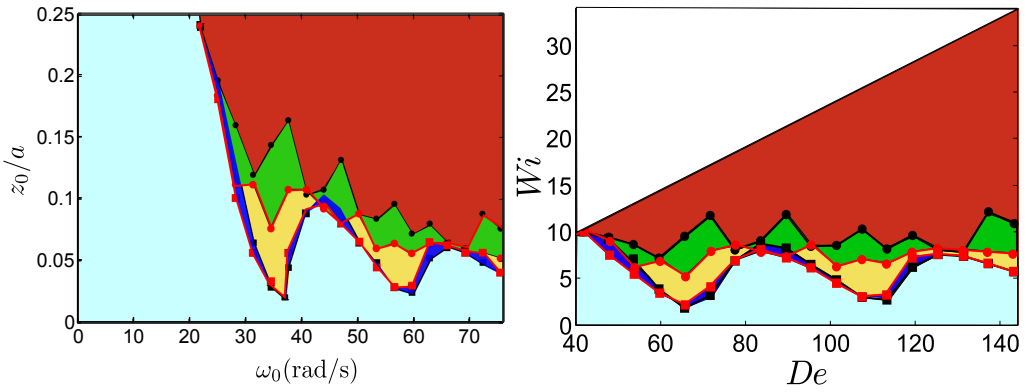

Figure 5.6: Stability phase diagram represented in terms of the (dimensionless) driving amplitude z_0/a vs. driving frequency ω_0 (left), or Wi vs. De (right), measured in the central region of the tube (*Reg. 4*). The laminar base flow is represented in pale blue, the vortical flow in orange and the non-symmetric vortical flow in red. The hysteretic regions for the first and second instabilities are depicted in blue and green.

The amount of hysteresis varies with driving frequency, being smallest close to the resonant frequencies.

Bifurcation diagram

A global order parameter, $\langle \sigma_{u_{z,r}} \rangle_{t,r}$, can be obtained by averaging the velocity fluctuations both in time (in one oscillation period) and in space (over the tube diameter). In Fig. 5.7 we draw the bifurcation diagram, $\langle \sigma_{u_{z,r}} \rangle_{t,r}$ vs. z_0, obtained at $\omega_0 = 31.4$ rad/s, in the central region of the tube, for the vertical and radial components of the velocity when ramping up and down the driving amplitude. At the critical driving amplitudes z^*_{1-up} and z^*_{1-down} of the first instability there is an abrupt increase (or decrease) of the global order parameter that accounts for the onset (or disappearance) of the vortical flow. The diagram reveals the asymmetry of the global order parameter below and above the transition, and the hysteresis in the forcing amplitude.

5.3.3 Local structure of the secondary flow

We study in detail the structure of the secondary flow exhibited by the micellar solution at $\omega_0 = 31.4$ rad/s. In Figs. 5.8 and 5.9 we show the temporal evolution, over a complete time period, of the in-plane velocity and azimuthal vorticity fields of the laminar flow obtained at $z_0 = 1.46$ mm, below the critical driving amplitude z^*_{1-up}.

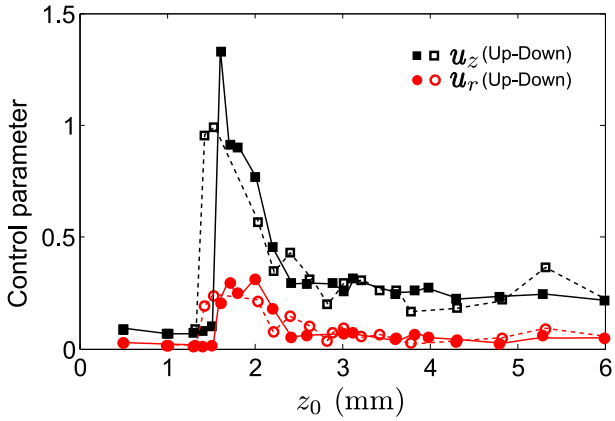

Figure 5.7: Bifurcation diagram obtained at $\omega_0 = 31.4$ rad/s (*Reg. 4*). Time and space averages $\langle \sigma_{u_{z,r}} \rangle_{t,r}$ have been used as control parameters.

As expected for the laminar regime, the velocity and vorticity fields are translationally invariant along the vertical coordinate, within experimental resolution. Fluctuations of these fields are not significant. They account for the uncertainty in the velocity measurements that results from the PIV cross-correlation method.

The fluid velocity follows the periodicity of the imposed driving. The largest axial velocity magnitudes, of about 300 mm/s, are found at $\omega_0 t = 0, \pi$. The maximum values of the vorticity do not exceed 50 s^{-1}, and are also found at these time phases, with the sign of the vorticity reversed every half period.

At this frequency the vorticity field exhibits four different vertical bands of alternated sign. The number of vorticity bands coincides with the number of concentric cylindrical layers of the laminar flow, plus one. The additional band results from the change of sign of the radial coordinate at the tube axis. For larger driving frequencies we expect the number of vorticity layers to increase.

Above the critical driving amplitude z^*_{1-up} the fluid flow drastically changes its spatio-temporal structure. Figures 5.10 and 5.11 show the velocity and vorticity fields of the secondary flow, measured at $z_0 = 1.62$ mm.

The secondary flow has been obtained in the following way: the laminar base flow measured at the same driving frequency and an equivalent time phase $\omega_0 t$, but at a smaller amplitude z_{lam}, has been rescaled by the proportionality factor z_0/z_{lam} and subtracted from the vortical flow. The secondary flow is therefore obtained as:

$$\tilde{\boldsymbol{u}}(r,z,t) = \boldsymbol{u}(r,z,t) - \frac{z_0}{z_{lam}} \boldsymbol{u}_{lam}(r,z,t). \tag{5.4}$$

This approximate procedure eliminates most of the flow structure of the oscillatory

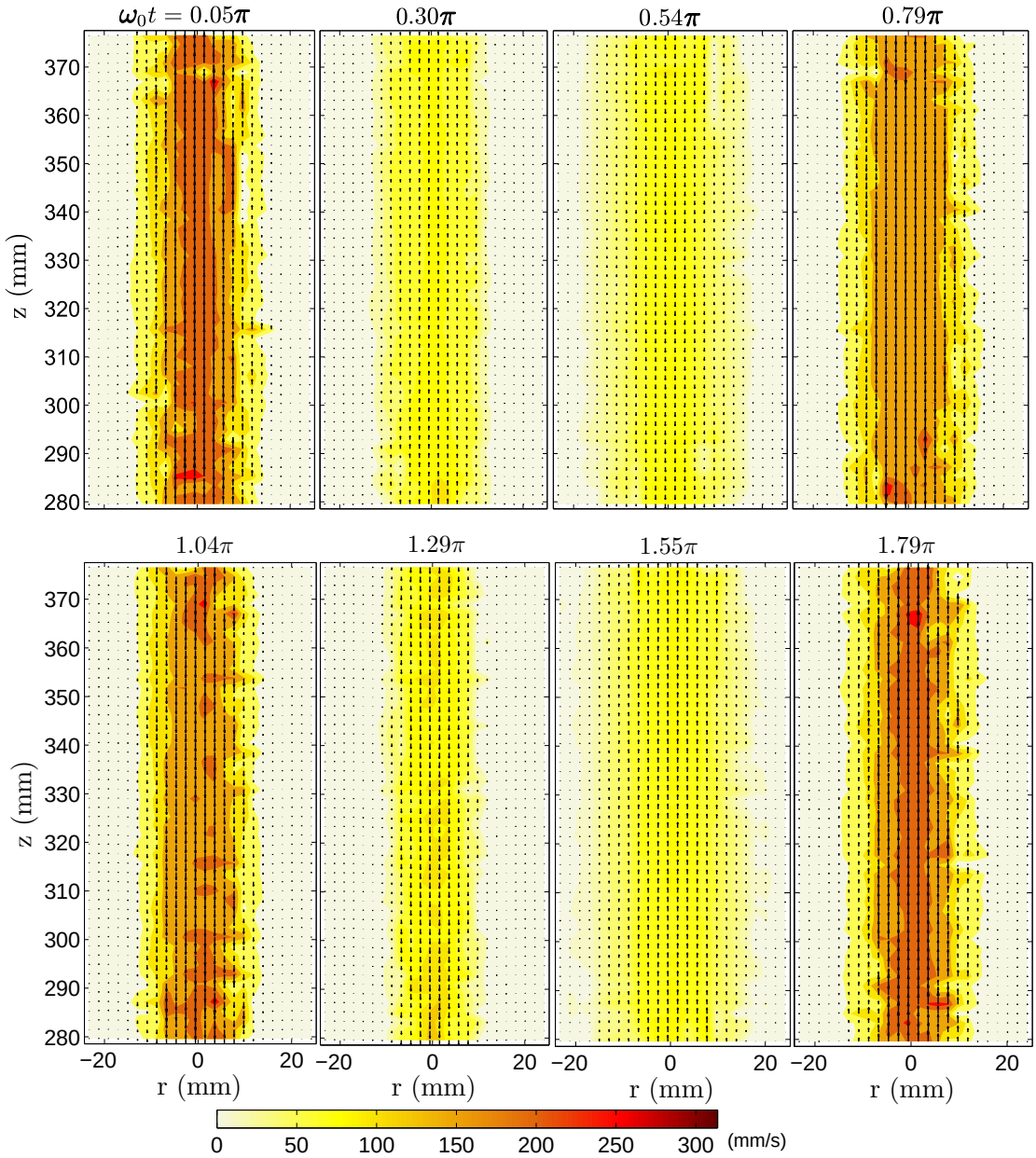

Figure 5.8: Velocity field obtained at $\omega_0 = 31.4$ rad/s and $z_0 = 1.46$ mm, in the meridional plane of the tube corresponding to (*Reg. 4*). Eight different equispaced time phases are shown, covering a complete oscillation period. The color bar corresponds to the magnitude of the velocity. The arrows (on a different scale in each panel) indicate the local direction and relative magnitude of the velocity field.

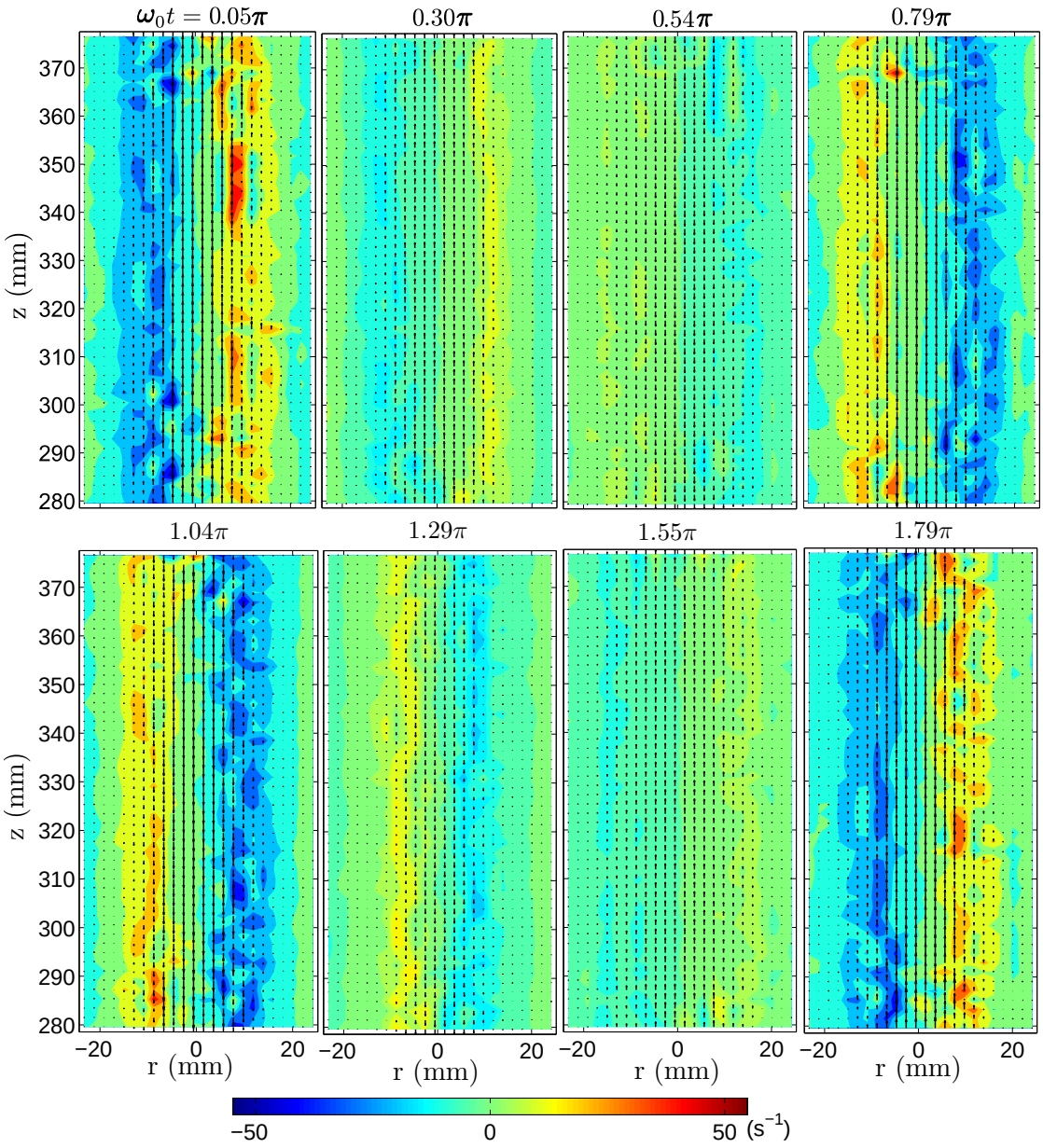

Figure 5.9: Vorticity field obtained at $\omega_0 = 31.4$ rad/s and $z_0 = 1.46$ mm, in the meridional plane of the tube corresponding to (*Reg. 4*). Eight different equispaced time phases are shown, covering a complete oscillation period. The colorbar corresponds to the vorticity field. The arrows (on a different scale in each panel) indicate the local direction and relative magnitude of the velocity field.

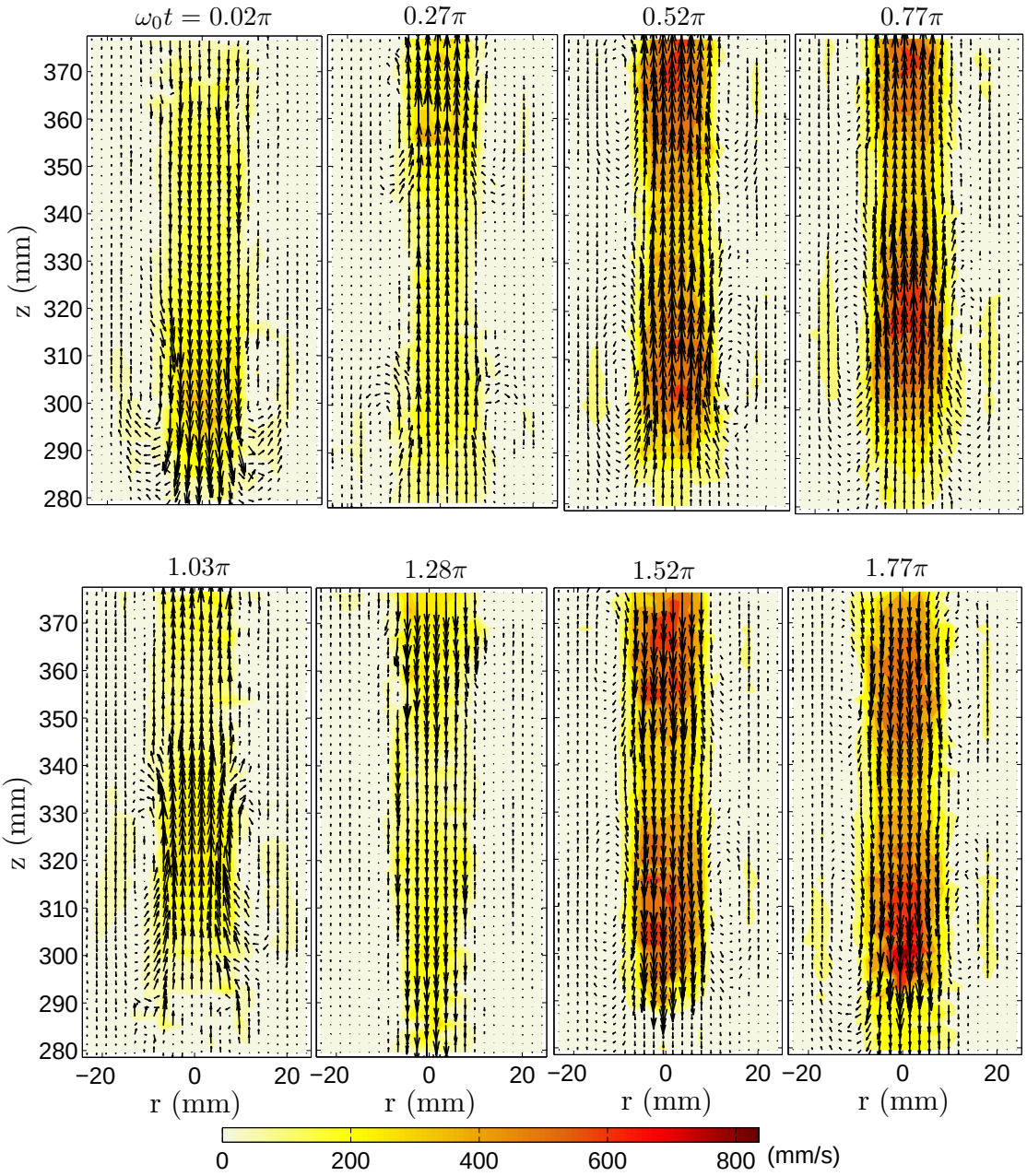

Figure 5.10: Velocity field of the secondary flow (see text for details) obtained at $\omega_0 = 31.4$ rad/s and $z_0 = 1.62$ mm, in *Reg. 4*. Eight different equispaced time phases are shown, covering a complete oscillation period. The colorbar corresponds to the velocity magnitude. The arrows (on a different scale in each panel) indicate the local direction and relative magnitude of the velocity field.

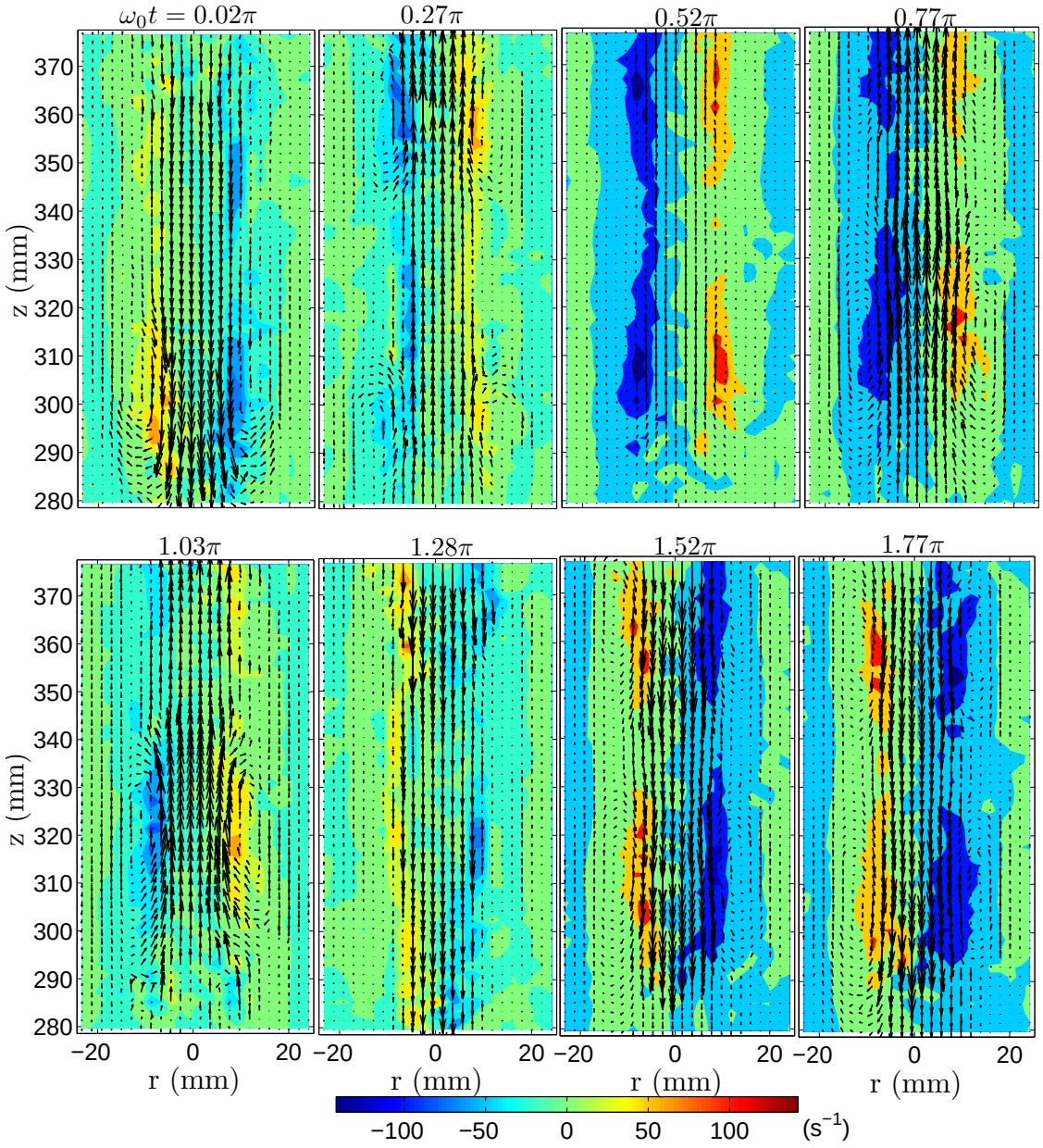

Figure 5.11: Vorticity field of the secondary flow (see text for details) obtained at $\omega_0 = 31.4$ rad/s and $z_0 = 1.62$ mm, in *Reg. 4*. Eight different equispaced time phases are shown, covering a complete oscillation period. The color bar corresponds to the vorticity field. The arrows (on a different scale in each panel) indicate the local direction and relative magnitude of the velocity field.

laminar flow, organized in several concentric layers, and isolates the secondary vortical flow.

As shown in Figs. 5.10 and 5.11, in the vortical flow regime the structure of the secondary fluid flow consists on pairs of counter-rotating elongated vortices that extend over approximately 50 mm along the axial direction. The largest values of the velocity field are found along the tube axis $|r| \lesssim 8$ mm. The vorticity field presents isolated domains of large vorticity values. Although the rescaled laminar flow has been subtracted, the largest values of the velocity and vorticity of the vortical secondary flow are more than two times larger than the values that would correspond to a laminar flow at the same driving amplitudes.

As in the laminar flow, both the velocity and vorticity fields follow the periodicity of the driving. After every half period the sign of both fields is reversed while the vortices keep counter-rotating. The two fields change sensibly within every half period, with the largest vorticity values found at the time intervals $\pi/2 \lesssim \omega_0 t \lesssim \pi$ and $3\pi/2 \lesssim \omega_0 t \lesssim 2\pi$. These two time intervals correspond to the acceleration phases of the piston (the phases when the modulus of the piston velocity increases in time).

From these observations we infer that the laminar flow is more likely to become unstable at the acceleration phases of the cycle, leading to a fully developed vortical flow at these lapses of time.

We can compare our results with early observations made by Hino et al. (1976) of the oscillatory pipe flow of a Newtonian fluid, discussed in Chap. 1. They also reported a temporal dependence of the fluid response: for disturbed laminar flows, only small amplitude perturbations appeared during the acceleration phases of the fluid. And conversely, for intermittently turbulent flows the turbulent bursts appeared in the deceleration phase of the cycle. It seems therefore that there exists an intrinsic similarity between the onset of weakly turbulent flows in Newtonian fluids and the onset of vortical flows in viscoelastic fluids, that favors the hydrodynamic instabilities to occur during particular time phases of the oscillatory cycle. This in spite of the fact that in Newtonian fluids the instabilities have their origin on fluid inertia ($Re \gtrsim 10^3$) while in viscoelastic fluids they are possibly triggered by fluid elasticity ($Re \simeq 0.3$, $Wi \simeq 4$).

5.3.4 Vortex properties

The vortices present an interesting spatio-temporal dynamics within one time period. Following the work of Jespersen et al. (2004) on the vortex dynamics around a solid ripple in oscillatory flow, we have defined a set of vortex properties that allows a quantitative characterization of the vortex dynamics: *vortex size*,

vortex intensity, and *vortex position*. We have computed these vortex properties for the secondary flow obtained by subtracting the oscillatory laminar base flow at corresponding time phases. We focus our analysis of the vortex dynamics on the central region of the tube (*Reg. 4*). The global spatio-temporal organization of the vortical flow in the whole tube length will be studied in Chap. 6.

Size of large vorticity regions. In order to quantify the extension of the regions with large vorticity values, we count the number of interrogation cells that present a vorticity above a threshold. Each interrogation cell has a size of 24×24 pixels, as explained in Sec. 2.2. We use a common threshold value of $w_{threshold} = 40\ \mathrm{s}^{-1}$, for all experiments performed at different driving amplitudes, that guarantees that most spurious fluctuations of the vorticity field are excluded from the count. The vortex size is rescaled by the total number of cells contained in the interrogation region, N_{reg}, so that the vortex size ranges from 0 to 1.

Vortex intensity. The vortex intensity is obtained by summing the absolute value of the vorticity of all the cells included in the regions with large vorticity values (i.e. above threshold):

$$I_{reg} = \frac{\sum_{i \in vortex} \omega_i}{N_{reg}}. \tag{5.5}$$

The vortex intensity is again rescaled by the total number of cells contained in the interrogation region.

Vortex position. In order to be able to locate the position of the vortices we define a center of vorticity, analogous to a center of mass, as

$$z_{cv} = \frac{\sum_{i \in vortex} \omega_i z_i}{\sum_{i \in vortex} \omega_i}, \tag{5.6}$$

and

$$r_{cv} = \frac{\sum_{i \in vortex} \omega_i r_i}{\sum_{i \in vortex} \omega_i}. \tag{5.7}$$

Since we are interested in identifying domains of strong vorticity, and disregard remaining spurious fluctuations of the vorticity around these domains, we define the center of vorticity only for regions with a local vortex intensity larger than a threshold value. We have verified that setting the threshold to the heuristic value $I_{threshold} = 2.0\ \mathrm{s}^{-1}$ most of the unwanted small vorticity domains are excluded. Again this same threshold value is used for experiments performed at different driving amplitudes.

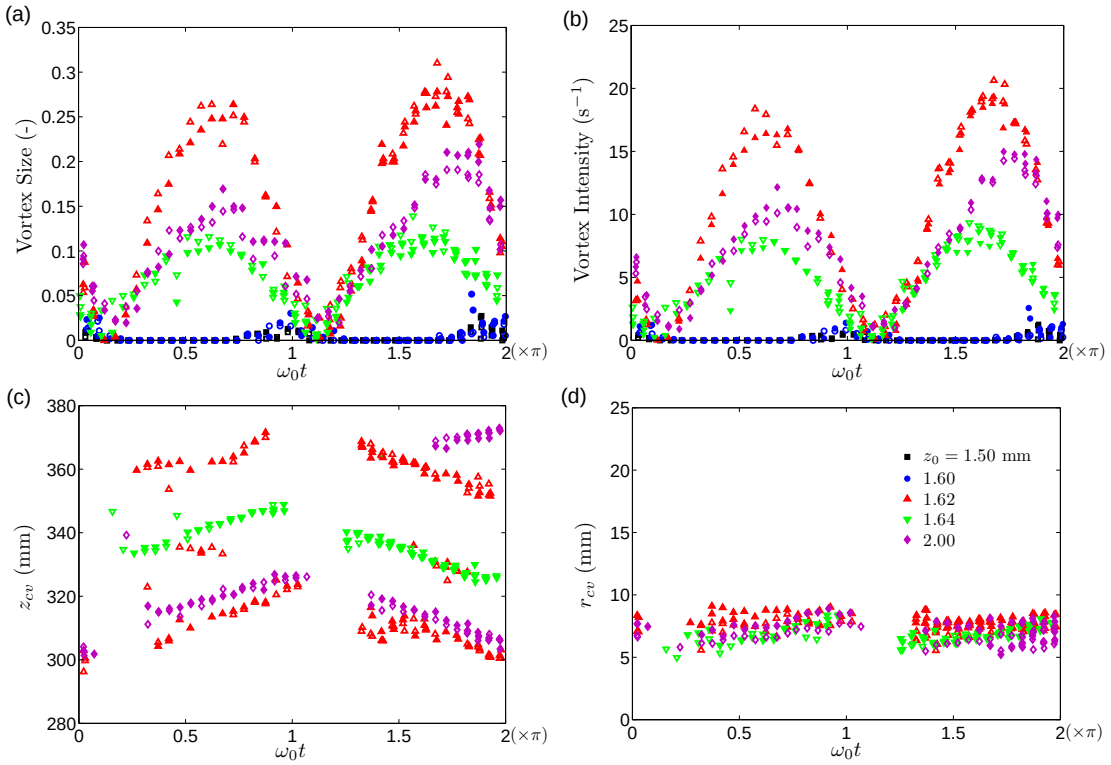

Figure 5.12: Vortex properties (vortex size (a), vortex intensity (b), vertical cv position (c), radial cv position (d)) computed for increasing driving amplitudes z_0 (*Reg. 4*). The color code is the same used in Fig. 5.3. Filled and empty symbols correspond to right and left sides of the tube axis, respectively.

Note that the center of vorticity does not coincide with the geometric center of the vortex (z_{center}, r_{center}), the point of zero velocity around which the fluid is rotating. In particular, the vertical location of the geometric center z_{center} fairly coincides with z_{cv} but r_{cv} is typically closer to the tube axis than the geometric center, r_{center}. These differences appear because, even though the laminar flow has been subtracted, the velocity reaches the largest magnitudes at the tube axis. Large velocity gradients generate large values of the local vorticity. Conversely, close to the geometric center the magnitude of the velocity and the velocity gradients are small, leading to a weak local vorticity. However, it is still more convenient to use the definition of the center of vorticity than the geometric center of the vortex because it is less sensitive to experimental noise and small flow distortions.

In axisymmetric flows the results obtained for the left and right side of the tube axis within the meridional plane should display a mirror-symmetry. We have considered both sides independently to check that the symmetry of the flow is indeed preserved, and to improve the statistics of the analysis.

As shown in Fig. 5.12 (z_0 = 1.50 mm and 1.60 mm) in the laminar regime

both vortex size and intensity are close to zero for most of the cycle. Only at the time phases where the velocity magnitude is largest ($\omega_0 t = 0$ and π) they show slightly non-zero values due to random fluctuations distributed all around the interrogation region that have remained even after the laminar base flow has been subtracted. Nevertheless, at these driving amplitudes no important isolated vorticity domains have been detected, and it is not possible to define the center of vorticity.

Vortex size and intensity in the vortical flow are periodic in time, with half the driving period. The largest values of size and intensity are found at time phases slightly shifted from $\omega_0 t \simeq \pi/2$ and $3\pi/2$. These same temporal trends were described for the radially averaged rms fluctuations. It is thus indubitable that the increase of the velocity fluctuations reflects the formation of local vorticity domains in the meridional plane of the tube, that we call *vortices*. The appearance of these vortices can also be observed in Fig. 5.11 where the vorticity field is depicted for an oscillation cycle. The presence of a temporal shift was also observed for the radially averaged rms fluctuations, and it was attributed to a latency time for generation of the vortices.

We can make connection with the flow structure observed in the laminar regime at the same driving frequency (Figs. 5.4, 5.8) to realize that precisely at the time phases $\omega_0 t = \pi/2$ and $3\pi/2$ the velocity magnitude is very small along the whole tube diameter and the quiescent points tend to rapidly move toward the tube axis. Therefore, it seems plausible to infer that from these time phases onwards the laminar flow is more likely to become unstable and induce the formation of the vortices. These time periods coincide with the time periods where largest values of the secondary vorticity field were observed ($\pi/2 \lesssim \omega_0 t \lesssim \pi$, $3\pi/2 \lesssim \omega_0 t \lesssim 2\pi$).

As the driving amplitude is ramped up, vortex size and intensity tend to decrease. At this point it is difficult to discern whether this effect is due to an actual decrease of the size of the regions with large vorticity values. The position of the vortices shifts slightly upward or downward in the interrogation region when the driving amplitude is modified (Fig. 5.12(c)). Since the vortex domains extend over approximately 50 mm in the vertical direction, their relative vertical position in the interrogation region (of size about 100 mm) may induce considerable changes in the vortical flow structure, and consequently in the computed vortex properties. For this reason a more comprehensive analysis of the vortex properties, including all seven vertical regions, will be addressed in Sec. 6.1.

In Fig. 5.12(c,d) the position of the center of vorticity (cv) is tracked along a complete period, for $z_0 > z_1^*$. The vortices are present at well defined time intervals, $\pi/4 \lesssim \omega_0 t \lesssim \pi$ and $5\pi/4 \lesssim \omega_0 t \lesssim 2\pi$, and vanish at the remaining lapses of time. The vertical motion displayed by the cv during an oscillation period is

similar at different z_0, although the precise vertical position of the cv does not coincide. The vortices move upward during the first half period, making a vertical translational displacement of about 20 mm, and go downward in the second half period, covering the same distance and recovering their initial vertical position after a complete period. Notice that the displacement is one order of magnitude larger than the amplitude of oscillation of the piston, z_0. The vertical position of the geometric center of the vortices, z_{center}, displays a temporal behavior analogous to z_{cv}, with upward/downward motion over a complete period.

The radial position of the cv remains constant around a fixed position, $r_{CV} = 8 \pm 3$ mm, and does not significantly change with z_0 for all explored driving amplitudes. This position coincides with the location of the peak observed for the time averaged rms fluctuations of u_r (Fig. 5.3(b)). The radial position of the geometric center of the vortices remains constant over a time period and does not change appreciably with z_0. It is placed at $r_{center} = 13 \pm 2$ mm, which is slightly further away from the tube axis than the radial position of the cv. We can make connection with the radial profile of the time averaged rms velocity fluctuations to realize that r_{center} corresponds to the minima of the rms fluctuations of u_z.

Finally, by comparing filled and empty symbols in Fig. 5.12, we check that the axial symmetry is preserved for the defined vortex properties at all driving amplitudes in the range $0.20 - 2.00$ mm. We can conclude that the vortical flow is indeed axisymmetric.

5.3.5 Large driving frequencies

We extend the study at local scale of the first hydrodynamic instability of the laminar oscillatory flow to larger driving frequencies. We have observed that the route from laminar to vortical flow exhibits qualitative differences as the characteristic timescale of the oscillatory driving increases. In analogy to the laminar flow, the structure of the vortical flow also becomes more complex at larger driving frequencies. We study the onset of the instability and the structure of the vortical flow at the following driving frequencies: $\omega_0 = 37.1$, 44.0, 56.5 rad/s.

First resonance frequency

We first focus on the driving frequency of the first resonance, $\omega_0 = 37.1$ rad/s ($De = 70.4$). At this resonant frequency the critical amplitude for the laminar flow to become unstable is $z^*_{1-up} = 1.25 \pm 0.05$ mm.

In Fig. 5.13 (a,b) we show the time averaged velocity fluctuations obtained when ramping up the driving amplitude. The dimensionless rms velocity fluctuations computed for this frequency show very similar features to those for $\omega_0 = 34.1$

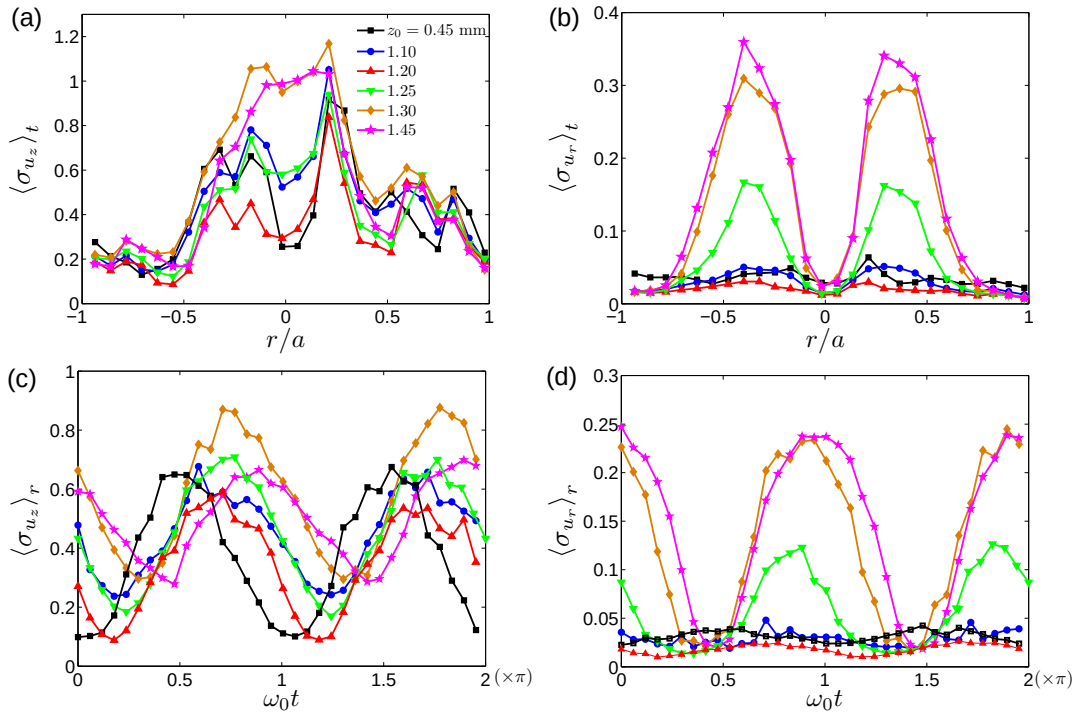

Figure 5.13: Time averaged (a,b) and spatially averaged (c,d) dimensionless rms fluctuations exhibited by the vertical and radial components of the velocity. Different symbols correspond to increasing driving amplitudes. The driving frequency is $\omega_0 = 37.1$ rad/s ($De = 70.4$).

rad/s. The time-averaged fluctuations of u_z and u_r increase very abruptly at z^*_{1-up}; the fluctuations of u_z display an M-shape within the laminar regime ($z_0 = 0.45$, 1.10, 1.20, 1.25 mm) and transition towards a bell-shape with two symmetric secondary peaks in the vortical flow ($z_0 = 1.30$, 1.45 mm); the fluctuations of u_r are nearly zero in the laminar regime but exhibit a neat M-shape in the vortical flow.

Regarding the temporal behavior, in Sec. 4.1 we found that resonant and non-resonant frequencies behaved very differently in the laminar regime: the velocity at the tube axis for the resonant frequencies was in phase (or in phase opposition) with the piston position, whereas for non-resonant frequencies velocity and piston position were in quadrature. We want to explore whether these temporal differences also manifest themselves in the vortical flow.

In Fig. 5.13(c,d) we show the velocity fluctuations averaged over the radial coordinate for $\omega_0 = 37.1$ rad/s. The fluctuations exhibit indeed a qualitative difference with respect to the results obtained at $\omega_0 = 34.1$ rad/s, that matches our expectations. The spatially-averaged fluctuations of u_z in the laminar flow are qualitatively similar to those measured at 34.1 rad/s but appear shifted by a time phase of about $\pi/2$ (their largest values are found now close to $\omega_0 t \simeq \pi/2, 3\pi/2,$

and their minima at $\omega_0 t \simeq 0, \pi$). As the instability threshold is crossed the amplitude of the fluctuations does not change significantly but the time phase shifts progressively up to about $\pi/2$. This shift of the time phase of the rms fluctuations by $\pi/2$when the vortical flow sets in is much more clear for the fluctuations of u_r. Whereas in the laminar regime they are nearly 0, above the critical driving amplitude they reach their largest value at $\omega_0 t = 0$ and π. At $\omega_0 t = \pi/2$ and $3\pi/2$ the fluctuations decrease and the vortices fade away.

Larger non-resonant frequencies

At driving frequencies moderately larger than the first resonant frequency, e.g. $\omega_0 = 44.0$ rad/s ($De = 83.5$), the laminar velocity profile is still very similar to the laminar profile obtained at $\omega_0 = 31.4$ rad/s and $\omega_0 = 37.1$ rad/s. It is formed by three concentric layers that oscillate with the periodicity of the driving (see Sec. 4.2, Figs. 4.16, 4.18).

Remarkably, however, a qualitatively different route from laminar to vortical flow has been observed at $\omega_0 = 44.0$ rad/s. At this frequency, the critical amplitude at which the laminar flow becomes unstable is $z^*_{1-up} = 2.6 \pm 0.1$ mm. The destabilization of the laminar regime is particularly difficult to follow experimentally because the translational vertical symmetry and the axial symmetry are broken almost at the same critical driving amplitude. This is shown in the Pipkin diagram of Fig. 5.1.

The main new features of the rms velocity fluctuations measured at $\omega_0 = 44.0$ rad/s lie on the time-averaged fluctuations of u_r (Fig. 5.14(b)). They do not show the M-shape observed at $\omega_0 = 31.4$ rad/s. Instead, a prominent peak appears at the tube axis as the unstable flow sets in. This abrupt increase of the fluctuations at the symmetry axis accounts for the early breakage of the axial symmetry at $z^*_{2-up} = 2.7$ mm. Thus at this driving frequency the fluid flow loses the vertical translational and axial symmetry almost at a the same critical amplitude ($z^*_{1-up} \simeq z^*_{2-up}$). Only for $z_0 = 2.6$ mm large fluctuations are observed for u_z but not yet for u_r.

The radially-averaged fluctuations of u_z (Fig. 5.14(c)) show a complicated temporal dependence in the unstable flow, with no prevailing periodicity. The corresponding fluctuations of u_r are largest at $\omega_0 t \simeq \pi/2$ and $3\pi/2$, similarly to the results reported for the lower non-resonant frequency $\omega_0 = 31.4$ rad/s.

We finally study an even larger non-resonant frequency, $\omega_0 = 56.5$ rad/s ($De = 107.4$). This particular driving frequency is analogous to the frequency $\omega_0 = 31.4$ rad/s that we have studied in great detail in Sec. 5.3.1, in the sense that it is slightly smaller than a resonant frequency (in this case the second resonant

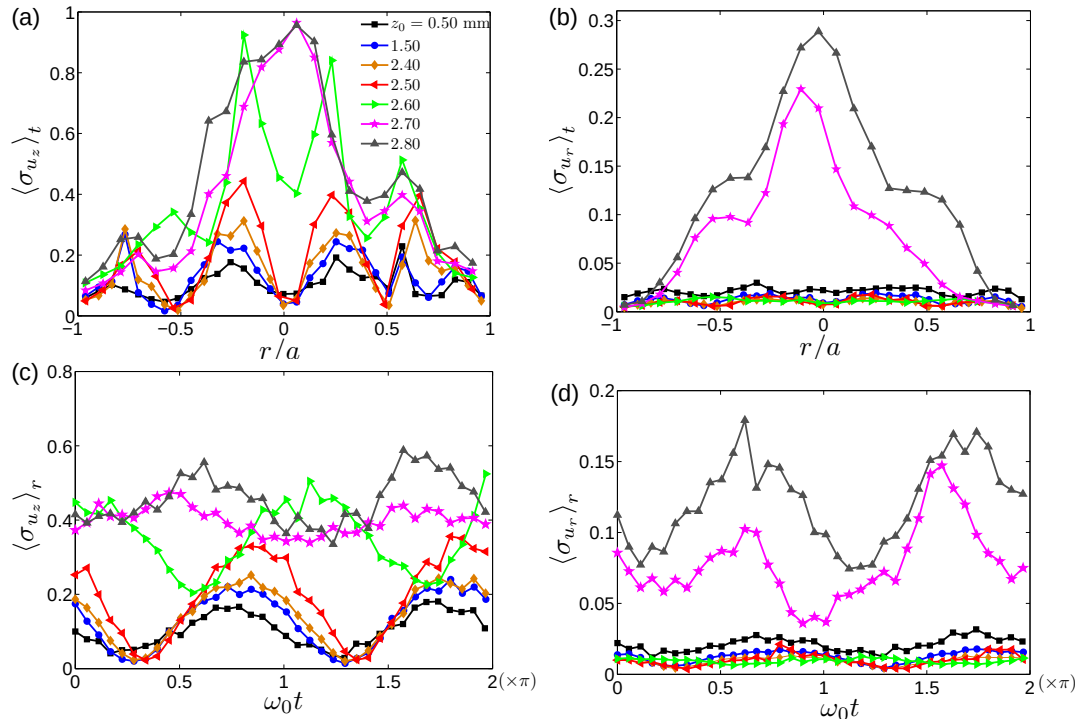

Figure 5.14: Time averaged (a,b) and spatially averaged (c,d) dimensionless rms fluctuations exhibited by the vertical and radial components of the velocity. Different symbols correspond to increasing driving amplitudes. The driving frequency is $\omega_0 = 44.0$ rad/s ($De = 83.5$).

frequency). The study of the flow behavior at this driving frequency will help in elucidating the influence that the structure of the laminar flow has on the spatio-temporal dynamics of the vortical flow.

The laminar velocity profile at $\omega_0 = 56.5$ rad/s consists of five concentric layers (Fig. 4.18). The time-averaged rms velocity fluctuations in the laminar flow, shown in Fig. 5.15(a,b), exhibit a qualitatively similar radial dependence with four symmetric peaks. Despite this additional spatial complexity, the overall trends of the velocity fluctuations at this frequency are comparable to those observed at $\omega_0 = 31.4$ rad/s. In particular, as the driving amplitude is ramped up the time-averaged fluctuations show an abrupt increase, now at $z^*_{1-up} = 0.7 \pm 0.1$ mm. In the vortical flow, the fluctuations of u_z display a central peak with two additional smaller symmetric elbows found at $r/a = \pm 0.5$ and ± 0.75. The fluctuations of u_r exhibit a symmetric double peak with acute minima at the axis and at $r/a = \pm 0.40$. This structure reveals the formation of two toroidal vortices (or two symmetric pairs of vortices if measured in the meridional plane of the tube). We can tell from the magnitude of the time-averaged fluctuations that the inner pair of vortices is more intense. The temporal dependence of the fluctuations displays

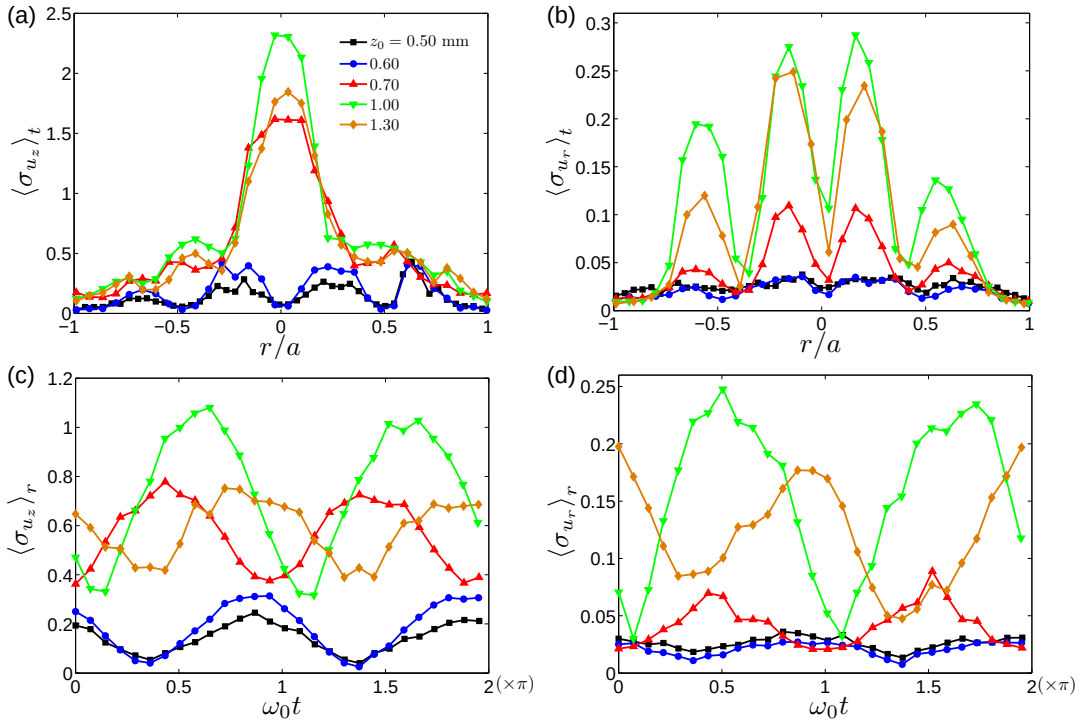

Figure 5.15: Time averaged (a,b) and spatially averaged (c,d) dimensionless rms fluctuations exhibited by the vertical and radial components of the velocity. Different symbols correspond to increasing driving amplitudes. The driving frequency is $\omega_0 = 56.5$ rad/s ($De = 107$).

also similar trends to those observed at $\omega_0 = 31.4$ rad/s. The largest fluctuations of u_z and u_r in the vortical flow occur at $\omega_0 t \lesssim \pi/2$ and $3\pi/2$.

Figures 5.16 and 5.17 show the velocity and vorticity fields of the oscillatory vortical flow at $\omega_0 = 56.5$ rad/s and $z_0 = 1.30$ mm (vortical flow), for a complete time period. And in Fig. 5.18 we depict the corresponding vortex properties for this same driving amplitude. Vortex size and intensity (panels (a,b)) follow the periodicity of the driving and exhibit comparable temporal trends as described for $\omega_0 t = 31.4$ rad/s (Fig. 5.12). From panels (c), (d) we observe that, regarding the radial location of the two vortices on each side of the axis, they remain nearly fixed at radial positions $r_{cv} \simeq 4$ and 15 mm. Around $\omega_0 t \simeq \pi$, 2π the outer vortices vanish and the inner ones move slightly outward. Regarding their vertical position, the two vortices on each side keep moving up and down, following a complex temporal evolution.

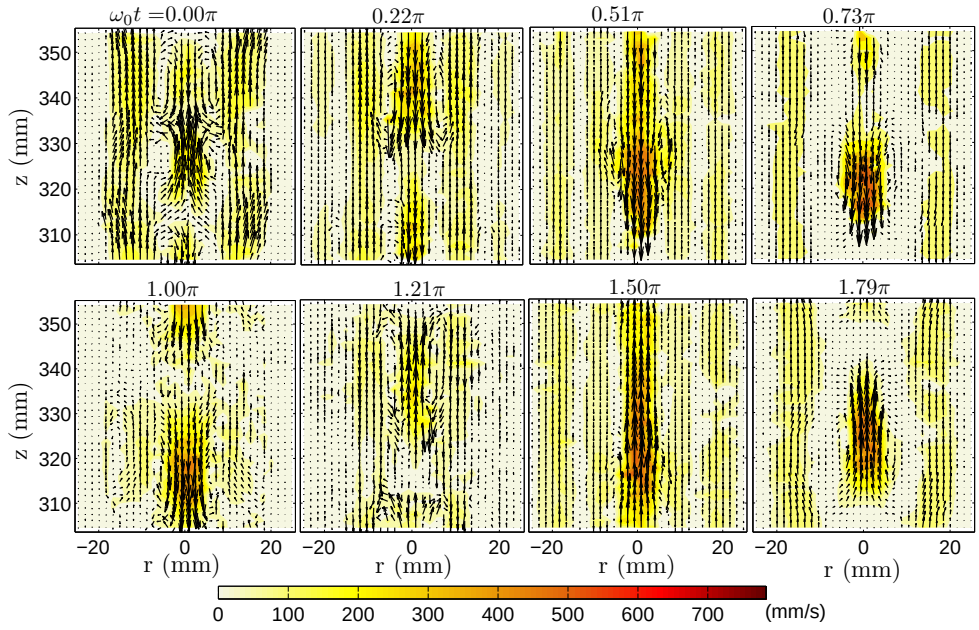

Figure 5.16: Velocity field obtained at $\omega_0 = 56.5$ rad/s and $z_0 = 1.30$ mm, in *Reg. 4*. Eight different equispaced time phases are shown, covering a complete oscillation period. The colorbar corresponds to the magnitude of the velocity. The arrows (on a different scale in each panel) indicate the direction and relative magnitude of the velocity field.

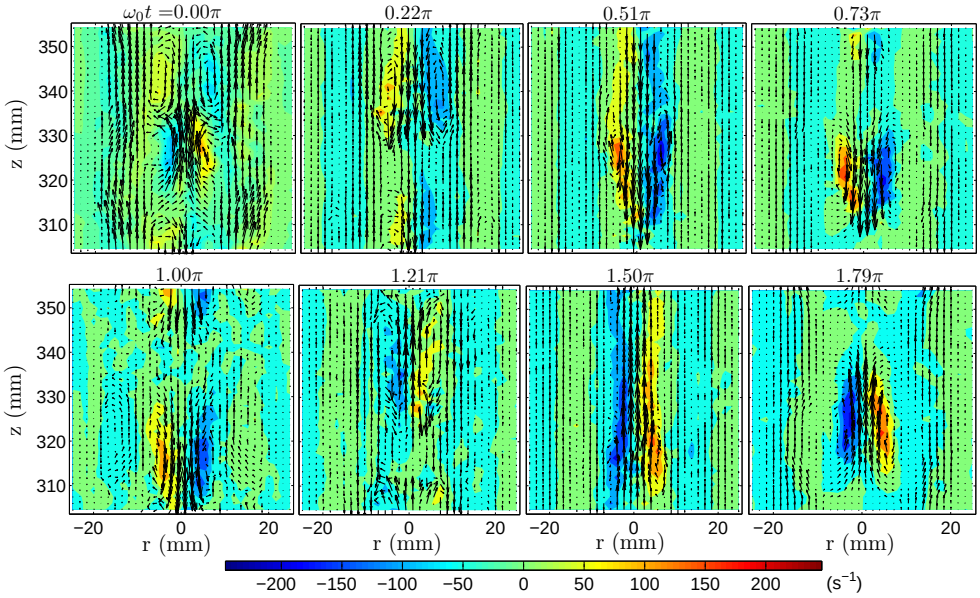

Figure 5.17: Vorticity field obtained at $\omega_0 = 56.5$ rad/s and $z_0 = 1.30$ mm, in *Reg. 4*. Eight different equispaced time phases are shown, covering a complete oscillation period. The colorbar corresponds to the vorticity. The arrows (on a different scale in each panel) indicate the direction and relative magnitude of the velocity field.

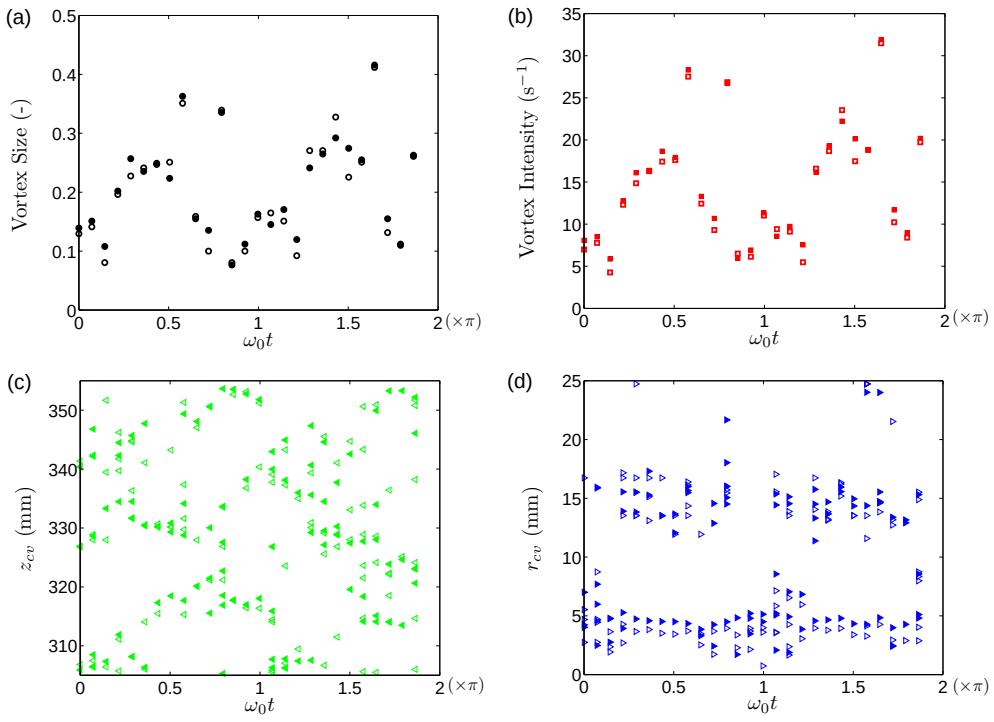

Figure 5.18: Vortex properties (vortex size (a), vortex intensity (b), vertical cv position (c), radial cv position (d)) computed for $\omega_0 = 56.5$ rad/s and $z_0 = 1.30$ mm (*Reg. 4*). Filled and empty symbols correspond to right and left sides of the tube axis, respectively.

5.4 Second instability: loss of axial symmetry

This section is devoted to the study of the transition from axisymmetric to non-axisymmetric vortical flows. We use the statistical methods described in Sec. 5.3 to identify the threshold for the onset of this second instability and to characterize the structure of the resulting secondary flow. We focus the analysis again on the central region of the cylinder (*Reg. 4*) and the particular driving frequency $\omega_0 = 31.4$ rad/s.

5.4.1 Onset of the non-axisymmetric vortical flow

The onset of the second instability can be identified by analysing the shape of the rms velocity fluctuations. In Fig. 5.19 we show the fluctuations measured at increasing driving amplitudes, $z_0 > z_1^*$, for the two components of the velocity, averaged in time (top panels) and over the radial coordinate (bottom panels). The radial profile of the time-averaged fluctuations of both u_z and u_r systematically decreases as the driving amplitude is ramped up beyond $z_0 = 2.00$ mm. The symmetric bell shape and the M-shape with a marked minima at the tube axis

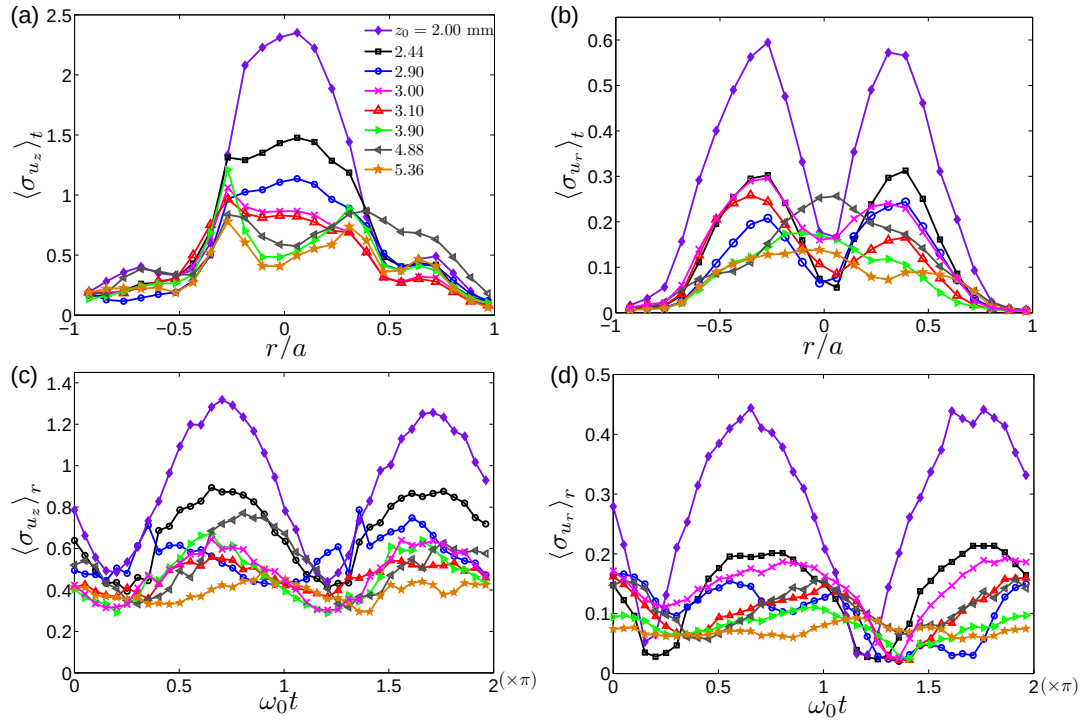

Figure 5.19: Time averaged (a,b) and spatially averaged (c,d) dimensionless rms fluctuations exhibited by the vertical and radial components of the velocity. Different symbols correspond to increasing driving amplitudes ($z_0 \leq 2.00$ mm). The frequency is kept constant at $\omega_0 = 31.4$ rad/s ($De = 59.7$).

observed, respectively, for the fluctuations of u_z and u_r in the vortical flow, are both preserved up to $z^*_{up-2} = 3.10 \pm 0.10$ mm. Above this critical amplitude the u_z fluctuations lose their axial symmetry and peak a bit to the left side of the tube. Simultaneously, the fluctuations of u_r loose the M-shape and increase at the tube axis. Thus, above this driving amplitude the axisymmetric vortical flow gets distorted and evolves towards a complex non-axisymmetric vortical flow, that is described in detail in Sec. 5.4.2.

Regarding the spatially averaged rms fluctuations, the well-defined temporal periodicity exhibited by the fluctuations in the axisymmetric vortical flow progressively vanishes as the driving amplitude is increased above 2.00 mm. Once the non-axisymmetric vortical flow sets in, the rms fluctuations of both u_z and u_r become featureless and follow with difficulty the periodicity of the driving.

Hysteresis

By ramping down the driving amplitude, we have found that this second hydrodynamic instability also presents hysteresis. At this particular frequency and in-

terrogation region the hysteresis in z_0 is $H = 0.35 \pm 0.10$ mm. Again, the presence of hysteresis implies that the transition from axisymmetric to non-axisymmetric vortical flow is also subcritical.

The hysteretic region observed for this second hydrodynamic instability for all the explored range of driving frequencies is depicted, in green, in Fig. 5.6. Note that the amount of hysteresis measured for this second instability is typically much larger than the hysteresis determined for the first instability. No clear trends are observed in terms of the driving frequency (or De).

5.4.2 Local structure of the non-axisymmetric vortical flow

Although the spatial organization of the flow is much more complex in the non-axisymmetric vortical regime, the flow still follows the periodicity of the applied driving. In Figs. 5.20 to 5.25 we show the velocity and vorticity fields, and the velocity divergence, in a complete period measured at $z_0 = 3.10$ and 4.88 mm and at $\omega_0 = 31.4$ rad/s.

As shown in Figs. 5.20, 5.21 the onset of vortical flow distortions occurs at time phases close to $\omega_0 t \simeq \pi/4$ and $5\pi/4$. At $z_0 = 3.10$ mm the vortices are still symmetric and resemble the structure of the vortices observed in the vortical flow regime. However at time phases close to $\omega_0 t = \pi/4$ and $5\pi/4$ the velocity field looses the axial symmetry. In particular some velocity vectors cross the symmetry axis, moving toward a preferred direction. Note that, although the rescaled laminar flow has been subtracted, the values of the velocity magnitude and vorticity (color bars) have considerably increased with respect to those of the axisymmetric vortical flow.

At $z_0 = 4.88$ mm the axial symmetry is perpetually broken. As shown in Figs. 5.23, 5.24, the velocity and vorticity fields show a clear asymmetry with respect to the tube axis. Remarkably, the periodicity is still preserved in average.

We have computed the divergence of the in-plane components of the velocity field, $\boldsymbol{\nabla}_{\parallel} \cdot \boldsymbol{u}$, to detect the possible existence of an out-of-plane component of the velocity, u_θ. At the onset of the non-axisymmetric vortical flow, the divergence field is still fairly isotropic (Fig. 5.22). However, the typical values of the divergence are considerably larger here than for the axisymmetric vortical flow, where they were generally below 100 s^{-1}. When the flow is non-axisymmetric over the complete oscillation period $\boldsymbol{\nabla}_{\parallel} \cdot \boldsymbol{u}$ (Fig. 5.25) exhibits some heterogeneities that reveal the presence of a non negligible u_θ in some parts of the interrogation region.

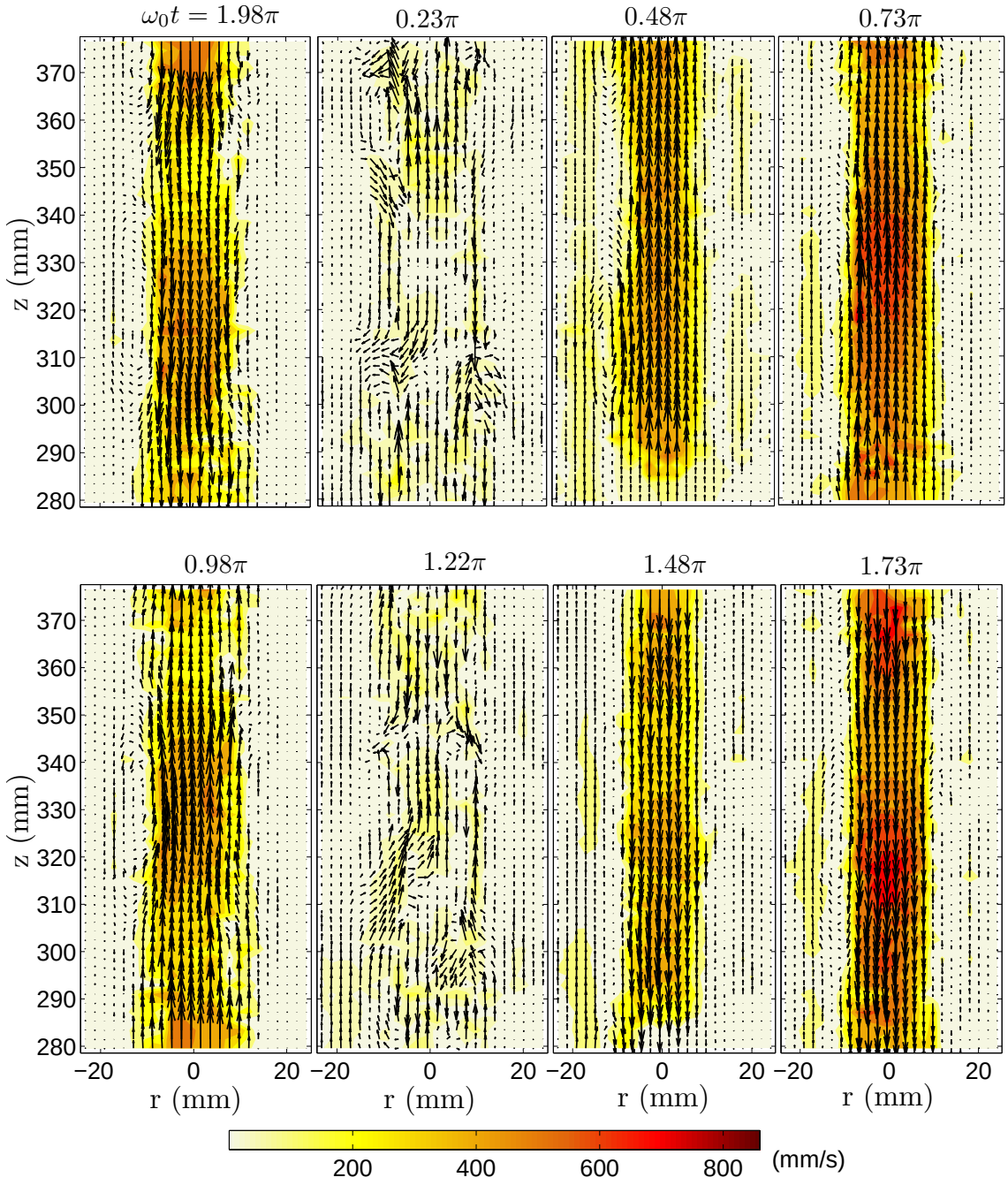

Figure 5.20: Velocity field obtained at $\omega_0 = 31.4$ rad/s and $z_0 = 3.10$ mm, in *Reg. 4*. Eight different equispaced time phases are shown, covering a complete oscillation period. The colorbar corresponds to the velocity magnitude. The arrows (on a different scale in each panel) indicate the direction and relative magnitude of the velocity field.

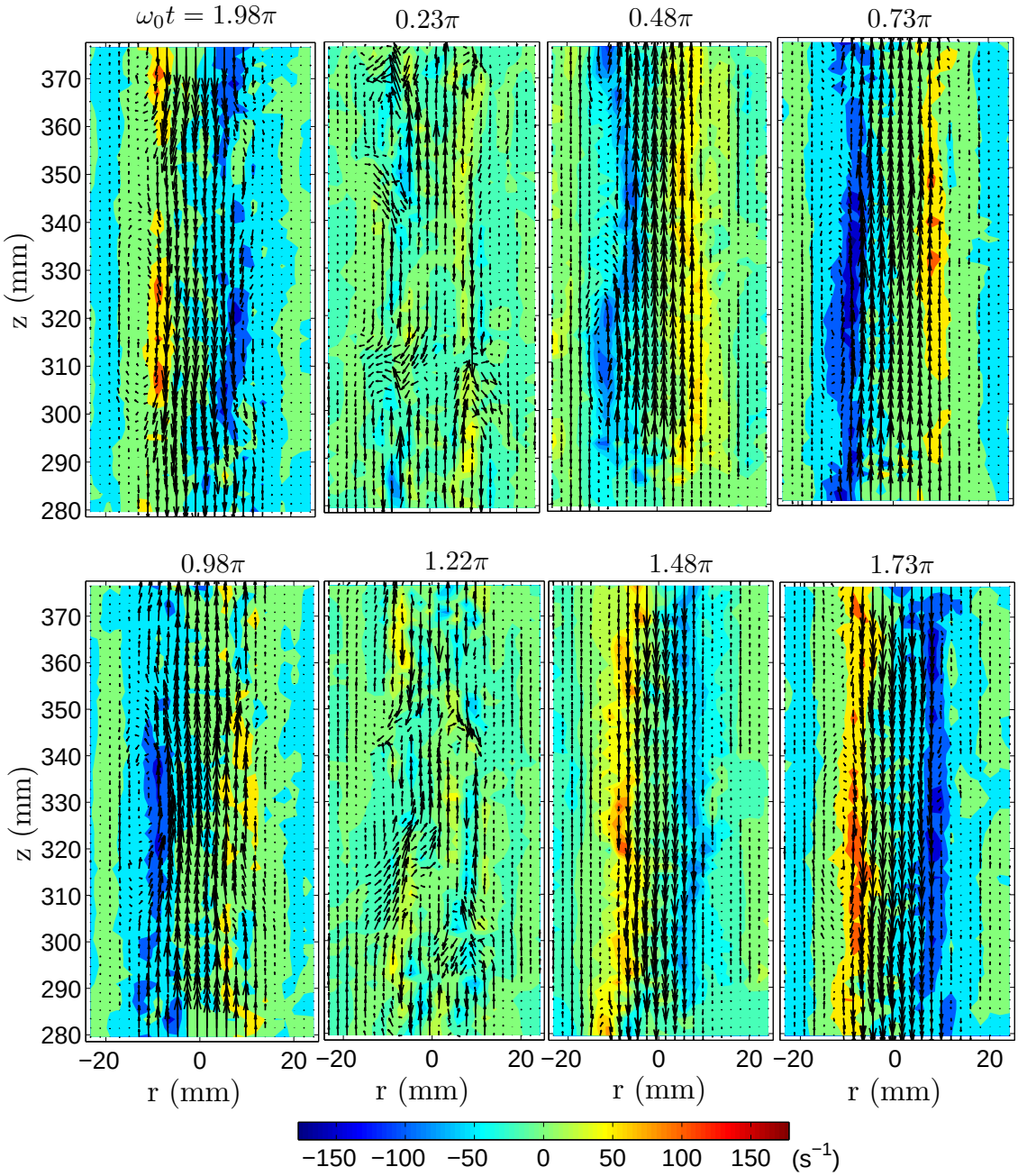

Figure 5.21: Vorticity field obtained at $\omega_0 = 31.4$ rad/s and $z_0 = 3.10$ mm, in *Reg. 4*. Eight different equispaced time phases are shown, covering a complete oscillation period. The colorbar corresponds to the vorticity field. The arrows (on a different scale in each panel) indicate the direction and relative magnitude of the velocity field.

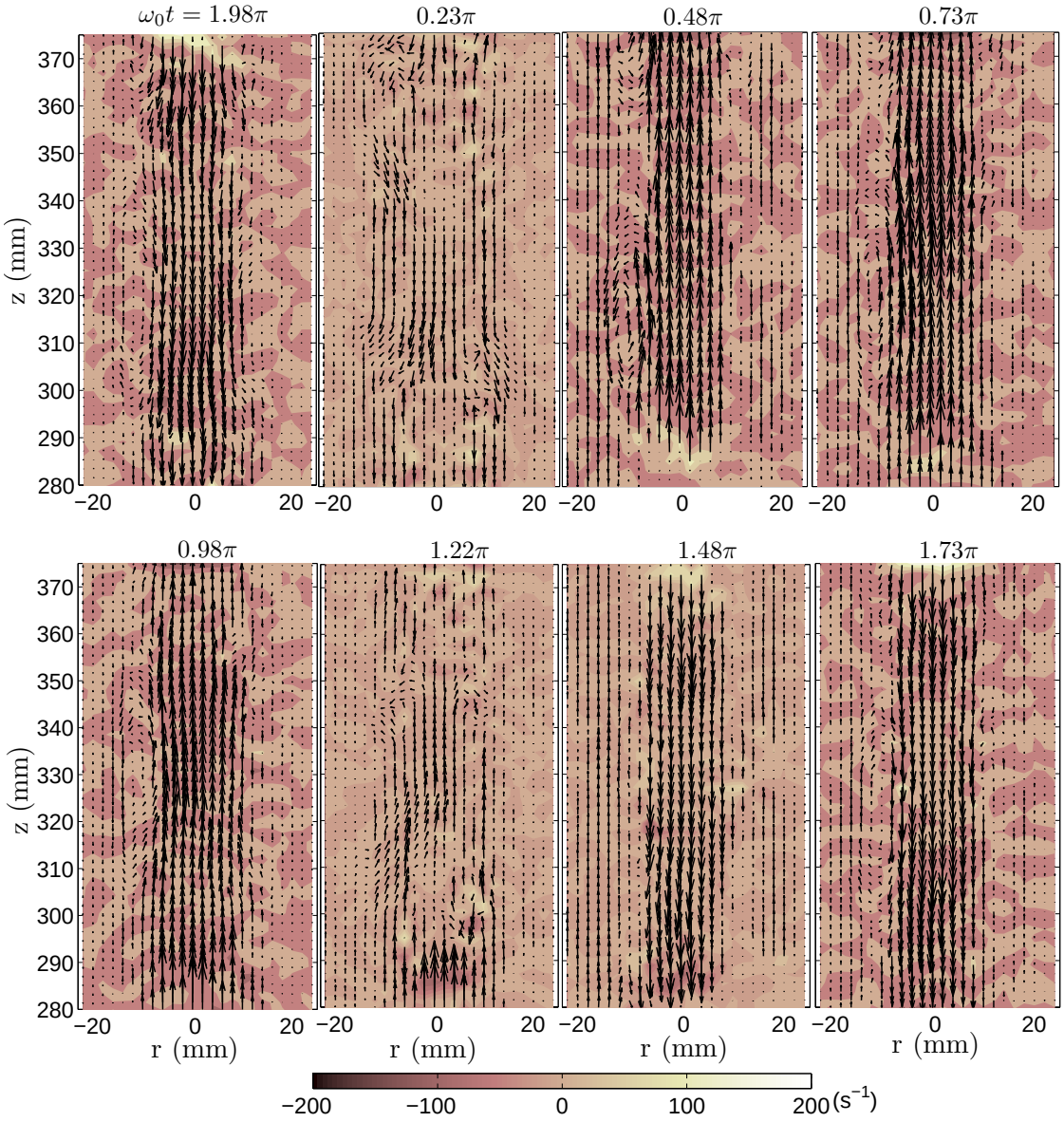

Figure 5.22: Divergence field obtained at $\omega_0 = 31.4$ rad/s and $z_0 = 3.10$ mm, in *Reg. 4*. Eight different equispaced time phases are shown, covering a complete oscillation period. The colorbar corresponds to the divergence field. The arrows (on a different scale in each panel) indicate the direction and relative magnitude of the velocity field.

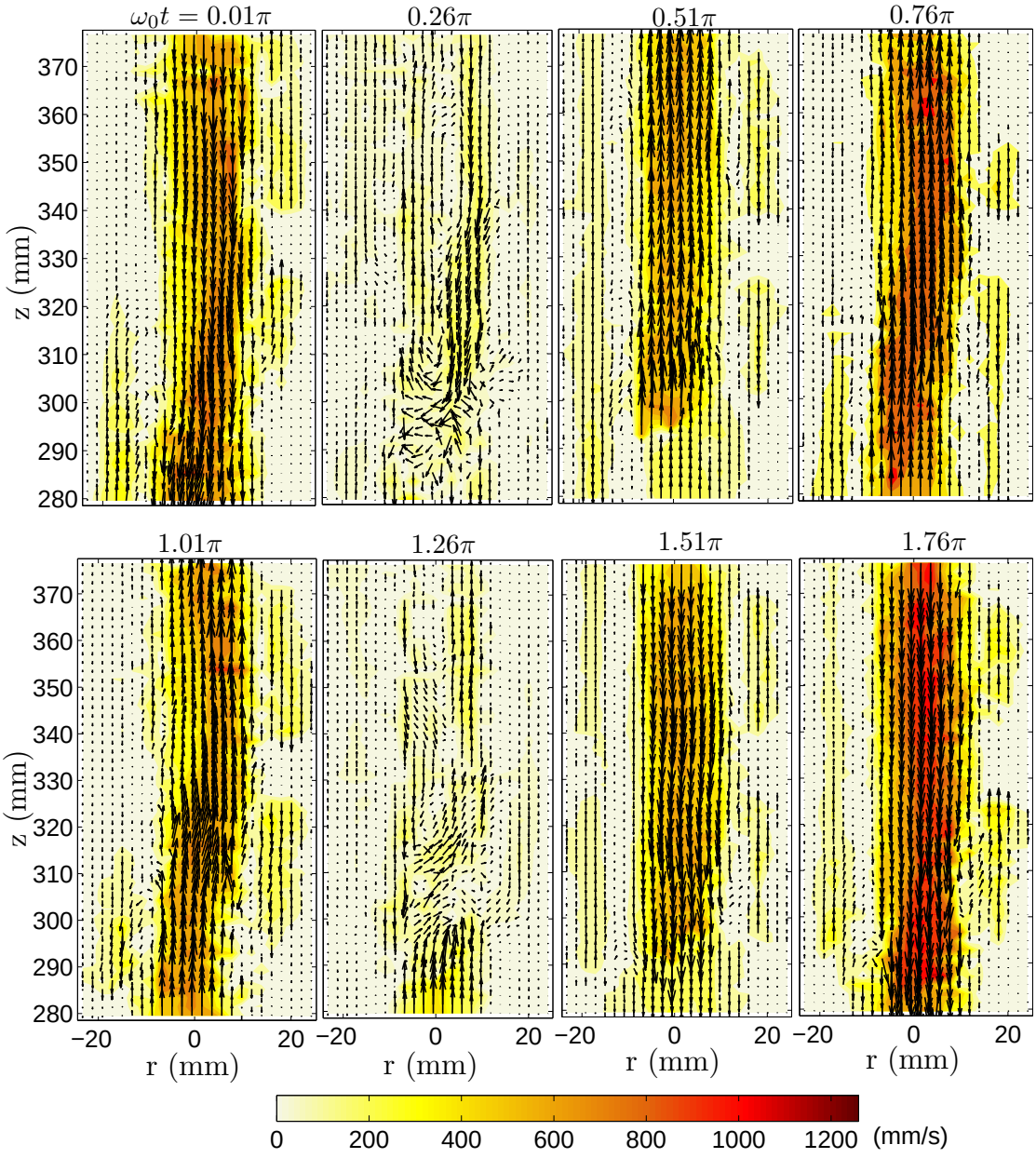

Figure 5.23: Velocity field obtained at $\omega_0 = 31.4$ rad/s and $z_0 = 4.88$ mm, in *Reg. 4*. Eight different equispaced time phases are shown, covering a complete oscillation period. The colorbar corresponds to the velocity magnitude. The arrows (on a different scale in each panel) indicate the direction and relative magnitude of the velocity field.

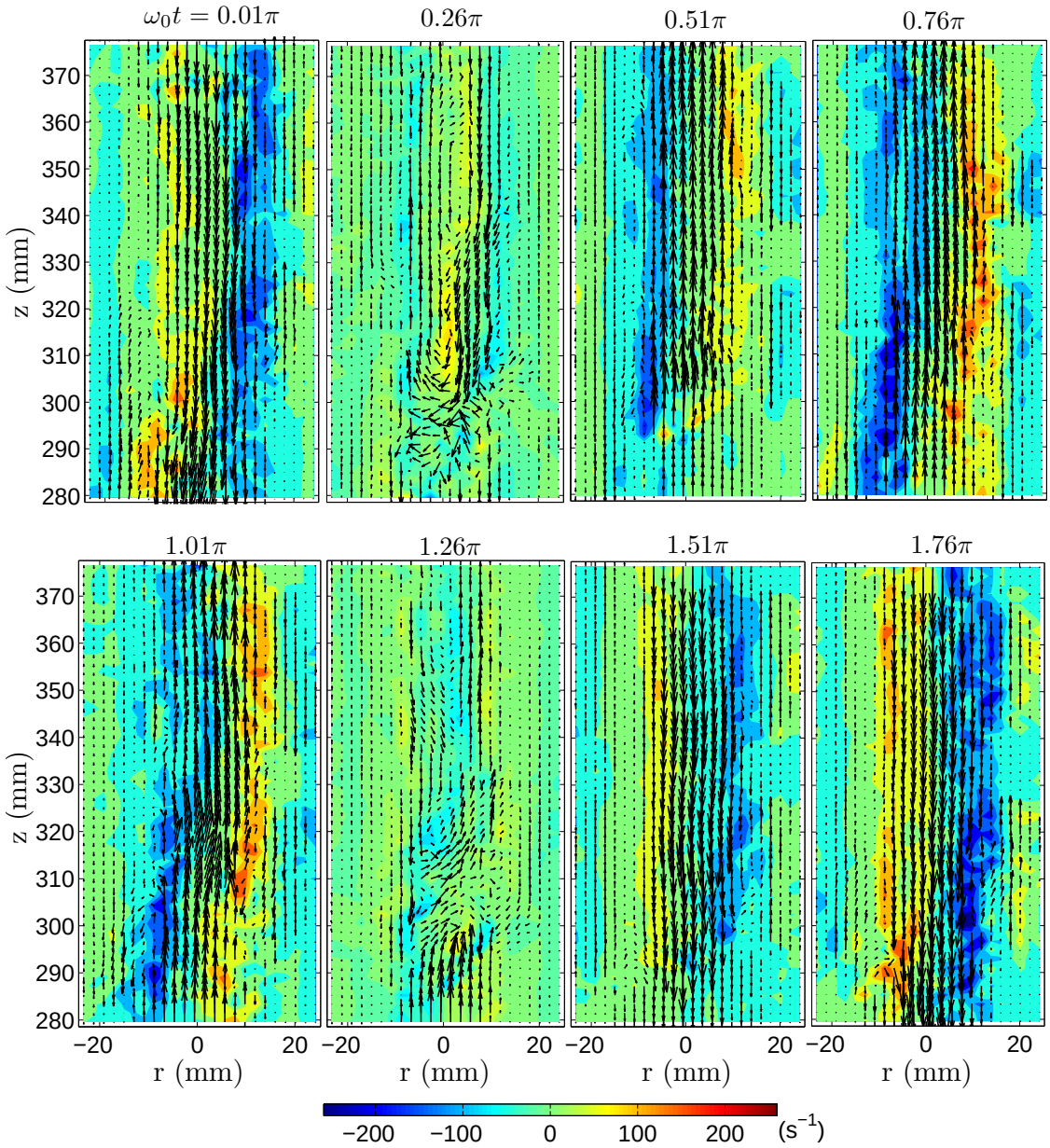

Figure 5.24: Vorticity field obtained at $\omega_0 = 31.4$ rad/s and $z_0 = 4.88$ mm, in *Reg. 4*. Eight different equispaced time phases are shown, covering a complete oscillation period. The colorbar corresponds to the vorticity field. The arrows (on a different scale in each panel) indicate the direction and relative magnitude of the velocity field.

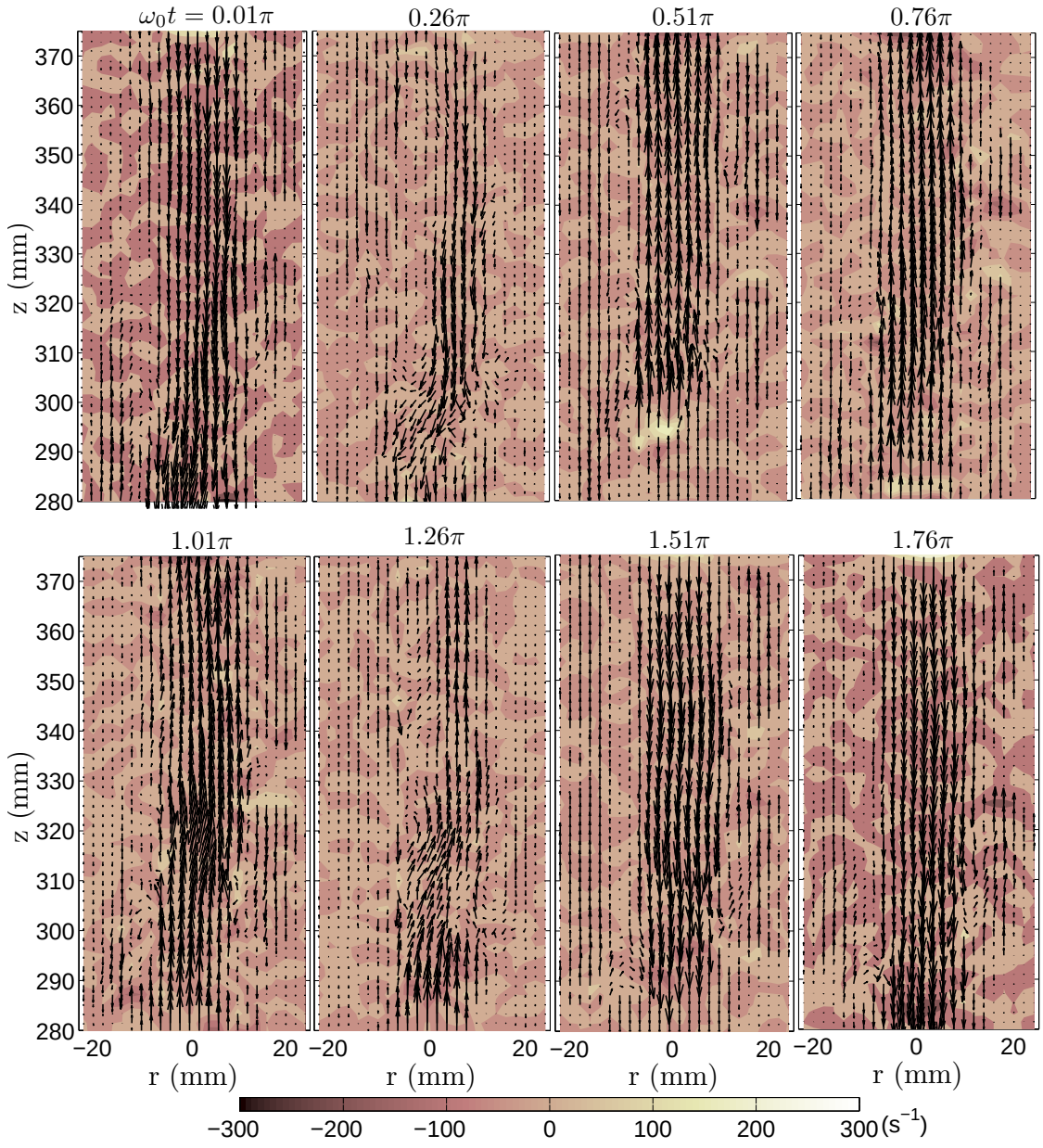

Figure 5.25: Divergence field obtained at $\omega_0 = 31.4$ rad/s and $z_0 = 4.88$ mm, in *Reg. 4*. Eight different equispaced time phases are shown, covering a complete oscillation period. The colorbar corresponds to the divergence field. The arrows (on a different scale in each panel) indicate the direction and relative magnitude of the velocity field.

Chapter 6

Large scale spatio-temporal flow organization and instability mechanisms

In the previous chapter the transition from laminar to more complex flows was analyzed at the central region of the tube. The critical amplitudes for the onset of the axisymmetric and non-axisymmetric vortical flows were determined in the whole range of applied forcing frequencies, and the spatio-temporal flow structure in this particular region was characterized for some particular frequencies. However, the fluid flow also presents a large scale spatio-temporal organization, which is studied in the present chapter.

In Sec. 6.1 we study the organization of the flow and its dynamics on short time scales (of the order of a few oscillation periods) in seven different regions of the tube covering the whole tube length.

A slow temporal evolution of the flow behavior at long time scales (much longer than the relaxation time of the fluid) has also been detected, specially in tube regions close to the driving piston. A characterization of the flow dynamics at long time scales in two different tube regions is addressed in Sec. 6.2.

Finally in Sec. 6.3 we discuss about possible mechanisms responsible for the onset of the observed hydrodynamic instabilities.

6.1 Spatial organization of the flow over the tube length on short time scales

As described in Sec. 4.2, the laminar flow is invariant along the vertical coordinate, except for the vicinity of the top and bottom ends. It thus suffices to analyze

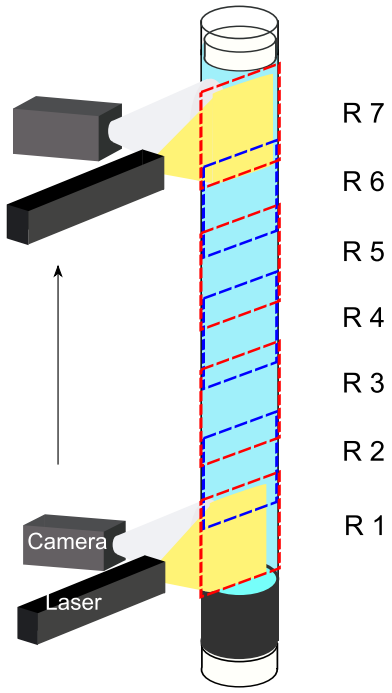

Figure 6.1: Sketch of the seven different regions chosen to characterize the velocity field over the entire tube length.

the flow organization in a fixed central tube region. However, in more complex flows the vertical translational invariance is not preserved. Therefore, it is convenient to measure the velocity field over the whole tube length to get a complete characterization of the flow.

6.1.1 Vertical reconstruction of the flow

In order to experimentally measure the fluid velocity in the entire tube, we first added a divergent lens in the laser path (Sec. 2.2) to make the interrogation region of the largest possible size, 10×5 cm^2. Next, as shown in Fig. 6.1, the tube length was virtually divided in seven regions (*Region 1* was located at the bottom end of the tube and *Region 7* at the top) of 100 mm length each, with an overlap of about 25 mm between consecutive regions. Using this method we could cover most of the tube length, 85 mm from the bottom piston and up to 555 mm (5 mm from the top lid). The region next to the driving piston ($z < 85$ mm) was not accessible with the camera and could not be characterized. A detailed study of the oscillatory flow in this region, addressed in Sec. 6.3.1, was possible thanks to a modification of the original piston. The velocity field in each region was measured independently. We made sure that the flow history was identical in equivalent experiments (Sec. 5.2), so that quantitative comparison between measurements in

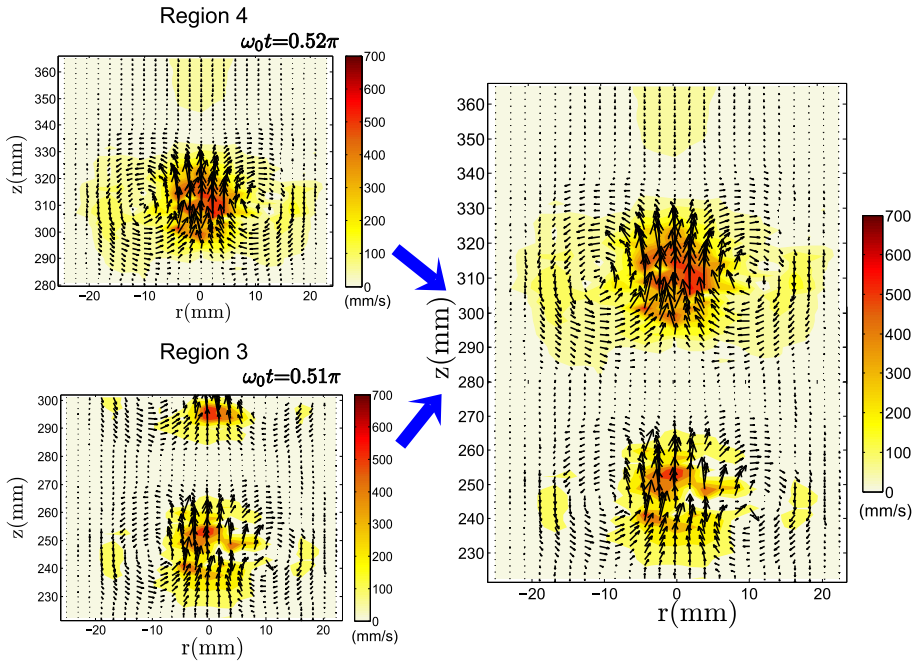

Figure 6.2: Reconstructed velocity field ($\omega_0 = 31.4$ rad/s, $z_0 = 1.66$ mm) obtained by matching regions 3 and 4, at a common time phase $\omega_0 t \simeq 0.51\pi$.

different regions was meaningful.

In the post-processing of the images the entire velocity field was reconstructed by spatially matching consecutive regions obtained at equivalent time phases. Occasionally, in order to improve the continuity of the velocity field between consecutive regions, a small spatial shift (±5 mm) was allowed in the matching process. In Fig. 6.2 we show an example of the reconstructed velocity field obtained by joining *Regs. 3* and *4*. However, this reconstruction process has been found particularly challenging at large driving amplitudes and specially in the regions close to the bottom piston. In these particular cases there is a remarkable lack of continuity of the velocity field between images in adjacent regions. It cannot be eliminated even by allowing a small spatial shift. Possible reasons for these difficulties are discussed in Sec. 6.2.

6.1.2 Shift of the onset of the instability

An analysis of the flow structure over the entire tube length reveals that close to the bottom piston the laminar flow becomes unstable at considerably smaller driving amplitudes than in other regions. We have determined the critical driving amplitude, z^*_{1-up}, at $\omega_0 = 31.4$ rad/s in all seven regions. It is clear from Fig. 6.3

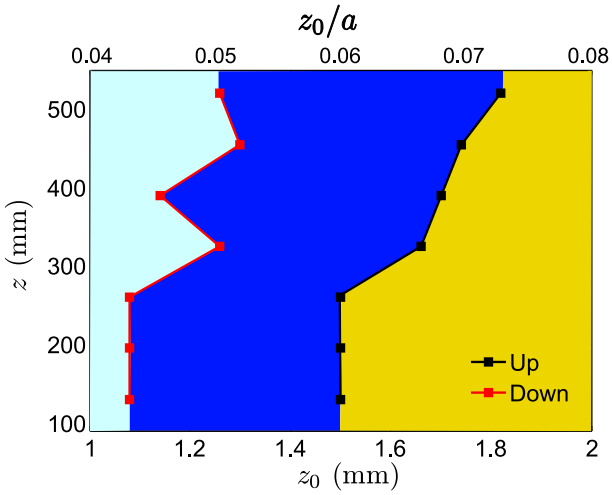

Figure 6.3: Stability phase diagram obtained for all seven regions at $\omega_0 = 31.4$ rad/s. The laminar base flow is represented in pale blue, the axisymmetric vortical flow in orange and the hysteretic region in dark blue.

that there is indeed a systematic shift of the critical amplitude as we move away from the driving piston. The lowest critical amplitude is obtained in *Reg. 1, 2, 3*, for which $z^*_{1-up} = 1.50 \pm 0.02$ mm. At this driving amplitude the flow is vortical in these bottom regions, but remains laminar in the upper regions (*Reg. 4, 5, 6, 7*). At the larger amplitude $z_0 = 1.62 \pm 0.02$ mm the vortical flow expands up to *Reg. 4* (in agreement with the results described in Sec. 5.3), while the flow in upper regions remains laminar. The fluid flow is vortical over the whole tube only above $z_0 = 1.80 \pm 0.02$ mm.

Figures 6.4, 6.5 and 6.6 exemplify this progressive onset of the instability. The figures show the velocity and vorticity fields obtained at a meridional plane of the tube at $z_0 = 1.40$, $z_0 = 1.66$, and $z_0 = 1.82$ mm, and two given time phases, $\omega_0 t = \pi$ and $3\pi/2$. In the laminar regime the reconstruction of the velocity and vorticity fields between consecutives regions is satisfactory. Vertical translational invariance is verified. Only a small recirculation zone of about 20 mm height is detected next to the top end of the tube, at the time phase $\omega_0 t = \pi$ corresponding to the largest velocity magnitudes in the oscillation (the extent of the fluid recirculation zone next to the bottom piston will be determined in Sec. 6.3.1).

At larger amplitudes ($z_0 = 1.66$ and 1.82 mm), the matching process for the secondary flow between interrogation regions works well in most cases. However, note that some particular regions have needed a slight vertical shift upwards or downwards in order to improve the agreement. We have distinguished them with a dashed line contour. Unfortunately in particular regions, specially close to the bottom piston, the match is not feasible. This is marked in red in the figures.

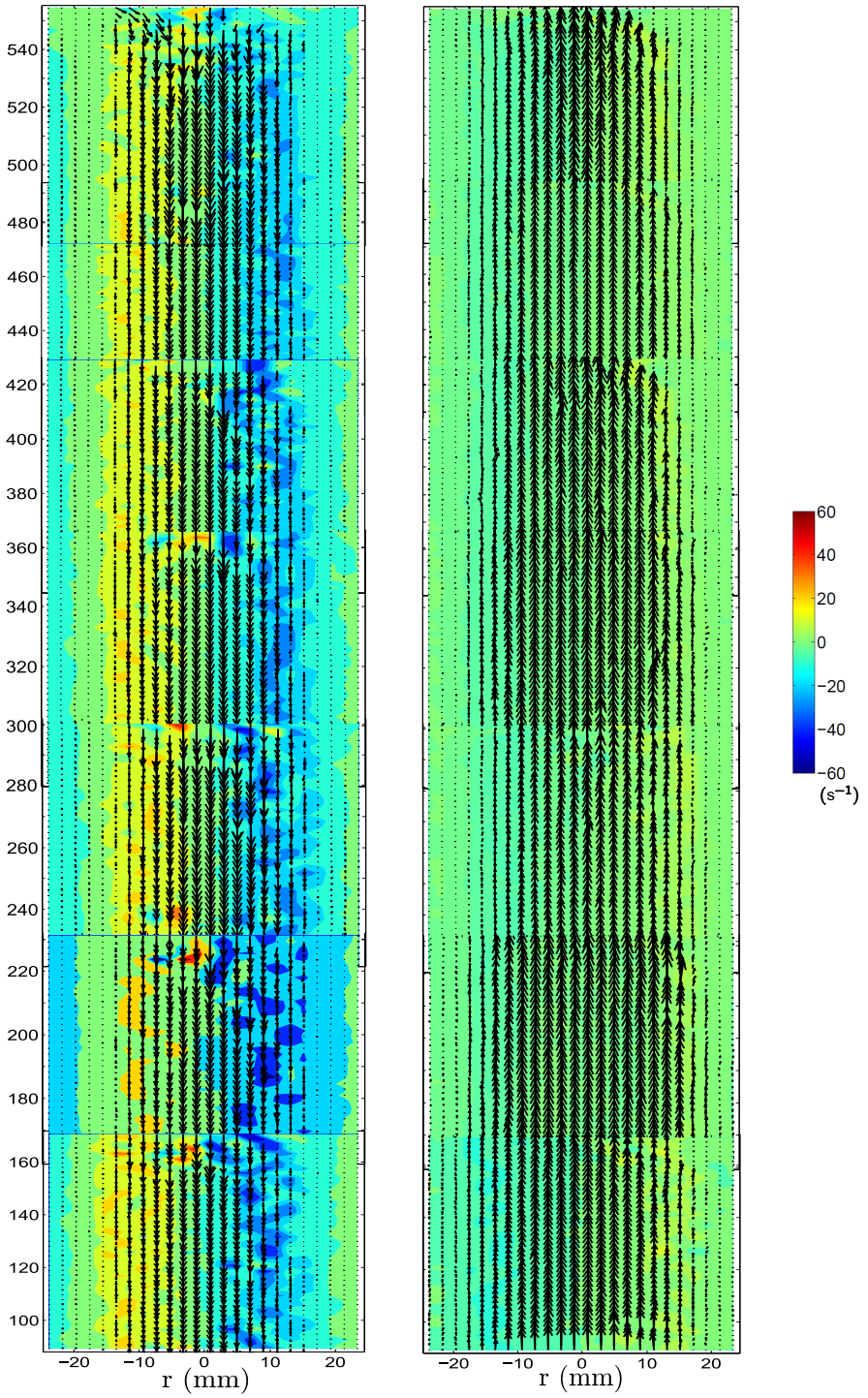

Figure 6.4: Velocity (arrows, a slightly different scale on each region) and vorticity (color code) fields measured at $\omega_0 = 31.4$ rad/s and $z_0 = 1.40$ mm in all seven tube regions (left: $\omega_0 t = \pi$, right: $\omega_0 t = 3\pi/2$).

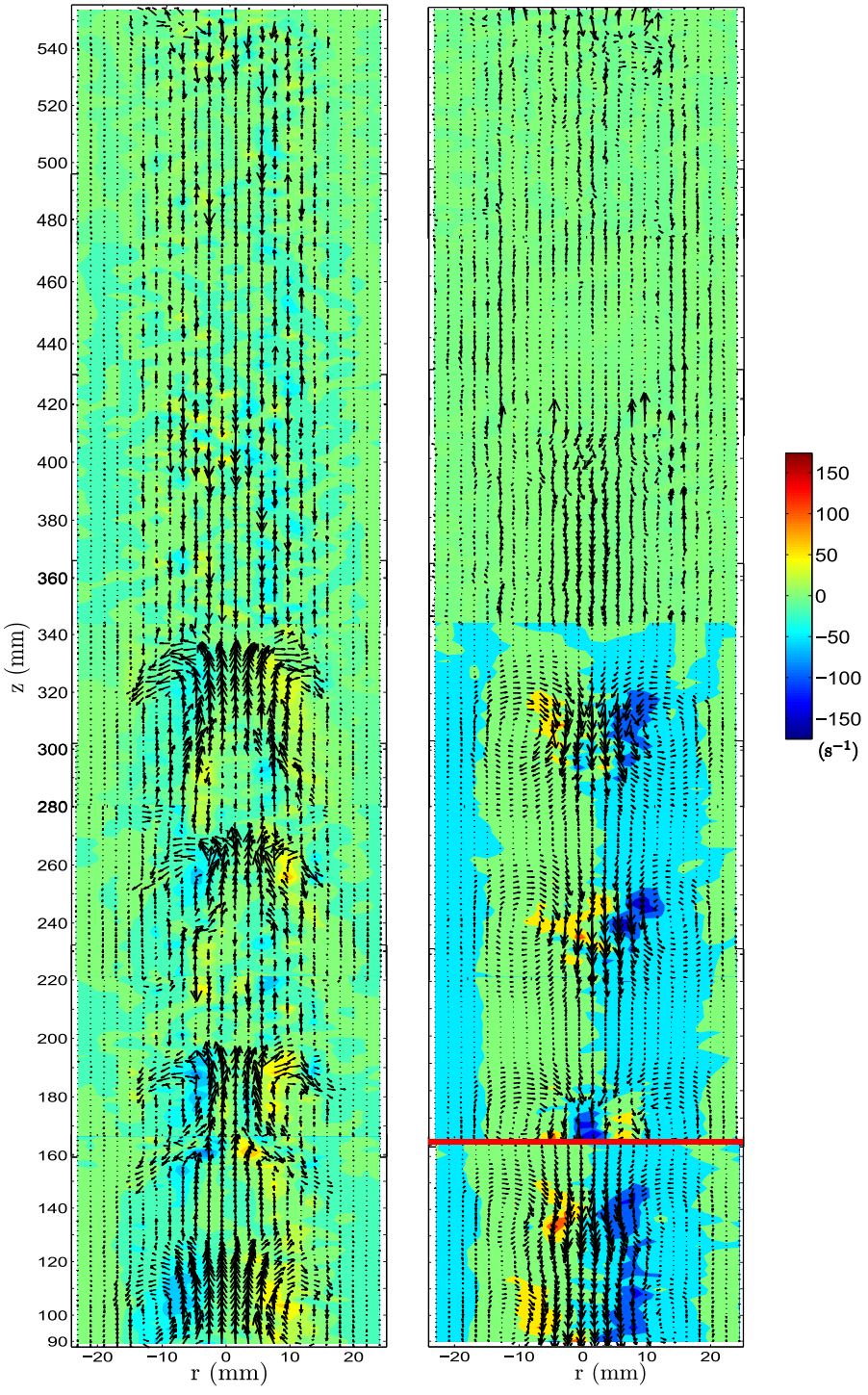

Figure 6.5: Velocity (arrows, a slightly different scale on each region) and vorticity (color code) fields of the secondary vortical flow measured at $\omega_0 = 31.4$ rad/s and $z_0 = 1.66$ mm in all seven tube regions (left: $\omega_0 t = \pi$, right: $\omega_0 t = 3\pi/2$).

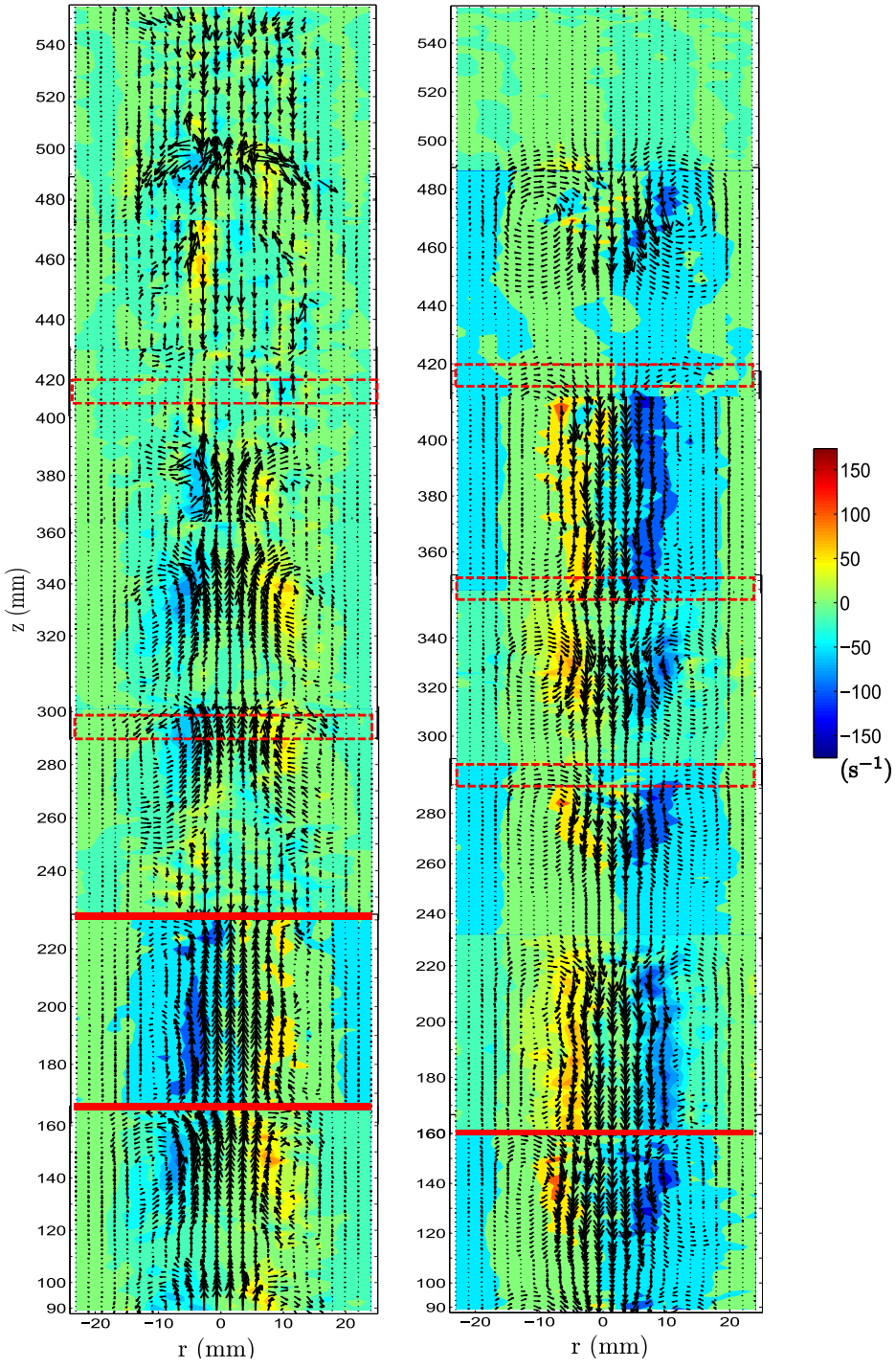

Figure 6.6: Velocity (arrows, a slightly different scale on each region) and vorticity (color code) fields of the secondary vortical flow measured at $\omega_0 = 31.4$ rad/s and $z_0 = 1.82$ mm in all seven tube regions (left: $\omega_0 t = \pi$, right: $\omega_0 t = 3\pi/2$).

At $z_0 = 1.66$ mm (Fig. 6.5) the secondary vortical flow extends up to *Reg. 4*. It displays four pairs of symmetric vortices stacked along the tube, and separated by a distance similar to the tube diameter. In the upper regions the flow looks featureless because the rescaled laminar base flow has been previously subtracted. The axial symmetry of the vortical flow is preserved all along the tube, except in the vicinity of the top lid, as discussed earlier.

At the largest driving amplitude, $z_0 = 1.82$ mm (Fig. 6.6), the secondary vortical flow reaches the entire tube length. Six pairs of vortices are formed, that present remarkable differences in morphology. In particular some vortices are very elongated and extend over approximately 70 mm (observed in *Regs. 2, 5*), whereas other vortices extend only over approximately 40 mm (observed in *Reg. 3, 4, 6*).

In the following, a quantitative analysis of the diversity of morphologies exhibited by the vortices is performed in terms of the vortex properties (*vortex size* and *vortex position*) previously defined in Sec. 5.3.4.

6.1.3 Large scale spatio-temporal vortex properties

The size of the large vorticity regions of the vortical flow generated at $\omega_0 = 31.4$ rad/s, $z_0 = 1.82$ mm, and computed in all regions is shown in Fig. 6.7. The vortex size obtained for *Regs. 2* and *5* is considerably larger than for the other regions. The vortex intensity, not shown, presents similar trends. These results are in agreement with previous observations done in the context of Fig. 6.6, where lengthened vortices were detected precisely in these regions. The vortex size seems therefore a good marker to track the vortex morphology of the vortical flow along the tube length. The temporal evolution of the vortices on short time scales follows the same trends as those described for *Reg. 4* (Sec. 5.3.4).

The morphology of the vortices can also be studied in terms of the magnitude of the rms velocity fluctuations. In Fig. 6.8 we show the time-averaged rms fluctuations of the vertical and radial components of the velocity, measured in all regions. In general, regions with a large vortex size (and lengthened vortices), *Regs. 1-2-5*, exhibit small values of the fluctuations for both u_z and u_r. Since the vortices extend over most of the interrogation region, the velocity field does not greatly change along the vertical coordinate, which results in small values of the fluctuations. Conversely, the regions with small vortex sizes (and localized vortices), *Regs. 3-4-6*, exhibit larger velocity fluctuations. In these regions the vortices cover a rather small portion of the interrogation region, and the velocity field shows therefore a manifest vertical dependence.

The radial and horizontal position of the vortices in the tube is shown in Fig. 6.7(b,c). While the radial position of the cv in all regions remains constant over

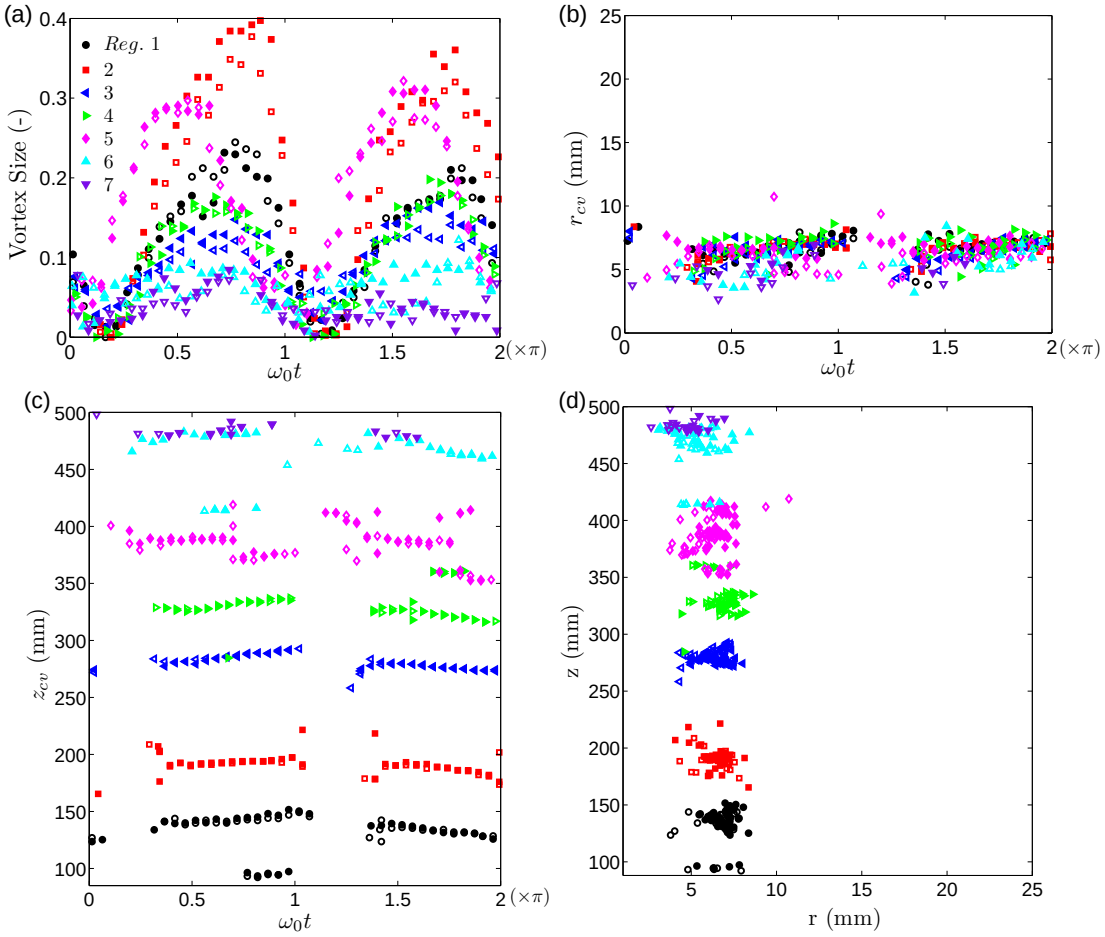

Figure 6.7: Vortex properties (vortex size (a), radial cv position (b), vertical cv position (c), vortex trajectories (d)) computed in the seven tube regions at $\omega_0 = 31.4$ rad/s and driving amplitude $z_0 = 1.82$ mm. Filled and empty symbols correspond to right and left sides of the tube axis.

a complete period at $r_{CV} = 8 \pm 3$ mm, the vertical position exhibits a periodic translational motion. As described for *Reg. 4* (Sec. 5.3.4) the vortices move upward in the first half period and downward in the second half, and at time phases $\omega_0 t \gtrsim 0$ and π the large vorticity domains vanish. All vortices move synchronously along the vertical axis, displaying a similar temporal evolution over a complete period.

We finally depict the vortex trajectories in a $r - z$ plot (Fig. 6.7(d)). The mean vertical separation between consecutive vortices is not constant over the tube length. However, in the upper regions (*Regs. 4-7*), where the matching of the velocity field of adjacent regions is more satisfactory, this distance is typically 50 mm. It coincides with the diameter of the cylinder.

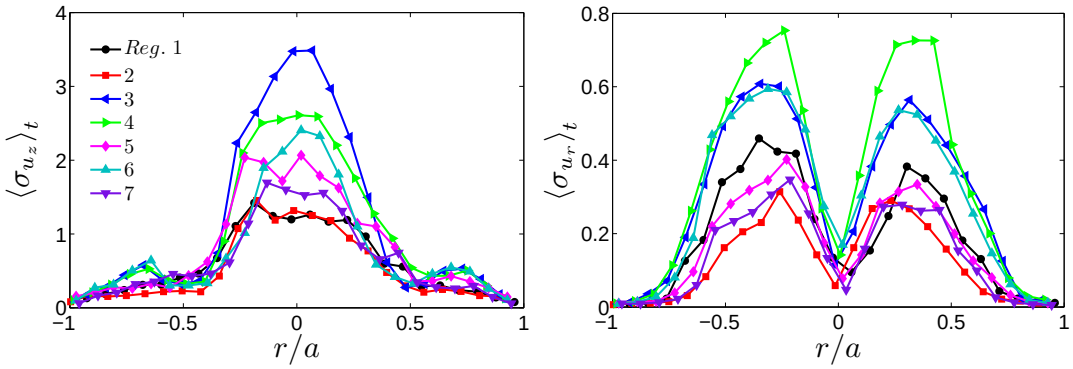

Figure 6.8: Rms of the time averaged fluctuations of the vertical (left) and radial (right) components of the velocity measured at $\omega_0 = 31.4$ rad/s and $z_0 = 1.82$ mm. Different colors correspond to different interrogation regions.

6.2 Flow on long time scales

In all the flow regimes investigated so far (laminar, axisymmetric vortical, non-axisymmetric vortical) the fluid flow follows the periodicity of the imposed driving at time scales comparable to the period of the oscillations, $T_0 = 2\pi/\omega_0$. At $\omega_0 = 31.4$ rad/s for instance, the time period is $T_0 = 0.2$ s, which is about ten times shorter than the characteristic relaxation time of the fluid ($\lambda = 1.9$ s). On these short time scales the flow is *quasi-steady*, in the sense that velocity and vorticity fields repeat themselves almost identically every time period. Accordingly, the vortices observed in the vortical regimes are also *quasi-steady*.

However, at much longer time scales (typically $t \geq 25\lambda$), although the flow follows the driving, an additional slow spatio-temporal evolution of the vortical flow is observed. This effect is more pronounced in the regions next to the driving piston.

Figure 6.9 shows the temporal evolution of the velocity and vorticity fields in the bottom and central regions (*Regs. 1* and *4*) at different time windows separated by lapses of time of 45 s each. Before recording the temporal sequence we let the fluid oscillate a time $t_0 = 75$ s, similar to the waiting time (t_w) that was spent in the experiments reported in previous sections. Comparing the flow organization measured at an equivalent time phase ($\omega_0 t = 3\pi/2$) we can visualize the evolution of the fluid flow on long time scales.

In the central region of the tube the vortical flow is *steady*, also on these long timescales. The vorticity field shows no significant differences and recovers an equivalent spatial structure after every lapse of 45 s, up to a total of 135 s, which is the longest time explored.

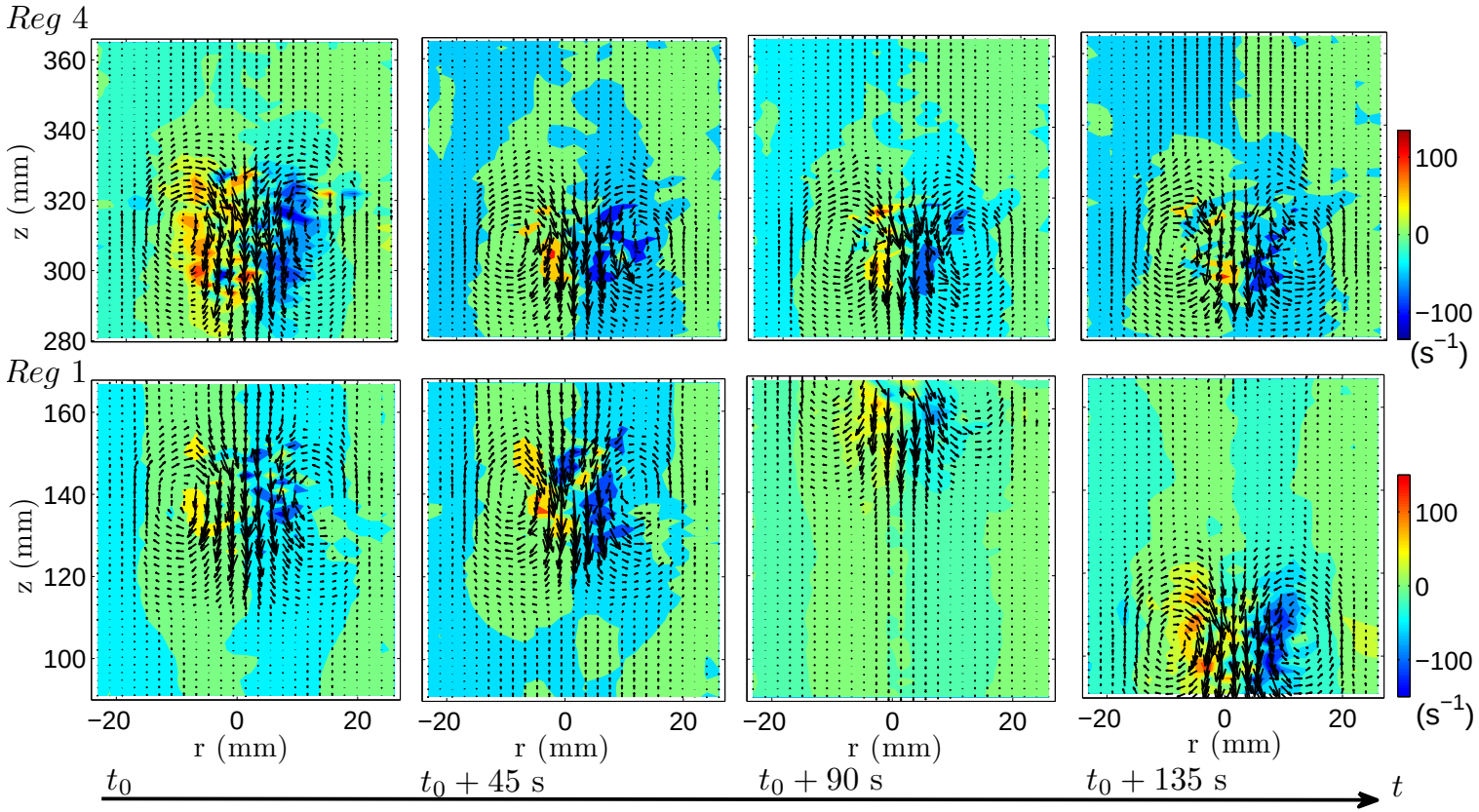

Figure 6.9: Velocity (arrows, a slightly different scale on each panel) and vorticity (color code) fields measured at $\omega_0 = 31.4$ rad/s and $z_0 = 1.62$ mm in the bottom *Reg. 1* (bottom) and the central *Reg. 4* of the tube (top). Panels are separated by a time lapse of 45 s, and $t_0 = 75$ s. All frames correspond to $\omega_0 t = 3\pi/2$.

Conversely, the flow measured in the bottom region preserves its spatial structure unaltered only over the first time interval of 45 s. In the following time window ($t_0 + 90$ s) the position of the pair of vortices has moved upwards a distance of about 20 mm. At $t_0 + 135$ s the vortices are no longer within the interrogation region. We presume that they have eventually moved upwards. And a new pair of vortices has emerged in the bottom part of the region. Thus, in the vicinity of the driving piston the spatio-temporal dynamics of the flow is more complex. The flow organization follows the periodicity of the driving on short time scales, a few periods T_0, but it becomes non-periodic at longer time scales. This slow evolution of the flow is less noticeable in regions placed further apart from the piston. Nevertheless, we have checked that at large enough driving amplitudes or long enough times it eventually affects the entire tube length.

This long time scale dynamics is surely responsible for the lack of continuity observed in the reconstructed velocity field in the regions of the tube near the piston (Sec. 6.1).

6.3 Instability mechanisms

This section presents a discussion of mechanisms that can be responsible for the onset of the laminar to vortical flow hydrodynamic instability uncovered and investigated in detail in previous sections.

It is clear that fluid elasticity plays a major role, since experiments performed by Torralba et al. (2007) with a Newtonian oil of similar density and shear viscosity at comparable drivings did not exhibit such instability. However, the instability may be not purely elastic. Additional factors may also contribute to make the laminar flow unstable. In the sequel, we evaluate in particular the influence of the finite length of the tube, by quantifying the fluid recirculation close to the driving piston and its propagation towards the bulk flow. The role of shear banding is also investigated, by performing experiments with a diluted non-shear-banding wormlike micellar solution. This section ends with a discussion on other potential triggering mechanisms.

6.3.1 Fluid recirculation

The finite length of the tube used in the experiments ($L = 60$ cm, aspect ratio $L/2a = 12$) causes unavoidably a fluid recirculation at the top and bottom ends. Since the oscillatory motion is generated by the piston motion at the bottom end, the recirculation zone is presumably more important in this region.

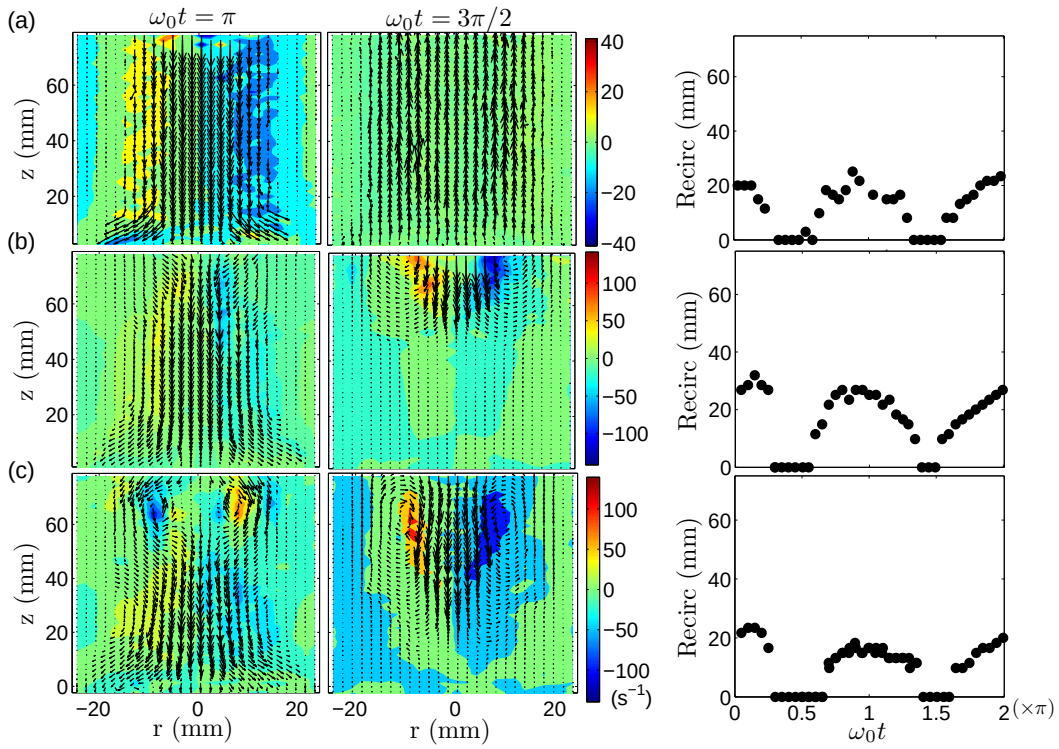

Figure 6.10: Velocity (arrows, a slightly different scale on each panel) and vorticity (color code) fields, measured at $\omega_0 = 31.4$ rad/s in *Reg. 0*, at two given time phases $\omega_0 t = \pi$, $3\pi/2$ and three different driving amplitudes: (a) $z_0 = 1.13$ mm; (b) $z_0 = 1.60$ mm; (c) $z_0 = 2.35$ mm. The temporal evolution of the height of the recirculation zone (*Recirc*) has been evaluated for the different amplitudes.

In order to study the fluid flow in the region adjacent to the piston we introduced a modification of the original setup consisting of enlarging the piston length. As described in Sec. 6.1 in the original setup the region of the tube close to the piston was not accessible with the camera (Fig. 6.1). In particular we could not measure the velocity field in a distance less than 85 mm from the piston end. A new cylindrical piece of 90 mm length, made of Teflon, carefully adjusted to the diameter of the tube, was attached to the original piston so that the end of the enlarged piston was now accessible with the camera. Note that with this setup modification the length of the fluid column was reduced by a 15%. The length of the fluid column might in turn modify slightly the spatial flow organization, but this study falls beyond the scope of the Thesis. We call *Region 0* the tube region next to the enlarged piston. In the following, we present a detailed study of fluid recirculation in this region. The area of fluid recirculation has been identified with the area where the radial component of the velocity obtained from PIV measurements is non zero. In Fig. 6.10 the velocity and vorticity fields measured in *Reg. 0*, at $\omega_0 = 31.4$ rad/s and increasing driving amplitudes, are shown. In

the laminar regime the recirculation zone is confined to a very small region next to the tube end. As described in Sec. 4.2, it does not affect the bulk flow in the upper regions. At $z_0 = 1.13$ mm (panel a) the recirculation area extends up to 20 mm from the piston (about 4% the length of the fluid column). The size of the recirculation area follows the periodicity of the driving, being more pronounced at the time phases where the velocity and vorticity fields are largest ($\omega_0 t \simeq 0$ and π) and nearly zero at the time phases where the velocity magnitude is smallest ($\omega_0 t \simeq \pi/2$ and $3\pi/2$).

When the vortical flow sets in ($z^*_{Reg0} = 1.60$ mm, panel (b)), the extent of the fluid recirculation enlarges up to 30 mm (about 6% the length of the fluid column). It is interesting to note that the first pair of vortices appears at the top part of the interrogation region ($z_{cv} > 75$ mm). They are not in contact with the recirculation zone. Vortices and recirculation zone are separated by a region where the flow is laminar. Besides, the vortices are more pronounced at the time phases where the size of the recirculation zone is nearly zero ($\omega_0 t \simeq \pi/2$ and $3\pi/2$). At larger driving amplitudes, although the size of the recirculation region does not change appreciably, the vortices appear closer to the bottom piston. Above $z_0 = 2.35$ mm, as shown in Fig. 6.10 (panel c), the vortices eventually merge with the recirculation region.

We have observed in Sec. 6.1 that the laminar flow becomes unstable earlier (i.e. at smaller forcings) in the vicinity of the piston. It could be arqued therefore that fluid recirculation favors the foramtion of vortex rings. The detailed observations presented in this section, however, show that vortical structures and fluid recirculation do not overlap at the onset of instability. This prompts us to exclude fluid recirculation as the triggering mechanism for the onset of the laminar to vortical flow instability.

6.3.2 Role of shear banding

The viscoelastic fluid used in the experiments exhibits a nonlinear rheological response for $Wi > \lambda\dot{\gamma}_c \simeq 1$, followed by the formation of shear bands (Sec. 3.2). In the vortical flow, where the typical applied driving amplitudes are large, the mean shear rate of the fluid largely overtakes the critical shear rate ($\dot{\gamma}_c$). For instance, close to the first resonant frequency ($\omega_0 = 34.6$ rad/s) where the critical dimensionless driving for the first instability is smallest, $Wi^*_{1-up} = 1.8 > 1$. It is difficult therefore to isolate shear banding from fluid elasticity, and to elucidate the possible influence of shear banding in triggering the instability.

In order to clarify the latter, we performed experiments with a more diluted wormlike micellar solution, CPyCl/NaSal [66:40] mM. This solution is still elastic but does not exhibit shear banding (Sec. 3.5).

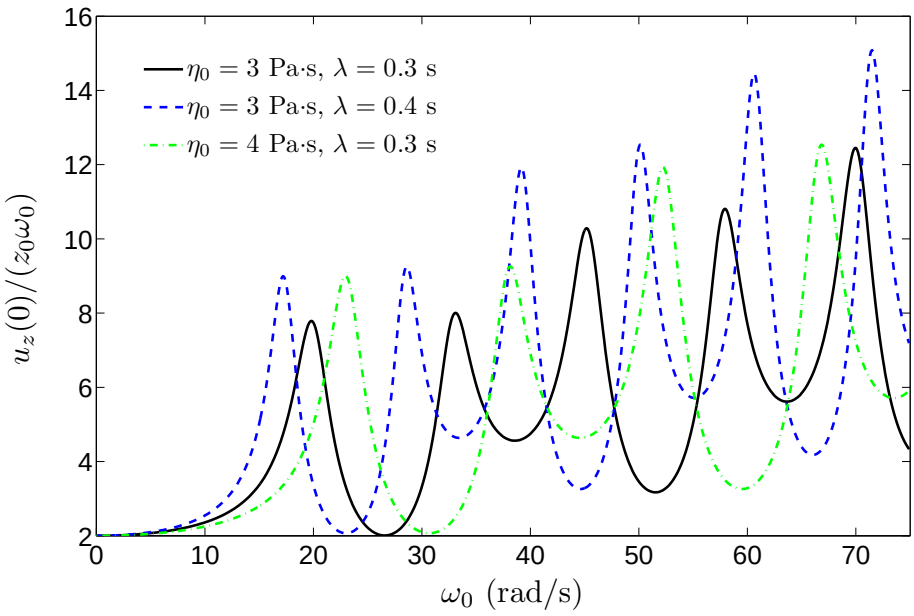

Figure 6.11: Dimensionless velocity magnitude at the tube axis vs. driving frequency. Different lines correspond to different rheological values, and $a = 25$ mm (cylinder radius).

Laminar oscillatory flow of the diluted wormlike micellar solution

We studied the laminar oscillatory pipe flow of the diluted wormlike micellar solution. The theoretical frequency response predicted using the Maxwell model is shown in Fig. 6.11. Although the linear viscoelasticity of this solution deviates from the behavior described by the Maxwell model, this ideal frequency spectrum is still useful to discuss the relevant driving frequencies for this fluid.

In the range of driving frequencies experimentally accessible, the fluid response exhibits a larger number of resonant frequencies than the original concentrated solution (Sec. 4.2). Since both the zero-shear viscosity and relaxation time of the diluted solution are small, these material parameters are subjected to large experimental relative errors ($\eta_0 = 3 \pm 1$ Pa·s, $\lambda = 0.3 \pm 0.1$ s). The frequency response of the diluted solution is very sensitive to small changes in the rheological properties, as shown in Fig. 6.11. This makes it difficult to predict the actual structure of the laminar flow, and make connection between experimental measurements and theoretical predictions.

As shown in Fig. 6.12, the theoretical predictions based on the UCM model lead to a number of concentric layers in the laminar flow that rapidly increases with driving frequency. Up to nine domains are expected at $\omega_0 = 75$ rad/s. Experimentally, at low driving frequencies ($\omega_0 = 14.2$ rad/s in the figure), the

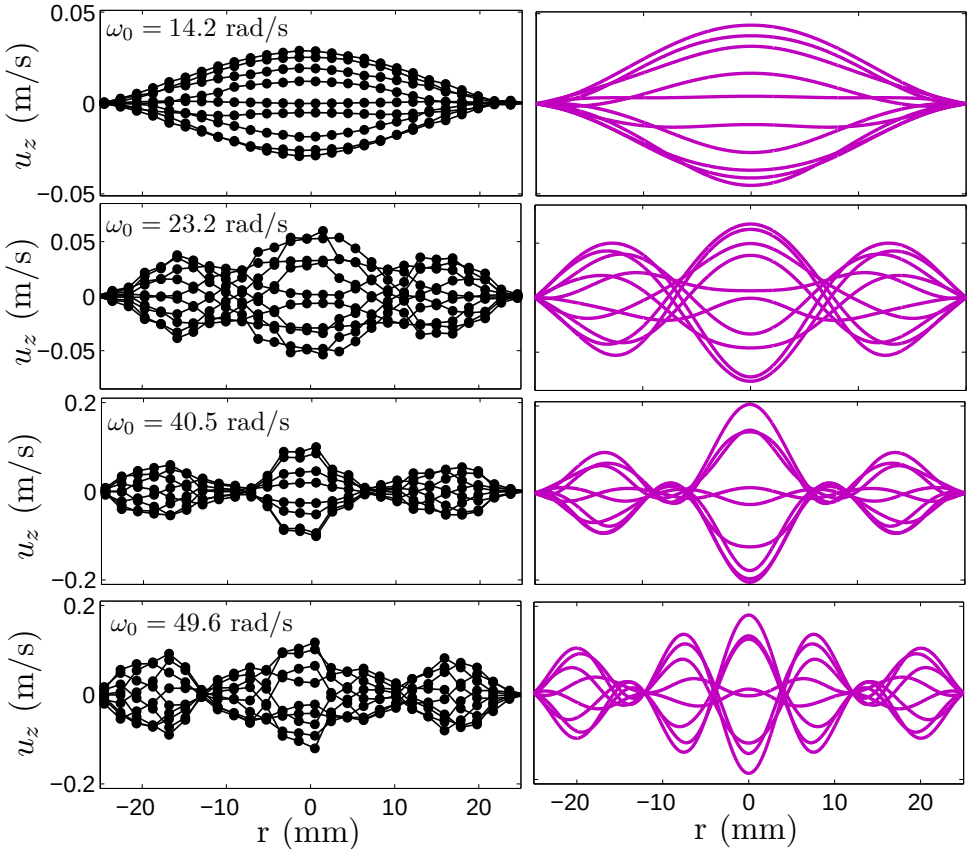

Figure 6.12: Experimental (left) and theoretical (right) velocity profiles obtained for the diluted micellar solution at $z_0 = 1.00$ mm and increasing driving frequencies: 14.2, 23.2, 40.5, 49.6 rad/s. The theoretical profiles have been obtained with $\eta_0 = 3$ Pa·s and $\lambda = 0.3$ s, using the UCM model predictions for the laminar flow.

velocity profiles follow the trends predicted theoretically with the Maxwell model: no inner quiescent points are detected at this frequency, and the no slip condition is accomplished at the boundaries. This is also true at slightly higher frequencies, such as 23.2 rad/s, for which one pair of inner quiescent points is already present. However, at larger frequencies ($\omega_0 = 40.5$ and 49.6 rad/s in the figure) the fluid response starts to deviate from the theoretical predictions. In particular the experimental profiles exhibit a smaller number of concentric layers, and the velocity magnitude is considerably smaller. The reason is that the linear rheological behavior of the diluted solution is not well described by the Maxwell model. We did not carry out a detailed investigation of the frequency response of the diluted solution in laminar flow. It is worth noting however that the determination of the frequencies of resonance, through the measurement of velocity and phase lag at the tube axis, could provide an accurate value of the main relaxation time of the fluid, which is largely undetermined from linear rheological measurements.

Flow stability

The laminar oscillatory flow of the diluted solution did not become unstable in any of the experiments that were performed scanning the whole range of accessible driving amplitudes and frequencies. In terms of dimensionless parameters for this solution, this range corresponds to maximum values $De \simeq 22$ and $Wi \simeq 5.4$.

Note that the largest De experimentally accessible for the diluted ([66:40] mM) micellar solution is much smaller than the critical De at which the concentrated micellar solution ([100:60] mM) exhibited the onset of the laminar to vortex flow instability, $De \gtrsim 45$ (Sec. 5.3). On the other hand, the critical dimensionless driving (Wi^*_{1-up}) measured for the onset of the instability of the concentrated solution exhibited a complicated frequency dependence. It oscillated in the range $1.8 < Wi^*_{1-up} < 8.5$. Consequently, it is difficult to judge whether the maximum Wi experimentally accessible for the diluted solution was large enough to trigger the flow instability.

Although the onset of a hydrodynamic instability has been observed for the concentrated solution, which exhibits shear banding, and not for the diluted solution, which does not shear band, it is not clear to us that shear banding is the triggering mechanism of the instability. It is known after the work of Hu and Lips (2005), Miller and Rothstein (2007), and Pipe et al. (2010) that shear bands take a certain time, typically $t \gtrsim \lambda$, to develop. The results provided in Appx. C for a steady shear flow also point towards the same direction. Besides, in recent experiments performed by Dimitriou et al. (2012) of large amplitude oscillatory shear flows of the same concentrated micellar solution (CPyCl/NaSal [100:60] mM), the formation of distinct shear bands was observed at time ratios $De \simeq 1$. In our experiments the transition to vortical flow has been observed at $45 < De < 143$, corresponding to timescales of flow much shorter than the results previously reported in the literature. We presume that these time scales are in fact too short to form stable shear bands in the oscillatory flow.

6.3.3 Other potential mechanisms

The underlying mechanism for the onset of an oscillatory vortical flow in the cylinder remains unsolved. But other possible triggering mechanisms could be further investigated.

In the laminar flow regime the vorticity field organizes in well defined vortex sheets, with alternate sign of the vorticity (Sec. 5.3). This flow organization results in large vorticity gradients in the radial direction.

The presence of these large vorticity gradients in the laminar flow, and the spatial structure of the toroidal vortices formed in the instability from laminar

to vortical oscillatory flow, are both highly reminiscent of the characteristic flow features accompanying the formation of vortex rings in Newtonian fluids.

In many flow configurations vortices form by rolling-up of vortex sheets which separate at the edge of a body (Didden, 1979). Vortex formation also occurs in impulsively-started flows around sharp edges. In the laboratory, vortex rings have been produced by ejecting fluid from an orifice or nozzle of diameter D by the motion of a piston pushing a column of fluid of length L (Didden, 1979; Glezer, 1988; Gharib et al., 1998). This results in the separation of a boundary layer at the edge of the orifice or nozzle, the formation of a cylindrical vortex sheet, and its subsequent spiral roll-up into a vortex ring, which moves downstream. The trailing jet behind the vortex ring may eventually pinch-off, leading to an isolated vortex ring moving downstream with a particular translational velocity. The dimensionless piston displacement $x(t)/D$ at which pinch-off occurs is known as the formation number. This number for water lies typically in the range from 3.5 to 4.5 for a broad range of flow conditions (Gharib et al., 1998). The large body of research carried out on the generation, formation and evolution of vortex rings in Newtonian fluids has been reviewed by Shariff (1987).

While the formation of vortex rings in Newtonian fluids was observed for L/D ratios larger than 1, vortex rings in the oscillatory pipe flow studied in this Thesis were generated much more easily, at forcing amplitudes as low as 1.0 mm, i.e. $L/D \simeq 1.0/50 = 0.02$. We argue that the structure of the flow of the micellar solution, consisting of coaxial layers in alternating upward/downward motion, results in cylindrical vortex sheets that are already detached from the cylindrical lateral wall in the laminar flow and hence can roll-up into a vortex ring much more easily. In support of this argument, Rosenfeld et al. (1998) showed numerically for a Newtonian fluid that blunting the jet velocity profile at the nozzle exit plane to a parabolic profile could reduce the formation number to approximately 1.

Another observation relevant to our work was made by Didden (1979), who showed that in general the vorticity flux provided by the separated shear layer is the main source of vorticity for the forming vortex ring. A termination of the piston motion should inhibit the flow of shear layer vorticity and thus its accumulation in the core region of the vortex ring. This being the case, the circulation in the fully-formed vortex ring should be approximately equal to the discharged circulation from the nozzle or orifice, a relation that was experimentally verified by Gharib et al. (1998) for vortex rings in water.

In our setup the driving piston moves periodically forward and backward in excursions of amplitude z_0. The onset of vortical flow would be given, in this framework, by a driving amplitude z_0 equal to the formation number that would correspond to that particular structure of the laminar flow, which is determined

by the setup dimensions, fluid rheological parameters and, more importantly, by the driving frequency ω_0.

If this picture applies, many interesting questions will ensue. One of the most relevant will be to unveil the mechanism by which the periodic motion of the driving piston is able to stabilize an ensemble of isolated vortex rings, stacked along the tube axis and displaying a time-periodic vorticity synchronized to the oscillatory forcing. To the best of our knowledge such a fascinating spatiotemporal arrangement of vortex rings has not been observed in any other flow.

Chapter 7

Conclusions

The subject of study of the present Thesis has been the oscillatory pipe flow of viscoelastic fluids.

We have first studied the laminar flow, from a theoretical perspective, using the Upper-Convected Maxwell and Oldroyd-B models. The validity of several theoretical predictions has been checked experimentally using wormlike micellar solutions.

For this purpose an experimental setup, consisting on a fluid-filled vertical pipe on which a piston driven oscillatory flow is induced, has been designed and assembled. The implementation of a time-resolved PIV technique with very good spatial and temporal resolution has allowed to measure the 2D velocity field in a meridional plane of the tube, and to characterize from it the response of the fluid to the oscillatory forcing in a large range of accessible driving frequencies and amplitudes.

We have studied, in second place, the onset of hydrodynamic instabilities in the oscillatory pipe flow. We have observed that the laminar flow becomes unstable, and evolves towards complex vortical flows, at increasing driving amplitudes. The spatio-temporal dynamics of these complex flows has been studied experimentally.

The main results obtained can be summarized as follows:

Laminar oscillatory flow

Theoretical approach

In wall-bounded oscillatory flows of viscoelastic fluids the two characteristic lengths of the Ferry waves, x_0 (damping length) and λ_0 (wavelength), together with the

characteristic separation of the walls, a, define all the flow properties for fluid models with a linear shear-stress equation in unidirectional flow. For fluids with a single relaxation time, and in the inertialess regime ($Re \ll 1$), the dependence on x_0, λ_0 and a can be expressed in terms of three independent dimensionless groups, t_v/λ (viscous to relaxation time), De (relaxation time to driving period) and X (viscosity ratio).

We have shown that in wall-bounded settings the possibility that shear waves generated at different locations superpose themselves before decaying depends on whether the system can be regarded as 'wide' or 'narrow', a property that can be characterized by the dimensionless number $\Lambda_{ve} \equiv a/x_0$, the analogue of the Stokes ratio for viscoelastic fluids. In 'wide' systems ($\Lambda_{ve} > 1$) the shear waves remain localized near the walls, and the flow in the central core of the system is inviscid. In 'narrow' systems ($\Lambda_{ve} < 1$) the shear waves interfere, giving rise to a resonant flow at well defined frequencies of driving. In parallel plate geometry and tube geometry resonances occur at universal values of the dimensionless ratio a/λ_0.

At resonances the velocity at the center of the system is in phase with the acceleration of the moving walls and its magnitude becomes strongly peaked. Plotted as functions of a/λ_0, magnitude and phase depend on Λ_{ve} only through t_v/λ, the ratio of viscous to relaxation time.

Studying the Oldroyd-B constitutive equation has enabled us to show that a Newtonian solvent contribution –even for extremely small ratios of the solvent to the solution viscosity, X– makes the resonances to fade out, particularly as the driving frequency increases. For realistic values of X (0.1 and above) the oscillatory flow becomes nearly identical to the Newtonian one. We conclude therefore that only special fluids such as wormlike micellar solutions (for which $X \simeq 0$) are expected to exhibit velocity resonances. Moreover, since local values of the shear rate drastically decrease above $X = 0$ we expect that Oldroyd-B fluids with a realistic solvent contribution will remain laminar for a much larger range of De, provided that Re remains small.

Experiments

We have presented an experimental investigation of the oscillatory piston driven flow of a wormlike micellar solution (CPyCl/NaSal [100:60]mM) in the laminar flow regime. The location of resonant peaks in the frequency response of the flow has been determined very precisely using two independent approaches. First, resonances have been identified by a huge increase of the velocity magnitude measured at the tube axis. Second, at resonances the phase lag between the fluid velocity at the tube axis and the piston position changes abruptly.

The measured frequency response of the velocity in the tube axis, conveniently decomposed in modulus and phase, is in quantitative agreement with linear theoretical predictions based on the UCM and Oldroyd-B models of the fluid rheology. At small forcings these models reproduce the experimental data with great accuracy. At resonances, however, the UCM model largely overestimates the fluid response. The Oldroyd-B model can better reproduce the data at larger forcings if a small newtonian solvent is included in a phenomenological way.

We have presented an accurate study of the laminar flow structure at resonant and non-resonant frequencies. The shape of the radial velocity profiles has been found to strongly depend on driving frequency. While at low frequencies all the fluid moves in the same direction, the flow becomes much more inflectional as the driving frequency increases and organizes in several concentric layers of upward/downward motion. The no-slip condition at the walls is well satisfied in all cases. We have tracked the quiescent points in the flow. The way they change their location in time within an oscillation, and their dependence on frequency, are both in good agreement with the theoretical predictions.

Finally, we have verified that the fluid response easily becomes nonlinear with the driving amplitude as this amplitude increases. This effect is very prominent at resonances. In order to capture the nonlinearities revealed by our experimental data, a constitutive equation with a nonlinear equation for the shear stress would be required, that could account for the nonmonotonicity of the shear flow curve of micellar solutions.

Hydrodynamic instabilities

From laminar to complex spatio-temporal vortical flows

The oscillatory pipe flow has been investigated in the whole range of experimentally accessible driving frequencies and amplitudes, and classified in three main flow regimes: laminar, axisymmetric vortical, and non-axisymmetric vortical. By ramping up and down the driving amplitude at constant frequency we have been able to characterize the transition from laminar to more complex flows, under controlled driving conditions.

The first hydrodynamic instability occurs when the laminar base flow becomes unstable against the formation of axisymmetric toroidal vortices (vortex rings) that appear distributed along the cylinder. The calculation of root-mean-square fluctuations in the vertical direction of the vertical and radial components of the velocity (averaged in time or over the tube diameter) has allowed to determine the critical amplitude at which the instability sets in, in the central region of the tube,

with high accuracy. In the laminar flow regime the velocity fluctuations are small and correspond to the experimental uncertainties in the velocity measurements. In the vortical flow, instead, an abrupt increase of the fluctuations is observed, that accounts for the loss of the vertical translational symmetry and the formation of vortices in the flow.

This transition exhibits hysteresis when the driving amplitude is ramped up and down, which makes us presume that the bifurcation from the laminar flow has a subcritical nature.

At progressively larger driving frequencies the route from laminar to axisymmetric vortical flow presents qualitative differences. At resonances, differences in the temporal behavior have been observed, similar to the temporal differences between the velocity profiles of the resonant and non-resonant frequencies predicted and observed for the laminar oscillatory flow.

A second hydrodynamic instability occurs at even larger driving amplitudes, when the vortical flow loses the axial symmetry. In this flow regime the vortices are heavily distorted and no longer axisymmetric. Non-negligible values of the divergence of the in-plane velocity field reveal the presence of non-zero azimuthal velocity components (perpendicular to the interrogation plane). Since this transition also presents hysteresis when ramping the driving amplitude up and down, we suggest that this second transition is also subcritical. When the fluid is oscillated at frequencies slightly larger than the first resonant frequency, the laminar flow evolves almost directly towards this non-axisymmetric vortical flow.

Flow organization at large scales

The velocity and vorticity maps of the vortical flow measured in a meridional plane of the tube appear periodic in time, on time scales comparable to the driving period. Interestingly, the vortex formation is favored in the acceleration phases of the piston oscillation. Besides, we have uncovered an spatio-temporal dynamics on long time scales ($t \gg \lambda$) that substantially modifies the flow organization. This slow dynamics is more effective in the bottom half of the cylinder, specially next to the driving piston.

A global inspection of the vortical flow along the tube length reveals that the instability takes place earlier in the bottom part of the tube, in the vicinity of the driving piston. Upon increasing the driving amplitude the boundary between laminar and vortical flow progressively raises towards the top regions. And above a critical driving amplitude the entire fluid flow is vortical.

The vortical flow organizes forming a set of toroidal vortices that are distributed along the cylinder. The vortex properties (*size*, *intensity*, *position*) have

been tracked over a time period and over the tube length, for a driving frequency just below the first resonance. Size and intensity of the vortices follow the periodicity of the driving: the vortices are fully developed at the time phases where the corresponding laminar flow exhibits the smallest velocity magnitude, and vanish at the complementary time phases. The radial location of the vortices remains fixed. However, the vortices display a periodic vertical motion synchronously in all regions. The distance between vortices is not very systematic but in general it is similar to the tube diameter.

At larger driving frequencies the structure of the vortical flow becomes more complicated. It exhibits an increasing number of concentric vortex rings, of different radii, in accordance with the structure of the laminar flow.

Instability mechanisms

The mechanism triggering the hydrodynamic instability from the laminar to the axisymmetric vortical flow is not yet clear. Fluid recirculation is present at the tube ends, and extends with increasing driving amplitude. However, we have observed that in the vortical flow the vortices appear first in a region separated from the recirculation zone by an intermediate laminar flow region. Therefore, although fluid recirculation surely modifies the flow organization, it does not seem to be the triggering mechanism of the instability.

In order to elucidate the relevance of shear banding on the instability we have performed experiments with a second wormlike micellar solution, with lower surfactant concentration, that does not shear band. The laminar flow of the diluted solution does not become unstable for any of the experimentally accessible driving amplitudes and frequencies.

These observations do not necessarily imply that shear banding is responsible for the onset of the instability in the concentrated solution. First, in terms of the dimensionless driving frequency (De) the range of accessible frequencies for the diluted solution is well below the critical De at which the laminar flow of the concentrated solution becomes first unstable. And, moreover, the formation of stable shear bands has been previously reported to require much longer time scales, typically larger than λ. Thus, we believe that shear banding is not the mechanism responsible for the observed instability, since the timescales at which the concentrated solution has been oscillated in the vertical pipe are too short to form stable bands.

The morphology of the toroidal vortices in the axisymmetric vortical flow is very reminiscent of that of vortex rings formed in Newtonian fluids by the roll-up of cylindrical vortex sheets. The velocity profiles observed in our setting for the

viscoelastic laminar flow are highly inflectional and generate a cylindrical vortex sheet already detached from the tube walls, that could favor the formation of vortex rings. The oscillatory forcing could prevent the vortex rings to vanish and, instead, stabilize them dinamically leading to the observed spatio-temporal pattern, with a number of vortex rings stacked along the cylinder and periodically oscillating with the driving. This fascinating scenario deserves further investigation.

Chapter 8

Resum en català

L'objectiu d'aquesta Tesi és estudiar el flux oscil·latori vertical en fluids micel·lars. Primer encarem el problema des d'una perspectiva teòrica i analitzem el flux laminar oscil·latori de fluids viscoelàstics utilitzant els models de Maxwell i Oldroyd-B. Les prediccions teòriques obtingudes pel flux laminar són validades duent a terme experiments de Velocimetria d'Imatges de Partícules (PIV) en un tub vertical, per amplituds petites del forçament oscil·latori. Quan s'incrementa l'amplitud de l'oscil·lació el flux laminar evoluciona cap a fluxos que presenten una dependència espacio-temporal més complexa. Estudiem en detall la transició del flux laminar al flux vortical, en el qual es formen anells de vorticitat distribuits a través del tub. També caracteritzem una segona inestabilitat que esdevé a amplituds del forçament encara més grans, per la qual el flux vortical perd la simetria axial.

8.1 Breu introducció

A començaments del segle XX, moment en què la indústria química així com la síntesi industrial de polímers rebé un fort impuls, es van començar a observar comportaments poc usuals en determinats fluids. L'equació de Newton per a la viscositat, juntament amb les equacions de Navier-Stokes no eren capaces de predir el moviment inusual d'aquest fluids. Fins i tot la divisió ordinària de la matèria en *sòlid - líquid - gas*, segons la qual un líquid manté la forma del recipient que el conté, tampoc es satisfeia per aquests materials. En general podem anomenar *fluids complexos* a totes les *substàncies espesses, gomoses o enganxifoses que desafien la definició clàssica de sòlids i líquids* (Larson, 1999). Els fluids complexos poden mostrar un comportament viscoelàstic intermig entre els sòlids i els líquids ja que poden mantenir la seva forma a escales de temps curtes però fluir a escales de temps més llargues. En contraposició als *fluids Newtonians*, que tenen una viscositat constant, els fluids complexos mostren un comportament no-Newtonià,

amb una viscositat que depèn del ritme de deformació. En la majoria dels casos la viscositat decreix quan augmenta el ritme de deformació (a la literatura aquests fluids es coneixen com *fluids shear-thinning*), tot i que en alguns casos la viscositat pot augmentar (*fluids shear-thickening*). Els *fluids yield-stress* també presenten propietats no-Newtonianes perquè no flueixen per sota d'un esforç mínim aplicat. Una característica important dels fluids complexos és la presència d'esforços normals: sota un flux de cisalla el fluid respon amb una força addicional normal a la direcció del a cisalla.

Hi ha una gran varietat de fluids complexos, com per exemple els fluids polimèrics, pastes, suspensions de partícules, espumes, emulsions, cristall líquids o solucions de tensioactius (en els quals nosaltres estem especialment interessats). Les molècules tensioactives són amfifíliques, i per tant tenen una part hidrofílica i una hidrofòbica. Quan es dissolen en aigua la formació de micel·les és favorable energèticament per concentracions per sobre d'una concentració micel·lar crítica. Les molècules que tenen una força iònica de la part hidrofílica més aviat feble tendeixen a agrupar-se formant micel·les cilíndriques amb forma de *cuc* (en anglès se les anomena *wormlike micelles*). En el règim *semi-diluït* de concentracions de tensioactiu en què nosaltres treballem les micel·les tipus cuc se sobreposen establint connexions entre elles, i formant una xarxa mesoscòpica que és responsable de la resposta viscoelàstica del fluid. Les micel·les tipus cuc també es coneixen com *polímers vivents* perquè, a diferència de les solucions polimèriques, tenen l'habilitat de reensemblar-se després d'haver-se trencat, per exemple degut a l'aplicació d'un esforç de cisalla. Els fluids micel·lars tipus cuc tenen diverses aplicacions industrials. S'utilitzen en la fabricació de detergents, emulsificants, encapsulants o lubricants. I en particular, aquests fluids han estat extensament utilitzats durant les darreres dècades amb finalitats científiques, des que Rehage i Hoffmann (1991) van mostrar que es comporten d'acord amb el model de Maxwell, amb un sol temps de relaxació, a ritmes de deformació lents. A ritmes de deformació més alts, en canvi, mostren normalment una viscositat fortament decreixent amb el ritme de cisalla.

Els fluxos oscil·latoris de fluids Newtonians o complexos en geometries confinades per parets han merescut força atenció tant des d'un punt de vista tèoric com experimentalment durant les darreres dècades. El fluxos oscil·latoris són especialment importants en fisiologia, en relació amb el sistema circulatori i respiratori d'éssers humans, i també en processos industrials com el bombejat de fluids, l'extracció de petroli o en acústica, i en particular són interessants en la caracterització reològica de fluids complexos. Els fluxos amb una certa dependència temporal (com per exemple els fluxos oscil·latoris) de fluids viscoelàstics mostren característiques molt interessants que són absents en els corresponents fluxos de fluids Newtonians.

8.2 Sistema experimental

Una contribució important de la Tesi ha estat la posta a punt del sistema experimental, incloent el disseny, implementació i cal·libracions de les diferents parts. El sistema experimental que hem utilitzat consisteix en una columna de fluid, continguda en un tub vertical transparent, que oscil·la periòdicament, gràcies al moviment sinusoïdal d'un pistó situat a la part inferior del tub. També s'ha implementat un sistema de PIV que ha fet possible la caracterització del camp de velocitats i vorticitats en un pla meridional del tub, amb una gran resolució espacial i temporal.

Aquest sistema és el primer d'aquest tipus que ha estat mai implementat al *Laboratori de Física no Lineal* de la Universitat de Barcelona. El nostre sistema es basa en un disseny original que es troba a la UNAM (Mèxic) però conté un seguit de noves implementacions que el milloren considerablement, ampliant els rangs de mesures i resolució i permetent així un gran ventall de mesures a realitzar.

El fluid que hem utilitzat en els experiments és una solució tensioactiva de clorur de cetilpiridini (CPyCl) i salicilat de sodi (NaSal) diluïts en aigua, en una concentració [100:60] mM. Aquesta dissolució és particularment interessant perquè presenta una reologia a ritmes de deformacions petits que segueix molt bé el model de Maxwell. A ritmes de deformació més grans la corba de flux lineal esdevé inestable i el fluid s'estructura formant diferents bandes de cisalla amb una viscositat efectiva ben diferenciada.

8.3 Principals resultats

Estudi teòric

L'estudi teòric de fluxos oscil·latoris confinats de fluids viscoelàstics mostra que les propietats del flux depenen exclusivament de les dues longituds característiques de les ones de Ferry generades a l'interior del tub, longitud d'esmorteïment i longitud d'ona, així com la separació característica entre les parets. Això, per models teòrics que presenten una relació esforç-ritme de cisalla lineal en fluxos unidireccionals, com el model de Maxwell.

Hem mostrat que en fluxos confinats existeix la possibilitat que les ones de cisalla generades a diferents posicions se sobreposin abans d'esmorteïr-se i eventualment donin lloc a un fenomen de ressonància. Pel cas d'un tub vertical, a les ressonàncies la velocitat al centre del tub es troba en fase amb l'acceleració del pistó, i el mòdul de la velocitat és màxim.

Amb l'equació constitutiva d'Oldroyd-B hem mostrat que l'addició d'un dissolvent Newtonià (per petita que sigui) fa que les ressonàncies desapareguin. Tan sols esperem observar aquest fenomen ressonant per fluids molt especials, com les solucions micel·lars de tipus cuc.

Experiments: règim laminar

Hem dut a terme una investigació experimental fent servir el fluid micel·lar descrit anteriorment. Hem fet experiments del flux oscil·latori per tot el rang de freqüències i amplituds petites del forçament i hem determinat amb gran precisió la posició dels pics de ressonància. Els resultats experimentals mostren un bon acord quantitatiu amb les prediccions teòriques.

Hem realitzat un estudi acurat de l'estructura del flux laminar a freqüències de ressonància i fora de les ressonàncies. La forma dels perfils de velocitat depèn fortament de la freqüència d'oscil·lació. A freqüències petites tot el fluid es mou en la mateixa direcció, però el flux esdevé molt més inflecional a mesura que la freqüència d'oscil·lació augmenta i el flux s'organitza en diferents regions concèntriques que es mouen amunt i avall. La condició de no-lliscament se satisfà a les parets del tub.

Finalment hem verificat que quan incrementem l'amplitud de les oscil·lacions la resposta del fluid esdevé fàcilment no-lineal. Per tal de capturar teòricament les no-linealitats presents en les nostres dades experimentals, caldria utilitzar una equació constitutiva amb un terme no-lineal per l'esforç de cisalla, que tingués en compte la no-monotonicitat de la corba de flux de les solucions micel·lars.

Experiments: inestabilitats hidrodinàmiques

Hem explorat el flux oscil·latori en un tub vertical per tot el rang de freqüències i amplituds del forçament accessibles experimentalment, i classificat el flux en tres règims ben diferenciats: laminar, vortical i vortical no-axisimètric. Fent rampes d'amplitud creixent a una freqüència fixada hem pogut caracteritzar la transició del flux laminar a fluxos més complexos, sota condicions de forçament ben controlades.

La primera inestabilitat apareix quan el flux laminar esdevé inestable amb la corresponent formació d'anells de vorticitat apilats al llarg del tub. Per tal de determinar amb gran precisió l'amplitud crítica a la qual el flux laminar esdevé vortical hem calculat la desviació típica de les fluctuacions de la component vertical i radial de la velocitat en la direcció vertical. A l'amplitud crítica en què la inestabilitat es manifesta s'observa un increment sobtat de les fluctuacions. Fent

rampes d'amplitud creixent i decreixent hem observat que aquesta primera bifurcació presenta histerèsi, de manera que la bifurcació del flux laminar al flux vortical és subcrítica.

Encara es manifesta una segona inestabilitat per amplituds del forçament més grans, per la qual el flux vortical perd la simetria axial. En aquest nou règim els vòrtex estan fortament distorsionats i no són axisimètrics. Aquesta segona transició també presenta histèresi i per tant també creiem que és de caràcter subcrític.

Una inspecció global de tot el tub ha permès elucidar que la inestabilitat apareix a forçaments més petits a les regions del tub més properes al pistó. D'altra banda hem descobert l'existència d'una dinàmica espacio-temporal que apareix a escales de temps llargues (molt més llargues que el temps de relaxació del fluid) que modifiquen substancialment l'organització del flux. Aquesta dinàmica lenta és més efectiva a les regions inferiors del tub.

El mecanisme desencadenant de les inestabilitats hidrodinàmiques que hem caracteritzat encara no és clar. La viscoelasticitat del fluid utilitzat juga un paper innegable ja que experiments previs fets per (Torralba et al., 2007) amb un oli Newtonià de densitat i viscositat similars a la solució micel·lar, i per forçaments comparables, no mostraven la inestabilitat. De tota manera, pot ser que la inestabilitat no sigui purament d'origen elàstic i que altres factors contribueixin a desencadenar-la. En particular hem avaluat la influència que pot tenir la recirculació de fluid prop del pistó (i que apareix com a conseqüència de la longitud finita del tub). I també hem mirat la possible influència de la inestabilitat de *shear banding* de la solució micel·lar (segons la qual el fluid es pot estructurar en diferents bandes de cisalla). Cap dels dos factors, però, sembla ser el causant de l'aparició del flux vortical.

List of publications

Part of the original work reported in this Thesis is based on the following publications:

- Casanellas, L., Ortín, J., (2012), "Laminar oscillatory flow of Maxwell and Oldroyd-B fluids: theoretical analysis", *J. Non-Newtonian Fluid Mech.*, **166**, 1315 - 1326.
- Casanellas, L., Ortín, J., (2012), "Experiments on the laminar oscillatory flow of wormlike micellar solutions", *Rheol. Acta*, **51**, 545 - 557.

Complementary work performed during my PhD, which has not been included in this Thesis, is reflected in the following publications:

- Dimitriou, C.J., Casanellas, L., Ober, T.J., McKinley, G.H., (2012), "Rheo-PIV of a shear-banding wormlike micellar solution under large amplitude oscillatory shear", *Rheol. Acta*, **51**, 395 - 411.
- Frigola, D., Casanellas, L., Sancho, J.M., Ibañes, M., (2012), "'Asymmetric Stochastic Switching Driven by Intrinsic Molecular Noise"', *PlosONE*, **7**, e31407.

The remainder of the results presented in the Thesis will be published in the near future. In the following I list the publications currently in preparation:

- Casanellas, L., Ortín, J., "Vortex ring formation in oscillatory pipe flow of wormlike micellar solutions", *In preparation.*
- Casanellas, L., Dimitriou, C.J., Ober, T.J., McKinley, G.H., "Spatiotemporal dynamics of multiple shear banding under imposed steady shear flow", *In preparation.*

Appendix A

Tensors

We provide in this Appendix the expressions for the stress and rate-of-strain tensors in the laminar flow, in a cylindrical geometry (and thus in cylindrical coordinates). An analogous derivation would apply for a rectangular geometry (in Cartesian coordinates). We also provide the expressions for their upper-convected derivatives, required for the UCM and Oldroyd-B constitutive equations (Eqs. (1.12), (1.13), (1.14)).

The fluid velocity, in the laminar flow, is restricted to the vertical direction and exhibits only a dependence on the radial coordinate, as $\boldsymbol{u} = (0, 0, u_z(r))$ (and in the case of a rectangular geometry $\boldsymbol{u} = (0, 0, u_z(x))$, Sec. 4.1.1). The stress tensor reads:

$$\boldsymbol{\tau} = \begin{pmatrix} \tau_{rr} & 0 & \tau_{zr} \\ 0 & \tau_{\theta\theta} & 0 \\ \tau_{zr} & 0 & \tau_{zz} \end{pmatrix}, \tag{A.1}$$

where we have used that $\boldsymbol{\tau}$ is symmetric (Bird et al., 1987). The matrix elements involving the azimuthal direction, $\tau_{\theta r}$ and $\tau_{\theta z}$ (and their symmetric counterparts), are zero in this configuration. The upper-convected derivative of the stress tensor (Eq. 1.13) reads,

$$\boldsymbol{\tau}_{(1)} = \frac{\partial \boldsymbol{\tau}}{\partial t} + (\boldsymbol{u} \cdot \boldsymbol{\nabla})\, \boldsymbol{\tau} - \left\{ (\boldsymbol{\nabla} \boldsymbol{u})^{\dagger} \cdot \boldsymbol{\tau} + \boldsymbol{\tau} \cdot (\boldsymbol{\nabla} \boldsymbol{u}) \right\}. \tag{A.2}$$

The nonlinear advective term in this geometry is identically zero, because the elements of the stress matrix, τ_{ij}, do not depend on the vertical coordinate z:

$$(\boldsymbol{u} \cdot \boldsymbol{\nabla})\boldsymbol{\tau} = u_z \frac{\partial}{\partial z} \begin{pmatrix} \tau_{rr} & 0 & \tau_{zr} \\ 0 & \tau_{\theta\theta} & 0 \\ \tau_{zr} & 0 & \tau_{zz} \end{pmatrix} = 0. \tag{A.3}$$

And the computation of the last term in the r.h.s of Eq. (A.2) leads to

$$(\boldsymbol{\nabla u})^{\dagger}\cdot\boldsymbol{\tau}+\boldsymbol{\tau}\cdot(\boldsymbol{\nabla u}) = (\boldsymbol{\tau}\cdot\boldsymbol{\nabla u})^{\dagger}+\boldsymbol{\tau}\cdot\boldsymbol{\nabla u} \quad (A.4)$$

$$= \frac{\partial u_z}{\partial r}\begin{pmatrix} 0 & 0 & \tau_{rr} \\ 0 & 0 & 0 \\ \tau_{rr} & 0 & 2\tau_{zr} \end{pmatrix}. \quad (A.5)$$

The upper-convected derivative for the (symmetric) rate-of-strain tensor reads:

$$\boldsymbol{\gamma}_{(1)} = \dot{\boldsymbol{\gamma}} = \boldsymbol{\nabla u} + (\boldsymbol{\nabla u})^{\dagger} = \begin{pmatrix} 0 & 0 & \frac{\partial u_z}{\partial r} \\ 0 & 0 & 0 \\ \frac{\partial u_z}{\partial r} & 0 & 0 \end{pmatrix}, \quad (A.6)$$

where the non-zero deviatoric terms account for the shear flow that is imposed.

We can write the Upper-Convected Maxwell constitutive equation (Eq.(1.12)) for each non-zero component of the stress tensor as

$$(1+\lambda\frac{\partial}{\partial t})\tau_{rr} = 0, \quad (A.7)$$

$$(1+\lambda\frac{\partial}{\partial t})\tau_{\theta\theta} = 0, \quad (A.8)$$

$$(1+\lambda\frac{\partial}{\partial t})\tau_{zz} - 2\lambda\tau_{zr}\frac{\partial u_z}{\partial r} = 0, \quad (A.9)$$

$$(1+\lambda\frac{\partial}{\partial t})\tau_{zr} - \lambda\tau_{rr}\frac{\partial u_z}{\partial r} = \eta_p\frac{\partial u_z}{\partial r}. \quad (A.10)$$

This set of equations can be used to estimate the normal stress differences $\tau_{zz}-\tau_{rr}$ in the cylindrical geometry and for specific shear flows. Note that both τ_{rr} and $\tau_{\theta\theta}$ decay exponentially in time (Eqs. (A.7) and (A.8)) so that we can assume that these two terms are zero. Using this simplification we arrive to the final equation for the deviatoric terms of the UCM constitutive equation

$$(1+\lambda\frac{\partial}{\partial t})\tau_{zr} = \eta_p\frac{\partial u_z}{\partial r}. \quad (A.11)$$

This is the expression used in the calculations developed in Sec. 4.1.

Appendix B

Stereo PIV

A new Stereo PIV system is currently being implemented in the *Laboratori de Física no Lineal* in Barcelona. This system will bring information about the out-of-plane component of the velocity, u_θ, and allow to completely characterize the velocity field (u_r, u_θ, u_z) in a 2D meridional plane of the tube. A second high speed camera is required for the stereo configuration. Also, the thickness of the laser sheet needs to be broadened, using an additional divergent lens placed within the laser path. The precise thickness of the laser sheet that is required depends on the magnitude of the out-of-plane component.

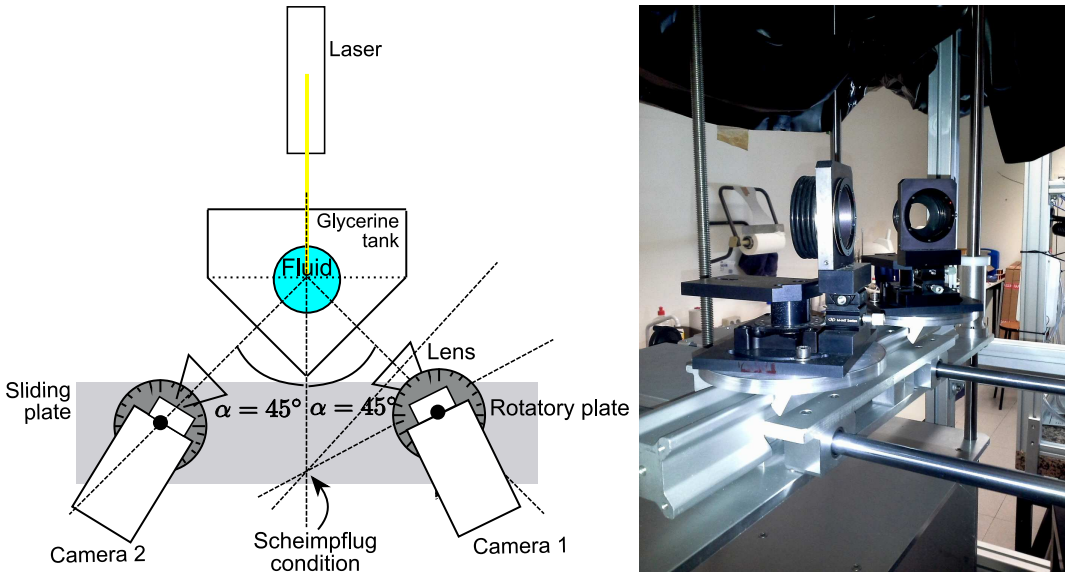

Figure B.1: Left: The different elements required for Stereo PIV (cameras, laser, outer tank, rotatory plates) and the accomplishment of the Scheimpflug condition are included. Right: Scheimpflug adapters and sliding plate implemented in the laboratory for the stereo PIV experiments.

Figure B.1 shows the arrangement of the two cameras and the laser light sheet. The cameras are placed at an angle of 90°, each one on a different side of the laser sheet. The measurement precision of u_θ increases with the opening angle between the two cameras and is maximum when this angle reaches 90° (Raffel et al., 2007; Hof et al., 2004). Thus, the proposed configuration should be optimal in resolving the azimuthal component of the velocity field. However, this recording configuration makes it more difficult to focus the image plane entirely. In order to partially solve this problem a Scheimpflug adapter is mounted on each camera, allowing the objective lens of each camera to rotate with respect to its own optical axis. The Scheimpflug condition states that the image plane, the lens plane and the object plane must intersect in a common line. This condition improves the focus of the seeding particles in the meridional plane of the tube, i.e. image plane (Prasad, 1995). On the other hand we have chosen to place the cameras at the back side of the tube, with respect to the laser beam. According to the Mie theory, the light scattered by the seeding particles is not homogeneous and it is significantly larger at the back. Hence, this recording configuration should maximize the brightness of the PIV images.

A final calibration, using a commercial Stereo PIV software, is needed to perform the geometric reconstruction of the complete velocity field, from the two projected planar displacement fields captured simultaneously by the two cameras.

A mechanical framework has also been implemented in the laboratory, to enable the rotation of the two cameras independently as well as their vertical and horizontal motion.

A new outer tank, built in polycarbonate, has been designed and fabricated with a convenient geometry for the stereo configuration. When filled with glycerine it should avoid most of the optical aberrations caused by the cylindrical surface of the tube. Two rear sides of the tank, through which the cameras record the fluid flow, form an angle of 90°, whereas the front one, through which the laser shines the fluid, is at 45° from them.

Appendix C

Spatiotemporal dynamics of multiple shear banding under imposed steady shear flow

The aim of this Appendix is to report the main results obtained during my second research stay at the Hatsopoulos Microfluids Laboratory at MIT, from April 1st to June 30th 2012. We studied the spatiotemporal dynamics of shear banding under an imposed steady shear flow.

In this work we used the same wormlike micellar solutions that have been described in Chap. 3, CPyCl/NaSal at [100:60] mM (concentrated solution) and [66:40] mM (diluted solution). As described in this previous chapter, the bulk rheology of the concentrated micellar solution has been extensively studied by many authors in the last decades (Rehage and Hoffmann, 1991; Berret et al., 1994; Grand et al., 1997; Porte et al., 1997; Pipe et al., 2010). However, the number of experiments on flow visualization using this micellar solution is more reduced. Britton and Callaghan (1997) performed the first visualization experiments using Nuclear Magnetic Resonance and unraveled the formation of shear bands under steady shear, in a cone-plate geometry. Their technique did not enable to visualize fast transients in the fluid response, becasue long times were required to process the NMR images. Most of the visualization experiments performed subsequently were realized on a Taylor-Couette flow (Sec. 1.1). Flow visualitzation of time dependent flows under steady shear was also studied by Miller and Rothstein (2007) and López-Gónzalez et al. (2006). The latter reported spatiotemporal fluctuations in shear-banded velocity profiles seen by NMR. The work by Hu et al. (2008) and Hu (2010) studied the kinetics and mechanism of shear banding for different surfactant concentrations using Particle Tracking Velocimetry, but also focused mainly on Taylor-Couette and plate-plate geometries.

The aim of our set of experiments was to characterize the transient response of wormlike micellar solutions under an imposed steady shear flow, in a cone-plate geometry. We combined conventional rheometry with a PIV visualization technique, which enabled to simultaneously couple the temporal stress response with the temporal evolution of the velocity field inside the sample. We used a well defined protocol, consisting on a stepped applied shear rate for increasing shear rate values, and explored both the linear and nonlinear response of the fluid. The two different micellar solutions with different surfactant concentrations were studied in order to investigate the effect of the concentration on the formation of shear bands.

C.1 Rheo-PIV experimental setup

We used a Rheo-PIV experimental setup, consisting on a controlled-stress rheometer AR-G2 (TA Instruments), with a cone-plate geometry, to which a Particle Image Velocimetry system was implemented. A top transparent plastic (or quartz) plate and a tilted mirror were required to illuminate the sample with a laser beam. An schematic view of the Rheo-PIV device is shown in Fig. C.1. A more detailed description is provided in Dimitriou et al. (2011). A new PIV configuration that had recently been implemented in the laboratory was employed, in which the PIV images were recorded through the tilted surface of the top plate (Fig. C.1(b)). This new configuration overcame the imaging difficulties encountered in the old configuration (Fig. C.1(a)), in which the images were recorded through the fluid meniscus, that were mainly caused by edge irregularities appearing at moderate shear rates. Besides, the new configuration enabled to image at different radial locations and characterize the velocity field along the radial coordinate.

Figures C.1 (c) and (d) show the calibration experiments performed using a Newtonian mineral oil. Within experimental error, the velocity profiles exhibit a linear dependence along the gap width, which is well captured with a linear fit. In the new configuration the theoretical velocity profiles exhibit a slight quadratic dependence on the vertical coordinate, y. However for relatively small angles of incidence of the laser beam ($\alpha_1 \lesssim 40^\circ$, Fig. C.1(b)), the theoretical velocity profiles are linear to a good approximation. In all cases quadratic deviations are much smaller than the experimental uncertainty.

Shearing protocol

Experimentally, we performed ramps of increasing imposed shear rates and measured the stress response of the fluid, shown schematically in Fig. C.2. Steps of

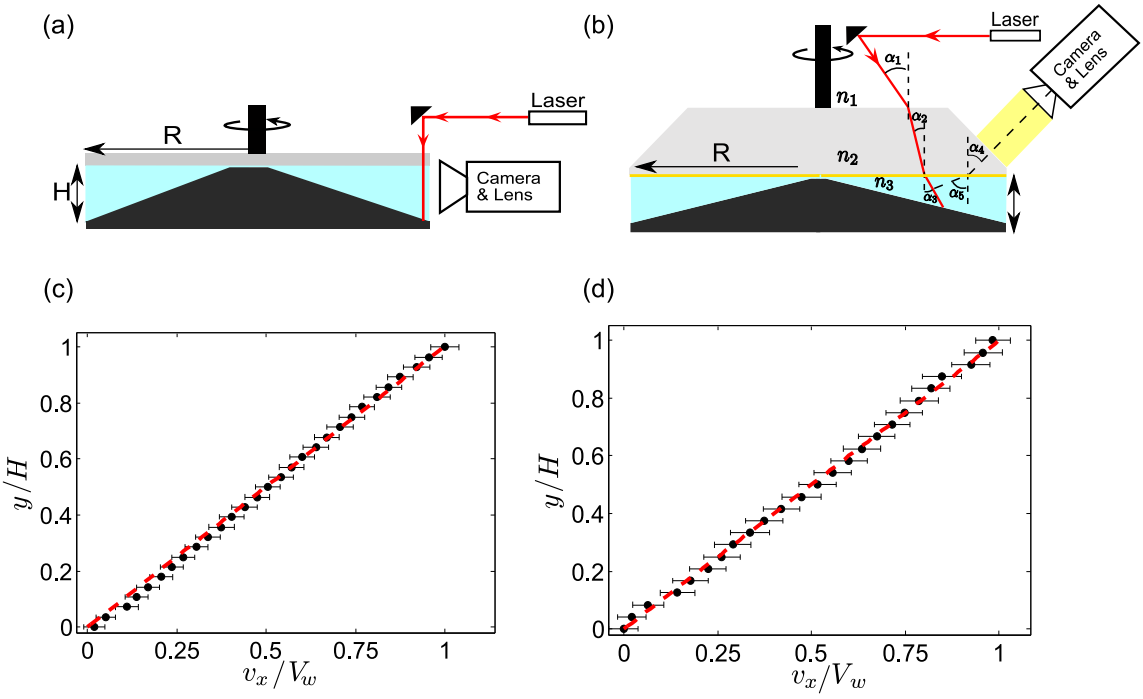

Figure C.1: Schematic view of the Rheo-PIV experimental setup. The imaging could be achieved either through the fluid meniscus (a) or through the tilted surface (b). In both configurations the calibration using a Newtonian mineral oil provided linear velocity profiles (panel (c): old configuration (a); panel (d): new configuration (b)). The vertical position along the gap y, has been made dimensionless dividing by the gap width H. The velocity along the x direction, v_x, has also been made dimensionless by measuring it in units of the velocity of the upper plate, V_w.

$\Delta\dot{\gamma} = 0.3$ s^{-1} were applied for the concentrated solution and $\Delta\dot{\gamma} = 0.6$ s^{-1} for the diluted solution, being $\dot{\gamma} = 0.1$ s^{-1} the initial shear rate applied in all experiments. Typically time intervals $\Delta t = 180$ s were spent at each shearing rate. All the experiments were performed at $T = 25.0$°C.

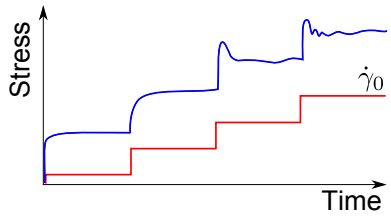

Figure C.2: Sketch of the shearing protocol used in the experiments, consisting on steps of increasing shear rates.

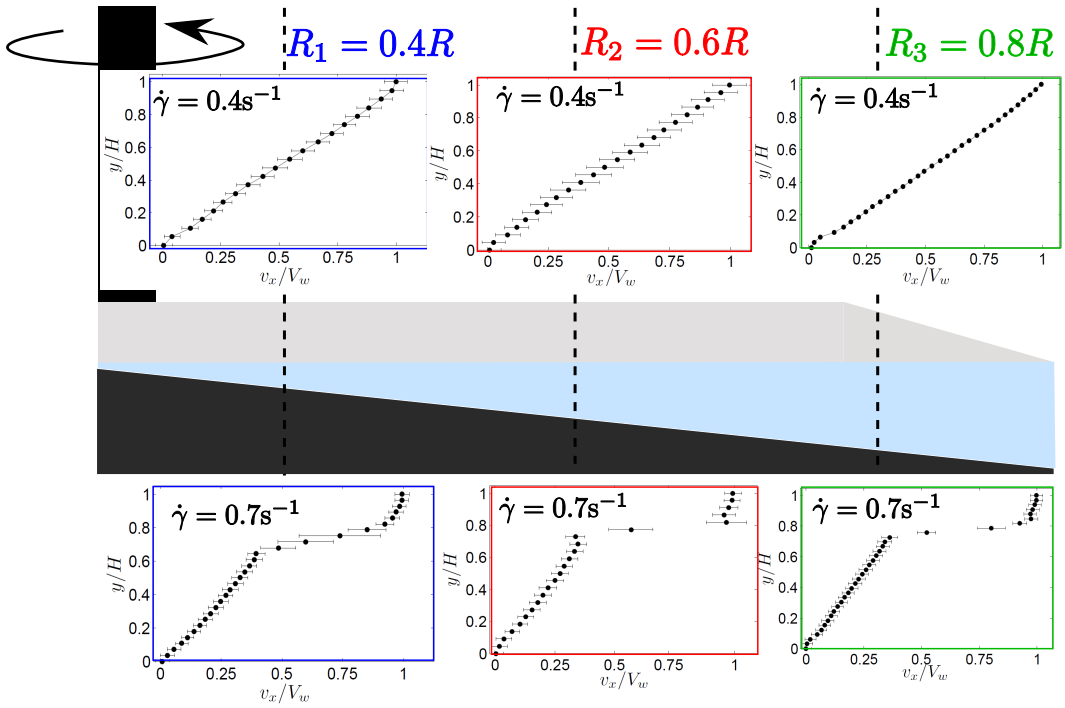

Figure C.3: Schematic view of the cone-plate geometry used in the experiments. The velocity profiles measured at different radii (0.4R, 0.6R, and 0.8R) are depicted in the top ($\dot{\gamma} = 0.4$ s^{-1}) and bottom panels ($\dot{\gamma} = 0.7$ s^{-1}).

Radial dependence

We measured the velocity field at different radial locations and verified that there was no substantial dependence on the radial coordinate. These observations were in good agreement with previous results reported by Britton and Callaghan (1997). Figure C.3 shows the velocity profiles measured at three different radii ($r_i = 0.4R$, $0.6R$, and $0.8R$) and two different shearing rates ($\dot{\gamma} = 0.4$ and 0.7 s^{-1}). In the linear regime (top panels) the velocity profiles are linear in the entire geometry. In the nonlinear regime the fluid experiences a non-homogeneous deformation that is mantained all along the radial coordinate. Only small differences are observed, regarding the steepness of the velocity profile. All the results provided in the rest of the appendix are obtained at $r_i \simeq 0.7R$.

C.2 Transient response under steady shear

Diluted micellar solution

The experiments performed using the diluted micellar solution are shown in Fig. C.4. The stress relaxes very fast ($t_{relax} \leq 10$ s) for all applied shear rates (even for

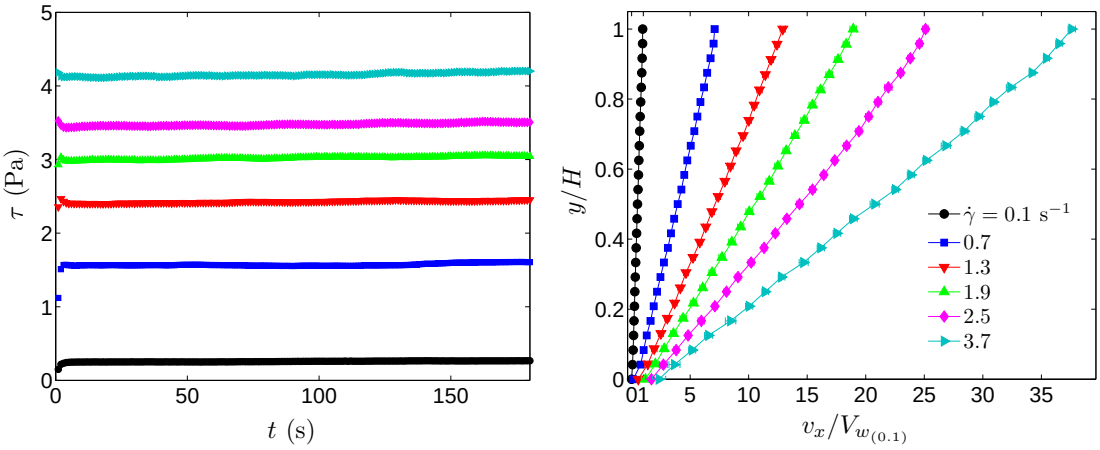

Figure C.4: Stress relaxation under imposed steady shear (left) and velocity profiles (right) measured at increasing shear rates for the diluted micellar solution CPyCl/NaSal [66:40] mM. The velocity has been made dimensionless by measuring it in units of the velocity of the upper plate corresponding to an imposed shear rate of $\dot{\gamma} = 0.1$ s^{-1}, $V_w(0.1)$.

$Wi > 1$). Accordingly, the velocity profiles are linear for all explored shear rates. Note that, even for shear rates belonging to the (nonlinear) shear-thinning regime the profiles look linear, and only a small amount of slip at the bottom surface is observed for the largest shear rates ($\dot{\gamma} = 2.5$, 3.7 s^{-1} in the figure).

These observations corroborate that the diluted micellar solution does not shear-band, at least for the range of shear rates explored. Although we are experimentally limited to this shearing range, both the monotonicity of the flow curve and the absence of hysteresis when ramping up and down the applied shear rate (Chap. 3) seem to indicate that this solution strongly shear-thins but does not shear-band.

Stress relaxation & Onset of elastic instability

The results are qualitatively different for the concentrated micellar solution, as shown in Fig. C.5. In the limit of small shear rates ($Wi < 1$), the stress also relaxes very fast, $t_{relax} < 20$ s. In this shearing regime ($\dot{\gamma} = 0.1$ and 0.4 s^{-1} in the figure) the velocity profiles look linear.

However, under imposed shear rates slightly above the critical shear rate, $\dot{\gamma} \gtrsim \dot{\gamma}_c = 0.5$ s^{-1}, the fluid response exhibits long transients. Figure C.6 shows the stress relaxation measured at $\dot{\gamma} = 0.7$ s^{-1}, over 900 s. The velocity profiles measured at different lapses of time reflect the progressive evolution of the spatiotemporal flow organization. Right after the shear rate is imposed, at timescales

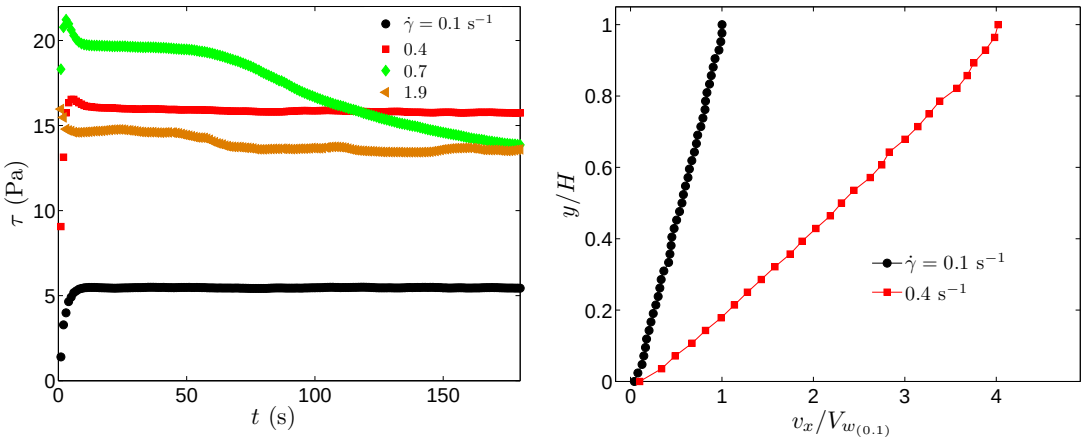

Figure C.5: Stress relaxation under imposed steady shear (a) and velocity profiles (b) measured at increasing shear rates for the concentrated micellar solution CPyCl/NaSal [100:60] mM. The velocity has been made dimensionless by measuring it in units of the velocity of the upper plate corresponding to an imposed shear rate of $\dot{\gamma} = 0.1$ s^{-1}, $V_w(0.1)$.

comparable to the fluid relaxation, there is an stress overshoot. After this sudden increase, the stress relaxation exhibits a long decay. At short times ($t \leq 50$ s) there exists an initial transient linear response (A in the figure). Next, the long decay in the stress relaxation is accompanied by the reorganization of the fluid in different shear bands (B, C). The fluid flow becomes structured in three different bands, with a highly-shear-rate band in the center, and two low-shear-rate bands at the boundaries. At longer times, $200 \leq t \leq 500$ s, the shear stress reaches a quasi-steady state ($\tau \simeq 12.5$ Pa). During this time interval the shear bands remain almost steady in time (D, E, F). At even longer times ($t > 500$ s) the stress slightly increases. We attribute this stress increase to the onset of a curved streamline instability (G) (Pakdel and McKinley, 1996; Grand et al., 1997; Lerouge et al., 2008). Once the elastic instability sets in we observe a dynamic shear-banding behavior. The location of the central highly sheared band moves significantly through the gap width (H, I, J, K).

Shear banded velocity profiles

At larger shear rates ($\dot{\gamma} > \dot{\gamma}_c$) the shear-banded profile is maintained. Well above the critical shear rate $\dot{\gamma}_c$, the transients in the stress response relax faster, and typically $t_{relax} \simeq 100$ s (Fig. C.5(left)). However the stress response does not reach a strict steady state and slight fluctuations still appear even on long time scales.

The 3-banded velocity profiles are consistent with previous results obtained by Britton and Callaghan (1997) under steady shear and Dimitriou et al. (2012) under

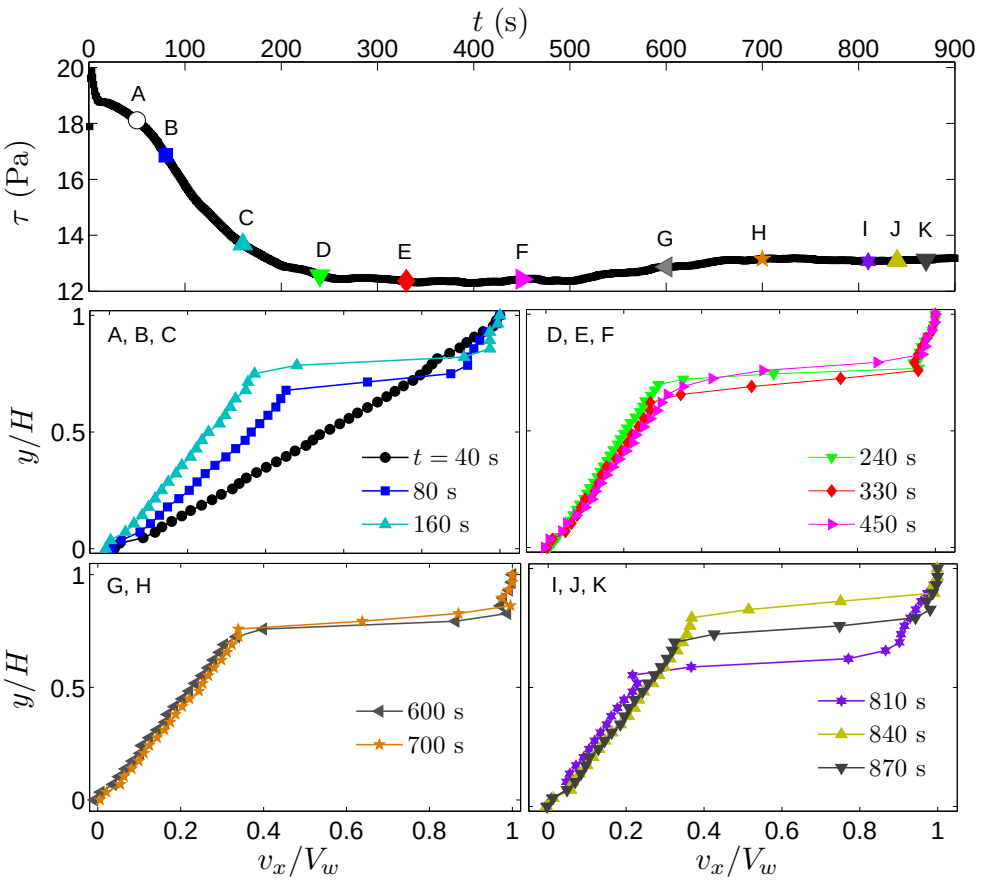

Figure C.6: Stress relaxation measured at $\dot{\gamma} = 0.7$ s^{-1} over 900 s for the [100:60] mM solution (top), and velocity profiles measured at different time lapses (denoted with letters in the figure). The velocity has been made dimensionless, in each case, by measuring it in units of the velocity of the upper plate, V_w.

large amplitude oscillatory shear flow. However the velocity profiles reported by the latter under LAOS exhibited a rather smoother shape than the profiles presented here. The velocity profiles under steady shear are well reproduced by the functional form provided by Dimitriou et al. (2012). In Fig. C.7(left) we show, as an example, the velocity profile measured at $\dot{\gamma} = 1.9$ s^{-1}. In red we depict the fit obtained using the functional form in Dimitriou et al. (2012) (Eq. 3). The shear rate provided by the fit for the low-shear-rate band is $\dot{\gamma} = 0.3$ s^{-1}, which fairly coincides with the shear rate at the beginning of the stress plateau, and $\dot{\gamma} \simeq 40$ s^{-1} for the high-shear-rate band. Unfortunately, this value is close to the largest shear rate that can be resolved with our experimental setup, that is limited by the cross-correlation process. However, the experimental shear rate obtained for the high-shear-rate band is still compatible with the shear rate value that would correspond to the end of the stress plateau, of $\dot{\gamma} \simeq 500$ s^{-1} (depicted in blue in the figure).

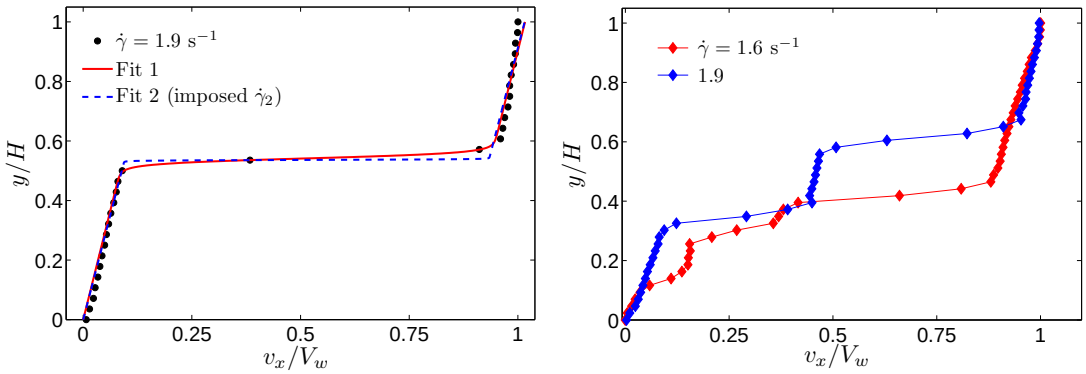

Figure C.7: Nonlinear velocity profiles obtained for the concentrated micellar solution [100:60] mM. Left: Three-banded velocity profile measured at $\dot{\gamma} = 1.9$ s^{-1}. The red and blue solid lines are fits to the experimental data. Right: five-banded and seven-banded velocity profiles measured at $\dot{\gamma} = 1.9$ s^{-1} and $\dot{\gamma} = 1.6$ s^{-1}, respectively. The velocity has been made dimensionless, in each case, by measuring it in units of the velocity of the upper plate, V_w.

In several tests, and for $\dot{\gamma} > \dot{\gamma}_c$, we have observed the formation of a larger number of bands. In particular five different bands have been frequently reported (Fig. C.7) and, on rare occasions, even seven! We have also observed in some cases velocity profiles with a clear spatio-temporal dependence, exhibiting an evolution from five to three bands, or viceversa. We have not identified a systematic criterion to predict the appearance of a larger number of bands, apart from $Wi > 1$.

Spatial fluctuations

This manifest temporal evolution of the shear banded profiles implicitly suggests that the velocity field indeed exhibits important spatial fluctuations, that in some cases may be strong enough to induce important changes in the flow organization (e.g. diminishing, or incrementing, the number of shear bands). In Fig. C.8 we show two particular examples of the velocity field obtained at $\dot{\gamma} = 1.3$ s^{-1} and $\dot{\gamma} = 1.9$ s^{-1}. In the panel on the right there is a homogeneous 3-banded profile that is maintained along the horizontal coordinate, and in this case is then appropriate to average along the horizontal coordinate to obtain the average velocity profile. In the panel on the left the velocity field is slightly more complicated, displaying five shear bands. More interestingly, significant heterogeneities are observed along the horizontal coordinate. These heterogeneities would translate into larger error bars if the averaged velocity profile was computed.

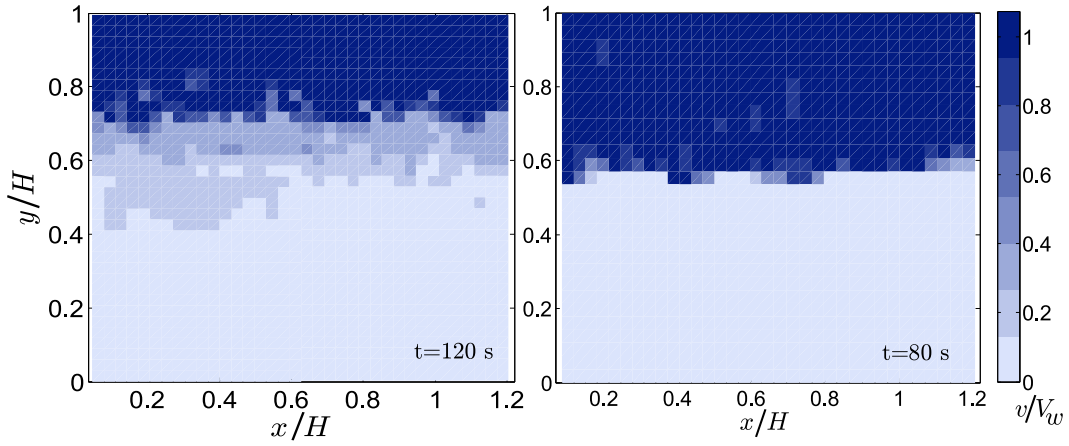

Figure C.8: Velocity field measured for the concentrated solution. Left: velocity field captured after 120 s from the start-up flow set to $\dot{\gamma} = 1.3\ s^{-1}$. Right: velocity field captured after 80 s from the start-up flow set to $\dot{\gamma} = 1.9\ s^{-1}$. The velocity (color bar) has been made dimensionless, in each case, by measuring it in units of the velocity of the upper plate, V_w.

We pressume that this complex spatiotemporal dynamics observed for the shear banded profiles might be caused by the existence of the onset of an elastic instability that would disturb the flow, leading to a complicated temporal flow evolution with important spatial fluctuations.

References

Adams, J. M., Fielding, S. M. and Olmsted, P. D. (2008), "The interplay between boundary conditions and flow geometries in shear banding: Hysteresis, band configurations, and surface transitions", *J. Non-Newtonian Fluid Mech.*, **151**, 101–118.

Adler, F., Sawyer, W. and Ferry, J. (1949), "Propagation of transverse waves in viscoelastic media", *J. Appl. Phys.*, **20**, 1036–1041.

Adrian, R. J. (1991), "Particle-Imaging Techniques for Experimental Fluid-Mechanics", *Annu. Rev. Fluid Mech.*, **23**, 261–304.

Akhavan, R., Kamm, R. and Shapiro, A. (1991), "An investigation of transition to turbulence in bounded oscillatory Stokes flows. Part 1. Experiments", *J. Fluid Mech.*, **225**, 395–422.

Andrienko, Y. A., Siginer, D. A. and Yanovsky, Y. G. (2000), "Resonance behavior of viscoelastic fluids in Poiseuille flow and application to flow enhancement", *Int. J. Non-Linear Mech.*, **35**, 95–102.

Azzouzi, H., Decruppe, J. P., Lerouge, S. and Greffier, O. (2005), "Temporal oscillations of the shear stress and scattered light in a shear-banding-shear-thickening micellar solution", *Eur. Phys. J. E*, **17**, 507–514.

Barnes, H., Townsend, P. and Walters, K. (1969), "Flow of non-Newtonian liquids under a varying pressure gradient", *Nature*, **224**, 585–587.

Barnes, H., Townsend, P. and Walters, K. (1971), "Pulsatile flow of non-Newtonian liquids", *Rheol. Acta*, **10**, 517–527.

Batchelor, G. K. (1967), *An Introduction to Fluid Dynamics*, Cambridge: Cambridge University Press.

Bécu, L., Manneville, S. and Colin, A. (2004), "Spatiotemporal dynamics of wormlike micelles under shear", *Phys. Rev. Lett.*, **93**, 018301:1–4.

Berret, J.-F. (1997), "Transient Rheology of Wormlike Micelles", *Langmuir*, **13**(8), 2227–2234.

Berret, J.-F., Roux, D. C. and Porte, G. (1994), "Isotropic-to-nematic transition in wormlike micelles under shear", *J. Phys. II France*, **4**, 1261–1279.

Bird, R. B., Armstrong, R. C. and Hassager, O. (1987), *Dynamics of Polymeric Liquids Vol. 1, 2*, second edn, John Wiley and Sons.

Blennerhassett, P. J. and Bassom, A. P. (2006), "The linear stability of high-frequency oscillatory flow in a channel", *J. Fluid. Mech.*, **556**, 1–25.

Boger, D. V. (1977), "A highly elastic constant-viscosity fluid", *J. Non-Newtonian Fluid Mech.*, **3**, 87–91.

Boukany, P. and Wang, S. Q. (2008), "Use of particle-tracking velocimetry and flow birefringence to study nonlinear flow behavior of entangled wormlike micellar solution: from wall slip, bulk disentanglement to chain scission", *Macromolecules*, **41**, 1455–1464.

Britton, M. and Callaghan, P. (1997), "Two-Phase Shear Band Structures at Uniform Stress", *Phys. Rev. Lett.*, **78**(26), 4930–4933.

Byars, J., Oztekin, A., Brown, R. and McKinley, G. (1994), "Spiral instabilities in the flow of highly elastic fluids between rotating parallel disks", *J. Fluid Mech.*, **271**, 173.

Callaghan, P. T. (2008), "Rheo NMR and shear banding", *Rheol. Acta.*, **47**, 243–255.

Cappelaere, E. and Cressely, R. (1997), "Shear banding structure in viscoelastic micellar solutions", *Coll. and Polym. Sci.*, **275**, 407–418.

Castrejón-Pita, J. R., del Río, J. A., Castrejón-Pita, A. A. and Huelsz, G. (2003), "Experimental observation of dramatic differences in the dynamic response of Newtonian and Maxwellian fluids", *Phys. Rev. E*, **68**, 046301–046305.

Cates, M. E. and Fielding, S. M. (2006), "Rheology of giant micelles", *Adv. Phys.*, **55**(7-8), 799–879.

Crandall, I. (1926), *Theory of Vibrating Systems and Sounds*, D. Van Nostrand Co., New York.

Cromer, M., Cook, L. P. and McKinley, G. (2011), "Pressure-driven flow of wormlike micellar solutions in rectilinear microchannels", *J. Non-Newtonian Fluid Mech.*, **166**, 180–193.

Davies, J., Bhumiratana, S. and Bird, R. (1978), "Elastic and inertial effects in pulsatile flow of polymeric liquids in circular tubes", *J. Non-Newtonian Fluid Mech.*, **3**, 237–259.

de Gennes, P.-G. (1979), *Scaling Concepts in Polymer Physics*, Cornell University Press, Ithaca.

Decruppe, J. P., Lerouge, S. and Berret, J.-F. (2001), "Insight in shear banding under transient flow", *Phys. Rev. E*, **63**, 022501:1–4.

del Río, J. A., López de Haro, M. and S., W. (1998), "Enhancement in the dynamic response of a viscoelastic fluid flowing in a tube", *Phys. Rev. E*, **58**, 6323–6327.

del Río, J. A., López de Haro, M. and S., W. (2001), "Erratum: Enhancement in the dynamic response of a viscoelastic fluid flowing in a tube [Phys Rev E **58**, 6323 (1998)]", *Phys. Rev. E*, **64**, 039901(E).

Didden, N. (1979), "On the formation of vortex rings rolling-up and production of circulation", *J. Appl. Math. and Phys. (ZAMP)*, **30**, 101–116.

Dimitriou, C. J., Casanellas, L., Ober, T. J. and Mckinley, G. H. (2012), "Rheo-PIV of a shear-banding wormlike micellar solution under large amplitude oscillatory shear", *Rheol. Acta*, **51**, 395–411.

Dimitriou, C. J., McKinley, G. H. and Venkatesan, R. (2011), "Rheo-PIV Analysis of the Yielding and Flow of Model Waxy Crude Oils", *Energy & Fuels*, **25**, 3040–3052.

Divoux, T., Tamarii, D., Barentin, C. and Manneville, S. (2010), "Transient shear banding in a simple yield stress fluid", *Phys. Rev. Lett.*, **104**, 208301.

Drazin, P. (2002), *Introduction to Hydrodynamic Stability*, Cambridge University Press.

Eckmann, D. and Grotberg, J. (1991), "Experiments on transition to turbulence in oscillatory pipe flow", *J. Fluid Mech.*, **222**, 329–350.

Ewoldt, R., Hosoi, A. and McKinley, G. (2008), "New measures for characterizing nonlinear viscoelasticity in large amplitude oscillatory shear", *J. Rheol.*, **52**(6), 1427–1458.

Fall, A., Bertrand, F., Ovarlez, G. and Bonn, D. (2009), "Yield Stress and Shear Banding in Granular Suspensions", *Phys. Rev. Lett.*, **103**, 178301.

Fardin, M. A., Divoux, T., Guedeau-Boudeville, M. A., Buchet-Maulien, I., Browaeys, J., McKinley, G. H., Manneville, S. and Lerouge, S. (2012), "Shear-banding in surfactant wormlike micelles: elastic instabilities and wall slip", *Soft Matter*, **8**, 2535–2553.

Fardin, M. A., Lasne, B., Cardoso, O., Grégoire, G., Argentina, M., Decruppe, J. P. and Lerouge, S. (2009), "Taylor-like Vortices in Shear-Banding Flow of Giant Micelles", *Phys. Rev. Lett.*, **103**(2), 028302.

Fardin, M. A., Lopez, D., Croso, J., Grégoire, G., Cardoso, O., McKinley, G. H. and Lerouge, S. (2010), "Elastic Turbulence in Shear Banding Wormlike Micelles", *Phys. Rev. Lett.*, **104**(17), 178303.

Ferry, J. (1980), *Viscoelastic properties of polymers*, John Wiley, New York.

Ferry, J. D. (1941), "Studies of the mechanical properties of substances of high molecular weight. I. A photoelastic method for study of transverse vibrations in gels", *Rev. Sci. Instrum.*, **12**, 79–82.

Ferry, J. D. (1942a), "Studies of the mechanical properties of substances of high molecular weight. II. Rigidities of the system polystyrene-xylene and their dependence upon temperature and frequency", *J. Am. Chem. Soc.*, **64**, 1323–1329.

Ferry, J. D. (1942b), "Studies of the mechanical properties of substances of high molecular weight. III. Viscosities of the system polystyrene-xylene", *J. Am. Chem. Soc.*, **64**, 1330–1336.

Fischer, P. and Rehage, H. (1997), "Rheological master curves of viscoelastic surfactant solutions by varying the solvent viscosity and temperature", *Langmuir*, **13**(26), 7012–7020.

Gerrard, J. H. and Hughes, M. D. (1971), "The flow due to an oscillating piston in a cylindrical tube : a comparison between experiment and a simple entrance flow theory", *J. Fluid Mech.*, **50**, 97–106.

Gharib, M., Rambod, E. and Shariff, K. (1998), "A universal time scale for vortex ring formation", *J. Fluid Mech.*, **360**, 121–14.

Glezer, A. (1988), "The formation of vortex rings", *Phys. Fluids*, **31**, 3532–3542.

Grand, C., Arrault, J. and Cates, M. E. (1997), "Slow transients and metastability in wormlike micelle rheology", *J.Phys. II France*, **7**, 1071–1086.

Groisman, A. and Steinberg, V. (2000), "Elastic turbulence in a polymer solution flow", *Nature*, **405**, 53 – 55.

Guyon, E., Hulin, J. P., Petit, L. and Mitescu, C. D. (2001), *Physical Hydrodynamics*, Oxford University Press.

Haward, S. J. and McKinley, G. H. (2012), "Stagnation point flow of wormlike micellar solutions in a microfluidic cross-slot device : Effects of surfactant concentration and ionic environment", *Phys. Rev. E*, **031502**, 1–14.

Herrera, E. (2010), "Study on the pulsating flow of a worm-like micellar solution", *J. Non-Newtonian Fluid Mech.*, **165**(3-4), 174–183.

Hino, M., Sawamoto, M. and Takasu, S. (1976), "Experiments on transition to turbulence in an oscillatory pipe flow", *J. Fluid Mech.*, **75**, 193–207.

Hof, B., van Doorne, C. W. H., Westerweel, J., Nieuwstadt, F. T. M., Faisst, H., Eckhardt, B., Wedin, H., Kerswell, R. and Waleffe, F. (2004), "Experimental observation of nonlinear traveling waves in turbulent pipe flow", *Science*, **305**, 1594.

Hu, Y. (2010), "Steady-state shear banding in entangled polymers?", *J. Rheol.*, **54**, 1307–1323.

Hu, Y. T. and Lips, A. (2005), "Kinetics and mechanism of shear banding in an entangled micellar solution", *J. Rheol.*, **49**, 1001–1027.

Hu, Y. T., Palla, C. and Lips, A. (2008), "Comparison between shear banding and shear thinning in entangled micellar solutions", *J. Rheol.*, **52**, 379–400.

Huilgol, R. and Phan-Thien, N. (1986), "Recent advances in the continuum mechanics of viscoelastic liquids", *Int. J. Eng. Sci.*, **24**, 161–261.

James, D. (2009), "Boger fluids", *Annu. Rev. Fluid Mech.*, **41**, 129–142.

Jespersen, S., Thomassen, J., Andersen, A. and Bohr, T. (2004), "Vortex dynamics around a solid ripple in an oscillatory flow", *Euro. Phys. J. B - Condensed Matter and Complex Systems*, **38**, 127–138.

Joseph, D., Narain, A. and Riccius, O. (1986a), "Shear-wave speeds and elastic moduli for different liquids. Part 1. Theory", *J. Fluid Mech.*, **171**, 289–308.

Joseph, D., Narain, A. and Riccius, O. (1986b), "Shear-wave speeds and elastic moduli for different liquids. Part 2. Experiments", *J. Fluid Mech.*, **171**, 309–338.

Krishan, K. and Dennin, M. (2008), "Viscous shear banding in foam", *Phys. Rev. E*, **78**, 051504.

Lambossy, P. (1952), "Oscillations forcées d'un liquide incompressible et visqueux dans un tube rigide et horizontal. Calcul de la force de frottement", *Helv. Physica Acta*, **25**, 371–386.

Larson, R. G. (1999), *The Structure and Rheology of Complex Fluids*, ninth edn, Oxford University Press.

Larson, R., Shaqfeh, E. and Muller, S. (1990), "A purely elastic instability in Taylor–Couette flow", *Journal of Fluid Mechanics*, **218**, 573.

Lerouge, S., Argentina, M. and Decruppe, J. P. (2006), "Interface instability in shearbanding flow", *Phys. Rev. Lett.*, **96**, 088301:1–4.

Lerouge, S. and Berret, J.-F. (2009), *Shear induced transitions and instabilities in surfactant wormlike micelles*, Springer-Verlag Berlin Heidelberg 2009.

Lerouge, S. and Decruppe, J. P. (2000), "Correlations between rheological and optical properties of a micellar solution under shear banding flow", *Langmuir*, **16**, 6464–6474.

Lerouge, S., Fardin, M., Argentina, M., Grégorie, G. and Cardoso, O. (2008), "Interface dynamics in shear banding flow of giant micelles", *Soft Matter*, **4**, 1808–1819.

Lettinga, M. P. and Manneville, S. (2009), "Competition between Shear Banding and Wall Slip in Wormlike Micelles", *Phys. Rev. Lett.*, **103**(24), 248302:1–4.

López-Gónzalez, M. R., Holmes, W. M. and Callaghan, P. T. (2006), "Rheo-NMR phenomena of wormlike micelles", *Soft Matter*, **2**, 855–869.

López-González, M. R., Holmes, W. M., Callaghan, P. T. and Photinos, P. J. (2004), "Shear Banding Fluctuations and Nematic Order in Wormlike Micelles", *Phys. Rev. Lett.*, **93**, 268302:1–4.

Macosko, C. H. (1994), *Rheology principles, measurements, and applications*, VCH Publishers, Inc.

Magda, J. and Larson, R. (1988), "A transition occuring in ideal elastic liquids during shear flow", *J. Non-Newtonian Fluid Mech.*, **30**, 1–19.

Mair, R. W. and Callaghan, P. T. (1997), "Shear flow of wormlike micelles in pipe and cylindrical Couette geometries as studied by nuclear magnetic resonance microscopy", *J. Rheol.*, **41**, 901–924.

Majumdar, S. and Sood, A. K. (2011), "Universality and scaling behavior of injected power in elastic turbulence in wormlike micellar gel", *Phys. Rev. E*, **84**, 015302.

Manero, O. and Walters, K. (1980), "On elastic effects in unsteady pipe flows", *Rheol. Acta*, **19**, 277–284.

Manneville, S. (2008), "Recent experimental probes of shear banding", *Rheol. Acta*, **47**(3), 301–318.

Masselon, C., Salmon, J. B. and Colin, A. (2008), "Nonlocal effects in flows of wormlike micellar solutions.", *Phys. Rev. Lett.*, **1**, 38301:1–4.

McKinley, G. H., Byars, J. A., Brown, R. A. and Armstrong, R. C. (1991), "Observations on the elastic instability in cone-and-plate and parallel-plate flows of a polyisobutylene Boger fluid", *J. Non-Newtonian Fluid Mech.*, **40**, 201–229.

Merkli, P. and Thomann, H. (1975), "Transition to turbulence in oscillating pipe flow", *J. Fluid Mech.*, **68**, 567–575.

Miller, E. and Rothstein, J. P. (2007), "Transient evolution of shear-banding wormlike micellar solutions", *J Non-Newtonian Fluid Mech*, **143**(1), 22 – 37.

Mitran, S., Forest, M., Yao, L., Lindley, B. and Hill, D. (2008), "Extensions of the Ferry shear wave model for active linear and nonlinear microrheology", *J. Non-Newtonian Fluid Mech.*, **154**, 120–135.

Møller, P., Rodts, S., Michels, M. and Bonn, D. (2008), "Shear banding and yield stress in soft glassy materials", *Phys. Rev. E*, **77**, 041507.

Méndez-Sánchez, A. F., López-González, M. R., Rolón-Garrido, V. H., Pérez-González, J. and de Vargas, L. (2003), "Instabilities of micellar systems under homogeneous and non-homogeneous flow conditions", *Rheol. Acta*, **42**(6), 56–63.

Morozov, A. N. and van Saarloos, W. (2005), "Subcritical Finite-Amplitude Solutions for Plane Couette Flow of Viscoelastic Fluids", *Phys. Rev. Lett.*, **95**, 024501.

Morozov, A. N. and van Saarloos, W. (2007), "An introductory essay on subcritical instabilities and the transition to turbulence in visco-elastic parallel shear flows", *Physics Reports*, **447**, 112 – 143.

Moyers-González, M., Owens, R. and Fang, J. (2009), "On the high frequency oscillatory tube flow of healthy human blood", *J. Non-Newtonian Fluid Mech.*, **163**, 45–61.

Müller, A. (1954), "Über die Verwendung des Pitot-Rohres zur Geschwindigkeitsmessung", *Helv Physiol Acta*, **12**, 98–111.

Nghe, P., Degré, G., Tabeling, P. and Ajdari, A. (2008), "High shear rheology of shear banding fluids in microchannels", *Appl. Phys. Lett.*, **93**(20), 204102.

Ober, T. J., Soulages, J. and McKinley, G. H. (2011), "Spatially resolved quantitative rheo-optics of complex fluids in a microfluidic device", *J. Rheol.*, **55**(5), 1127–1159.

Ohmi, M., Iguchi, M., Kakehasi, K. and Masuda, T. (1982), "Transition to turbulence and velocity distribution in an oscillating pipe flow", *Bull. of the JSME*, **25**, 365–371.

Olmsted, P. D. (2008), "Perspectives on shear banding in complex fluids", *Rheol. Acta*, **47**(3), 283–300.

Pakdel, P. and McKinley, G. (1996), "Elastic instability and curved streamlines", *Phys. Rev. Lett.*, **77**, 2459:1–4.

Pan, L., Morozov, A., Wagner, C. and Arratia, P. E. (2012), "A nonlinear elastic instability in channel flows at low Reynolds numbers", *arXiv:1204.4660 [physics.flu-dyn]*, .

Panadès, C., Marquès, F. and López, J. (2011), "Transitions to three-dimensional flows in a cyclinder driven by oscillations of the sidewall", *J. Fluid Mech.*, **681**, 515– 536.

Phan-Thien, N. (1978), "Pulsating flow of polymeric fluids", *J. Non-Newtonian Fluid Mech.*, **4**, 167–176.

Phan-Thien, N. (1980), "Flow enhancement mechanisms of a pulsating flow of non-Newtonian liquids", *Rheol. Acta*, **19**, 285–290.

Phan-Thien, N. (1981), "On a pulsating flow of polymeric fluids: strain–dependent memory kernels", *J. Rheol.*, **25**, 293–314.

Phan-Thien, N. and Dudek, J. (1982a), "Pulsating flow revisited", *J. Non-Newtonian Fluid Mech.*, **11**, 147–161.

Phan-Thien, N. and Dudek, J. (1982b), "Pulsating flow of a plastic fluid", *Nature*, **296**, 843–844.

Pipe, C. J., Kim, N. J., Vasquez, P. A., Cook, L. P. and McKinley, G. H. (2010), "Wormlike micellar solutions: II. Comparison between experimental data and scission model predictions", *J. Rheol.*, **54**(4), 881 – 913.

Pipe, C. J., M. T. and McKinley, G. H. (2008), "High shear rate viscometry", *Rheol. Acta*, **47**, 62–642.

Porte, G., Berret, J.-F. and Harden, J. L. J. (1997), "Inhomogeneous flows of complex fluids: Mechanical instability versus non-equilibrium phase transition", *Phys. II*, **7**, 459 – 472.

Prasad, A.K., J. K. (1995), "Scheimpflug stereocamera for particle image velocimetry to liquid flows", *Appl. Optics*, **34**, 7092–2074.

Radulescu, O., Olmsted, P. D., Decruppe, J. P., Lerouge, S., Berret, J.-F. and Porte, G. (2003), "Time scales in shear banding of wormlike micelles", *Eur. Phys. Lett.*, **62**, 230–236.

Raffel, M., Willert, C., Werely, S. and Kompenhans, J. (2007), *Particle Image Velocimetry, A Practical Guide*, Springer.

Rehage, H. and Hoffmann, H. (1991), "Viscoelastic Surfactant Solutions - Model Systems for Rheological Research", *Molec Phys*, **74**(5), 933–973.

Rosenfeld, M., Rambod, E. and Gharib, M. (1998), "Circulation and formation number of laminar vortex rings", *J. Fluid Mech.*, **376**, 297–318.

Salmon, J.-B., Colin, A. and Manneville, S. (2003), "Velocity Profiles in Shear-Banding Wormlike Micelles", *Phys. Re.v Lett.*, **90**(22), 228303:1–4.

Sergeev, S. (1966), "Fluid oscillations in pipes at moderate Reynolds numbers", *Fluid Dyn.*, **1**, 121–122.

Shaqfeh, E. S. G. (1996), "Purely elastic instabilities in viscometric flows", *Annu. Rcv. Fluid. Mech.*, **28**, 129–185.

Shariff, K., L. A. (1987), "Vortex Rings", *Annu. Rev. Fluid Mech.*, **24**, 235–279.

Shikata, T., Hirata, H., Takatori, E. and Osaki, K. (1988), "Nonlinear viscoelastic behavior of aqueous detergent solutions", *J. Non-Newtonian Fluid Mech.*, **28**, 171–182.

Siginer, A. (1991), "On the pulsating pressure gradient driven flow of viscoelastic liquid", *J. Rheol.*, **35**, 271–311.

Stokes, G. G. (1851), "On the effect of the internal friction of fluids on the motion of pendulums", *Trans. Camb. Phil. Soc.*, **9**, 8.

Tapadia, P., Ravindranath, S. and Wang, S. Q. (2006), "Banding in entangled polymer fluids under oscillatory shearing", *Phys. Rev. Lett.*, **96**, 196001,1:4.

Thurston, G. (1975), "Elastic effects in pulsatile blood flow", *Microvas. Res.*, **9**, 145–157.

Thurston, G. (1976), "The effects of frequency of oscillatory flow on the impedance of rigid, blood-filled tubes", *Biorheology*, **13**, 191–199.

Thurston, G. B. (1959), "Theory of oscillation of a viscoelastic medium between parallel planes", *J. Appl. Phys.*, **30**, 1855–1860.

Thurston, G. B. (1960), "Theory of oscillation of a viscoelastic fluid in a circular tube", *J. Acoust. Soc. Am.*, **32**, 210–213.

Torralba, M., Castrejón-Pita, a., Hernández, G., Huelsz, G., del Río, J. and Ortín, J. (2007), "Instabilities in the oscillatory flow of a complex fluid", *Phys. Rev. E*, **75**(5), 1–9.

Torralba, M., Castrejón-Pita, J., Castrejón-Pita, a., Huelsz, G., del Río, J. and Ortín, J. (2005), "Measurements of the bulk and interfacial velocity profiles in oscillating Newtonian and Maxwellian fluids", *Phys. Rev. E*, **72**(1), 1–9.

Truesdell (1953), "Notes on the History of the General Equations of Hydrodynamics", *The American Mathematical Monthly*, **60**, 445–458.

Tsiklauri, D. and Beresnev, I. (2001a), "Enhancement in the dynamic response of a viscoelastic fluid flowing through a longitudinally vibrating tube", *Phys. Rev. E*, **63**, 046304.

Tsiklauri, D. and Beresnev, I. (2001b), "Non-Newtonian effects in the peristaltic flow of a Maxwell fluid", *Phys. Rev. E*, **64**, 036303.

Vasquez, P. A., Cook, L. P. and McKinley, G. H. (2007), "A network scission model for wormlike micellar solutions:I. Model formulation and viscometric flow predictions", *J. Non-Newtonian Fluid Mech.*, **144**, 122–139.

Waigh, T. (2007), *Applied Biophysics. A molecular Approach for Physical Scientists*, Chichester: Wiley.

Womersley, J. R. (1955), "Method for the calculation of velocity, rate of flow and viscous drag in arteries when the pressure gradient is known", *J. Physiol.*, **127**, 553–563.

Yamamoto, T., Hashimoto, T. and Yamashita, A. (2008), "Flow analysis for wormlike micellar solutions in an axisymmetric capillary channel", *Rheol. Acta*, **47**(9), 963–974.

Yesilata, B., Clasen, C. and McKinley, G. H. (2006), "Nonlinear shear and extensional flow dynamics of wormlike surfactant solutions", *J. Non-Newtonian Fluid Mech*, **133**(2-3), 73–90.